Imaging p53 in Pancreatic Ductal Adenocarcinoma



Sofia Koustoulidou

St Peter's College

University of Oxford

A thesis submitted for the degree of

Doctor of Philosophy

Trinity Term 2017

Contents

Dedication **xiv**

Acknowledgements **xv**

Abstract **xvii**

Abbreviations **xix**

1 General introduction **1**

1.1 Cancer 2

1.2 Pancreatic cancer 3

1.2.1 Risk factors 3

1.2.2 Anatomy and physiology of the pancreas 5

1.3 Pancreatic ductal adenocarcinoma 6

1.3.1 Molecular background 9

1.3.1.1 The MAPK pathway 11

1.3.1.2 p16^{Ink4A} and cell cycle regulation in PDAC 13

1.3.1.3 SMAD4 and TGF-β signaling 14

1.4 The p53 tumour suppressor 15

1.4.1 p53 as a transcription factor 16
1.4.2 The p53-MDM2 interaction 18
1.4.3 Response to DNA damage 19
1.4.4 p53 in cell cycle regulation and apoptosis 22
1.4.5 p53 and cellular senescence 23
1.4.6 p53 and PDAC 24
1.5 Diagnosis and therapy of PDAC 25
1.6 Clinical implications of p53 imaging in PDAC 28
1.7 Molecular imaging 30
1.7.1 SPECT imaging 32
1.8 Antibodies as imaging agents 34
1.9 Cell penetrating peptides 36
1.9.1 Uptake mechanisms of CPPs 38
1.9.1.1 Direct penetration 39
1.9.1.2 Endocytosis 40
1.9.2 The TAT peptide 42
1.10 Aims of the study 43

2 General materials and methods 45

2.1 Cell lines and cell culture reagents 46
2.1.1 Cell line maintenance 46
2.1.2 Cryopreservation and storage of cells 47
2.2 Cell culture plasticware 48

2.3 Antibodies 48
2.4 Western blotting 49
2.4.1 Lysis buffer 49
2.4.2 SDS loading sample buffer (5 ×) 49
2.4.3 NuPAGE® MES SDS running buffer (20 ×) 50
2.4.4 NuPAGE® Transfer Buffer (20 ×) 50
2.4.5 Cell pellet preparation 50
2.4.6 Whole cell extraction 51
2.4.7 Bradford protein assay 51
2.4.8 Sample loading 52
2.4.9 Electrophoresis 52
2.4.10 Protein transfer 52
2.4.11 Membrane blocking and antibody probing 53
2.4.12 Enhanced chemiluminescence detection 54
2.5 Sub-cellular protein fractionation 55
2.6 Statistical analysis 56

3 Imaging p53 – *in vitro* antibody validation 57

3.1 Introduction 58
3.2 Materials and methods 60
3.2.1 p53 detection with flow cytometry 60
3.2.1.1 Data acquisition and analysis 61
3.2.2 siRNA-mediated gene silencing 61

3.2.3 Immunocytochemistry 62
3.2.3.1 p53 staining 62
3.2.4 Enzyme linked immunosorbent assay 63
3.2.5 Statistical analysis 64
3.3 Results 64
3.3.1 Validation of the anti-p53(1C12) antibody 64
3.3.1.1 Western blot analysis 65
3.3.1.2 Flow cytometric analysis 67
3.3.1.3 Evaluation by siRNA-mediated protein knockdown . 69
3.3.2 Intracellular localisation of p53 using confocal microscopy . . . 70
3.3.3 Evaluation of antibody affinity by ELISA 72
3.4 Discussion 74
3.5 Conclusions 77

4 Synthesis and *in vitro* validation of radioconjugates 79

4.1 Introduction 80
4.2 Materials and methods 83
4.2.1 Conjugation to TAT cell penetrating peptide 83
4.2.2 Antibody labelling with the Cy3-NHS dye 85
4.2.2.1 Evaluation of conjugation efficiency by SDS-PAGE . 86
4.2.3 *In vitro* evaluation of TAT internalisation 87
4.2.4 Immunoreactivity of TAT-conjugated anti-p53 (1C12) antibody 88
4.2.5 Synthesis of radioconjugates 88

4.2.5.1 Conjugation to *p*-SCN-Bn-DTPA 88
4.2.5.2 Radiolabelling with $^{111}InCl_3$ 89
4.2.5.3 Quality control by iTLC 90
4.2.5.4 Isotopic dilution assay 90
4.2.5.5 *In vitro* stability in serum 91
4.2.5.6 Retention of ^{111}In-labelled radioconjugates *in vitro* . 92
4.2.6 Resazurin cell viability assay 92
4.2.7 Statistical analysis 94
4.3 Results 94
4.3.1 Evaluation of the TAT internalisation properties 94
4.3.2 Immunoreactivity of TAT-conjugated antibody 98
4.3.3 Binding affinity of BnDTPA-p53 (1C12)-TAT 100
4.3.3.1 Radiochemical purity of ^{111}In-labelled antibodies . . . 102
4.3.3.2 *In vitro* stability of ^{111}In-labelled antibodies 103
4.3.3.3 Retention of ^{111}In-labelled antibodies 105
4.3.3.4 Effect of BnDTPA-p53 (1C12)-TAT on cell viability . 107
4.4 Discussion 108
4.4.1 Conjugation of cell penetrating peptide facilitates intracellular delivery 109
4.4.2 Evaluation of radiolabelling with ^{111}In 111
4.5 Conclusions 114

5 *In vivo* imaging of p53 **117**

5.1 Introduction 118
5.2 Materials and methods 121
5.2.1 Animal models 121
5.2.1.1 Cell preparation for inoculations 122
5.2.1.2 KPC tumour allograft models 122
5.2.2 The KPC genetically engineered mouse model 123
5.2.2.1 KPC mice screening 124
5.2.3 SPECT imaging–NanoSPECT/CT^{PLUS} 124
5.2.3.1 *Ex vivo* biodistribution studies 125
5.2.3.2 Image analysis 126
5.2.4 PET/SPECT imaging–VECTor^{4}CT 126
5.2.4.1 Image analysis 127
5.2.5 Staining of tissue sections 127
5.2.5.1 Autoradiography and histology 128
5.2.5.2 Immunofluorescence staining of frozen mouse sections 129
5.2.5.3 Lysis of tissue for western blot analysis 130
5.2.6 Statistical analysis 130
5.3 Results 130
5.3.1 *In vivo* evaluation in the KPC-allograft mouse model 130
5.3.1.1 Growth rate of the subcutaneous KPC-tumours . . . 131
5.3.1.2 *Ex vivo* biodistribution analysis 131
5.3.1.3 SPECT imaging 134
5.3.2 *In vivo* optimisation 139

5.3.2.1 p53 expression in B8484 and P2FIR allograft tissue . 144
5.3.2.2 Tissue distribution of ^{111}In-activity in B8484 and P2FIR allograft tumours 147
5.4 Discussion 149
5.4.1 Imaging p53 in KPC-derived cell line allografts 150
5.5 Conclusions 156

6 *In vivo* imaging of extracellular targets 158

6.1 Introduction 159
6.2 Materials and methods 163
6.2.1 Cell lines 163
6.2.2 Animal models 163
6.2.3 Antibody conjugation and radiolabelling 164
6.2.4 SPECT imaging 164
6.2.5 Statistical analysis 165
6.3 Results 165
6.3.1 Biodistribution of ^{111}In-BnDTPA-T1-116C 165
6.3.2 SPECT imaging 167
6.4 Discussion 171
6.5 Conclusions 173

7 Summary and future work 174

7.1 Summary 175
7.1.1 Unravelling TAT 176

7.1.2 Imaging p53 as a diagnostic tool 178

7.1.3 Extracellular versus intracellular targets 179

7.2 Future work 180

Bibliography **184**

A Appendix **235**

A.1 Full developed gel 235

A.2 *In vitro* reproducibility 236

A.3 Sub-cellular fractionation 236

A.4 Imaging of KPC genetically engineered mouse models 237

A.4.1 Tissue distribution of ^{111}In-BnDTPA-p53 (1C12)-TAT in the KPC model 241

List of Figures

1.1 Anatomy and location of the pancreas in the human body. 6

1.2 Progression model of PDAC. 10

1.3 The MAPK pathway. 12

1.4 The $p16^{Ink4A}$ in cell cycle regulation. 14

1.5 The TGF-β pathway. 15

1.6 Schematic representation of the domain structure of p53. 17

1.7 p53 response to cellular stress and its subsequent regulation of different mechanisms. 20

1.8 Cellular uptake mechanisms of CPPs. 38

3.1 Antibody validation by western blot. 65

3.2 p53 protein expression levels in B8484, P2FIR and MEF cell lines. . . 66

3.3 Antibody validation using flow cytometry. 68

3.4 Antibody validation by siRNA-mediated knockdown. 69

3.5 Intracellular localisation of p53 in KPC-derived cell lines. 71

3.6 Evaluation of non-specific fluoresence in B8484-KPC derived cells. . . 72

3.7 Evaluation of binding affinity by ELISA. 73

4.1 Antibody-TAT conjugation *via* EDC/Sulfo-NHS chemistry. 84

4.2 Chemical structures of EDC and Sulfo-NHS. 84

4.3 Cy3 mono NHS ester 86

4.4 Chemical structure of S-2-(4-Isothiocyanatobenzyl)- diethylenetriamine pentaacetic acid (*p*-SCN-Bn-DTPA) 89

4.5 Radiolabelling with $^{111}InCl_3$. 90

4.6 Resazurin cell viability assay principle. 93

4.7 Conjugation of Cy3 dye to anti-p53 (1C12)-TAT. 95

4.8 Cellular localisation of IgG_1-TAT-Cy3 over time in B8484 cells. 96

4.9 Cellular localisation of IgG_1-TAT-Cy3 over time in P2FIR cells. 97

4.10 Cellular localisation of anti-p53 (1C12)-TAT-Cy3 and anti-p53 (1C12)-Cy3 in B8484 and P2FIR cells. 99

4.11 Immunoreactivity of anti-p53 (1C12)-TAT by western blot analysis. . 100

4.12 Determination of the BnDTPA-p53 (1C12)-TAT binding affinity. . . . 101

4.13 iTLC chromatograms of ^{111}In-BnDTPA-p53 (1C12)-TAT. 102

4.14 Stability of ^{111}In-BnDTPA-p53 (1C12)-TAT. 104

4.15 Cellular retention of ^{111}In-BnDTPA-p53 (1C12)-TAT. 106

4.16 Resazurin cell viability assay upon treatment with BnDTPA-p53 (1C12)-TAT. 108

5.1 Tumour growth curves of the B8484 and P2FIR allograft-bearing mice. 131

5.2 *Ex vivo* biodistribution and ROI analysis of ^{111}In-BnDTPA-p53 (1C12)-TAT. 133

5.3 Region of interest (ROI) analysis of selected tissues of SPECT images. 135

5.4 Whole-body SPECT MIPs showing biodistribution of ^{111}In-BnDTPA-p53 (1C12)-TAT in B8484 allograft-bearing mice. 137

5.5 Whole-body SPECT MIPs showing biodistribution of ^{111}In-BnDTPA-p53 (1C12)-TAT in P2FIR allograft mice. 138

5.6 Repetition of ^{111}In-BnDTPA-p53 (1C12)-TAT biodistribution. 140

5.7 Representative MIP SPECT images of B8484 and P2FIR allograft-bearing mice 72 h post-injection with ^{111}In-labelled conjugates. 142

5.8 Tumour-to-blood (T/B) uptake ratios 72 h after administration of ^{111}In-labelled conjugates. 143

5.9 Western blot analysis of tissue extracts from B8484 and P2FIR allograft tumours. 144

5.10 Immunohistochemical analysis of p53 expression levels in allograft tumours. 146

5.11 *Ex vivo* autoradiography and H&E histology images of ^{111}In-BnDTPA-p53 (1C12)-TAT and ^{111}In-BnDTPA-IgG$_1$-TAT distribution in B8484 tumours. 148

5.12 *Ex vivo* autoradiography and H&E histology images of ^{111}In-BnDTPA-p53 (1C12)-TAT and ^{111}In-BnDTPA-IgG$_1$-TAT distribution in P2FIR tumours. 149

6.1 Schematic representation depicting the antigens presented by the MHC class-I molecules. 160

6.2 Biodistribution of ^{111}In-BnDTPA-T1-116C and ^{111}In-BnDTPA-IgG2a in MDA-MB-468 and MDA-MB-231 breast cancer xenograft-bearing mouse models. 166

6.3 Representative SPECT maximum intensity projections of ^{111}In-BnDTPA-T1-116C in MDA-MB-468 xenograft-bearing mice. 168

6.4 Representative SPECT maximum intensity projections of ^{111}In-BnDTPA-T1-116C in MDA-MB-231 xenograft-bearing mice. 169

6.5 Tumour uptake and tumour-to-blood ratios for ^{111}In-BnDTPA-T1-116C as determined by ROI analysis. 170

A.1 Full developed film of p53 protein expression levels. 235

A.2 p53 protein expression levels in B8484 and P2FIR KPC-derived cells. 236

A.3 Sub-cellular fractionation in B8484 KPC-derived cell line. 236

A.4 Identification of pancreatic tumours by MRI. 237

A.5 *Ex vivo* biodistribution analysis showing uptake of ^{111}In-BnDTPA-p53 (1C12)-TAT in KPC mice 72 h post-injection. 238

A.6 *Ex vivo* Biodistribution of ^{18}F-FDG in the KPC mouse model. 239

A.7 *In vivo* imaging of the KPC mice by SPECT/PET/CT. 240

A.8 Distribution of ^{111}In-BnDTPA-p53 (1C12)-TAT in the pancreas of a KPC mouse model. 241

A.9 Distribution of ^{111}In-BnDTPA-p53 (1C12)-TAT in the dissected pancreatic tumour of a KPC mouse model. 242

A.10 Endogenous p53 expression levels in KPC-derived tissues. 243

List of Tables

1.1 Commonly affected genes and their associated signaling pathways in PDAC. 11

1.2 Advantages and disadvantages of imaging modalities. 31

1.3 The most well-studied CPPs their origin and sequences. 37

2.1 Anti-p53 (1C12) mouse mAb-Product information. 48

2.2 List of anti-p53 antibodies tested and applications. 49

2.3 Antibody dilutions applied for western blotting. 54

Στην οικογένειά μου,

στην οικογένεια Κλικλίκου.

Acknowledgements

First and foremost, I would like to thank Prof. Bart Cornelissen for giving me the opportunity to undertake this project. Without his trust, encouragement and constant support the completion of this thesis would not have been possible. Thank you for all the help, patience, and guidance not only through my adventure into scientific research but also for teaching me a great deal of important lessons in life; thank you for believing in me (I promise I will improve my maths ☺). Many thanks to Prof. Eric O'Neill for his help and advice. A big thanks goes to Cancer Research UK and Medical Research Council for funding this project.

I would like to thank all the amazing people of the Cornelissen's group. A very big thanks goes to Mike (you finally got rid of the Greek ☺), James, and Cristina for all the help. I will miss the grumpiness, the laughs, and the monkey photos ☺. Thanks to Mary-Ann, the best desk partner that you could possibly ask for. Many thanks to Mat for all the cakes and a big thanks to Elvin for his contribution to this project. I am eternally grateful to the "Heathers": Julia, Sam, and Deb. Thank you for all the encouragement, for making my days enjoyable, and for improving the ethanol tolerance of my liver ☺. I could not have asked for better colleagues, thank you all!

I would also like to thank all the members of the Vallis group, especially Nadia (your advice was invaluable), Bas and Martin for all the TAT conversations. Thanks to the imaging core team, especially Veerle, Danny, and Ana whose help was priceless. Also, a big thanks goes to the Greek gang of the RRI, Christina, Kleopatra, and Irini for making me feel less homesick. Σας ευχαριστώ πολύ για όλα.

A big thanks to Fatimah for being a great friend since the first day I arrived to the U.K. Thanks to Siobhan, my eternal animal party ☺. Shivons you still owe me a bingo game! Thanks to Bruno, Carina, Mattia, Michela, Arnaud, and Emma for the good times we spent together.

Very special thanks must go to Giulia and Daniel. Your support and encouragement was worth more than I could possibly express on paper. Thank you for being there for me in every moment of this journey. It has been a great privilege to have met you and I am sure we will have much more to experience together ☺.

Many thanks to my friend Ioanna. Ιωάννα μου σε ευχαριστώ ατελείωτα μέσα από καρδιάς για τη συνεχή συμπαράσταση.

Ευχαριστώ απέραντα τους γονείς μου και την τρελή τρελή οικογένειά μου ☺, χωρίς την βοήθεια των οποίων δεν θα τα είχα καταφέρει. Σας ευχαριστώ μέσα απο την καρδία μου για τη στήριξη και αγάπη που δείξατε όλα αυτά τα χρόνια. Σας ευχαριστώ που πιστέψατε σε μένα! Σας αγαπώ όλους μέχρι το φεγγάρι ☺.

Last, but certainly not least, my deepest thanks goes to my partner Victor. I know I promised not to be too emotional but without you this would not have been possible. Thank you for all the love and support (and I don't mean the diet only ☺), thank you for keeping me sane (I am sure you lost yours ☺). Words are not enough...Thank you!

To all of you THANK YOU! Ευχαριστώ!

Abstract

Imaging p53 in Pancreatic Ductal Adenocarcinoma
A thesis submitted in partial fulfillment for the requirements of the degree of Doctor of Philosophy
Trinity Term 2017
Sofia Koustoulidou, St Peter's College

Pancreatic ductal adenocarcinoma (PDAC) represents 90% of pancreatic cancer cases and is characterised by poor survival rates and resistance to current therapeutic regimes as the majority of patients present with an already advanced disease at the time of diagnosis. Mutations of the *TP53* tumour suppressor gene are a frequent event in tumourigenesis and appear in around 75% of pancreatic cancer cases just before the full development of PDAC and metastasis into the surrounding tissues. Molecular imaging tools, such as SPECT, using monoclonal antibodies specific towards tumour associated antigens, could aid the *in vivo* characterisation of biological processes and provide a non-invasive method for early diagnosis of cancer.

Toward this end, a commercially available mouse monoclonal antibody against total p53 protein (anti-p53 (1C12)) was selected. Anti-p53 (1C12) was first evaluated *in vitro* regarding its specificity and affinity in cell lines with variable p53 status, derived from a genetically engineered mouse model of PDAC (KPC mice). The subcellular localisation of the p53 protein in the cell lines used was also studied.

Following the selection of the antibody, the anti-p53 (1C12) was conjugated to the cell penetrating peptide TAT to facilitate cellular and nuclear translocation and then to *p*-SCN-Bn-DTPA to allow labeling with ^{111}In. Further *in vitro* evaluation was performed on the conjugated antibody, conferring subcellular translocation in fixed cells, unaffected binding affinity, favourable radiochemical yield and purity, and stability of the radioconjugate in serum. Retention of the radioconjugates was also observed and was significantly different when compared to radiolabeled non-specific IgG_1-TAT in cells harbouring mutant p53.

The ability of ^{111}In-BnDTPA-p53 (1C12)-TAT to selectively target endogenously expressed p53 was assessed *in vivo* using mouse allograft tumour models of the cell lines

evaluated *in vitro*, and in genetically engineered KPC mice. This provided a preliminary "proof-of-principle" concept for diagnostic detection of PDAC. The knowledge acquired from the current study may be used to develop a first imaging tracer against p53 which could significantly improve the biological evaluation of cancer.

Abbreviations

alt-EJ – Alternative end-joining

ATM – Ataxia telangiectasia mutated

ATR – Ataxia telangiectasia Rad3-related

BCL-2 – B-cell lymphoma 2

BER – Base excision repair

BRCA1/2 – Breast and ovarian cancer susceptibility protein 1/2

BSA – Bovine serum albumin

bSSFP – Balanced steady-state free precession

CA19-9 – Carbohydrate antigen 19-9

CBP/p300 – CREB-binding protein/p300

CDK – Cyclin dependant kinase

CDKN2A – Cyclin dependant kinase inhibitor 2A

CEA – Carcinoembryonic antigen

CEB – Cell extraction buffer

CPP – Cell penetrating peptide

CT – Computed tomography

DAPI – 4',6-diamidino-2-phenylindole

DMEM – Dulbecco's modified Eagle's medium

DMSO – Dimethyl sulfoxide

DNA – Deoxyribonucleic acid

DNA-PK – DNA-dependant protein kinase

DSBs – Double strand breaks

ECL – Enhanced chemiluminescence

EDC – 1-ethyl-3-(3-dimethylaminopropyl)carbodiimide hydrochloride

EDTA – Ethylenediaminetetraacetic acid

ELISA – Enzyme linked immunosorbent assay

$\mathbf{e}_n$ – Embryonic day n

EPR – Enhanced permeability and retention

ER – Endoplasmic reticulum

ERK 1/2 – Extracellular signal-regulated kinase 1/2

FBS – Foetal bovine serum

FDA – Food and drug administration

^{18}**F-FDG** – 2-deoxy-2-[^{18}F]fluoro- D-glucose

FIAU – 2'-fluoro-2'-deoxy-1beta-D-arabinofuranosyl-5-iodouracil

FM – Fluorescein-5-maleimide

FOV – Field of view

FSC-A – Forward-scatter linear area

FSC-H – Forward-scatter area

FSC-W – Forwrad-scatter linear width

GADD45 – Growth arrest and DNA damage 45

GDP – Guanosine diphosphate

GOF – Gain of function

GRB2 – Growth factor receptor-bound protein 2

GTP – Guanosine triphosphate

HCl – Hydrogen chloride

HDM2 – Human double minute 2 homologue

H&E – Hematoxylin and eosin

HEPES – 4-(2-hydroxyethyl)-1-piperazineethanesulfonic acid

HER-2/neu – Human epidermal growth factor receptor 2

HIV – Human immunodeficiency virus

HLA – Human leukocyte antigen

HR – Homologous recombination

HRP – Horseradish peroxidase

HS – Heparan sulfates

ICC – Immunocytochemistry

ID/g – Injected dose per gram

IHC – Immunohistochemistry

IP – Immunoprecipitation

IPMNs – Intraductal papillary mucinous neoplasms

iTLC – Instant thin layer chromatography

i.v. – Intravenous

JNK – C-Jun N-terminal kinase

KCl – Potassium chloride

KPC – *LSL-Kras*$^{G12D/+}$, *LSL-Trp53*$^{R172H/+}$, *Pdx-1-Cre*

KRAS – Kirsten rat sarcoma viral oncogene homologue

LSL – Lox-Stop-Lox cassette

mAb – Monoclonal antibody

MAPs – Model amphipathic peptides

MAPK – Mitogen activated protein kinase

MCNs – Mucinous cystic neoplasms

MDM2 – Mouse double minute 2 homologue

MEB – Membrane extraction buffer

MEF – Mouse embryonic fibroblast

MEK – MAPK/ERK kinase

MES – 2-(N-morpholino)ethanesulfonic acid

MHC – Major histocompatibility complex

MIF – Median fluorescence intensity

MRI – Magnetic resonance imaging

MRN – Mre-11/Rad50/NBS1

NaI(Tl) – Sodium iodide doped with thallium

NaOH – Sodium hydroxide

NEB – Nuclear extraction buffer

NHEJ – Non-homologous end-joining

NLS – Nuclear localisation sequence

NOXA – Phorbol-12-myristate-13-acetate-induced protein 1

PanINs – Pancreatic intraepithelial neoplasias

PBS – Phosphate-buffered saline

PCR – Polymerase chain reaction

PCV – Packed cell volume

PDAC – Pancreatic ductal adenocarcinoma

Pdx-1 – Pancreatic and duodenal homeobox-1

PET – Positron emission tomography

PFA – Paraformaldehyde

PI – Propidium iodide

PMTs – Photomultiplier tubes

PNA – Peptide-nucleic acid

PSMA – Prostate-specific membrane antigen

PTDs – Protein transduction domains

PUMA – p53 upregulated modulator of apoptosis

PVDF – Polyvinylidene fluoride

PVE – Partial volume effect

pVEC – Peptide from vascular endothelium cadherin protein

Raf – Rapidly accelerated fibrosarcoma

Rb – Retinoblastoma protein

ROI – Region of interest

s.c. – Subcutaneous

SDS – Sodium dodecyl sulfate

SEM – Standard error of mean

Ser – Serine

siRNA – Small interfering RNA

SMAD4 – Mothers against decapentaplegic homologue 4

SOS – Son of sevenless

SPECT – single photon emission computed tomography

SSBs – Single strand breaks

SSC-H – Side-scatter area

Sulfo-NHS – N-hydroxysulfosuccinimide

SV40 – Simian virus 40

TAD – Transactivation domain

TAP – Transporter associated with antigen presentation

TAT – Trans-activator of transcription

TCR – T cell receptor

TE – Echo time

TGF-β – Transforming growth factor beta

TMB – 3,3',5.5'-tetramethylbenzidine

TNB – Tris-NaCl buffer

TR – Time internal

Tris – 2-Amino-2-(hydroxymethyl)propane-1,3-diol

US – Ultrasound

VEGFR2 – Vascular endothelial growth factor receptor 2

Chapter 1

General introduction

1.1 Cancer

Cancer, a name given to a set of diseases characterised by abnormal cell proliferation, is one of the leading causes of mortality worldwide with the number expected to increase by 70% in the next two decades (Vineis and Wild, 2014). Despite improvements in treatment, the cancer burden still persists, highlighting the need to address the problem through a preventive approach (Umar et al., 2012). The expected increase has been attributed to several factors such as ageing population and changes in the distribution of risk factors (e.g. spread of tobacco use in low-income and middle-income countries), making cancer a complex public health problem (Mayne et al., 2016).

With the knowledge accumulated through years of cancer research, it is commonly agreed that it is a disease which involves dynamic changes in the genome. In their seminal review, Hanahan and Weinberg suggested six hallmarks of cancer (Hanahan and Weinberg, 2000), with two additional hallmarks added later (Hanahan and Weinberg, 2011), that provided a stepping stone for the understanding of the biology of the disease. These are: i. sustained proliferation, ii. evasion of apoptosis, iii. resistance to cell death, iv. angiogenesis, v. invasion and metastasis, vi. replicative immortality, vii. deregulation of cellular energetics and metabolism, and viii. avoidance of immune destruction. Genomic instability and mutation as well as inflammation caused by cells of the immune system, were also described as important contributors towards the acquisition of hallmark characteristics (Kerr et al., 2016). Most forms of cancer require the combination of the aforementioned hallmarks, each one serving a

unique role in promoting the development, progression, and resistance of tumours.

1.2 Pancreatic cancer

Pancreatic cancer is the 7th most common cancer worldwide and 11th in the UK with an estimated 5-year survival of less than 5%. It is the 5th most common cause of cancer death and accounts for 9,618 new cases in 2014 in the UK and more than 338,000 in the world (2012), more than 50% of which occurred in high income countries (Ilic and Ilic, 2016). It typically affects the elderly, affecting mostly males (5% of all male cancer deaths). Reported incidence rates have increased since the 1970s largely thanks to improvements in available diagnostics (Kleeff et al., 2016). However, the diagnostic technology is not good enough to improve the outcome of the disease.

1.2.1 Risk factors

Most pancreatic cancer cases are attributed to two key risk factor groups: host and environmental (Midha et al., 2016). Age is the main host risk factor with more than 90% of cases occurring in patients of > 40 years of age, while the younger group tend to include cases with underlying genetic predisposition (Krejs, 2010). Gender (more common in males than females), ethnicity, blood group (lower risk for group O) are amongst the rest of host risk factors responsible for pancreatic cancer. Like other cancers, pancreatic cancer is a genetic disease caused by both inherited and acquired genetic mutations. More than 80% of the cases develop due to sporadically occurring mutations while a small number is due to inherited genetic alterations. Mu-

tations in breast and ovarian cancer susceptibility protein 1/2 (*BRCA1* and *BRCA2*) genes were found to be linked to pancreatic cancer, though less strongly than other types. Increased risk has been also found to be associated with familial cancer syndromes (e.g. cystic fibrosis, pancreatitis, breast and ovarian cancer, fanconi anaemia, Li-Fraumeni syndrome) (Turati et al., 2013). Chronic pancreatitis shows a direct association to pancreatic cancer (13-fold increased risk) (Dhar et al., 2015), as inflammatory processes occurring during pancreatitis are known to support the development of genetic alterations and promote carcinogenesis. Hereditary pancreatitis has been characterised by mutations in the cationic trypsinogen (*PRSSI*) gene which were also identified in pancreatic cancer patients (Greer and Whitcomb, 2009). A number of epidemiological studies have also suggested a link between diabetes mellitus and pancreatic cancer (Huxley et al., 2005; Ben et al., 2011) with patients presenting a new-onset of diabetes to be at higher risk. Furthermore, diabetes can also act as a diagnostic factor as it is often caused by pancreatic cancer itself (Type 3c diabetes) (Bosetti et al., 2014).

Regarding environmental risk factors, tobacco smoking is highly associated with the incidence of pancreatic cancer as smokers have a two-fold higher risk of developing the disease when compared to non-smokers (Gandini et al., 2008). Obesity, dietary factors and alcohol (due to its connection to chronic pancreatitis) can also lead to increased risk for the disease (Casari and Falasca, 2015).

1.2.2 Anatomy and physiology of the pancreas

The pancreas is an organ of endodermal origin and the largest gland in the human body, lying in the back of the abdominal wall behind the stomach (Figure 1.1). Anatomically it is divided into the head, neck, body, and tail (Ellis, 2013) and is the main regulator of protein and carbohydrate digestion, and glucose homeostasis (Hezel et al., 2006). In particular, the exocrine pancreas, composed of a group of duct and acinar cells closely interlinked, produces fluids containing enzymes important for digestion that are secreted into the main pancreatic duct and from there to the duodenum. The endocrine pancreas, responsible for metabolism, consists of islet cells that generate hormones such as insulin and glucagon, regulating blood sugar levels. The exocrine tissue comprises 95% of the organ while the endocrine accounts for approximately 5%.

During embryonic development both endocrine and exocrine cells originate from the same precursors, the pancreatic progenitor cells (Pour et al., 2003) that arise from cells coming from the developing foregut (Wells and Melton, 1999). In mice, the development of pancreas becomes evident at approximately embryonic day 9 (e9) when epithelial buds appear on both sides of the foregut. The pancreatic buds then elongate across the duodenum and stomach, fusing into a single organ by e12.5. Finally, the proliferation of cells leads to an increase in size of the buds, forming branched tubular structures. These changes are accompanied by differentiation of endocrine, acinar, and ductal cells leading to organisation of the mature organ (Shih et al., 2013).

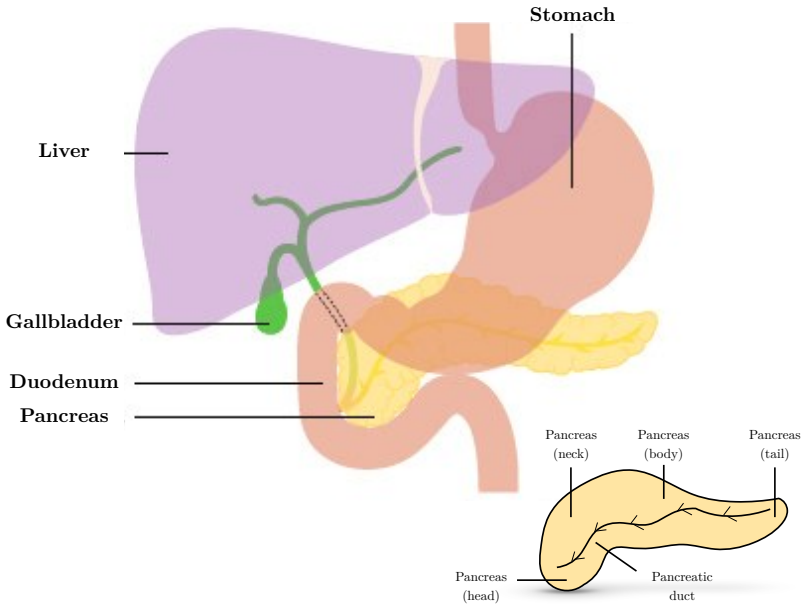

Figure 1.1: Anatomy and location of the pancreas in the human body. The pancreas lies behind the stomach and is divided into the head, neck, body, and tail. As a large gland, it produces juices and insulin that are excreted through the pancreatic duct and into the duodenum. Image adapted from Cancer Research UK (http://www.cancerresearchuk.org/about-cancer/pancreatic-cancer/about).

The vast majority of pancreatic neoplasms, approximately 95%, arise from the exocrine pancreas and of those pancreatic ductal adenocarcinoma (PDAC) represents 90% of all cases (Hidalgo et al., 2015).

1.3 Pancreatic ductal adenocarcinoma

Pancreatic ductal adenocarcinoma (PDAC) appears mainly at the head of the pancreas with often infiltration to the surrounding tissue, especially the spleen and the peritoneal cavity and metastasis to the liver and lungs (Hezel et al., 2006). The duct-like morphology of PDAC suggests the involvement of ductal cells at the origin of transformation even though some propose that the endocrine or acinar cells play a role as well (Hernńdez-Muñoz et al., 2008; Aichler et al., 2012).

Knowledge of the tumourigenesis of PDAC has significantly improved in the past years and it is now evident that it originates from several precursor lesions (Brosens and Offerhaus, 2013). Histological and genetic studies have reported three distinctive precursor lesions of ductal origin: pancreatic intraepithelial neoplasias (PanINs) within intralobular ducts, intraductal papillary mucinous neoplasms (IPMNs) in the main pancreatic duct, and mucinous cystic neoplasms (MCNs), epithelial mucin-producing neoplasms (Guerra and Barbacid, 2013).

The most studied precursor lesions are PanINs which appear at the head of the pancreas, and are usually smaller than 5 mm, a characteristic that distinguishes them from IPMNs, which are usually greater than 1 cm in size. Depending on the degree of cytologic atypia, PanINs can be classified into three main stages: PanIN-1, -2, and -3. PanINs can be further classified into PanIN-1A, characterised by a flat epithelium, and containing columnar mucinous cells with uniform nuclei, while PanIN-1B lesions show a more papillary-like architecture. The progression then leads to stage PanIN-2 neoplasms which present higher architectural disorganisation with loss of nuclear polarity and hyperchromasia, suggestive of intermediate grade dysplasia. Finally, PanIN-3 lesions show high grade dysplasia with great cytologic atypia, loss of nuclear polarity and hyperchromasia as in PanIN-2, and presence of mitotic figures (Hruban et al., 2000; De Wilde et al., 2012). These PanIN neoplasms are often surrounded by lobular parenchymal atrophy that could be used as a biomarker in patients at high risk (Brune et al., 2006).

IPMNs are characterised by papillary growths with thick mucin secretion and at risk of malignant transformation, usually appearing at the head of the pancreas (De Wilde

et al., 2012). Morphologically, they are divided into the main (MD-IPMN) and branch duct (BD-IPMN) types, according to their site of origin. MD-IPMN often show dilatation of the pancreatic duct (> 6 mm) contrary to BD-IPMN which show no signs of dilatation (Distler et al., 2014). IPMNs are classified into low-, intermediate-, high-grade dysplasia IPMN, and IPMN with associated carcinoma (Bosman et al., 2010).

MCNs are the least frequent precursor lesions, typically located in the pancreatic body and tail. MCNs are large cystic lesions where the epithelial lining consists of columnar cells with varying grades of dysplasia. One third of MCNs usually becomes invasive, most often forming ductal adenocarcinomas (Baker et al., 2012).

Distinction between PanINs and other neoplasms, such for example IPMNs, can be at times difficult. It has been hypothesised that both PanINs and IPMNs are biologically related processes affecting different areas of the duct, and that the former may act as a precursor for the development of IPMNs and therefore, can be morphologically insuperable (Xiao, 2012). Simultaneous appearance of PanINs and IPMNs is rare apart from PanIN-1 lesions that are common in atrophic areas near IPMNs. The prognosis for non-invasive IPMNs as well as MCNs is good and surgical treatment is often achievable (Haugk, 2010).

The morphological description of the precursor lesions in PDAC has allowed their characterisation by molecular genetic studies, further supporting the notion that PanINs are precursors to the progression towards invasive adenocarcinoma and that the increasing grades of dysplasia observed are accompanied by genetic alterations (Brosens et al., 2015).

1.3.1 Molecular background

Like other cancers, PDAC is predominantly a genetic disease caused by alterations in cancer-related genes (Ottenhof et al., 2011). The synergistic effect of mutations in tumour-suppressor genes, oncogenes, and genome maintenance genes results in the progression towards an invasive tumour. In 2000, Hruban *et al.* (Hruban et al., 2000) proposed a stepwise progression model for PDAC on the basis of the presence of alterations in cancer genes. The authors suggested the appearance of activating point mutation in the *KRAS* oncogene (G12D) (> 90%) as well as overexpression of the *HER-2/neu* (2.1%) gene product in pancreatic ductal lesions with minimal cytologic atypia (mainly PanIN-1) (Chou et al., 2013). The prevalence of these early occurring mutations in both *KRAS* and *HER-2/neu* increases with increasing degree of atypia which are followed by inactivation of the $p16^{Ink4A}$ tumour suppressor gene (approximately 95% of the cases) which occurs later during progression and correlates with severe cytologic atypia in ductal lesions. Patients with familial mutations in the *p16* gene show 22-fold higher risk of developing pancreatic cancer (Shi et al., 2009). Finally, loss of *TP53* (75%), *SMAD4 (DPC4)* (55%), and *BRCA2* (7-10%) genes are often observed in the later stages in PanIN-3 lesions and are characterised as the late events in the development of PDAC (Figure 1.2).

Later in 2008, Jones *et al.* (Jones et al., 2008) characterised a broader spectrum of the alterations involved in PDAC as well as the signalling pathways affected, that helped to unravel the complexity of the disease. More than 21,000 genes were screened from PDAC patient samples, which led to the identification of 63 genetic alterations

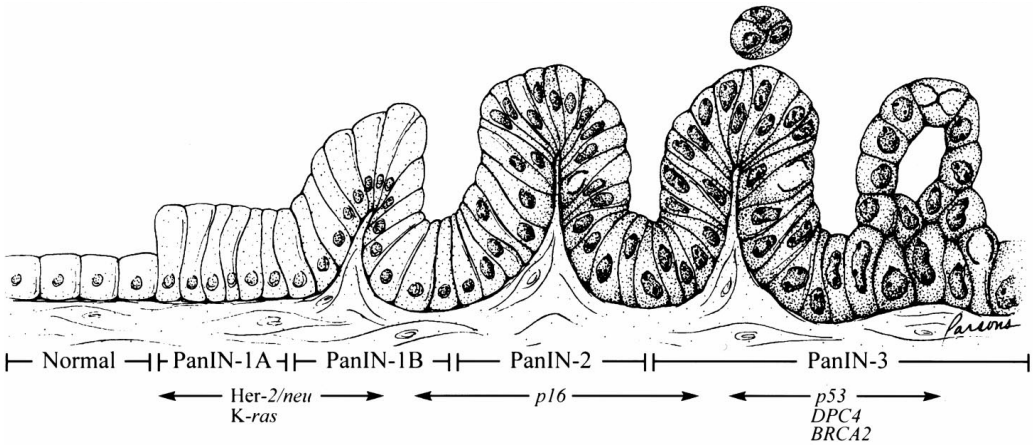

Figure 1.2: Progression model of PDAC with the mutations listed below the associated lesions, reprinted from Hruban *et al.*. Progression model from pancreatic cancer. Clinical Cancer Research 6, 2969-2972 with permission from AACR Journals.

in each sample, involving 12 overlapping signalling pathways. Of the 12 pathways identified, 5 were involved in cellular functions: DNA damage repair, apoptosis, cell cycle regulation, cell – cell adhesion, and invasion while the remaining related to TGF-β-, MAPK-, and embryonic-signalling pathways. An overview of the genetic alterations associated with PDAC and their corresponding signalling pathways is presented in Table 1.1. The role of the pathways and their most frequently altered genes will be described in more detail in the ensuing sections.

Gene type	Gene	Pathway	Prevalence in PDAC
Tumour suppressor genes	*$p16^{Ink4A}$*	Cell cycle	95%
	TP53	DNA damage repair Apoptosis Cell cycle	75%
	SMAD4	TGF-β	55%
Oncogenes	*KRAS*	MAPK	90%
Genome maintenance genes	*BRCA2*	DNA damage repair	7-10%

Table 1.1: The most commonly affected genes and their associated signalling pathways in PDAC, as described in Section 1.3.1.

1.3.1.1 The MAPK pathway

Mitogen-activated protein kinase (MAPK) pathway is a chain of highly conserved proteins in the cell that communicate extracellular signals and control cellular processes such as proliferation, growth, differentiation, migration, and apoptosis (Dhillon et al., 2007). Three major groups of MAPKs have been described in mammals so far: the extracellular signal-regulated kinase (ERK1/2), the c-Jun N-terminal kinase (JNK) and p38. Of those, the ERK1/2 module is the most well studied (Krens et al., 2006). The pathway is illustrated in Figure 1.3.

Activation of the pathway occurs upon binding of a ligand to a cell surface receptor, leading to tyrosine phosphorylation and consequent generation of binding sites for the recruitment of proteins such as growth factor receptor-bound protein 2 (GRB2). GRB2 facilitates the translocation of the guanine nucleotide exchange factor son of sevenless (SOS), which binds to the inactive guanosine diphosphate (GDP) membrane bound Ras, changing it into its active guanosine-triphosphate (GTP) state. In its ac-

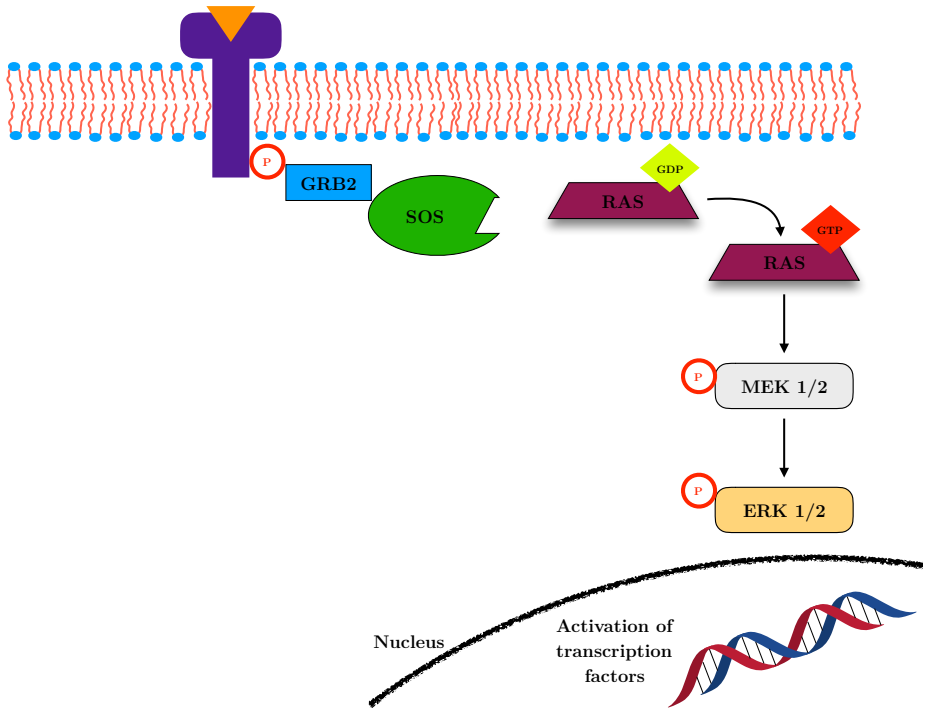

Figure 1.3: The MAPK pathway. Binding of a ligand to a cell surface receptor initiates transformation of RAS-GDP inactive form to its active GTP-bound state. RAS-GTP is then bound to several effector proteins, enabling the activation nuclear transcription factors facilitating several cellular processes. Circled P depicts phosphorylation.

tive GTP-bound state, Ras is able to bind several effector proteins, most importantly Raf which leads to the phosphorylation and activation of MEK1/2 kinases and the subsequent phosphorylation and activation of ERK1/2. This sequence then triggers several nuclear and cytoplasmic factors responsible for several cellular processes (Cseh et al., 2014).

Upon point mutations at codon 12, Ras protein persists in the active state (GTP-bound) leading to over-activation of the pathway and the downstream targets as observed in PDAC. The resulting elevated Ras activity levels can cause aberrant cell differentiation, and in the PDAC setting it has been associated with increased acinar cell proliferation (Logsdon and Lu, 2016). It has been shown that activation of the

Raf/MEK/ERK pathway in mouse pancreas, at the level of Raf, can lead to a more aggressive tumour phenotype characterised by the presence of a greater number of PanINs and therefore, has been the focus of pharmacological targeting for PDAC (Collisson et al., 2012).

1.3.1.2 $p16^{Ink4A}$ and cell cycle regulation in PDAC

The tumour suppressor protein $p16^{Ink4A}$, encoded by the cyclin-dependent kinase inhibitor 2A (*CDKN2A*) gene, is a G1 cyclin-dependant kinase (CDK) inhibitor, playing an important role in cell cycle progression. It performs this function by binding to CDK4 and CDK6, preventing them from forming a complex with cyclin D, thus inactivating the retinoblastoma protein (Rb) and thereby blocking entry into S-phase (Li et al., 2011). Upon mutation of $p16^{Ink4A}$, the loss of inhibitive control of Rb protein leads to constant progression of cell cycle from G1 to S-phase and aberrant cell proliferation (Figure 1.4).

Alterations of $p16^{Ink4A}$ have been reported in a variety of cancer types and inactivation of the gene has been observed in 30-40% of pancreatic cancer cases, indicating its important role in tumourigenesis of the disease (Jeong et al., 2005). The simultaneous activation of *KRAS* and inactivation of $p16^{Ink4A}$ have been reported to promote tumourigenic transformation of human immortalised pancreatic cells and progression towards PDAC (Chang et al., 2014).

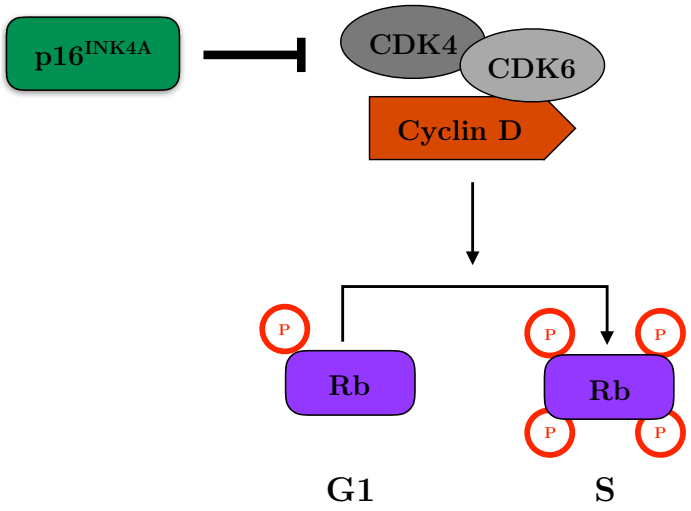

Figure 1.4: The p16^{Ink4A} in cell cycle regulation. The tumour suppressor protein p16^{Ink4A} inhibits the CDK-complex formation, resulting in inactivation of the Rb protein and subsequent arrest in G1 phase of the cell cycle. Upon inactivation of *p16*^{Ink4A}, its function is abrogated leading to an uncontrolled cell proliferation.

1.3.1.3 SMAD4 and TGF-β signaling

Transforming growth factor-β (TGF-β) is a multifunctional cytokine responsible mainly for the control of cell growth, cell proliferation and differentiation, and apoptosis. TGF-β signalling is mediated through serine/threonine kinases, TGF-β type-I (TβRI) and TGF-β type II (TβRII) receptors. Following complex formation between the two receptor types and their subsequent activation, phosphorylation of selected mothers against decapentaplegic (SMAD) proteins occurs (SMAD2 and SMAD3), resulting in a complex with SMAD4. The activated complexes then translocate into the nucleus, interacting with DNA-binding transcription factors and regulating the transcription machinery (Maier et al., 2010) (Figure 1.5).

The TGF-β pathway plays a significant role in gastrointestinal homoeostasis by keeping balance between cell renewal, differentiation and loss. Disruption of this balance

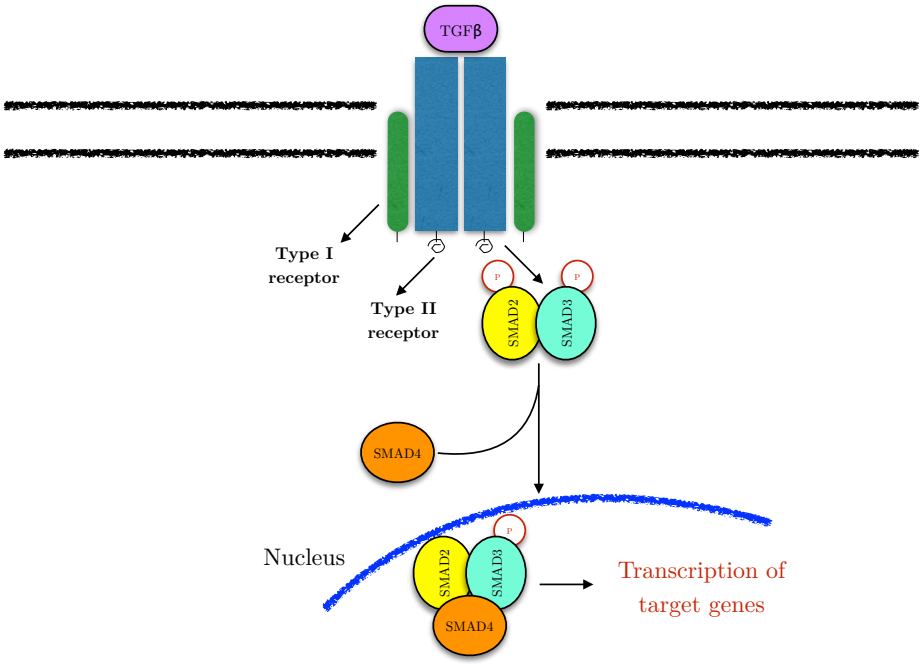

Figure 1.5: The TGF-β pathway. The complex formation between the TGF-β type-I and type II receptors is followed by phosphorylation of SMAD2 and SMAD3 proteins, resulting in a complex with SMAD4. The fully formed complex translocates into the nucleus where it regulates the transcription of other factors.

often results in tumour promotion and development (Ahmed et al., 2017). Under normal conditions, the signalling of TGF-β/SMAD4 exerts a tumour suppressive behaviour through *SMAD4*-regulated genes and upon tumourigenesis, mainly due to loss of *SMAD4*, this function is lost and the pathway rather acts as tumour promoter.

1.4 The p53 tumour suppressor

The p53 tumour suppressor, characterised as the "guardian of the genome" (Lane, 1992), is one of the most studied genes and proteins with 87,000 PubMed-listed publications reported so far. Approximately 40 years ago, Lane and Crawford reported the presence of a new protein, with a molecular weight of 53 kDa, forming a tight complex with SV40 large T-antigen upon immunoprecipitation with anti-T antibodies

from extracts of SV40-transformed cells (Lane and Crawford, 1979). At first, it was believed that p53 acts as an oncogene, caused by the observation that SV40 regulates over-production of p53 in SV40-transformed cells and therefore, p53 itself should be an important effector of this transformation (Linzer et al., 1979). Few years later, Baker *et al.* suggested the tumour suppressor function of p53 by showing that wild-type p53 alleles were lost by mutations and/or deletion in human colorectal cancer specimens, resulting in tumour cells with no wild-type p53 function, a characteristic of tumour suppressor genes (Baker et al., 1989). The observation of such mutation came later from other types of cancer and it soon became clear that p53 is the most frequently mutated gene of the whole genome (Levine and Oren, 2009).

1.4.1 p53 as a transcription factor

Following the initial understanding of the importance of p53 in cell regulation and cancer, the next quest was to unravel its relevant functions. p53 consists of 393 amino acids, divided into distinct domains: i. the amino-terminal transactivation domain (TAD, residues 1-62), containing two sub-domains (TAD-I, residues 20-40 and TAD-II, residues 40-60); ii. a proline-rich domain (residues 63-94); iii. the DNA-binding core domain (residues 94-292); iv. a linker region (residues 292-325), connecting the DNA-binding core domain and v. the tetramerisation domain (residues 324-355); vi. and finally a carboxyl-terminus domain (residues 356-393) (Beckerman and Prives, 2010) (Figure 1.6).

The most well-studied biochemical function of p53 is that of a transcription factor, regulating expression of several genes in response to cellular stress. p53 binds DNA

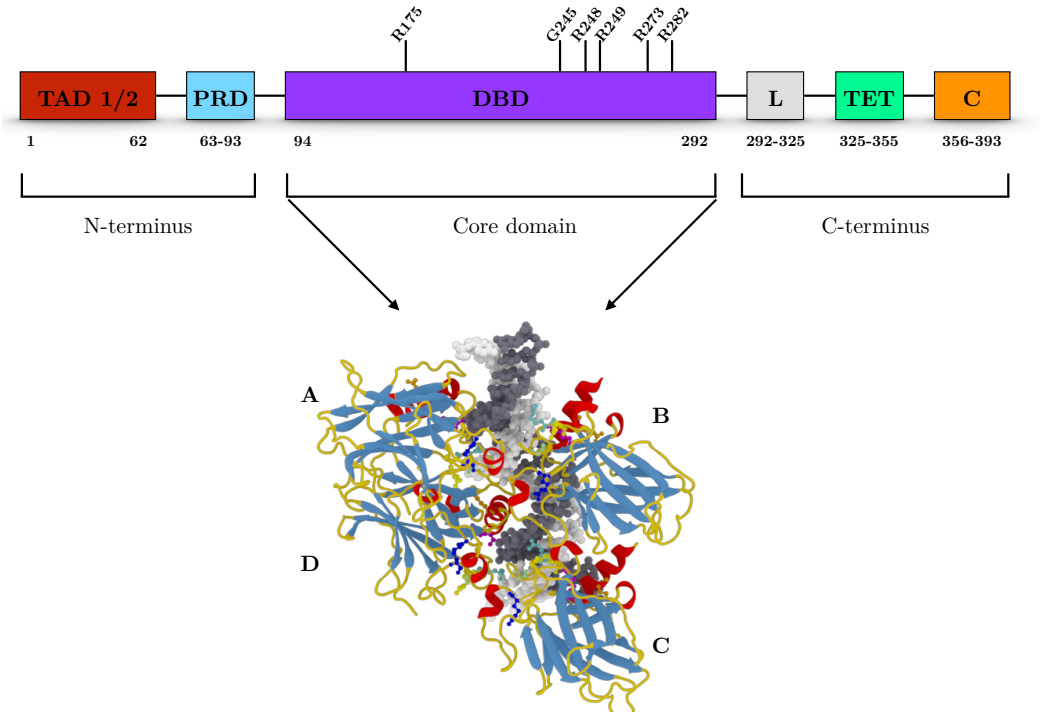

Figure 1.6: Schematic representation of the domain structure of p53. Each regions are detailed in the main text. Four p53 core domain molecules interact with two double-stranded DNA half-sites, forming a tetramer made of a dimer of two identical dimers (A-B, C-D). The colour code is based on the secondary structure where β-sheets are blue, loops are yellow, α-helices are red, and DNA backbones are grey. The molecular structure in ball and stick representation highlights the hotspot mutations. Crystal structure was solved by Kitayner *et al.* (Kitayner et al., 2006). TAD: transactivation domain, PRD: proline-rich domain, DBD: DNA-binding domain, L: linker region, TET: tetramerisation domain, C: carboxyl-terminus domain.

as a tetramer through its DNA binding domain in a sequence-specific manner, p53-dependant gene expression is encoded through the DNA target sites allowing it to perform its tumour suppression function (Joerger and Fersht, 2010). The TAD-I and TAD-II domains are equally important for p53 regulation as they comprise sites of various post-translational modifications and interaction with other regulatory proteins (Espinosa and Emerson, 2001). Examining the coding sequence of the *TP53* gene, it was noted that > 80% of the mutations observed in human tumours are within the

DNA-binding domain, predominantly around exon 4-9, suggesting the importance of p53 transcriptional role in tumour suppression (Olivier et al., 2010). These mutations are mostly missense, resulting in substitution of one single amino acid and fall within the six "hotspot residues": R175, G245, R248, R249, R273, R282 (Cho et al., 1994). The ability of p53 to bind specific sequences and transactivate genes, is the main factor that distinguishes wild-type p53 from any mutant form. Such mutations can abolish the direct binding of p53 to DNA (contact mutations). Furthermore, such mutations also affect the correct folding or oligomerisation of the protein (conformational mutations) which further impede p53's ability to correctly bind to the DNA domains (Hoe et al., 2014).

Many target genes have been identified and reported to be transactivated by p53 through its binding to response elements located downstream or within the genes, and proteins encoded by these genes are known to be involved in DNA damage repair, cell cycle regulation or apoptosis and cellular senescence (Menendez et al., 2009).This process is increased upon stress stimuli such as DNA damage, hypoxia, or hyperproliferative signals, where p53 becomes stabilised through decreased interaction with its main regulator, MDM2 (Beckerman and Prives, 2010).

1.4.2 The p53-MDM2 interaction

The mouse double minute 2 homologue (MDM2) protein (human homologue HDM2) has been described as the key regulator of p53 that binds to p53 through its transactivation domain and inhibits its biochemical activity (Oliner et al., 1993). By acting as a p53-specific E3 ubiquitin ligase, MDM2 also promotes its ubiquitination and sub-

sequent degradation by the proteasome machinery (Haupt et al., 1997). As MDM2 is a direct transcriptional target of p53, the two proteins form a negative feedback loop where induction of MDM2 expression by p53 leads to degradation of p53 and quenching of its cellular activity (Barak et al., 1993). This p53-MDM2 loop serves to keep p53 under tight control, and is responsible for the low basal level of p53 function observed in non-stressed cells. However, under various stress conditions (e.g. DNA damage, oncogene activation, hypoxia), the affinity of p53 for MDM2 is reduced, leading to lowered degradation and increased protein stability of p53. This response ultimately initiates a number of p53-dependent effects on cellular gene expression (Hu et al., 2012) (Figure 1.7).

The significance of this p53-MDM2 loop was first demonstrated by studies performed in *MDM2* knock-out mice, suggesting the tight relationship of p53 and MDM2 in early development. In particular, MDM2 null mice showed embryonic lethality due to inappropriate apoptosis. However, upon concurrent deletion of p53 this phenotype was completely rescued, demonstrating the important role of MDM2 in developmental stages through the regulation of p53 function (Jones et al., 1995; Montes de Oca Luna et al., 1995).

1.4.3 Response to DNA damage

Of the many cellular stresses upon which p53 response is initiated, the molecular mechanisms following DNA damage are the most well-understood. DNA abnormalities can result from exposure to exogenous factors, either physical or chemical, or as byproducts of physiological processes (spontaneous or enzymatic) (Helleday et al.,

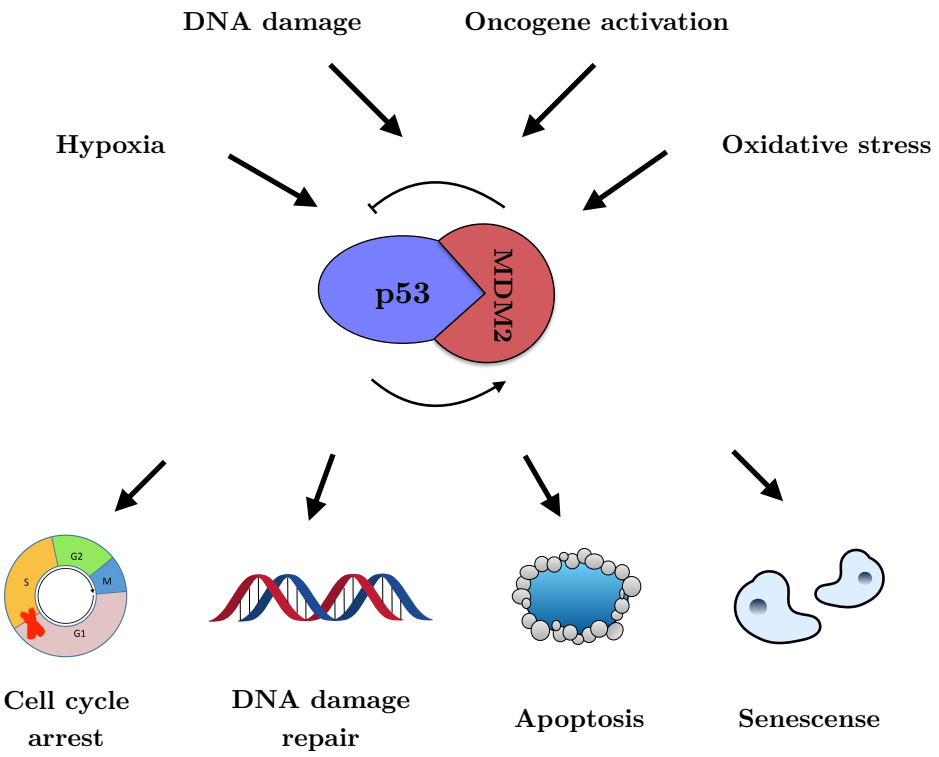

Figure 1.7: p53 response to cellular stress and its subsequent regulation of different mechanisms. The p53-MDM2 interaction is the main regulator of p53 response. Various cellular stress signals (DNA damage, oncogene activation, oxidative stress, hypoxia etc.) can affect the tight regulation of p53 by MDM2, leading to increases in p53 protein expression levels and activity and induction of responses to the stress.

2014). These result in, on average, tens of thousands of DNA lesions per day (Bernstein et al., 2013). Fortunately, there are various mechanisms to repair resultant damages, both double strand breaks (DSBs) and single strand breaks (SSBs), thus retaining genome integrity. The detailed outline of each one of the pathways involved is beyond the scope of this study and are described briefly. Specifically, for the DSBs repair: non-homologous end-joining (NHEJ), performs repair by end ligation independently of sequence homology; homology-based repair pathways such as homologous recombination (HR), alternative end-joining (alt-EJ) and single-strand annealing (SSA) (Ceccaldi et al., 2016). For SSB repair, base excision repair (BER) is

the primarily mechanism responsible for the removal and replacement of single-strand lesions, leading to maintenance of genome stability (Wallace, 2014).

p53 takes an important role in the response to DNA damage, and it is this response that mediates its tumour suppression function. Activation of p53 occur *via* two stages: the stabilisation of the protein, resulting in p53 accumulation in the nucleus; and activation of p53's biochemical functions (Meek, 2009). Such activation is usually regulated by a number of post-translational modifications, including phosphorylation, acetylation, ubiquitination, methylation, and sumoylation (Dai and Gu, 2010). The activation of p53 upon damage is coordinated by two main protein kinases: the ataxia-telangiectasia mutated (ATM) and the ataxia-telangiectasia Rad3-related (ATR) proteins, inducing a range of post-translational modifications. More specifically, phosphorylation of p53 by ATM at serine 15 (Ser-15) reduces its affinity for MDM2, resulting in decreased p53 degradation, thus enhancing its stabilisation, activity and nuclear localisation (Hu et al., 2012). In addition, both phosphorylation at Ser-15 and total p53 protein levels are reduced upon complete abrogation of ATM, suggesting the importance of ATM in the p53 stability.

Apart from ATM and ATR, p53 has been shown to be regulated by other kinases: CDKs at Ser-315 (Wang and Prives, 1995), casein kinase 1 and 2 at Ser-6/9 and Ser-392, respectively (Hall et al., 1996), DNA-PK at Ser-15/37 (Shieh et al., 1997), MAPK at threonine 73 (Thr-73) (Milne et al., 1994). These post-translational modifications occur at the N-terminus and C-terminus regulatory domains, disrupting the p53-MDM2 binding (Lakin and Jackson, 1999). All of these discoveries were part of *in vitro* studies. *In vivo* however, regulation of p53 is somewhat more complicated.

Studies in mice, bearing p53 mutations, showed that phosphorylation of p53 at Ser-18 (mouse) did not affect cellular proliferation. This then suggested that phosphorylation may not have an immediate affect on its own but rather occurs as part of several post-translational modifications (Sluss et al., 2004).

Acetylation has been also described, although to a lesser extent, to regulate activation of p53 in response to DNA damage, promoting its transcriptional activity. C-terminus lysine residues (164, 305, 370, 372, 373, 381, and 382) are known to be acetylated by the CREB-binding protein/p300 (CBP/p300) disrupting the interaction of p53 with MDM2, leading again to its stabilisation (Wang et al., 2004). The same lysine residues are also ubiquitinated by MDM2 . *In vivo* studies have shown that upon replacement of the C-terminus lysine residues with arginines, p53 levels were not altered significantly, suggesting that these modifications are not essential for p53 regulation, as previously thought, but rather contribute to homeostatic control *in vivo* (Krummel et al., 2005).

1.4.4 p53 in cell cycle regulation and apoptosis

The eukaryotic cell cycle is tightly controlled by a regulatory network of checkpoints that monitor cellular perturbations and arrest progression until errors are fixed (Barnum and O'Connell, 2014), with p53 being the main regulator of the G1/S checkpoint, which prevents replication of damaged DNA (Giono and Manfredi, 2006). p53 performs this role by activating its main target gene, p21 (also known as $p21^{WAF-1/CIP-1}$), which binds and inhibits the activity of CDK-complexes (cyclinE/CDK2), thus preventing the G1/S transition (Abbas and Dutta, 2009).

Another checkpoint involving p53 is the G2/M (Taylor and Stark, 2001), which is maintained by a number of targets. GADD45 (growth arrest and DNA damage) has a similar function to p21 by disrupting the binding of CDc2 to cyclin B1 (Zhan et al., 1999) and the 14-3-3-6-σ protein has been also described to be regulated by p53, causing G2 arrest by interference with the cyclin B1/CDc2 complex (Hermeking et al., 1997).

In addition to its key function in the aforementioned cell cycle checkpoint, p53 is also involved in the regulation of apoptosis. The primarily contribution of p53 to apoptosis is largely dependant on its transcriptional activity, regulating the expression of a number of genes involved in the process. Amongst these targets, two are of a particular importance: PUMA and NOXA members of the BCL-2 family proteins (Pietsch et al., 2008), as demonstrated by the defective p53-dependant apoptotic machinery observed in knock-out mice, suggesting its necessity for p53-mediated cell death (Jeffers et al., 2003).

The p53-regulated balance between these intricate processes, cell cycle arrest or apoptosis, is dependant upon several extracellular or intracellular factors, including, but not limited to, p53 expression levels; type of the stress signal; cellular context; time of exposure to damage (Sionov et al., 2013).

1.4.5 p53 and cellular senescence

Senescence refers to a stress response where cells leave the cell cycle and lose their capability to proliferate, preventing cells with mutations from expansion (Rufini et al., 2013). The first demonstration of p53's involvement in the regulation of senescence

was performed using the SV40 T antigen that causes inactivation of p53 upon binding. As a result of this inactivation, increased lifespan of human fibroblasts and DNA replication was observed (Ide et al., 1983). This phenomena was later confirmed by Shay and co-worker, suggesting the important role of an active p53 in the regulation of senescence (Shay et al., 1991). The transcriptional activity of p53 has been reported to increase upon senescence even though it is not clear whether the increase is specific to senescence or is related to cell growth arrest (Vaziri et al., 1997). In addition to increased p53 activity, it was reported that levels of p21 also increase, suggesting that p53 initiates senescence growth arrest through induction of p21 (Dulić et al., 2000).

1.4.6 p53 and PDAC

PDAC is characterised by missense mutations in the *TP53* gene accumulated throughout the later stages of the PDAC progression model, leading to a mutant p53 protein increasingly incapable of identifying the p53 wild-type DNA-binding sites in the promoter of p53 target genes, also acquiring oncogenic properties, know as the "gain of function" (GOF) effect (Muller and Vousden, 2013).

The GOF effect of p53 was first proposed over two decades ago, where the growth advantage of mutant p53 was demonstrated in the absence of endogenous wild-type p53 *in vitro* (Dittmer et al., 1993). Later, experiments in animal models showed that mice with one mutant p53 allele, present a higher number of neoplastic lesions in combination with increased metastatic potential and genomic instability when compared to p53 null mice (Lang et al., 2004; Liu et al., 2010). In 2010, Morton *et al.*, confirmed that p53 mutation rather than p53 loss is required to drive metastasis

in genetic models of human PDAC (Morton et al., 2010).

Two main p53-related mechanisms have been proposed to drive metastasis in cancer cells (Muller et al., 2011). Firstly, mutant p53 is able to acquire a transcription function of its own and therefore, influencing the promoter activity through the transactivation domain and this may be sufficient to trigger expression of target genes (Weisz et al., 2004). Secondly, mutant p53 has been also suggested to act by modifying the function of other proteins or even mask the activity of transcription factors. It was shown that interaction of mutant p53 with Mre-11 nuclease leads to suppressed binding of Mre-11/Rad50/NBS1 (MRN) complex, responsible for the repair of DSBs, followed by incomplete activation of ATM kinase and impaired DNA damage repair (Song et al., 2007). Regarding its interaction with other transcription factors, p53 has been known to negatively regulate the pro-apoptotic function of its family members, p63 and p73, affecting their ability to induce growth suppression (Lang et al., 2004).

1.5 Diagnosis and therapy of PDAC

As discussed earlier, important scientific advances have been made to enhance the understanding of the molecular mechanisms underlying PDAC development and progression. Progress towards better diagnosis and treatment of the disease in the clinic however, has been relatively slower than other cancers due to several obstacles: lack of specific symptoms or biomarkers lead to diagnosis at a very late stage; presence of dense desmoplastic stroma that limits drug delivery, causing therapy resistance (Long et al., 2011a); and the limited number of patients that are eligible for surgical

resection, currently the only viable option for long-term survival (Dhayat et al., 2017). Computed tomography (CT) is currently the gold standard method for the detection of PDAC and evaluation prior to surgical resection thanks to its relatively high sensitivity (Egorov et al., 2013). Despite the great impact of CT in PDAC detection, it is still limited due to its inability to detect small lesions (tumour detection limit 5-8 mm), microscopic lymph node metastasis, and to distinguish inflammatory from neoplastic lymph node growth (Heiken, 2015). Ultrasound (US) is also often used as a detection tool in patients experiencing abdominal pain due to its cost-effectiveness and non-invasive nature. It is particularly useful in detecting small masses and pancreatic head tumours but less so for the visualisation of the tail of the pancreas as the presence of gas in stomach and transverse colon may mask the sensitivity (Lee and Lee, 2014). With a better soft-tissue contrast, magnetic resonance imaging (MRI) is considered superior to CT as it allows detection of smaller tumours and determination of vascular involvement. However, MRI is limited by the inability to accurately distinguish the tumour from chronic pancreatitis due to biliary ductal obstruction observed in both pathologies (Miura et al., 2006). Finally, imaging with positron emission tomography (PET) using ^{18}F-FDG (2-deoxy-2-[^{18}F]fluoro-*D*-glucose analogue), has shown to be a promising modality for differentiation between benign and carcinogenic lesions, based on the increased glucose consumption by tumours (Chang and Kundranda, 2017). However, in spite of the good sensitivity (70-100%) and specificity (65-90%) of FDG-PET, it can also result in false-positive and false-negative interpretations as it does not separate between PDAC and chronic pancreatitis or hyperglycemia (Jha and Bijan, 2015).

To date, no screening methods have been identified for detection of early-stage tumours, and the applicability of biomarkers used in the clinic is questionable for tumour progression or recurrence (Cid-Arregui and Juarez, 2015). Serum levels of carbohydrate antigen 19-9 (CA19-9), an epitope of sialylated Lewis A blood group antigen, is the only biomarker utilised in the clinic for PDAC detection and monitoring. Its use however, has been hampered by its poor sensitivity and overexpression of the antigen has been associated with benign diseases and chronic pancreatitis (Parikh et al., 2014).

Surgical removal of stage-1 and stage-2 tumours and in some cases stage-3, will add a significant survival benefit to PDAC patients. However, most of the patients carry an already advanced disease at the time of clinical presentation and even if surgery is an option, the additive benefit is often questionable considering the patient's physical inability and aggressive nature of the disease (Chari et al., 2015).

The only treatment approach for patients diagnosed with locally advanced or metastatic disease is palliative chemotherapy (Vincent et al., 2011). Gemcitabine, approved in the late 90s, offered a marginally increased survival rate and even in combination with other chemotherapy regimes (irinotecan) does not improve the overall survival (Rocha Lima et al., 2004). The treatment was slightly improved with the recently introduced FOLFIRINOX (leucovorin, 5-fluorouracil, irinotecan, oxaliplatin), which showed improved therapy response and overall survival over treatment with gemcitabine (11.1 *vs.* 6.8 months), however, it also elicited a greater toxicity profile (Conroy et al., 2011).

Based on the discussed treatments, it is clear that despite the efforts made in im-

proving the diagnostic potential that could lead to more effective treatment options, PDAC still remains one the most deadliest cancers, and their treatment and prognosis are in dire needs of further improvements.

1.6 Clinical implications of p53 imaging in PDAC

As mentioned earlier, the p53 gene mutation is found in approximately 50% of human cancers underlying its importance in tumour suppression and providing the basis for a diagnostic assay. The correlation of p53 mutations to the prognosis of PDAC were first studied back in the 90s (Nakamori et al., 1995). The authors examined 37 pancreatic adenocarcinomas for the presence of p53 mutations and correlated that to the disease prognosis. When compared to tumours with no p53 mutations, those bearing mutant p53 showed a significantly shorter median survival (6 months *vs.* 15 months in the no-mutation group). Later, Grochola *et al.* studied the expression of transcriptional variants from P1 promoter of MDM2 gene in a cohort of patients with PDAC and found that individuals with high P1 transcript levels were associated with increased risk for tumour-related death. They concluded that transcriptional induction from P1 promoter is dentrimental to upregulation of MDM2 in PDAC, leading to abrogation of p53 pathway and worse clinical outcome (Grochola et al., 2011). In a different study, Ormanns *et al.*, studied the effect of p53 mutations in erlotinib-treated advanced pancreatic cancer. The authors assessed the p53 status in 50 dissected patient tissues by immunohistochemistry (IHC) and genome sequencing showing that overexpression of p53 was correlated with dismal progression free survival.

Despite the correlations shown in the aforementioned studies, these were performed in relatively small sample size ($n \leq 50$), and are not yet sufficient to support the use of p53 as a prognostic and diagnostic marker (Ormanns et al., 2014). In fact, there still exists great debates on whether this information can be used (Xin, 2012; Muller and Vousden, 2014). In particular, a clear distinction should be made between somatic and germline p53 mutations as each could lead to a different range of consequences. Furthermore, the identification of a specific mutation may be informative as several studies have shown a strong correlation with increased risk of developing tumours. For example, in a study of 36 patients with childhood cortical adenocarcinoma and their families, 35 out of 36 showed the same mutation of p53 encoding an R337H amino acid substitution (Ribeiro et al., 2001). For somatic lesions however, using p53 as a diagnostic and prognostic tool is somewhat more complicated. Most of the currently developed methods for p53 detection are highly sensitive, and it is this sensitivity that can contribute to false positives findings as mutations of p53 in a single cell may not provide any further information other than that of the mutation itself (Ling et al., 2001).

Patients with PDAC are often divided into three groups: those with resectable; locally advanced; and metastatic disease, with the first being the key stage of identification for the enhancement of overall survival and representing early stage tumours (Jenkinson et al., 2015). Discrimination of early tumours, however, may often be confused by the presence of inflammatory disease, such as chronic pancreatitits, due to morphological similarities between the two and better tools are always needed for accurate staging, for which the detection of p53 may be a powerful supplementary diagnostic

tool. In their study, Mu *et al.*, evaluated p53 overexpression and serum concentrations of CA19-9 in patients with suspected pancreatic cancer. The authors showed that CA19-9 alone does not show strong specificity for the detection of pancreatic cancer. However, when combined with detection of p53 overexpression, the diagnostic sensitivity was enhanced, allowing the distinction between cancer from chronic pancreatitis (Mu et al., 2003). In a different review paper, Strobel *et al.* discussed tha additive effect of FDG-PET in pancreatic cancer diagnosis, concluding that on its own it can only provide minor help to the identification of operative tumours and combination strategy of different biomarkers can significantly optimise the diagnosis of pancreatic tumours (Strobel and Büchler, 2013). Therefore, a p53 tracer together with the aforementioned gold standard methods could enhance the rate of accurate detection of PDAC in an earlier stage, especially on high-risk populations (Zhang et al., 2017).

1.7 Molecular imaging

One of the most significant advancements in cancer diagnosis has been in the area of molecular imaging modalities. In oncology, molecular imaging can be considered as the *in vivo* characterisation of biological processes that are important to the malignant state (Kircher et al., 2012). It can be achieved by either using endogenous information or exogenous probes that target specific biomolecules. A number of modalities are currently being used in pre-clinical and clinical settings. These include the aforementioned imaging tools, PET, CT, MRI, US, single photon emission com-

puted tomography (SPECT), and optical imaging. The modalities can be divided into two groups based on the information they provide, i.e. structure: CT, MRI, and US; and functional: PET, SPECT, and optical (Khalil et al., 2011). The increasing availability of these techniques has revolutionised the field of molecular imaging and combination or fusion of different methodologies into a single modality could provide more valuable diagnostic information than when a single method is utilised. The key advantages and disadvantages of the aforementioned techniques are summarised in Table 1.2, and the selection of the technique should comply with the research question being posed.

Modality	Advantages	Disadvantages
CT	Structural imaging High spatial resolution High depth penetration Short scan time	Radiation dose Poor soft-tissue contrast
MRI	No radiation dose High spatial resolution Excellent soft-tissue contrast	Expensive Long scan time Low sensitivity
US	No radiation dose High spatial resolution & sensitivity cheap	Operator dependant No wb imaging
PET	Quantitative Wb imaging High depth penetration Combination with CT/MRI	Radiation dose Expensive Low spatial resolution (0.6 mm) Long scan time
SPECT	Quantitative Wb imaging High depth penetration Combination with CT	Radiation dose Expensive Low spatial resolution (0.3-1 mm) Long scan time
Optical	No radiation dose Inexpensive High spatial resolution & sensitivity	Limited depth penetration

Table 1.2: Advantages and disadvantages of imaging modalities currently used in the clinic. Table adapted from Pysz *et al.* (Pysz et al., 2010). Wb: whole body.

For example, on the one hand, CT and MRI are favoured for their superior spatial resolution; on the other hand, the sensitivity of PET and SPECT makes them superior functional imaging methods, allowing detection of radiopharmaceuticals in the

nanomolar or even picomolar range as well as being non-invasive, quantitative, and functional imaging modalities for cancer biology (Pysz et al., 2010; De Jong et al., 2014). Based on the consideration of the project reported here, SPECT is the main imaging modality and will be the focus in the ensuing section.

1.7.1 SPECT imaging

Cancer research has hugely benefited from the development of SPECT imaging systems due to the detection ability of specific tumour sites, which together with CT fusion, can provide accurate anatomical references (Hicks and Hofman, 2012). SPECT has several advantages over other imaging modalities thanks to a number of factors, such as lower cost (especially when compared to PET), greater accessibility and availability of various tracers that can be applied to wider range of biological mechanisms. Over the past decade, SPECT has greatly improved in the preclinical setting, resulting in better spatial resolution outperforming preclinical PET (0.25 mm *vs.* 1 mm, respectively) (Goorden et al., 2013).

SPECT imaging relies on the tracer principle to detect any functional abnormalities within the body. Briefly, a γ-emitting radiotracer is delivered into the patient through injection into the bloodstream and following radioactive decay, single photon will be emitted in all directions, allowing detection by a γ-camera (Van Audenhaege et al., 2015). The high-energy photons are absorbed by a scintillation crystal, typically thallium doped sodium iodide (NaI(Tl)), resulting in a scintillation or light flash which is detected by a set of photomultiplier tubes (PMTs) at the back of the crystal. The PMTs then convert every scintillation light-flash into a pulse of electrical current

which will be processed by the electronics of the system, determining the energy and the position of the incident. To provide additional spatial information, a collimator is positioned in front of the crystal, comprising of multiple holes to allow the emitted photons to travel in a parallel direction to the holes and interact with the crystal. Subsequent count data is then generated for image reconstruction. There is a constant improvement in the current technologies in instrumentation and reconstruction algorithms, to enhance SPECT/CT performance beyond its current level, with multi-pinhole collimator systems being most competitive (Peremans et al., 2005; Livieratos, 2012).

SPECT probes, consists of a target-specific biomolecule and a γ-emitting radionuclide, can be classified into two main categories according to their biodistribution properties: the ones determined by their physical and chemical properties; and those determined by their interaction with a biological target of interest (Müller and Schibli, 2013). The majority of diagnostic SPECT tracers utilise metallic radionuclides with a wide range of characteristics (Bhattacharyya and Dixit, 2011). The choice of radionuclide must be considered during tracer development. Technetium-99m (^{99m}Tc), isotopes of non-metallic iodine (^{123}I, ^{131}I, ^{125}I), Indium-111 (^{111}In), Gallium-67 (^{67}Ga), Lutetium-177 (^{177}Lu), and Yttrium-90 (^{90}Y) are the most common SPECT radionuclides used in the clinic to date. More specifically, one should consider the type of study (diagnostic or therapeutic), and the potential targeting biomolecules or ligands based on their biological characteristics (half-life, stability). Following the selection process, the radionuclide can be identified based on its nuclear properties (physical half-life, decay characteristics, stability, toxicity, availability) (Yeong et al., 2014).

1.8 Antibodies as imaging agents

One of the major recent advances in biomolecules was that of the monoclonal antibodies, with their diverse ability of tumour recognition, making them attractive for the development of imaging agents for a non-invasive identification of cancer (Wu, 2014). Most diagnostic tests using antibodies rely on the immunohistochemical detection of the target of interest in a biopsy. Despite being simple and inexpensive, this method has several disadvantages such as tissue handling and diagnostic interpretation variabilities; need of multiple biopsies for conclusive results as sampling from a single site does not account for tumour heterogeneity (Fleuren et al., 2014).

The large bank of monoclonal antibodies available, together with their unique capability of identifying specific protein targets, has been invaluable to *in vitro* and *in vivo* diagnostic research. The advent of immunotherapy and "biologicals" in oncology (Knowles and Wu, 2012), has resulted in more than 50 antibodies being tested in clinical trials (Reichert, 2017). The pharmacokinetic profile, biodistribution, toxicity, and side effects of antibodies are well known and several have been already approved by FDA for use in the clinic as imaging agents (^{111}In-satumomab pendetite, ^{111}In-Prostascint, ^{111}In-Trastuzumab, ^{99m}Tc-Rituximab) (Bohdiewicz, 1998; Kaur et al., 2012). On the one hand, the large size of antibodies (150 kDa) results in long plasma circulation time (days-weeks) as they exceed the renal clearance threshold ($\approx$ 70 kDa), preventing clearance from the kidneys. Therefore, it is necessary that imaging sessions are performed days after administration due to the high blood background (Warram et al., 2014). On the other hand long circulation time could potentially lead

to a longer and higher tumour-specific uptake when compared to smaller molecules, especially when target expression is low.

Development of antibody-based imaging agents has mainly focused on extracellular or cell-surface targets involved in disease development due to their limited access to the cytoplasm and nucleus, leading to a large amount of surface-based imaging agents, which in turn expanded the imaging capabilities of other functional processes, such as angiogenesis, invasion and metastasis, immunotherapy (Halin and Neri, 2001). Antibodies have been used to image classic markers such as carcinoembryonic antigen (CEA) (Hong et al., 2008), prostate-specific membrane antigen (PSMA) (Bouchelouche et al., 2010), CA19-9 (Girgis et al., 2011) and others.

The limited penetration of antibodies into intracellular compartments has created the need for exploring possibilities that will enable this delivery. Several methods have been described in the past, including DNA transfection of native or engineered proteins (Kim and Eberwine, 2010), electroporation (Sharei et al., 2013), or microinjection of protein-based biosensors (Postupalenko et al., 2014). However, these techniques tend to be limited to *in vitro* applications, as they are challenged by poor delivery efficiency, cell death, protein aggregation when applied *in vivo* applications. One of the methods utilised to overcome the aforementioned limitations is the use of cell penetrating peptides (CPPs), containing nuclear localisation sequence(NLS), to enable intracellular entry of different cargoes both *in vitro* and *in vivo* (Munyendo et al., 2012; Copolovici et al., 2014). *In vivo* delivery of large biomolecules was first demonstrated by Schwarze *et al.*, where the delivery of β-galactosidase protein into tissue, including the brain, was facilitated by the conjugation of CPP via intraperi-

toneal administration (Schwarze et al., 1999). Later, Costantini *et al.* (Costantini et al., 2007) and Cornelissen *et al.* (Cornelissen et al., 2011) reported similar results *in vivo*, opening new possibilities for intracellular targeting of proteins.

1.9 Cell penetrating peptides

Since their discovery (Frankel and Pabo, 1988), cell penetrating peptides (CPPs), also known as protein transduction domains (PTDs), have been considered invaluable tools for delivery of various cargos into the cell. It was demonstrated that the trans-activator of transcription (TAT) protein of the human immunodeficiency virus (HIV-1) was able to enter cells in an *in vitro* system and trans-activate the viral promoter, contrary to common dogma that the cell membrane is impermeable to hydrophilic molecules (Bechara and Sagan, 2013). After the discovery of TAT, more followed and in 1991, the homodomain of *Drosophila antennapedia* displayed internalisation into neuronal cells derived from the third helix of the homodomain and named penetratin (RQIKIYFQNRRMKWKK) (Joliot et al., 1991; Derossi et al., 1994). Later, the minimal essential sequence of TAT (GRKKRRQRRRPPQ) responsible for cellular uptake was identified (Vives et al., 1997). Since then, a large number of peptides have been described, from protein-derived (pVEC from vascular endothelium cadherin protein) to the chimeric (Transportan), and synthetic (polyarginines, model amphipathic peptides (MAPs)). Table 1.3 presents the sequences of some of the most studied peptides.

Peptide	Origin	Sequence	References
Protein-derived			
Tat(48-60)	HIV-1 protein	GRKKRRQRRRPPQ	Vives et al. (1997)
Penetratin	Antennapedia	RQIKIYFQNRRMKWKK	Derossi et al. (1994)
pVEC	Cadherin	LLIILRRRIRKQAHAHSK	Elmquist et al. (2001)
Chimeric			
Transportan	Galanin & Mastoparan	GWTLNSAGYLLGKINLKALAALAKKIL	Pooga et al. (1998)
Synthetic			
Polyarginines	TAT-based	≥ 6 aa	Mitchell et al. (2000)
MAP	Model aphipathic	KLALKLALKALKAALKLA	Oehlke et al. (1998)

Table 1.3: The most well-studied CPPs their origin and sequences. aa: amino acids.

These CPPs consist of short residue (between 5-30 amino acids) sequences and are highly variable in both 3D-structure and amino acid composition and can contain cationic, anionic, and neutral sequences with different degrees of hydrophobicity and polarity (Milletti, 2012). Most CPPs contain a section of positively charged, or cationic, residues, and they are considered key to their enhanced cellular uptake. In addition, the type of cargo can be covalently or non-covalently attached to the CPP, resulting in different modes of uptake.

On the one hand, covalent attachment of the cargo to the peptide can be achieved through chemical modification (disulfide bonds, amide bonds, linker) or cloning (expression of the CPP as part of a fusion protein). On the other hand, physical complexation is performed through hydrophobic or electrostatic interactions between the CPP and the cargo molecule and the formation of this non-covalent interaction will depend on the physicochemical properties of both. Both approaches have their own advantages and disadvantages. While covalent interaction results in a well-defined molecule, it is usually a very laborious process and careful optimisation of the pro-

tocol is needed. Even though simpler, physical complexation can produce a pool of structures varying in size and composition and thus, the method of choice should depend on biochemical properties of both the CPP and the cargo (Kristensen et al., 2015).

1.9.1 Uptake mechanisms of CPPs

Despite the many studies performed on CPPs and their successful outcome, the mechanism of cellular entry remains inconclusive. It is commonly accepted that different translocation mechanisms are utilised by CPPs despite their similar cationic nature of peptide sequences, and the mechanism employed is dependent on the experimental conditions (Madani et al., 2011). The most widely accepted pathways will be discussed herein: direct penetration and endocytosis (Guo et al., 2016). A simplified schematic of these uptake pathways is shown in Figure 1.8.

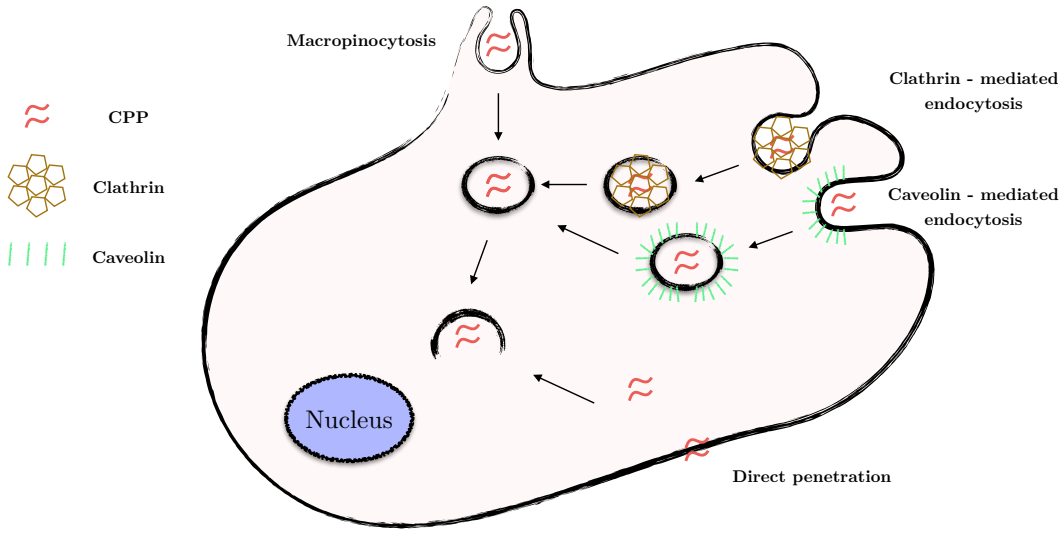

Figure 1.8: Cellular uptake mechanisms of CPPs. Schematic depicting the most accepted pathways of CPP cellular entry, namely direct penetration and endocytosis (macropinocytosis, clathrin- and caveolin-mediated endocytosis).

1.9.1.1 Direct penetration

Direct penetration of CPPs relies on plasma membrane destabilisation in an energy-independent manner. Several mechanisms have been proposed including micelle formation (Derossi et al., 1996), pore formation (Matsuzaki et al., 1996), membrane-thinning (Lee et al., 2005), and a carpet-like model (Pouny et al., 1992). All of the proposed models are initiated by the interaction between positively charged CPP and the negatively charged membrane components, such as heparan sulfates (HS) and phospholipid bilayer. This then leads to the destabilisation of membrane binding sites and entrance of the CPP with its cargo into the cell.

The micelle formation model was first proposed as a translocation mechanism for penetratin (Derossi et al., 1996). In this model the destabilisation of membrane leads to reorganisation of the neighbouring lipids and formation of the inverted micelle that traps the peptide in its interior. Disruption of the membrane will releases the peptide into the cell.

In the pore formation model, interaction of the peptides with phosphate groups leads to their accumulation on the outer leaflet of the membrane, causing a thinning of the bilayer, which ultimately result in the formation of a pore through which peptides can diffuse inside.

Lastly, in the membrane-thinning and carpet-like models, the positively-charged amino acids of the CPP interact with the hydrophobic core of the membrane, leading to disruption of the lipid packing and peptide internalisation.

1.9.1.2 Endocytosis

In comparison to direct translocation, endocytosis is an energy-dependent pathway and consists of two steps: endocytic entry and endosomal escape (Bechara and Sagan, 2013). Endosomal escape plays an important role in preventing degradation of the cargo in lysosomes. It is generally described as a regulated cellular process of biomolecule internalisation characterised by the formation of vesicles (Patel et al., 2007). Two main mechanisms of endocytosis have been described, phagocytosis and pinocytosis. Of the two studied mechanisms, phagocytosis is used in the uptake of larger particles (*e.g.* viruses, bacteria) and is restricted mostly to cells such as macrophages and leukocytes; pinocytosis is used for the uptake of smaller particles by all known cell types, and encompasses a set of pathways: macropinocytosis, clathrin- and caveolin-mediated endocytosis (Mayor and Pagano, 2007; Trabulo et al., 2010). Macropinocytosis involves ruffling of the outer membrane surface, causing formation of macropinosomes surrounded by a membrane similar to cell membrane. It has been considered an attractive pathway for intracellular delivery as it involves entry of extracellular fluids and it has been proposed that since the CPPs are outside the membrane surface, they may enter the cell with the fluids (Patel et al., 2007).

In clathrin- and caveolin-mediated endocytosis, clathrin and caveolin respectively, are responsible for the uptake as they cover the intracellular part of the membrane and are necessary for the folding of the membrane, leading to vesicle formation (Madani et al., 2011).

Endosomal escape following endocytosis, may determine the efficiency of cargo deliv-

ery to the cytosol. However, understanding of the processes involved remains poor to date (Erazo-Oliveras et al., 2012). Several assays to monitor the efficiency of CPP escape have been developed, with fluorescence-based methods showing that CPPs conjugated to fluorescently-labelled molecules are entrapped with the endocytic route (Gillmeister et al., 2011). On the other hand, some suggest that CPPs may disrupt the lipid bilayer of the endocytic organelles allowing escape to occur. Yang *et al.* proposed a model of delivery into the cytosol, according to which cationic CPPs induce leaky fusion, associated with membrane permeabilisation, resulting in the delivery of peptides and their cargoes into intraluminal vesicles. That is then followed by back-fusion of the intraluminal vesicles, releasing their load into the cytosol (Yang et al., 2010).

Studies have suggested that internalisation of CPPs was achieved mainly through direct penetration based on observations that peptides can enter the cell even at 4°C, suggesting an energy independent route (Vives et al., 1997). However, most of the techniques of visualising CPP uptake rely on fixed cells which has been suggested to introduce experimental artefacts (Richard et al., 2003). Endocytosis has been suggested as the main mechanism for uptake of most of the CPPs, even though different conditions may influence the mechanism of choice such as CPP conformation and sequence length, amino acid constitution, concentration, type of cargo, and binding methodology of cargo to CPP (Kersemans and Cornelissen, 2010).

1.9.2 The TAT peptide

The TAT protein acts as a transcription activator for viral gene expression of HIV viruses 1 and 2 (HIV-1/2). Despite its role as a transcription factor, TAT also possesses unique properties of cell internalisation. This ability of the TAT protein to enter the cells is largely dependent on the integrity of the main region of the protein, a 9-amino acid, arginine-rich sequence that comprises the nuclear localisation portion as well. Short peptides corresponding to this amino acid sequence can rapidly be internalised by the cells (Fittipaldi and Giacca, 2005). Truncated versions of the full TAT protein were later investigated, reducing the transduction motif to a short sequence of 49-57 residues (TAT_{49-57}) (Park et al., 2002a). The mechanism of entry both of TAT peptide and TAT-fused molecules have been the subject of debate. A few mechanisms were proposed, with the first being that cell entry of TAT peptide was endocytosis-independent (Vives et al., 1997); a temperature-dependant caveolar-mediated pathway was later suggested by Fittipaldi *et al.* (Fittipaldi et al., 2003); finally, it was proposed by Mishra *et al.*, that TAT is able to achieve multiple interactions with the membrane, cytoskeleton, and receptors, thus producing different pathways of internalisation upon different conditions (Mishra et al., 2011).

Various TAT peptide constructs have been used for applications in molecular imaging (Kersemans and Cornelissen, 2010) and the most important for this present work are those with intracellular or intranuclear targets. In early 2000, Polyakov *et al.*, first demonstrated the use of TAT modified with a peptide-based motif labelled with ^{99m}Tc, which efficiently accumulated in human Jurkat cells, presenting rapid up-

take kinetics ($t_{1/2}$ < 2 min) and quick washout of ^{99m}Tc (Polyakov et al., 2000). Later, Bullok *et al.* (Bullok et al., 2002), reported the uptake of TAT labelled with fluorescein-5-maleimide (FM) and ^{99m}Tc in cells, confirming the subcellular localisation of the peptide and similar biodistribution to the previous study, opening new possibilities in intracellular cargo delivery. While these studies were primarily concentrated on the distribution of CPP alone, the Reilly group showed the utilisation of TAT in delivering ^{123}I- or ^{111}In-labelled monoclonal antibodies into the nucleus *in vivo*, interacting with intracellular targets (Cornelissen et al., 2007; Hu et al., 2007; Cornelissen et al., 2009). Following these works, in 2011 Cornelissen *et al.* employed a similar methodology to target γH2AX, a DNA damage marker *in vivo* in breast cancer xenograft models (Cornelissen et al., 2011), formed via the phosphorylation of H2A X-isoform upon DSB formation, which acts as a protein scaffold for the initiation of the repair process (Banáth and Olive, 2003). Upon irradiation-induced DNA damage, the authors reported the *in vitro* colocalisation of the formed γH2AX foci with the anti-γH2AX-TAT conjugate labelled with a fluorophore, increasing the retention of ^{111}In-labelled probe and finally high tumour uptake. This study demonstrated the potential of such method as a non-invasive approach towards clinical imaging of DNA damage.

1.10 Aims of the study

The primary aim of this study was the development and evaluation of a p53 imaging agent for the visualisation of p53 mutations in PDAC. The potential of such an

imaging target could provide diagnostic benefits in PDAC, but also other types of cancer, as identification of such mutations before the full onset of the tumour and metastasis into the surrounding tissue may offer more patient stratification options for treatments available, based on their p53 status. However, it is beyond the scope of the current study to fully realise the envisioned goal. Therefore, the current study will serve as the initial "proof-of-concept" phase, which aims to explore the following aspects.

The properties of the selected monoclonal antibody against endogenous p53 were evaluated *in vitro*. The specificity and affinity were characterised in p53 mutant and p53 null cell lines derived from PDAC mouse models (Chapter 3).

Following *in vitro* validation, the monoclonal antibody was then conjugated to a cell penetrating peptide, TAT, and a metal ion chelator that allowed radiolabelling with ^{111}In radioisotope. Validation of the functional characteristics of the antibody-conjugate was performed after each modification step (Chapter 4).

Finally, the ability of ^{111}In-labelled anti-p53 antibody conjugate to target p53 protein *in vivo*, was evaluated in two mouse models of PDAC using SPECT imaging (Chapter 5).

In a separate study (Chapter 6), and through a collaborative work with professor Alison Banham, a novel antibody, recognising a p53-derived peptide presented by human leukocyte antigen haplotype (HLA-A2) on the cell surface, was also evaluated regarding its biodistribution and tumour uptake *in vivo*. This extracellular imaging target provided means of comparison with the previously discussed antibody targeting intracellular p53.

Chapter 2

General materials and methods

The following chapter summarises the materials and experimental techniques used throughout the present thesis. Each section is broken down into its corresponding experimental chapters. A brief outline of the methods will also be given at the beginning of each result chapter.

2.1 Cell lines and cell culture reagents

All KPC mouse-derived cell lines used in this study were kindly provided by Professor Eric O'Neill (Department of Oncology, University of Oxford, UK), as described by Hamilton *et al.* (Hamilton et al., 2014). B8484 cells originated from *LSL-Kras*$^{G12D/+}$, *LSL-Trp53*$^{R172H/+}$, *Pdx-1-Cre* KPC mice. P2FIR cells were derived from *LSL-Kras*$^{G12D/+}$, *LSL-Trp53*^{flox}, *Pdx-1-Cre* KPC mice and used as negative controls.

2.1.1 Cell line maintenance

Unless otherwise stated, all cell lines were cultured in Dulbecco's modified Eagle's medium (DMEM) (Sigma Aldrich, UK), supplemented with 10% (v/v) of foetal bovine serum (FBS) (Gibco, USA), 100 units/mL penicillin, 100 µg/mL streptomycin and 2 mM L-glutamine (Sigma Aldrich). Cells were maintained at 37 °C and in a 5% CO_2 humidified chamber, and handled in a class II microbial safety hood. Cell lines were cultured in T-75 flasks (Greiner Bio-One, UK). Once cells had reached 80% confluence, the culture media was aspirated, cells were washed with phosphate buffered saline (PBS) (Merck Chemicals Ltd, UK) and were detached from the flask

by addition of 3 mL trypsin-ethylenediaminetetraacetic acid (Trypsin-EDTA) (Sigma-Aldrich), keeping a ratio of trypsin to growing surface at 1 : 25 (1 mL for a T-25 flask). Cells were incubated for 2 min at 37 °C prior to dilution with 8 mL of fresh culture media and reseeding in new flasks at an appropriate ratio (1 : 10). Where required, cells were counted using a Countess II automated cell counter (Thermo Fisher Scientific, UK) and the appropriate amount of cells were plated into selected well plates 24 h prior to each experiment. Details of each experiments are listed in respective chapters.

2.1.2 Cryopreservation and storage of cells

Cells were harvested, as described in Section 2.1.1, and counted to ensure cell viability was over 90%. The cell suspension was then centrifuged at 100 × g for 5 min in a Heraeus™ Megafuge™ 40 centrifuge (Thermo Fisher Scientific). The cell pellet was re-suspended in growth media containing 10% (v/v) dimethyl sulfoxide (DMSO) (Sigma-Aldrich) (cell suspension of 1×10^6 cells/mL). Aliquots of the cell suspension (1 mL each) were dispensed into 2 mL cryogenic storage vials (Greiner Bio-One), and were placed in a CoolCell® cell freezing container (Biocision, USA) that ensured a standardised, controlled, temperature decrease of −1 °C/min, preventing cell lysis. Vials were kept at −80 °C overnight prior to long term storage in the gas phase above liquid nitrogen (−190 °C to −135 °C).

2.2 Cell culture plasticware

The plasticware used for all cell culture and assays were purchased from Greiner Bio-One (Greiner Bio-One Ltd,UK) unless otherwise stated. Immunocytochemistry assays were performed in 6-well plates (9.6 cm^2 growth area). *In vitro* assays using radiolabelled compounds were performed in 24-well plates (1.9 cm^2 growth area).

2.3 Antibodies

The main antibody used for this study was the anti-p53 (1C12) mouse monoclonal antibody (Cell Signaling, USA). Product information, reactivity and immunogenicity are provided in Table 2.1. The different antibodies tested in parallel with the anti-p53 (1C12) are listed in Table 2.2 as per application.

Name	Species Cross-Reactivity	Isotype	Immunogen	Supplied in
Anti-p53 (1C12)	H, M, R Mk, Hm	Mouse IgG_1 κ**	Around Ser20 Hp53	10 mM Na–HEPES (pH 7.5) 150 mM NaCl 100 µg/mL BSA 50% glycerol >0.02% sodium azide

Table 2.1: Anti-p53 (1C12) mouse mAb-Product information. H: human, M: mouse, R: rabbit, Mk: monkey, Hm: hamster, HEPES: (4-(2-hydroxyethyl)-1-1piperazineethanesulfonic acid), BSA: bovine serum albumin.

Name	Species Cross-Reactivity	Applications	Supplier
Anti-p53 (1C12)	H, M, R Mk, Hm	Western Blotting, IHC, ICC Flow cytometry, IP, Chromatin-IP, ELISA	Cell Signaling USA
OP29L | anti-p53 (Ab-3) (Mutant) Mouse Mab Pab240	bovine, chicken H, M, R, Hm	Flow cytometry, Frozen sections Immunoblotting, ICC IP, Paraffin sections	Merck Millipore, Germany
Anti-p53 (PAb1620)	Bovine, H, M, R Non-human primate	ICC, IP IHC-Frozen, IHC-Paraffin	Abcam, UK
Anti-p53 (A-1) Sc-393031	M, R	Western Blotting, IP, ICC ELISA	Santa Cruz USA

Table 2.2: List of anti-p53 antibodies tested and applications. H: human, M: mouse, R: rabbit, Mk: monkey, Hm: hamster. ICC: immunocytochemistry, IHC: immunohistochemistry, IP: immunoprecipitation.

2.4 Western blotting

All reagents and buffers were purchased from Sigma-Aldrich unless otherwise stated.

2.4.1 Lysis buffer

Lysis buffers I and II were prepared as described in Tanaka *et al.* (Tanaka et al., 1992). Buffer I was composed of 10 mM 2-Amino-2-(hydroxymethyl)propane-1,3-diol hydrochloride (Tris-HCl) (pH 7.8) and 200 mM potassium chloride (KCl). Buffer II was composed of 10 mM Tris-HCl (pH 7.8), 600 mM KCl, 40% (v/v) glycerol, 0.1 mM EDTA, and 0.2% (v/v) Nonidet P-40.

2.4.2 SDS loading sample buffer (5 ×)

The sodium dodecyl sulfate (SDS) loading sample buffer was composed of 25 mM Tris-HCl (pH 6.8), 1% (v/v) SDS (10% stock solution), 5% (v/v) glycerol, 1 mM EDTA (0.5 M stock), 2.5% (v/v) β-mercaptoethanol, and 0.01% (v/v) bromophenol

blue (1% stock solution).

2.4.3 NuPAGE® MES SDS running buffer (20 ×)

2-(*N*-morpholino)ethanesulfonic acid (MES) running buffer (20 ×, Thermo Fisher Scientific) was composed of 50 mM MES, 50 mM Tris base (pH 7.3), 0.1% (v/v) SDS, and 1 mM (EDTA). For electrophoresis the buffer was diluted 1 : 20 with deionised H_2O (dH_2O) from the 20 × stock.

2.4.4 NuPAGE® Transfer Buffer (20 ×)

NuPAGE Transfer buffer (20×, pH 7.2, Thermo Fisher Scientific) was composed of 25 mM bicine, 25 mM Bis-Tris (free base), and 1 mM EDTA. Prior to use, the buffer was diluted 1 : 20 in dH_2O and 20% (v/v) methanol.

2.4.5 Cell pellet preparation

A total of 5×10^5 cells were seeded onto a 10 cm diameter culture dish and incubated at 37 °C overnight. The media was aspirated and cells were washed twice with 5 mL followed by an additional 10 mL of ice-cold PBS. Cells were scraped off the dish, using a cell scraper (Greiner Bio-One Ltd,UK) and transferred into a 15 mL centrifuge tube. The dish was further washed with 5 mL of PBS and the remaining cells were added to the same centrifuge tube. The samples were then centrifuged at 252 × g at 4 °C for 5 min using an Eppendorf 5417R centrifuge. The supernatant was removed and the pellet was resuspended in 1 mL of PBS and transferred into a 1.5 mL microcentrifuge tube (Costar, Corning, USA). The resuspended cells were

centrifuged further at 252 × g at 4 °C for 5 min. After decanting the supernatant, all cell pellets were stored at −80 °C if not used immediately.

2.4.6 Whole cell extraction

Whole cell extracts were prepared as described by Tanaka, *et al.* (Tanaka et al., 1992). After determining the packed cell volume (PCV) of the pellet, cells were resuspended in one PCV of lysis buffer I (Section 2.4.1), containing 'Complete' proteinase inhibitor cocktail EDTA free (1 tablet/10 mL buffer, Roche, Germany). Two PCVs of buffer II, also containing proteinase inhibitor cocktail, was then added. The cell suspension was mixed thoroughly before being placed onto a rotator (Stuart, SB2, Cole-Parmer, UK) for 1 h at 4 °C. Finally, the cell lysate was centrifuged at 49,304 × g at 4 °C for 35 min and the supernatant was collected and stored at −80 °C.

2.4.7 Bradford protein assay

The protein concentration of each sample was determined using the Bradford protein assay. BSA was used as a protein standard (stock solution of 0.2 mg/mL) using a serial dilution, ranging from 1-10 µg/mL. Samples (40 µL) of each concentration were transferred to a 1 mL disposable cuvette (Fisherbrand™, Thermo Fisher Scientific) and combined with 960 µL dye reagent (Bradford reagent) and a standard curve was generated. The unknown samples were diluted in 1 mL at an approximate concentration of 1-10 µg/mL, mixed with 960 µL reagent, and incubated for 5 min at room temperature. Absorbance at 595 nm were measured using a Jenway 6505 UV/Vis spectrophotometer (Keison International Ltd, UK). The instrument was calibrated

with a blank sample, containing dH_2O together with 960 µL dye reagent. The protein concentration of the unknown samples was determined by comparing the net absorbance values at 595 nm against the standard curve.

2.4.8 Sample loading

4-12% Bis-Tris protein gels (10 well, NuPAGE™ Novex™, Thermo Fisher Scientific) were used. The samples to be loaded were prepared in a total volume of 30 µL by adding 20 µg of protein, 6 µL of 5× SDS loading sample buffer and the remaining volume dH_2O. The samples were denatured by heating for 10 min at 72 °C before gel loading.

2.4.9 Electrophoresis

Gel cassettes were placed in an XCell *SureLock*® Mini-Cell system (Thermo Fisher Scientific) after removing the tape covering the back of the gel cassette. The upper buffer chamber was filled with 1× running buffer (as described in Section 2.4.3) (≈ 200 mL) prior to filling the lower buffer chamber. The PageRuler™ Plus prestained protein ladder (Thermo Fisher Scientific) was loaded in the first lane (5 µL) followed by the samples. The gels were then run at 125 V for 1.5 h, with the voltage controlled by the PowerPac™ High-Current power supply (Bio-Rad Laboratories Ltd., UK).

2.4.10 Protein transfer

Protein transfer was carried out using the XCell II™ blot module (Thermo Fisher Scientific). Blotting pads and filter papers (2.5 mm thickness, Invitrogen, USA) were

pre-soaked in transfer buffer, detailed in Section 2.4.4. A hydrophobic polyvinylidene fluoride (PVDF) membranes (0.45 µm pore size, Merck Millipore, Germany) were pre-wet for 30 s in methanol, then washed in dH_2O briefly (15 s) and soaked in transfer buffer for another 2 min. The cathode core of the blotting module was filled in a specific order, while ensuring no air bubble was introduced, with the followings: blotting pad, filter paper, gel, PVDF membrane, filter paper, blotting pad. Additional pre-soaked blotting pads were then added to hold and secure the gel/membrane sandwich and the anode core was placed on top of the pads. The assembled blotting module was subsequently placed inside the XCell *SureLock*® Mini-Cell system and filled with transfer buffer. The tank was filled with ice-cold dH_2O and transfer was performed at 25 V for 1.5 h .

2.4.11 Membrane blocking and antibody probing

After transfer, the PVDF membrane was removed, washed with 1× PBS for 5 min and placed in a blocking solution of 5% w/v non-fat milk powder (Amresco, USA) in 1× PBS-T (0.1% (v/v) Tween-20) for 1 h at room temperature before probing with primary antibodies. The antibodies used in the study are listed in Table 2.3.

The antibodies were diluted in 2.5% (w/v) non-fat milk powder in PBS-T and incubated for 1 h at room temperature unless otherwise stated. After incubation of the primary antibody, the membrane was washed three times with PBS-T and consequently incubated with the secondary horseradish peroxidase (HRP) conjugated antibody (1 h at room temperature). Subsequently, the membrane was washed again three times with PBS-T and kept in PBS at 4 °C until development.

Antibody	Species	Cat.#	Supplier	Dilution	Mol. Weight (kDa)
p53 (1C12)	Mouse	2524	Cell Signalling USA	1 : 1,000	53
p53 (CM5)	Rabbit	NCL-L-p53-CM5p	Leica Biosystems UK	1 : 2,000	53
β-Actin	Mouse	MCA5775GA	AbD Serotec UK	1 : 10,000	41.7
Anti-Integrin beta 1	Rabbit	ab179471	Abcam, UK	1 : 2,000	140-150
Anti-Lamin B1	Rabbit	ab133741	Abcam, UK	1 : 1,000	70
Anti-alpha Tubulin	Rabbit	ab176560	Abcam, UK	1 : 2,000	50
Goat anti-Mouse IgG (H/L): HRP	Mouse	5178-2504	Bio-Rad	1 : 3,000	N/A
Goat anti-Rabbit IgG (H/L): HRP	Rabbit	65-6120	Thermo Fisher Scientific	1 : 3,000	N/A

Table 2.3: Antibody dilutions applied for western blotting. Catalogue number, company, as well as dilutions used and the molecular weight of protein recognised by each antibody is provided.

2.4.12 Enhanced chemiluminescence detection

Pierce™ enhanced chemiluminescence (ECL) western blotting substrate (Thermo Fisher Scientific) was used for ECL detection. After removal of PBS buffer, the membrane was incubated with the ECL substrate working solution, prepared by mixing equal parts of detection reagents 1 and 2. After 1 min of incubation at room temperature, the membrane was removed from the working solution and placed on a clear plastic wrap and taped into an X-ray cassette (18 cm × 24 cm) with the protein side facing up. The excess liquid was removed while ensuring no air bubbles were formed between the blot and the membrane protector. Under red safe light, X-ray film (Fuji Super RX-N, Fujifilm, Japan) was then placed on top of the membrane. Exposure times were varied, depending on the quality of the primary antibody and the intensity

of the signal. The film was removed from the cassette and placed into the Compact X4 film processor (Xograph, UK). The molecular weights of each of the protein bands were marked on the film by placing it over the membrane.

2.5 Sub-cellular protein fractionation

Sub-cellular protein fractionation was performed using a fractionation kit and all buffers were supplemented with proteinase inhibitors at all times, unless otherwise stated (Thermo Fisher Scientific), according to manufacturers guidelines. More specifically, cells (1×10^6 in 1 mL) were seeded in T-75 flasks and left at 37 °C, 5% CO_2. Cells were harvested upon reaching 80% confluence, as described in Section 2.1.1, and were subsequently centrifuged at 500 × g for 5 min at 4 °C. Cell pellets were then prepared as described in Section 2.4.5. Ice-cold cell extraction buffer (CEB) was added to the cell pellet (1 mL CEB per 100 µL cell packed volume) and incubated for 10 min at 4 °C with gentle mixing. Samples were then centrifuged 500 × g for 5 min at 4 °C and the supernatant, consisting the cytoplasmic extract, was transferred to a pre-chilled 1.5 mL tube. To the pellet, an ice-cold membrane extraction buffer (MEB) was added and the samples were again incubated for 10 min at 4 °C with gentle mixing followed by centrifugation at 300 × g for 5 min. The supernatant, the membrane fraction, was then transferred to a new pre-chilled tube as before. Nuclear extraction buffer (NEB, ice-cold) was then added to the pellet and samples were incubated for 30 min at 4 °C with gentle mixing. Samples were then centrifuged at 5,000 × g for 5 min and the supernatant, the nuclear extract, was transferred to a 1.5 mL tube.

Samples were stored at −80 °C until used.

2.6 Statistical analysis

All statistical analyses and non-linear regression were performed using GraphPad Prism 5 (GraphPad Software,USA) and the specific tests and methods performed in each chapter are detailed where therein. The data were obtained in at least triplicates and results are reported and graphed as mean ± standard error mean (SEM), unless otherwise stated.

Chapter 3

Imaging p53 – *in vitro* antibody validation

3.1 Introduction

p53 is one of the most extensively studied tumour suppressor proteins and mutations responsible for the loss of p53 function result in the expression of p53 protein that has an abrogated wild-type role, exerting a dominant negative effect over any remaining wild-type p53 (Petitjean et al., 2007; Muller and Vousden, 2014). It has been widely known since the late 90's that under normal conditions, wild-type p53 has a very short half-life as it is constantly targeted for degradation by its main regulator MDM2, while mutant proteins escape this feedback loop leading to a high p53 accumulation in cancer cells (Midgley and Lane, 1997; Ashcroft and Vousden, 1999; Hailfinger et al., 2007). Most mutations correspond to a single amino acid substitution within the full 393 amino acid protein sequence of the central DNA binding domain, with a number of hotspots being identified (R175, G245, R248, R249, R273, R282). These changes result in the presence of p53 protein that is misfolded and highly unstable, a phenotype crucial for the acquisition of "gain-of-function" (GOF) characteristics (Muller and Vousden, 2013).

As detailed in Section 1.3, pancreatic ductal adenocarcinoma (PDAC) makes up more than 90% of pancreatic cancer cases and is characterised by a distinct genetic landscape throughout its progression, starting with mutations in the *KRAS* oncogene followed by loss of *TP53* function in approximately 50% of cases due to a missense mutation (R175H) in the later stages of development (Hruban et al., 2000; Moore et al., 2003; Bailey et al., 2016). This mutation of p53 has been strongly correlated with a malignant phenotype in PDAC as well as other cancers, thus, the detection of

p53 mutations could aid the optimum therapeutic selection (Waddell et al., 2015). Therefore, and as stated in Section 1.10, the main goal of this study was the development of a non-invasive imaging probe for the detection of p53 mutations in PDAC mouse models *in vivo*. Imaging agents are designed to provide an image format of the accurate reflection on disease biochemical behaviour of the disease in real-time. Hence, the optimal probe should exhibit high target specificity and binding affinity to avoid non-specific uptake in other tissues and false positive results which will affect image analysis (Chen and Chen, 2010). The first step towards achieving this vision is the characterisation of a commercially available antibody used as the p53-targeting vector, based on the methodology published by Cornelissen *et al.* (Cornelissen et al., 2011). In this chapter a number of assays were used to validate the specificity and affinity parameters in two cell lines with positive or negative p53 profile. The cell lines used were derived from a genetically engineered mouse model of PDAC (KPC), first described by Olive *et al.* (Olive et al., 2004; Olive and Tuveson, 2006), that replicates the human histopathology and metastatic profile characterised by a mutation in KRAS (G12D) and a differential p53 status. B8484 cells were derived from a KPC-mouse with *LSL-Kras*$^{G12D/+}$, *LSL-Trp53*$^{R172H/+}$, *Pdx-1-Cre* status, while P2FIR cells were derived from KPC-mouse with *LSL-Kras*$^{G12D/+}$, *LSL-Trp53*^{flox}, *Pdx-1-Cre*. Both cell lines were used throughout this study in an *in vitro* an *in vivo* setting (Hamilton et al., 2014).

3.2 Materials and methods

All buffers and solutions are detailed in Chapter 2, unless otherwise stated.

3.2.1 p53 detection with flow cytometry

Cells were seeded in a 10 cm diameter culture dish (1×10^6 cells) and left to adhere overnight at 37 °C and 5% CO_2. After trypsinisation (detailed in Section 2.1.1), cells were centrifuged for 5 min at 300 × g at 4 °C in 15 mL centrifuge tubes using the Heraeus™ Megafuge™ 40 centrifuge (Thermo Fisher Scientific). After the removal of supernatant, cells were washed once with PBS and centrifuged once more for 5 min at 300 × g before resuspending the pellet in 4% paraformaldehyde (PFA) (500 µL) and incubating for 10 min at 37 °C. The PFA was then removed by centrifugation (5 min, 300 × g), cells were washed with PBS and immediately permeabilised using 500 µL of 0.1% Triton-X-100 in PBS for 20 min at 4 °C. Samples were treated with blocking solution containing 2% FBS (v/v) in PBS for 20 min at room temperature under stirring. Cells were then incubated with the primary mouse anti-p53 (1C12) diluted in blocking solution (1 : 3,200 dilution) for 1 h at room temperature or with a monoclonal mouse IgG_1 isotype control (1 : 200 dilution, 1 mg/mL stock, R&D Systems, USA). Cells were washed twice with PBS, each time removing the supernatant by centrifugation (300 × g, 5 min). Finally, secondary antibody Alexa Fluor 488 goat anti-mouse IgG, diluted 1 : 200 in blocking solution, was added and the samples were agitated for 40 min at room temperature. Cells were then washed one last time with PBS and resuspended in 1 mL PBS for analysis. Data

was acquired using a Becton Dickinson FACSCalibur™ (BD, USA) and analysis, including histogram overlays, were performed using FlowJoV10 software (FlowJo, LLC, USA).

3.2.1.1 Data acquisition and analysis

For each sample, a total of 15,000 detection events were acquired at an approximate rate of 150-300 events per second. The control sample contained no primary antibody and was used to adjust the side-scatter area (SSC-H) versus forward-scatter area (FSC-H) axes to reveal the general cell population (Forment and Jackson, 2015). Single cells were gated from the general population by plotting forward-scatter linear width (FSC-W) against forward-scatter linear area (FSC-A) values from the single cell population. The detected fluorescence at 488 nm was displayed in histogram mode (FL1-H) where the horizontal axis represents the fluorescent signal value in channel numbers and the vertical axis the number of events per channel.

3.2.2 siRNA-mediated gene silencing

Cells were seeded in a 6-well plate (1×10^5 cells per well) and left to adhere overnight. The following sequences in the p53 coding region were targeted with pre-designed ON-TARGETplus mouse Trp53 siRNA-SMARTpool (Dharmacon, USA) at a working concentration of 50 nM. The four p53 siRNA sequences in the pool are: siRNA1 GUAAACGCUUCGAGAUGUU, siRNA2 AAAUUUGUAUCCCGAGUAU, siRNA3 GAGGAGUCACAGUCGGAUA, and siRNA4 CAGUCUACUUCCCGCCAUA. Transfections were carried out using Lipofectamine RNAiMAX reagent (Invitrogen, UK)

according to manufacturer's specifications. More specifically, siRNA and lipid pre-mixed samples were prepared separately in serum-free DMEM media by mixing 5 µL of 20 µM siRNA (final concentration of 50 nM) and 7.5 µL Lipofectamine RNAiMAX respectively. Each mix was then incubated for 5 min at room temperature before the siRNA was added to the lipid pre-mix and incubated for a further 20 min. The siRNA-lipid complex was then added to each well and cells were incubated at 37 °C for 48 h. Control transfections were performed using identical procedures but without the siRNA mix and with the Lipofectamine reagent only to ensure that the effects observed were independent of the transfection agent used.

3.2.3 Immunocytochemistry

For immunocytochemistry studies with labelled secondary antibodies, cells (2×10^5 cells per well) were seeded in 6-well plates, equipped with a sterile cover glass (24 × 24 mm) at the bottom of each well. Cells were then incubated overnight at 37 °C and in a 5% CO_2 humidified chamber before fixation and labelling with antibodies.

3.2.3.1 p53 staining

After incubation, cells were washed with 1 mL PBS and immediately fixed with 4% (w/v) PFA in PBS (500 µL) (Sigma-Aldrich) for 30 min at room temperature. The cells were then washed three times with PBS for 5 min each followed by permeabilisation with 500 µL of 0.2% (v/v) Triton-X-100 in PBS (Sigma-Aldrich) for 10 min at 4°C. Cells were then washed three times with PBS and blocked with 500 µL of blocking solution composed of 2% (w/v) BSA in PBS for 1 h at room temperature.

Primary mouse anti-p53 (1C12) antibody was prepared in blocking solution (1 : 4,000 dilution) and 300–400 µL was added to each well, and incubated at room temperature for 1 h or overnight at 4 °C. After incubation with the primary antibody, cells were washed three times with PBS and incubated with 300–400 µL secondary antibody, Alexa Fluor 488 goat anti-mouse IgG (Thermo Fisher Scientific), 1 : 500 dilution in blocking buffer, for 1 h at room temperature. Subsequently, cells were washed three times with PBS for 5 min at room temperature. The prepared glass cover (at the bottom of each well) were then mounted onto a microscope slide (Thermo Fisher Scientific) following the addition of a drop of Vectashield® mounting media containing 4',6-diamidino-2-phenylindole (DAPI) (Vector Laboratories, USA). Samples were imaged using a Leica TCS SP8 confocal laser Scanning platform (Leica microsystems, UK) equipped with 63 × oil-immersion objective lenses and an excitation maximum wavelength of 358 nm and 490 nm for DAPI and Alexa Fluor 488, respectively.

3.2.4 Enzyme linked immunosorbent assay

For the enzyme linked immunosorbent assay (ELISA), 1×10^4 cells per well were seeded in a 96-well plate and incubated overnight at 37 °C in a 5% CO_2 humidified chamber. The cell media was aspirated and cells were washed with PBS prior to cell fixation with 100 µL of 4% PFA for 10 min at 4 °C. After the removal of PFA, cells were washed with PBS and then permeabilised with 100 µL of permeabilisation solution, containing 1% (v/v) Triton-X-100 in PBS for 15 min at room temperature. Cells were then blocked with 100 µL of ELISA blocking buffer (Thermo Fisher Scientific) for 45 min at room temperature. Serial dilutions of the primary mouse anti-p53 (1C12)

monoclonal antibody in blocking solution were added in triplicates to the cells and were incubated for 1 h at room temperature. After removing the primary antibody, cells were washed twice with Tris-buffered saline wash buffer, supplemented with 0.1% (v/v) Tween-20 in deionised H_2O (dH_2O) (TBS-T) and consequently incubated at a 1 : 5,000 dilution of goat anti-mouse IgG (H/L) : HRP secondary antibody for 40 min at room temperature. At the end of the incubation period, cells were washed twice with TBS-T wash buffer and 100 µL of 3,3',5,5'-tetramethylbenzidine (TMB) substrate solution (Abcam, UK) was added to each well, resulting in a visible blue colour. To the samples, 100 µL of stop solution (1 N HCl, 0.6 N sulfuric acid) was added and the absorbance at 450 nm was measured using the Infinite® 200 Pro microplate reader (Tecan Group Ltd, Switzerland).

3.2.5 Statistical analysis

For flow cytometry, data were reported as mean ± SEM (standard error of mean) and statistical analysis were performed using GraphPad Prism 5 (GraphPad Software,USA). A Mann-Whitney test was used to compare medians between groups.

3.3 Results

3.3.1 Validation of the anti-p53(1C12) antibody

The mouse monoclonal (mAb) anti-p53 (1C12) antibody, which detects endogenous levels of total p53 protein, was selected from a panel of others (Table 2.2, Section 2.3) due to its application range, literature references and pricing. Considering the vari-

able quality of commercially available antibodies, the anti-p53 (1C12) was validated using a set of criteria evaluating its specificity, reproducibility, and affinity. B8484 (*LSL-Kras*$^{G12D/+}$, *LSL-Trp53*$^{R172H/+}$, *Pdx-1-Cre*) and P2FIR (*LSL-Kras*$^{G12D/+}$, *LSL-Trp53*^{flox}, *Pdx-1-Cre*) KPC-derived cell lines were used throughout this study as p53-positive and p53-negative controls, respectively.

3.3.1.1 Western blot analysis

To test the specificity of the anti-p53 (1C12) antibody, western blot analysis was performed as the first verification whereby specificity was confirmed by the presence of a single band at a corresponding molecular weight of the protein of interest. Whole cell extracts from B8484 and P2FIR samples (20 µg total protein) (see Section 2.4.6) were loaded onto 4-12% Bis-Tris protein gels followed by immunobloting for p53 and results are shown in Figure 3.1.

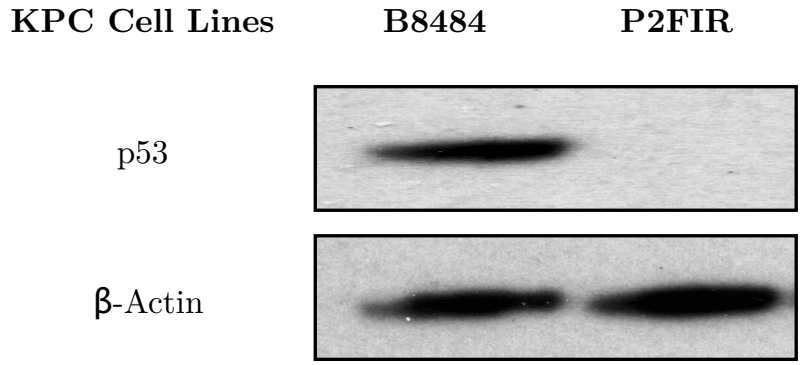

Figure 3.1: Antibody validation by western blot. Representative western blot of p53 protein expression in B8484 and P2FIR KPC-derived cells. Whole cell protein extracts (20 µg total protein) were loaded on SDS-PAGE, followed by immunoblotting with mouse monoclonal anti-p53 (1C12) antibody (Lot No:7). β-Actin was used as a loading control.

As can be seen in Figure 3.1, B8484 KPC-derived cell lines, harbouring a p53 missense mutation (R172H), presented a high level of p53 basal protein expression and there was indeed a singular band at a molecular weight of approximately 53 kDa corresponding to p53 protein (see full developed film in Appendix, Figure A.1). In contrast, no protein product was detected in the p53-null P2FIR negative control cells.

To confirm that the signal observed in B8484 cells originate from the mutant variant of p53, as well as to gain clearer insight of the expression level in the wild-type cells, a comparison was made between the B8484, P2FIR, and mouse embryonic fibroblast (MEF) that carry wild-type p53. As evident in Figure 3.2, there was a very faint p53 signal in the MEF cells when compared to the highly accumulated p53 protein in B8484 cells.

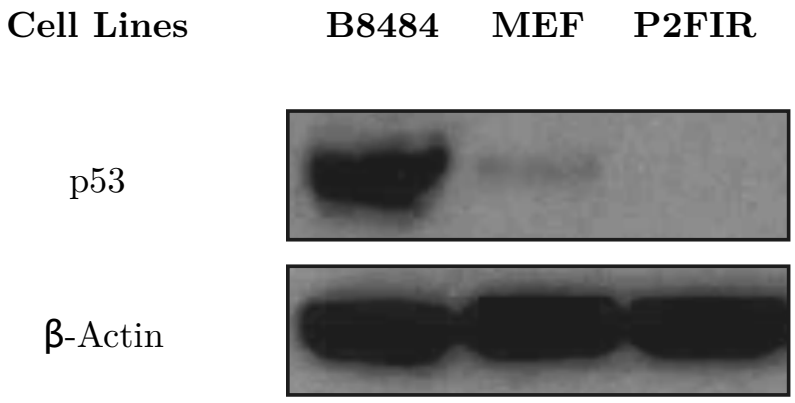

Figure 3.2: Representative western blot of p53 protein expression levels in B8484 ($Trp53^{R172H/+}$), P2FIR ($Trp53^{flox}$) and MEF ($Trp53^{+/+}$) cell lines. Total protein (30 µg) was loaded on SDS-PAGE, followed by immunoblotting with mouse monoclonal anti-p53 (1C12) antibody . β-Actin was used as a loading control.

These results were reproducible amongst different lots of the anti-p53 (1C12) antibody (see Appendix, Figure A.2), where only a single band was present at 53 kDa.

3.3.1.2 Flow cytometric analysis

In addition to western blot, flow cytometry was performed to quantitatively evaluate the ability of the anti-p53 (1C12) antibody to detect p53 protein at a single-cell level. Cells were incubated with the primary anti-p53 (1C12) antibody followed by a secondary Alexa Fluor 488-conjugated antibody, as detailed in Section 3.2.1, producing a signal while they individually passed through a beam of light. Data were acquired and analysed using FlowJoV10 software as described in Section 3.2.1.1.

From the 15,000 events acquired per sample, the percentage of p53-positive cells was calculated from the gated cells in forward (FSC-H) and side (SSC-H) scatter profile as can be seen in the dot plots for both B8484 and P2FIR KPC-derived cell lines with each cell registered as a single dot (Figure 3.3a and Figure 3.3b, respectively). Median fluorescence intensity (MFI) was used to quantify the differences in cellular fluorescence of each cell population. The MFI values for each sample were plotted on GraphPad Prism 5 whilst correcting for background (samples stained only with secondary antibody). As shown in Figure 3.3c, B8484 cells present more than a 10-fold greater MFI than that observed in P2FIR cells. Furthermore, evident fluorescence intensity shift (histogram mode, FL1-H) was detected in B8484 cells while the signal from P2FIR cells was similar to background levels (Figure 3.3d). Cells incubated with IgG_1 isotype control or fluorophore-labelled secondary antibodies alone served as non-specific binding and background controls, respectively, but were also important for the correct identification of positively and negatively labelled cell populations.

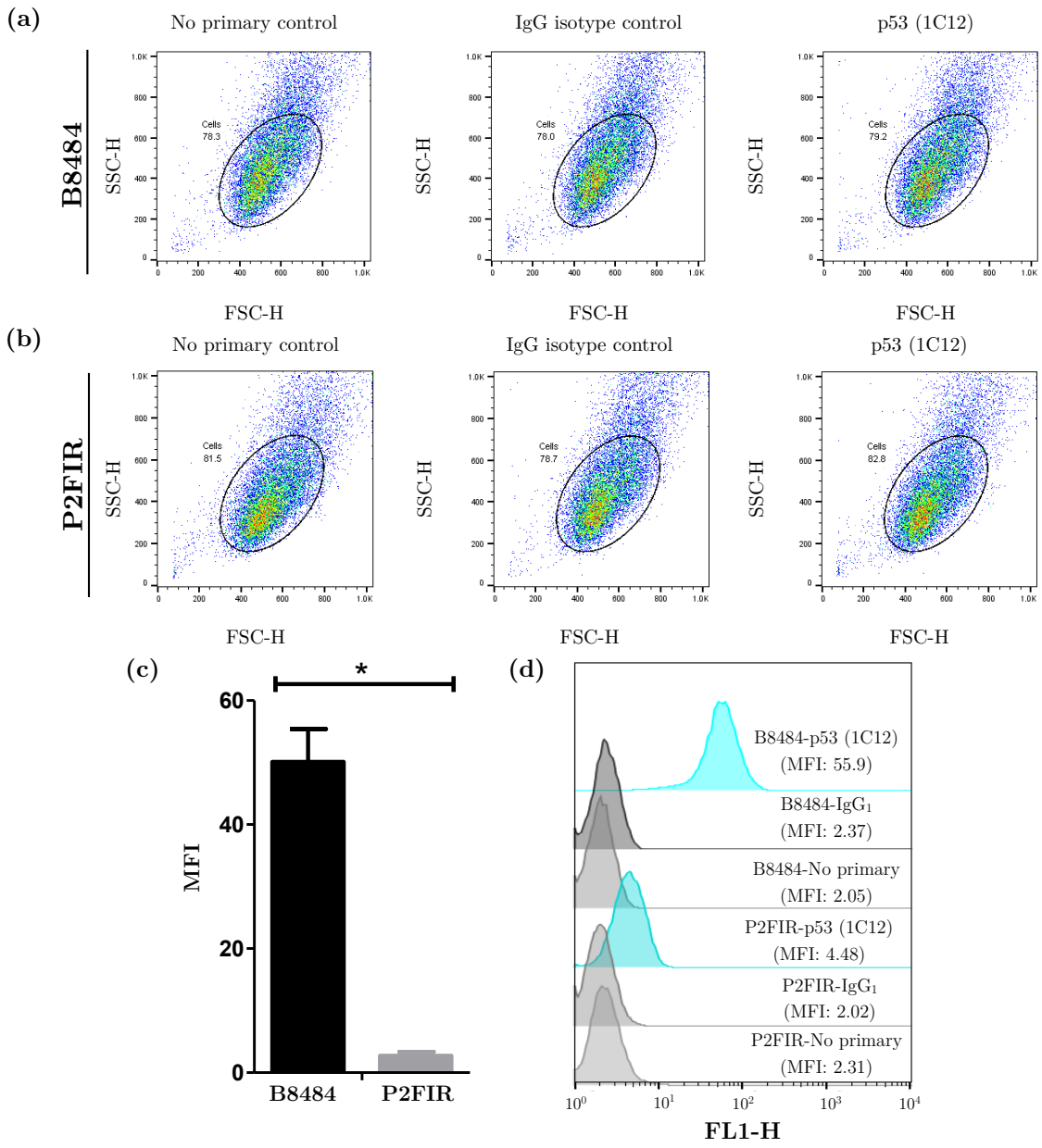

Figure 3.3: Antibody validation using flow cytometry. (a) and (b) Dot blot of all 15,000 events and the representative gated cell population for B8484 and P2FIR cells, respectively (c) p53 expression in B8484 and P2FIR KPC-derived cell lines determined by median fluorescence intensity (MFI) values. Error bars represent mean ± standard error mean (SEM) (n = 3 independent biological experiments) (d) Representative histogram of the FL1-H parameter (Alexa Fluor 488 fluorescence), indicating the population of p53-positive cells. IgG_1 or fluorophore-only stained cell populations were used as background controls.

3.3.1.3 Evaluation by siRNA-mediated protein knockdown

Additional antibody validation by siRNA gene silencing for *Trp53* gene was performed to further ensure if the observed differences represented true protein detection. siRNA transfections were performed in B8484 KPC-derived cells as described in Section 3.2.2, using RNAiMAX transfection reagent. p53 expression was depleted using a p53 siRNA pool at a working concentration of 50 nM. Non-transfected (**NT**) cells were added to allow side by side comparisons. Expression of p53 protein was then assessed by western blot 48 h post-transfection using the 1C12 antibody (Figure 3.4).

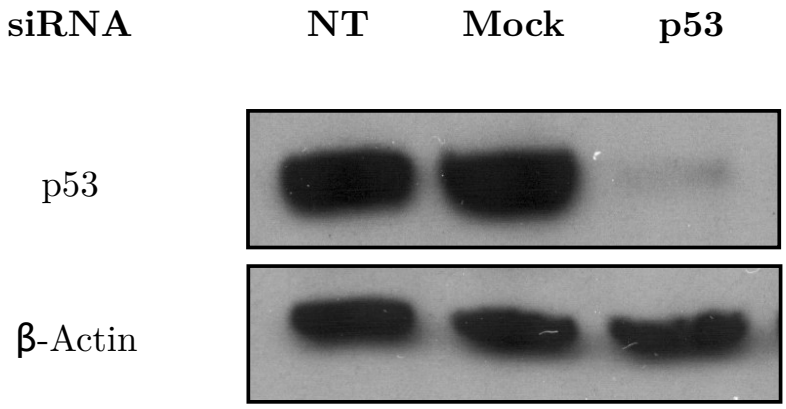

Figure 3.4: Validation of 1C12 antibody by siRNA-mediated protein knockdown in B8484 cell line. B8484 cells were incubated with either a p53-targeting siRNA pool or transfection-reagent only (Mock), and harvested 48 h after for western blot analysis. Non-transfected cells (NT) were also prepared as controls. Total protein (10 μg) was loaded on SDS-PAGE, followed by immunoblotting with mouse monoclonal 1C12 antibody. β-Actin was used as the loading control.

Whole cell protein extracts (10 μg total protein) were used following procedures described in Section 2.4. Compared to mock-transfected B8484 cells (**Mock**, Figure 3.4), a reduction in p53 expression level of greater than 50% was observed in cells treated with the p53 siRNA pool (**p53**, Figure 3.4). This depletion of p53 in B8484

cells was not affected by the transfection reagent as there was no difference in protein expression levels between the non-transfected and mock-transfected (**NT** and**Mock**, Figure 3.4) samples.

3.3.2 Intracellular localisation of p53 using confocal microscopy

The intracellular localisation of p53 has been extensively studied since the early 80's (Dippold et al., 1981; Middeler et al., 1997; Marchenko et al., 2007). It was demonstrated that p53 mainly resides in the cytoplasm of normal cells, however, due to a compromised degradation of mutant p53 (as discussed in Section 1.4.2), it accumulates to high levels in tumour cells, especially in the nucleus. Taking this understanding of p53 localisation into account, p53 distributions within the B8484 and P2FIR KPC-derived tumour cells were determined by indirect immunofluorescence using confocal microscopy (Figure 3.5). Cells were processed with procedures described in Section 3.2.3, and probed with anti-p53 (1C12) antibody followed by staining with a fluorophore-conjugated secondary antibody (Alexa Fluor 488 goat anti-mouse IgG) and images are shown in Figure 3.5.

As seen in Figure 3.5a, B8484 cells presented enhanced nuclear staining (as observed by colocalisation with the DAPI nuclear stain) of the p53 mutant protein with a significant fraction in the cytoplasm. In contrast, no p53 staining was detected in p53 null P2FIR cells (Figure 3.5b).

This distribution of p53 both in the nucleus and in the cytoplasm is in agreement with studies that observed a similar localisation pattern for the R175H mutant (human equivalent of the murine R172H mutant), when transfected into $p53^{-/-}$ human colon

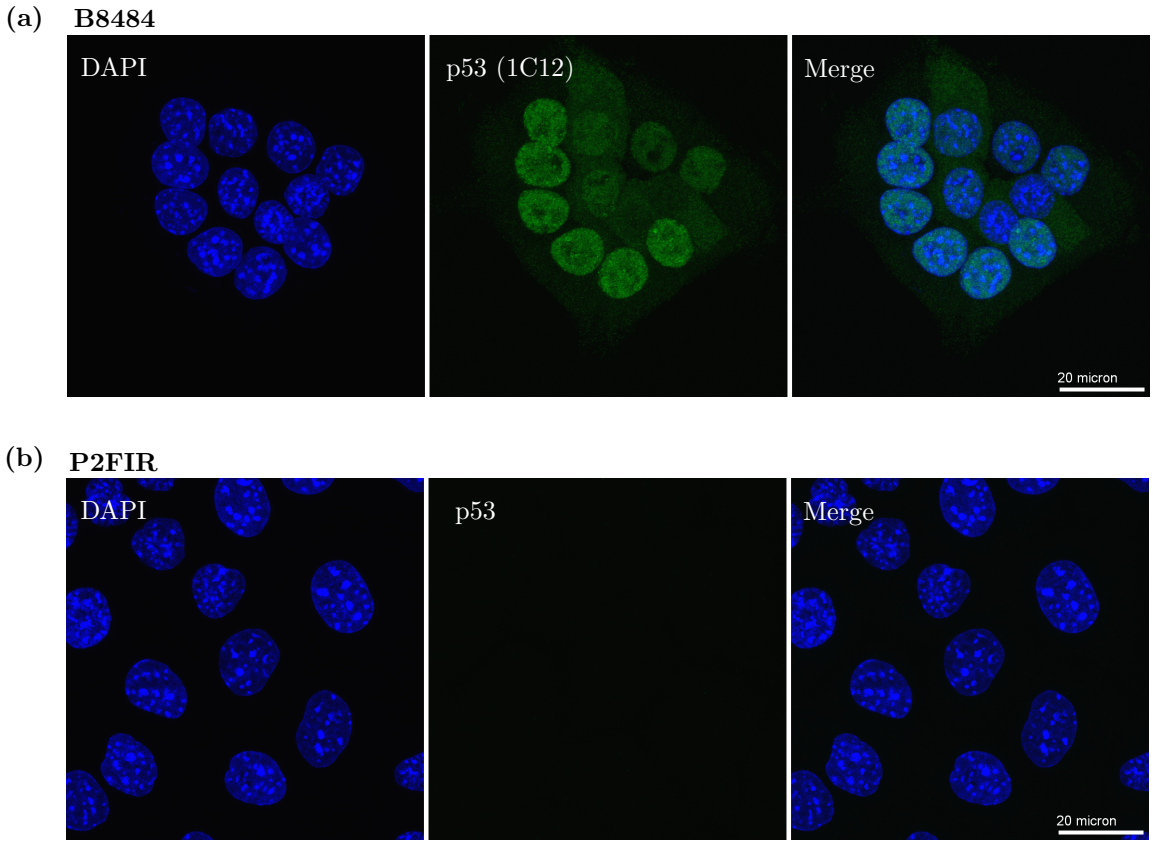

Figure 3.5: Representative microscopy images of intracellular localisation of p53 in KPC-derived cell lines. B8484 (a) and P2FIR (b) cells were stained with the anti-p53 (1C12) primary antibody followed by an Alexa Fluor 488-conjugated anti-mouse secondary antibody (green). Nuclei were visualised using DAPI (blue, left panel). Images were acquired using a Leica TCS SP8 confocal laser scanning platform. Scale bar is 20 μm for all images.

carcinoma HCT 116 cells (Morselli et al., 2008). No signal was detected on the membrane of either cell line.

Finally, to support the validity of staining and to ensure that the secondary antibody exhibit no non-specific binding towards endogenous IgG, a control staining without primary antibody was applied to the B8484 cells, where little to no background staining was observed (Figure 3.6). These results confirm that the staining observed above was representative of endogenous p53 expression. All images were processed using Fiji (ImageJ, USA) using the same analysis parameters.

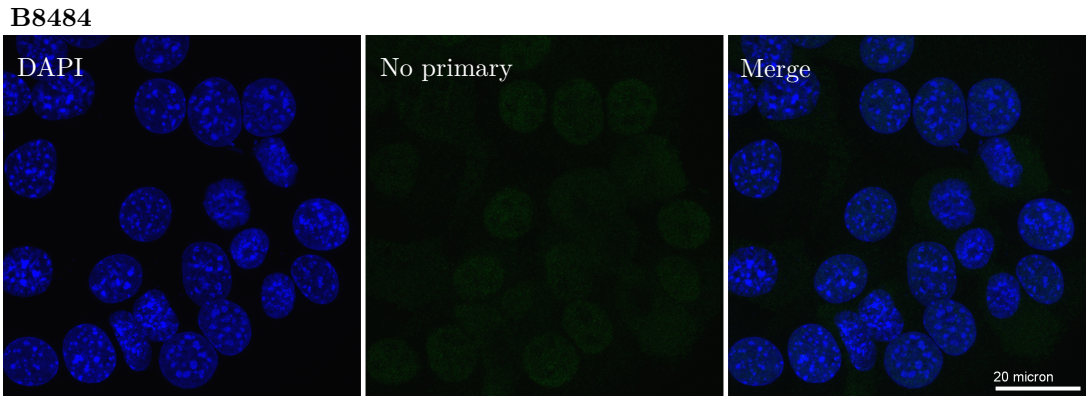

Figure 3.6: Evaluation of non-specific fluoresence in B8484-KPC derived cells. Cells were incubated with fluorophore-conjugated antibody only (Alexa Fluor 488). DAPI (blue) was used to stain nuclei. Scale bar is 20 μm.

The sub-cellular distribution of p53 in B8484 cells was also evaluated by fractionation studies, as described in Section 2.5, where each of the sub-cellular compartments (membrane, cytoplasm, nucleus) was prepared separately and probed for the presence of p53 protein by western blot. However, the results obtained from three independent biological experiments (see a representative blot in Appendix A.3) do not agree with the p53 distribution presented above (Figure 3.5a). More specifically, the p53 protein seems to appear not only in the nucleus and cytoplasm but also in the membrane fraction. This can be attributed to a possible cross-contamination by various compartments during the fractionation protocol as evident by the presence of α-tubulin, a cytoplasmic marker, in all three fractions invalidating the process.

3.3.3 Evaluation of antibody affinity by ELISA

In order to gain insight of the interaction between the antigen binding site of anti-p53 (1C12) and the p53 epitope, the equilibrium dissociation constant (K_D) was characterised. An interaction of high affinity is represented by a low K_D, where the

association rate (k_{on}) is many orders of magnitude faster compared to the dissociation rate (k_{off}).

Indirect enzyme-linked immunosorbent assay (ELISA) was used, as described in Section 3.2.4. In this experiment, an antigen immobilised to a surface, is bound to an antibody linked to an enzyme (horseradish peroxidase, HRP). Detection is then performed using a substrate-chromogen reagent that recognises the conjugated enzyme and allows the colour to develop. The absorbance is then measured at 450 nm.

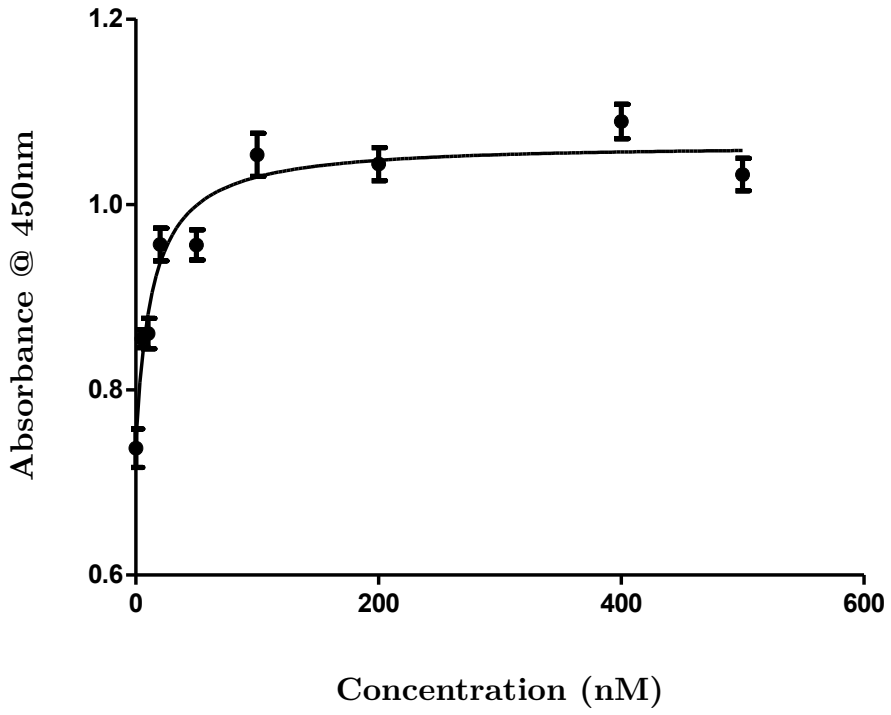

Figure 3.7: Evaluation of binding affinity by ELISA. Saturation binding curve representing the binding of the p53 (1C12) mouse monoclonal antibody to the p53 antigen in fixed and permeabilised B8484 cells. The K_D was estimated as 9 ± 2.2 nM (n = 5 independent biological experiments) by non-linear regression analysis.

The K_D value was determined for the B8484 cells using a range of concentrations for the anti-p53 (1C12) antibody. In Figure 3.7, a representative binding curve is displayed, indicating binding of the anti-p53 (1C12) antibody to the p53 antigen, reach-

ing saturation at approximately 200 nM with an affinity constant K_D of 9 ± 2.2 nM. The data was fitted to a saturation binding curve using a non-linear regression fitting model of the GraphPad Prism 5 software to the following equation:

$Y = B_{max} \times X^n / (K_D + X^n)$

where B_{max} is the maximum specific binding, X is the concentration in nM, n is the curve slope factor, and K_D is the dissociation constant. The background was constrained to the reading obtained where no concentration of antibody was added, representing non-specific binding. When determining the affinity in P2FIR cell line using same concentrations as in B8484 cells, the resulting binding curve was interrupted and no K_D value was generated. This K_D value in the low nanomolar range suggests high affinity of the anti-p53 (1C12) antibody for its antigen in B8484 cells.

3.4 Discussion

In this chapter the mouse monoclonal (mAb) anti-p53 (1C12) antibody was validated *in vitro* by several assays to confirm its suitability for this study as a tool for the recognition of mutant p53.

The anti-p53 (1C12) antibody specificity was first tested using western blot, a commonly used method in biological research. A panel of cancer cell lines with a known p53 status were used as a first step to understand whether the antibody recognises the antigen in its denatured form. A single band was observed at the molecular weight of approximately 53 kDa for the p53-positive B8484 KPC-derived cell line (Figure 3.1) whereas no signal was detected in the p53-null P2FIR cells. The observed strong

signal in B8484 cells suggests a significant accumulation of the p53 mutant protein, likely due to the lack of efficient degradation by the proteasome as well as a complete abrogation of the existing wild-type allele (Blagosklonny, 1997; Muller and Vousden, 2013). No other bands were present across the membrane at different molecular weights, which strongly suggests the lack of any breakdown products or splice variants.

The positive B8484 cells presented a great accumulation of the mutant p53 protein as shown by the comparison made with the p53 wild-type MEF cells (Figure 3.2). Taken together, the observations are in great agreement with the common notion that mutations of p53 lead to the expression of a full-length mutant protein with abrogated functions, that usually presents a dominant negative effect over the remaining wild-type p53 allele (Petitjean et al., 2007). This phenomenon is observed in many types of cancer, including pancreatic ductal adenocarcinoma (PDAC).

While these data suggest the strong specificity towards the epitope in its denatured form of the antibody utilised in the study, information provided by western-blots are semi-quantitative in nature. This was therefore supplemented by the flow cytometric analysis of p53 protein expression levels, which provided information on single cell level, based on their fluorescent properties. The data generated by flow cytometry corroborates those obtained from western blot as significant difference in p53 expression levels was observed between the B8484 and P2FIR cells (Figure 3.3c). The combined results from western blot and flow cytometry not only confirmed the good specificity of the anti-p53 (1C12) mAb, but also the reproducibility as different lots were tested providing comparable results.

Genetic strategies such as siRNA knockdown have been used extensively for antibody validation, where the target messenger RNA (mRNA), coding the target protein, is degraded to knockdown the production of a specific protein in the cell. This approach provides a strong correlation between the gene and the target protein and its recognition by the antibody. Therefore, it is a particularly useful method to test the specificity of an antibody towards proteins that come from relevant genes (Uhlen et al., 2016). In Section 3.3.1.3, the western blot assaying p53 compared siRNA knockdown of the protein in the B8484 cell line with a mock control (no siRNA) where a strong reduction of antibody staining was observed after treatment with p53 siRNA pool. This data set suggest favourable antibody specificity, especially against related proteins, such as other p53 family members.

After characterisation of the specificity of the antibody, the sub-cellular distribution of p53 was evaluated in both cell lines of interest (B8484 and P2FIR, Section 3.3.2). These experiments showed that p53 protein was mainly localised in the nucleus in B8484 cells with some diffuse staining in the cytoplasm (Figure 3.5a), which is in agreement with previously published literature (Yu et al., 2000; Morselli et al., 2008; Comel et al., 2014). No staining was observed in P2FIR cells (Figure 3.5b). These findings were similar to those observed by the Human Protein Atlas (Atlas, 2017). More specifically, in a panel of human tumour sections, including pancreatic cancer, p53 protein was found primarily in the nucleus using antibodies against human p53. However, further validation using fractionation studies were unsuccessful, thus making these observations inconclusive.

Finally, antibody affinity was determined using an ELISA method, a quantitative and

high-throughput assay, which gave the K_D value of 9 ± 2.2 nM (Figure 3.7). Such a K_D value at the nano-molar range are usually associated with high affinity, thus indicating the strong affinity of the anti-p53 (1C12) mAb for the p53 antigen in B8484 cells.

3.5 Conclusions

The work presented in this chapter demonstrated, through a number of characterisation methods, the suitability of the anti-p53 (1C12) mAb for the purposes of this study as a high quality antibody, proving good specificity, reproducibility and affinity. However, the techniques utilised were not without their shortcomings: i, the results could be assay dependent; ii, detection systems could be highly sensitive to environmental factors; and iii, the non-specific binding of antibody could lead to fluctuations between cell lines. Therefore, it would be interesting to carefully evaluate the abundance of p53 antigen in these KPC-derived cell lines and also estimate any potential binding partners that might have similar sequences to p53. One such approach could be similar to that reported by Marcon *et al.* (Marcon et al., 2015), a novel method based on mass spectrometry (MS) evaluation of antibodies mainly used for immunoprecipitation studies. The authors generated a standard operating procedure where 1,124 synthetic antibodies were applied for immunoprecipitation of their respective antigens from HEK293 cells and analysed by MS with the aim of identifying any bound proteins. With further development of this technique, it could serve as a strong supplementary method for the validations performed in the present

chapter.

In conclusion, the data in this chapter support the feasibility of using the anti-p53 (1C12) antibody, considering its optimal binding properties for the target of interest.

Chapter 4

Synthesis and *in vitro* validation of radioconjugates

4.1 Introduction

Antibodies have been widely used as the basis of imaging agents thanks to their well-known biodistribution, lack of toxicity and side effects, pharmacokinetic characteristics as well as high target affinity and specificity. Compared to small molecules, the size of antibodies (150 kDa) facilitates the long plasma half-life (24–56 h) which often lead to higher tumour uptake, hence giving a greater tumour-to-background level (Warram et al., 2014). However, their large size and hydrophilicity also limits their application in intracellular delivery due to poor permeability and specificity. Furthermore, even the ones that could enter the cell through endocytosis, they are likely to be degraded by lysosomes, without interacting with their target. While a number of techniques exist for cellular injection of antibodies, such as microinjection, electroporation, and liposome encapsulation (Chakrabarti et al., 1989; Park et al., 2002b; Zhang and Yu, 2008; Yang and Hinner, 2015), these are limited to *in vitro* applications as their invasive nature (disruption of cell membrane, cell-to-cell variability) make them unsuitable for *in vivo* or clinical applications.

Since their discovery, cell penetrating peptides (CPPs), also referred to as protein transduction domains (PTDs), have been extensively used to facilitate the intracellular entry of large biomolecules, overcoming the selective nature of the cell membrane (Kersemans and Cornelissen, 2010). The transactivator of transcription protein (TAT), derived from the human immunodeficiency virus (HIV-1) has been reported to deliver various cargos into the cell both *in vitro* and *in vivo* (Mann and Frankel, 1991; Cornelissen et al., 2011; Schwarze et al., 1999). However, the mechanism of

entry is still unclear, with many pathways implicated over the years (as discussed in Section 1.9.1). The positive charge of the peptide as well as the α-helix formation are considered to play an essential role in the cellular uptake. In particular, the number of arginines in the TAT sequence (GRKKRRQRRRPPQGYG) are responsible for the membrane translocation while the presence of KKRR nuclear localisation sequence accounts for nuclear import (Schmidt et al., 2010).

Several studies have suggested that the internalisation process may be energy and endocytosis independent (Vives et al., 1997; Torchilin et al., 2001) and furthermore was affected by various parameters such as cell type, cargo size, linkage type, as well as membrane composition. Despite these debates, the main pathway of internalisation is widely accepted to be endocytosis (Richard et al., 2003) with the escape mechanism also being poorly understood (El-Sayed et al., 2009).

The use of cell penetrating peptides in molecular imaging has been reported previously, mostly to target intracellular or intranuclear biomarkers (Kersemans and Cornelissen, 2010). The first TAT-conjugated monoclonal antibody imaging agent was described by Hu *et al.*, where the authors characterised the cellular and nuclear uptake of TAT-conjugated molecules labelled with ^{123}I (^{123}I-IgG-TAT) both *in vitro* and *in vivo*, in breast cancer xenografts suggesting a potential method of imaging intracellular and especially nuclear targets (Hu et al., 2006).

While modalities such as magnetic resonance imaging (MRI), computed tomography (CT) and ultrasound have been widely used in diagnostic clinical applications, these techniques can only provide anatomical and physiological information. The aforementioned imaging methods utilising radioisotopes coupled to antibodies, namely single

photon emission tomography (SPECT) and positron emission tomography (PET) (Kaur et al., 2012), offer great sensitivity in visualisation and quantification of biological processes involved in cancer tumourigenesis and progression at a whole body level (Freise and Wu, 2015). While PET offers better sensitivity, greater spatial resolution could be achieved by SPECT in the submillimeter range (≤ 1 mm) in pre-clinical scanners, making SPECT a more suitable imaging modality for pre-clinical assessment of radiolabelled antibodies (Rahmim and Zaidi, 2008; Khalil et al., 2011). The selection of radioisotope has to meet several criteria for applications in *in vivo* imaging studies, such as compatibility to human physiology, half-life, cost and ease of production (Rangacharyulu and Roh, 2015). Of all the different radioisotopes available for SPECT imaging, Indium-111 (^{111}In) was chosen in this study due to its ideal half-life (67.32 h), low cost, and well-established chemistry. Radiolabelled antibodies have been used in the clinic before, with ^{111}In-satumomab pendetite being the first FDA approved labelled monoclonal antibody against a tumour-associated antigen, TAG-72, found in many cancer types (Bohdiewicz, 1998). FDA approval of antibody based imaging agents opened the door to more possibilities for the development of imaging biomarkers.

Taken together, the overall aim of the investigations in this chapter is to validate the radiolabelled anti-p53 (1C12) monoclonal antibody following its characterisation as described in Chapter 3. Considering the important role of p53 in carcinogenesis and cancer progression, an imaging agent would provide an invaluable tool for characterising tumours based on their p53 status. The anti-p53(1C12) was conjugated to the TAT cell penetrating peptide, radiolabelled and evaluated *in vitro*. Assays to

evaluate labelling yield, cell internalisation, binding characteristics were performed in order to assess the potential suitability of these radioconjugates for subsequent *in vivo* imaging.

4.2 Materials and methods

Radioconjugate synthesis was carried out as described by Cornelissen *et. al.* (Cornelissen, B. 2011). All buffers, water, and PBS were de-metallated using Chelex-100 resin (Bio-Rad Laboratories, Inc.) and were filtered through a sterile 0.22 μM syringe filter device with a polyethersulfone (PES) membrane (Merck Millipore, USA).

4.2.1 Conjugation to TAT cell penetrating peptide

The first step towards targeting p53 for imaging was the conjugation of the anti-p53 (1C12) mAb antibody to a CPP , the transactivator of transcription (TAT) protein of HIV-1, which facilitates the delivery of the antibody across the plasma membrane and into the nucleus. The conjugation method exploited the 1-ethyl-3-(3-dimethylaminopropyl)carbodiimide hydrochloride (EDC)/N-hydroxysulfosuccinimide sodium salt (Sulfo-NHS) chemistry whereupon EDC, a crosslinking agent, is used to couple carboxyl groups, present at the side chains of the biomolecule, to primary amines forming an active intermediate. To increase the stability of the intermediate, Sulfo-NHS is then used converting it into an amine-reactive Sulfo-NHS ester reacting with the amines from the TAT peptide forming an amide bond (Figure 4.1). The chemical structures of both EDC and Sulfo-NHS are shown in Figure 4.2a and

Figure 4.2b, respectively.

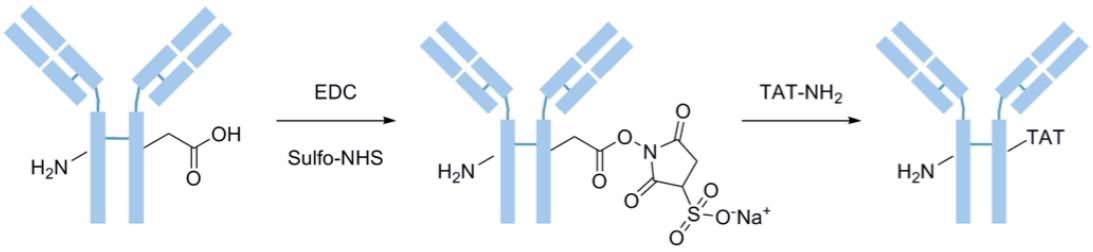

Figure 4.1: Antibody-TAT conjugation *via* EDC/Sulfo-NHS chemistry. EDC/Sulfo-NHS facilitates the activation of carboxyl groups to amine-reactive Sulfo-NHS ester, followed by TAT conjugation through an amide bond formation.

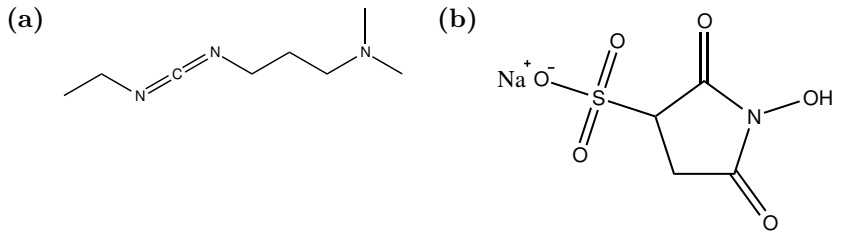

Figure 4.2: Chemical structures of EDC (a) and Sulfo-NHS (b).

More specifically, anti-p53 (1C12) mouse monoclonal antibody or mouse monoclonal IgG_1 non-specific control (R&D Systems Inc., USA) were first buffer exchanged to 0.1 M 2-(N-morpholino)ethanesulfonic acid (MES, pH 6) using an Amicon ultra-centrifugal filter with a nominal molecular weight cut off of 30 kDa, (0.5 mL, Merck Millipore). The filter device was centrifuged for 8 min at 12,300 × g using a Micro Star 12 desktop microcentrifuge (VWR, USA) for three consecutive rounds of concentration and dilution. The final concentration of antibodies was maintained at approximately 1 mg/mL in 100 µL total volume. The antibody was diluted to 200 µL of 0.1 M MES (pH 6) and then 3.1 µL of EDC (130 mM in 0.1 M MES, pH 6) (Thermo Fisher Scientific) and 8.8 µL of Sulfo-NHS (115 mM, in 0.1 M MES,

pH 6) (Thermo Fisher Scientific) were added to give a final concentration of 2 mM and 5 mM, respectively. The resultant solutions were then mixed by vortexing for 15 min at room temperature. The Sulfo-NHS modified antibodies were then buffer exchanged to PBS (pH 7.4) in a final volume of 100 µL and the cell penetrating peptide TAT (GRKKRRQRRRPPQGYG, molecular weight = 1996.3 g/mol) (Cambridge Peptides, UK) was reacted with the antibody for 2 h at room temperature (TAT : antibody ratio at 5 : 1 , TAT stock concentration = 1.4 mg/mL in PBS). Unreacted TAT was removed using Sephadex® G50 gel filtration (Sigma-Aldrich) in PBS (fractionation range 1.5-30 kDa), eluted with 0.1 M sodium bicarbonate buffer at pH 9 (100 µL/fraction, 16 fractions). The fractions with the highest antibody concentration, as determined by Nanodrop 1000 (A_{280}) (Thermo Fisher Scientific), were combined, concentrated and used for the next step (Section 4.2.5.1).

4.2.2 Antibody labelling with the Cy3-NHS dye

Cyanine 3 mono-reactive dye (Cy3-NHS, the chemical structure of the Cy3-NHS dye is shown in Figure 4.3) (GE Healthcare), dissolved in DMSO (10 mg/mL), was reacted with a solution of 1 mg/mL TAT-conjugated antibody (in 0.1 M sodium bicarbonate buffer, pH 9) at a 100 : 1 ratio for 1 h at room temperature. The excess non-reactive reagent was removed by G50 gel filtration medium and the antibody-dye conjugate was eluted in PBS.

The absorbance of the Cy3-antibody conjugate was measured at 280 nm and 550 nm using a spectrophotometer (Nanodrop 1000) (Thermo Fisher Scientific). The degree of labelling was estimated using the method described in Hayashi-Tanaka *et al.* by

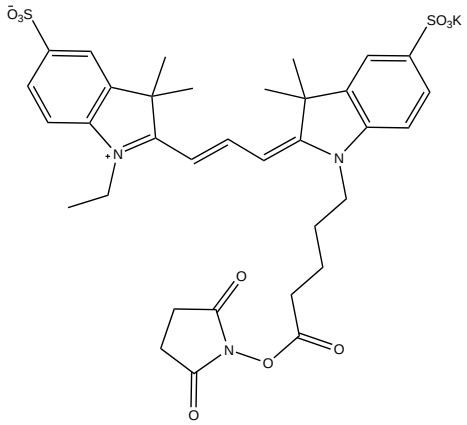

Figure 4.3: Cy3 mono NHS ester.

the following expressions (Hayashi-Tanaka, Y. *et. al.* 2014):

$$\text{Ab Concentration (M)} = \frac{\text{A}_{280} \times \text{A}_{\text{dye}}}{\epsilon_{\text{Ab}}} \times CF \tag{4.1}$$

$$\text{Dye Concentration (M)} = \frac{A_{\text{dye}}}{\epsilon_{\text{dye}}} \tag{4.2}$$

$$\text{Dye: Ab ratio} = \frac{\text{Dye Concentration (M)}}{\text{Ab Concentration (M)}} \tag{4.3}$$

where A_{280} is the absorbance of the cyanine 3-antibody (Cy3-Ab) conjugate at 280 nm for a 1 cm path length and A_{dye} is the absorbance of Cy3 at 550 nm; the correction factor (CF) is the ratio of Cy3 absorbance alone at 280 nm to A_{dye}; ϵ_{dye} is the extinction coefficient of Cy3 at the excitation wavelength (550 nm); ϵ_{Ab} is the extinction coefficient of antibody at 280 nm.

4.2.2.1 Evaluation of conjugation efficiency by SDS-PAGE

Following the synthesis of Cy3-Ab conjugate, 10 μg of sample was prepared in 30 μL total volume with 6 × glycerol based Orange G loading dye (Alfa Aesar, UK). The

samples were subsequently loaded onto a 4-12% Bis-Tris protein gels (Section 2.4.8) and run at 200 V for 32 min (Section 2.4.9), using a prestained protein ladder (PageRuler™, Thermo Scientific) as a molecular weight marker. After the electrophoresis, detection of fluorescent bands was performed with the Odyssey® Fc imaging system (LI-COR, USA) with the 600 nm channel (excitation/emission maxima of 520/600 nm). Thereafter, the gel was stained with coomassie stain (SimplyBlue™ safe stain, Thermo Scientific) at room temperature for 45 min and destained overnight in dH_2O, achieving detection of both the protein ladder and the separated antibody bands.

4.2.3 *In vitro* evaluation of TAT internalisation

B84848 and P2FIR cells were seeded onto sterile cover glass slips with a density at 2×10^5 per well in 6-well plates and left to adhere overnight at 37 °C, in a 5% CO_2 humidified chamber. Cells were then incubated with the fluorophore-labelled conjugates (0.125 μg/mL) for a time period up to 4 h. Medium was then removed and cells were washed twice with PBS prior to fixation with cold 4% PFA for 10 min at room temperature. After fixation, cells were directly mounted onto a microscope slide, using Vectashield mounting media with DAPI. Images were then taken using a confocal laser scanning platform (TCS, SP8; Leica microsystems, UK) equipped with 63 × oil-immersion objective lenses and an excitation wavelength of 548 nm for the Cy3 dye and 358 nm for DAPI.

4.2.4 Immunoreactivity of TAT-conjugated anti-p53 (1C12) antibody

B8484 and P2FIR whole cell protein extracts were prepared, as described in Section 2.4.6, with 20 µg loaded onto a 4-12% Bis-Tris protein gels. Membranes were then blotted in parallel with anti-p53 (1C12) and the modified anti-p53 (1C12)-TAT at the same dilution as seen previously (1 : 1,000 in 2.5% (w/v) milk powder in PBS-T) (Section 2.4.11).

4.2.5 Synthesis of radioconjugates

$^{111}InCl_3$ was chosen for the labelling of monoclonal antibodies due to its preferable half life ($t_{1/2}$ = 67.32 h) for antibody plasma half-life of several days (Unverdorben et al., 2016). Prior to labelling with the radioisotope, the anti-p53 (1C12)-TAT was first reacted with *S*-2-(4-isothiocyanatobenzyl)-diethylenetriamine pentaacetic acid (*p*-SCN-Bn-DTPA) chelator prior to labelling with $^{111}InCl_3$, which reacts with the free amine group, leading to its conjugation at the lysine residue sites. The chelator facilitates strong coordination complexes with metals such as $^{111}InCl_3$, the chemical structure of the chelator is shown in Figure 4.4.

4.2.5.1 Conjugation to *p*-SCN-Bn-DTPA

TAT-conjugated antibodies, in 0.1 M sodium bicarbonate buffer (pH 9) (Section 4.2.1), were reacted with a 20-molar excess of *p*-SCN-Bn-DTPA at 2 mg/mL, in DMSO (3 mM) (Macrocyclics, USA), for 1 h at 37 °C. The unreacted *p*-SCN-Bn-DTPA was removed using Sephadex® G50 gel filtration medium as described previously, using

0.5 M MES (pH 5.4) as the elution buffer. The resulting BnDTPA-TAT conjugated antibodies were then transferred to a 30 kDa Amicon ultra centrifugal filters and concentrated (1 mg/mL) in 0.5 M MES (pH 5.4) prior to radioisotope labelling.

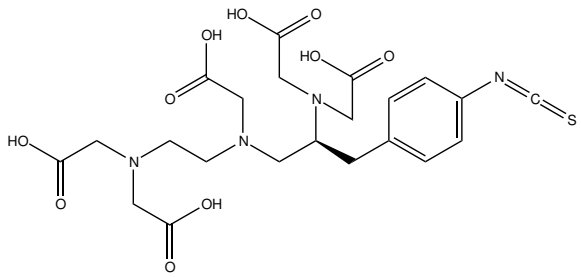

Figure 4.4: Chemical structure of *S*-2-(4-Isothiocyanatobenzyl)-diethylenetriamine pentaacetic acid (*p*-SCN-Bn-DTPA).

After modification with the *p*-SCN-Bn-DTPA, the binding affinity of the conjugate was determined by enzyme linked immunosorbent assay (ELISA), as described in Section 3.2.4 and compared to the unmodified anti-p53 (1C12) antibody.

4.2.5.2 Radiolabelling with $^{111}InCl_3$

For *in vitro* experiments, 0.1 MBq/μg of indium-111 chloride ($^{111}InCl_3$) was added to 20-100 μg of the BnDTPA-TAT conjugated antibodies in 0.5 M MES (pH 5.4) (≤ 100 μL reaction volume) and the solution was incubated at room temperature for 1 h. The reaction schematic is depicted in Figure 4.5. The radiolabelling yields were determined by instant thin layer chromatography (iTLC). In cases were the radiolabelling yield was below 95%, free $^{111}InCl_3$ was removed using Sephadex® G50 gel filtration medium. Finally, the buffer was exchanged to PBS by centrifugation prior to *in vitro* or *in vivo* experiments.

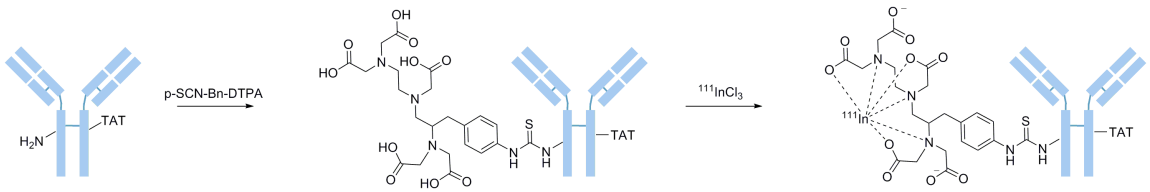

Figure 4.5: Radiolabelling with $^{111}InCl_3$. TAT-conjugated antibodies were first reacted with *p*-SCN-Bn-DTPA followed by labelling with $^{111}InCl_3$ in 0.5 M MES (pH 5.4) buffer.

For *in vivo* experiments, a minimum of 500 µg of the the BnDTPA-TAT conjugated antibodies was used, depending on the scale of experiment. $^{111}InCl_3$ (1 MBq/µg) was added to antibodies and the procedure was followed as described above.

4.2.5.3 Quality control by iTLC

The radiochemical purity was determined using iTLC. iTLC strips (8–10 mm wide) impregnated with salicylic acid (Agilent Technologies, USA) were used as a stationary phase and freshly prepared 50 mM EDTA buffer (pH 7) was applied as the mobile phase. For each iTLC, 2 µL of analytes under investigation were spotted onto the strip (baseline of ≈ 10 mm), placed in the mobile phase for approximately 5 min (run for ≈ 9 cm), and the radioactivity was measured using a radio-TLC AR-2000 imaging scanner (Eckert & Ziegler, Germany).

4.2.5.4 Isotopic dilution assay

The average number of chelators per antibody were determined by radiometric isotopic dilution assay based on previously described methods (Holland et al., 2010; Price et al., 2014). The following modifications to the methods were made for the utilisation of ^{111}In: aliquots of 60 KBq of $^{111}InCl_3$ were added to 14 solutions con-

taining serial dilutions (from 250-0 pmol) of cold $InCl_3$ (5 µL fractions in 0.5 MES buffer pH 5.4). The mixtures were then vortexed for 30 s prior to the addition of 5 µg anti-p53 (1C12) antibody conjugated to TAT peptide and *p*-SCN-Bn-DTPA; after incubation for 2 h at room temperature, the reaction was terminated by quenching with 50 mM DTPA in 0.5 MES buffer pH 7 (CheMatech, France). The degree of complexation was determined by iTLC, using the DTPA buffer (50 mM) as a mobile phase, counting the activity at the baseline and solvent front. Radiolabelling yield (in percentage) was plotted against the log[M] concentration (M = molar concentration) of $InCl_3$ in GraphPad Prism 5 (GraphPad Software,USA). Using a non-linear fitting algorithm, the point of 50% reduction of the antibody labelling efficiency was used and the number of chelators was estimated from the gradient by the following equation where $n(C)$ is the number of chelators, $n(InCl_3)$ is the number of total $InCl_3$ added, and $n(Ab)$ is the concentration of antibody:

$$n(C) = \mathrm{Ab}\frac{n(InCl_3)}{n(Ab)}$$

4.2.5.5 *In vitro* stability in serum

^{111}In-BnDTPA-p53 (1C12)-TAT (1 MBq/10 µL) was diluted in 500 µL of mouse serum (Sigma-Aldrich) and incubated at 37 °C for 24 h, 48 h, and 72 h in a thermomixer (at 300 rpm, Eppendorf, UK). At each time point, 20 µL of the radioconjugate, diluted in PBS, was loaded onto a 4-12% Bis-Tris protein gel (200 V, 35 min). The gel was then exposed to Super Resolution Phosphor screens (12.5 × 25.2 cm, Type SR, PerkinElmer) and developed on the Cyclone Plus Storage Phosphor system

(PerkinElmer). For reference, the gel was stained with coomassie stain (SimplyBlue™) to correlate each radioactive band to specific protein weights.

4.2.5.6 Retention of ^{111}In-labelled radioconjugates *in vitro*

After evaluating the internalisation properties of fluorophore-labelled TAT-conjugates *in vitro* (detailed in Section 4.2.3), cellular retention of the radiolabelled compounds was also assessed. B8484 and P2FIR cells (2×10^5 cells per well) were seeded in 24-well plates and incubated overnight at 37 °C, in a 5% CO_2 humidified chamber. The ^{111}In labelled compounds were then added into each well (containing 500 µL media) at 0.125 µg/mL (equivalent to amounts used *in vivo*) and incubated for 2 h. Subsequently, the media was removed, and cells were washed with 500 µL PBS, replenished with fresh media, and further incubated for 1 h, 2 h, 4 h, 24 h, 48 h, and 72 h. For the initial time point, after PBS wash, cells were immediately lysed with 0.1 M NaOH in dH_2O for 8 min at 4 °C. The lysate was transferred into counting tubes and each well was washed three times with ice-cold PBS, combining each wash with the previously collected lysate. After the collection of samples, radioactivities were measured and expressed as percent counts per minute (cpm) retained over time.

4.2.6 Resazurin cell viability assay

Cell viability of cells after addition of BnDTPA-TAT conjugated anti-p53 (1C12) antibody was determined by resazurin assay. The assay applied relies on the non-fluorescent resazurin being converted to the highly fluorescent resorufin upon entering viable cells (Figure 4.6). The amount of resorufin produced is correlated to the number

of viable cells present in the sample (Riss et al., 2016).

B8484 and P2FIR cells (1×10^4 cells per well) were seeded in 96-well plates at a final volume of 100 µL per well and incubated overnight at 37 °C, in a 5% CO_2 humidified chamber to adhere. The BnDTPA-TAT conjugated anti-p53 (1C12) antibody was then added at a concentration of 0.125 µg/mL and cells were incubated for a further 2 h at 37 °C. Negative and positive controls were included in the forms of no-treatment and 20 µM staurosporine (100 µM stock in DMSO, Cayman Chemical, USA), respectively. Following incubation, media was removed, cells were thoroughly washed, fresh media (50 µL) was added and cells were incubated for 0 min, 1 h, 2 h, 24 h and 48 h. At each time point, 20 µL of 0.025% resazurin solution (0.1% stock in PBS, Sigma-Aldrich) was added to each well and incubated until colour change was detected (≈ 2 h). Fluorescence was then measured (530–570 nm for excitation and 580–620 nm emission) using an Infinite® 200 Pro microplate reader (Tecan Group Ltd, Switzerland).

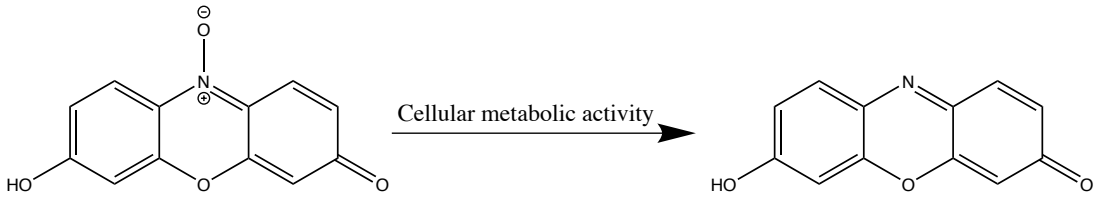

Figure 4.6: Resazurin cell viability assay principle. Resazurin is reduced to the fluorescent resorufin in viable cells. Figure adapted from Riss et al. (2016).

4.2.7 Statistical analysis

Data were reported as mean ± standard error of mean (SEM) and statistical analysis were performed using GraphPad Prism 5 (GraphPad Software,USA). A p-value of less than 0.05 was considered significant. A Student's t-test (2-tailed, unpaired) was used to compare individual datasets. To compare nested models in ELISA assays, the extra of sum-of-squares F-test was employed.

4.3 Results

4.3.1 Evaluation of the TAT internalisation properties

The ability of the anti-p53 (1C12)-TAT conjugate to penetrate the cell membrane and enter the nucleus was first validated by confocal microscopy on fixed cells. The direct visualisation of the antibody entry into the cell and the nucleus was achieved using a Cy3-NHS fluorophore-labelled antibody conjugates (Section 4.2.2). The concentration of the anti-p53 (1C12)-TAT and the Cy3 : antibody ratio was measured from the absorbance at 280 and 550 nm using a spectrophotometer.

The resultant Cy3-labelled anti-p53 (1C12)-TAT (anti-p53 (1C12)-TAT-Cy3) gave a dye to antibody ratio of approximately 40, suggesting efficient labelling. Conjugation of antibody to dye was also tested using SDS-PAGE with an unmodified IgG_1 mouse monoclonal antibody as control for the TAT-conjugated anti-p53 (1C12), assessing the molecular weight by both fluorescent imaging and coomassie staining (Figure 4.7).

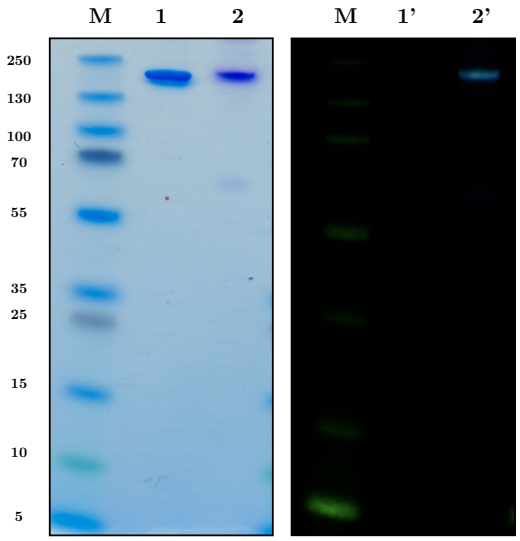

Figure 4.7: Conjugation of Cy3 dye to anti-p53 (1C12)-TAT. The anti-p53 (1C12)-TAT-Cy3 was run on 4-12% Bis-Tris gel together with an unmodifiedIgG_1 and subsequently scanned to determine the presence of Cy3 fluorescence at the molecular weight of the antibody (right panel). The gel was then stained with coomassie blue staining (left panel) to determine the molecular weight of the fluorescent band. M = marker, 1 = unmodified IgG_1, 2 = anti-p53 (1C12)-TAT-Cy3. 1' and 2' represents same samples but for the fluorescent image.

As shown in Figure 4.7, the Cy3 dye was efficiently attached to the anti-p53 (1C12)-TAT (2'), evident by the single band observed when compared to IgG_1 (1'), where no signal was detected. The molecular weight of anti-p53 (1C12)-TAT-Cy3 (2) was then determined by coomassie blue staining, which showed that the fluorescent band corresponded to the 150 kDa band same as the unmodified IgG_1 (1), confirming migration behaviour typical for IgG antibodies.

Following the synthesis and characterisation of the fluorescently-labelled conjugates, their internalisation properties were evaluated in B8484 and P2FIR cells. The IgG_1-TAT-Cy3 control was used to perform the first set of studies due to its wide availability and low cost relative to anti-p53 (1C12) antibodies. After 1 h, 2 h, and 4 h of incubation period at 37 °C, at a concentration of 0.125 μg/mL, similar to the

previously reported method (Cornelissen et al., 2011), cells were imaged as described in Section 4.2.3. In B8484 cells, minimum accumulation of the antibody into the cell was observed within an hour with the maximum uptake at 2 h post-incubation (Figure 4.8) where most cells exhibited intracellular, most notably cytoplasmic and nuclear, fluorescence when compared to the earlier (1 h) or later (4 h) time points.

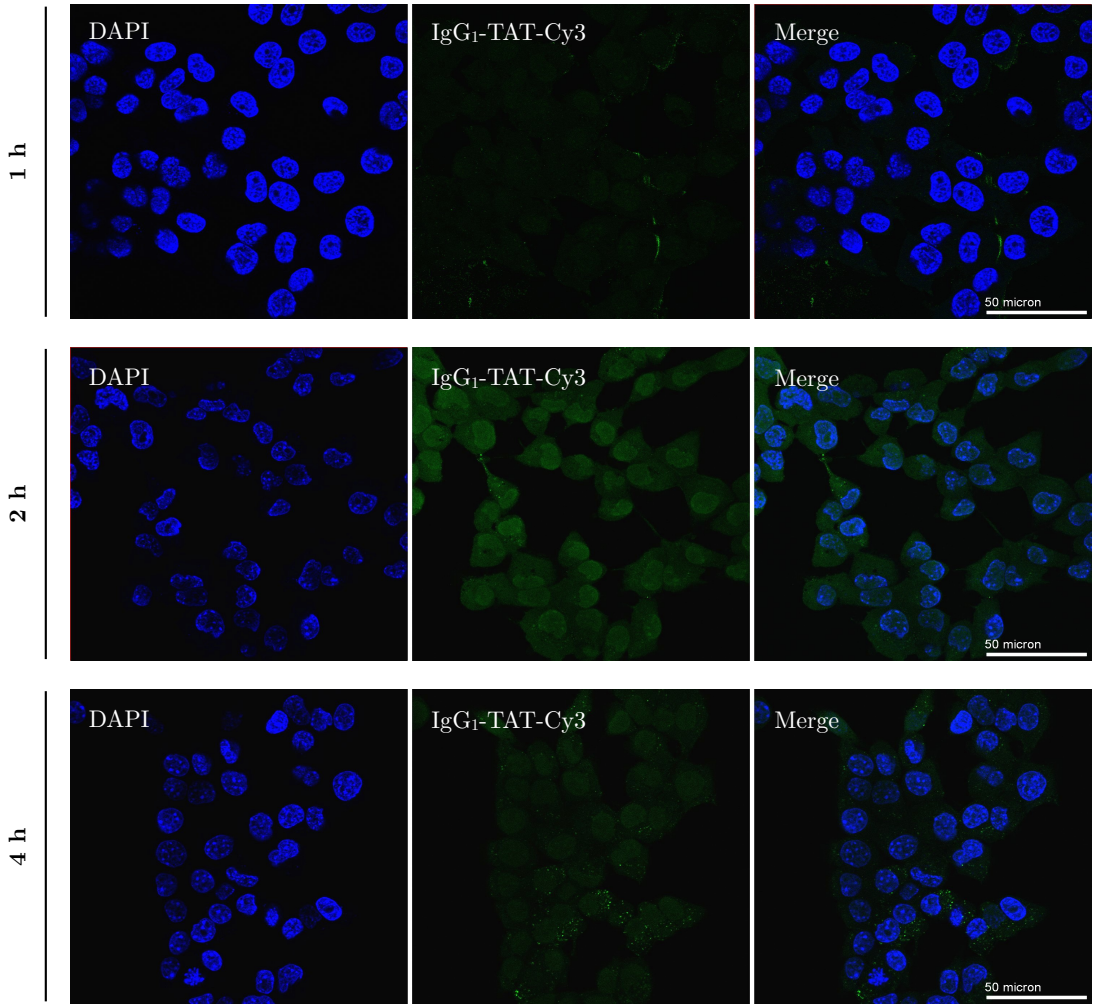

Figure 4.8: Cellular localisation of IgG_1-TAT-Cy3 over time in B8484 cells. Fluorescence microscopy images of IgG_1-TAT-Cy3 conjugate (green) internalisation in B8484 cells after 1 h, 2 h, and 4 h incubation. Cells were then washed and fixed. Nuclei were visualised using DAPI (blue). Scale bars are 50 µm.

The uptake pattern of the IgG_1-TAT-Cy3 in P2FIR cells was different from that of

B8484 cells, showing a very low Cy3 fluorescence at all time points, with maximum signal observed at 4 h which appeared to localise outside the nucleus and mostly in vesicles (Figure 4.9). Therefore, to avoid vesicular entrapment in P2FIR cells, a 2 h incubation period was chosen for the subsequent set of validation experiments to evaluate internalisation of the TAT-conjugated anti-p53 (1C12) antibody in both cell lines.

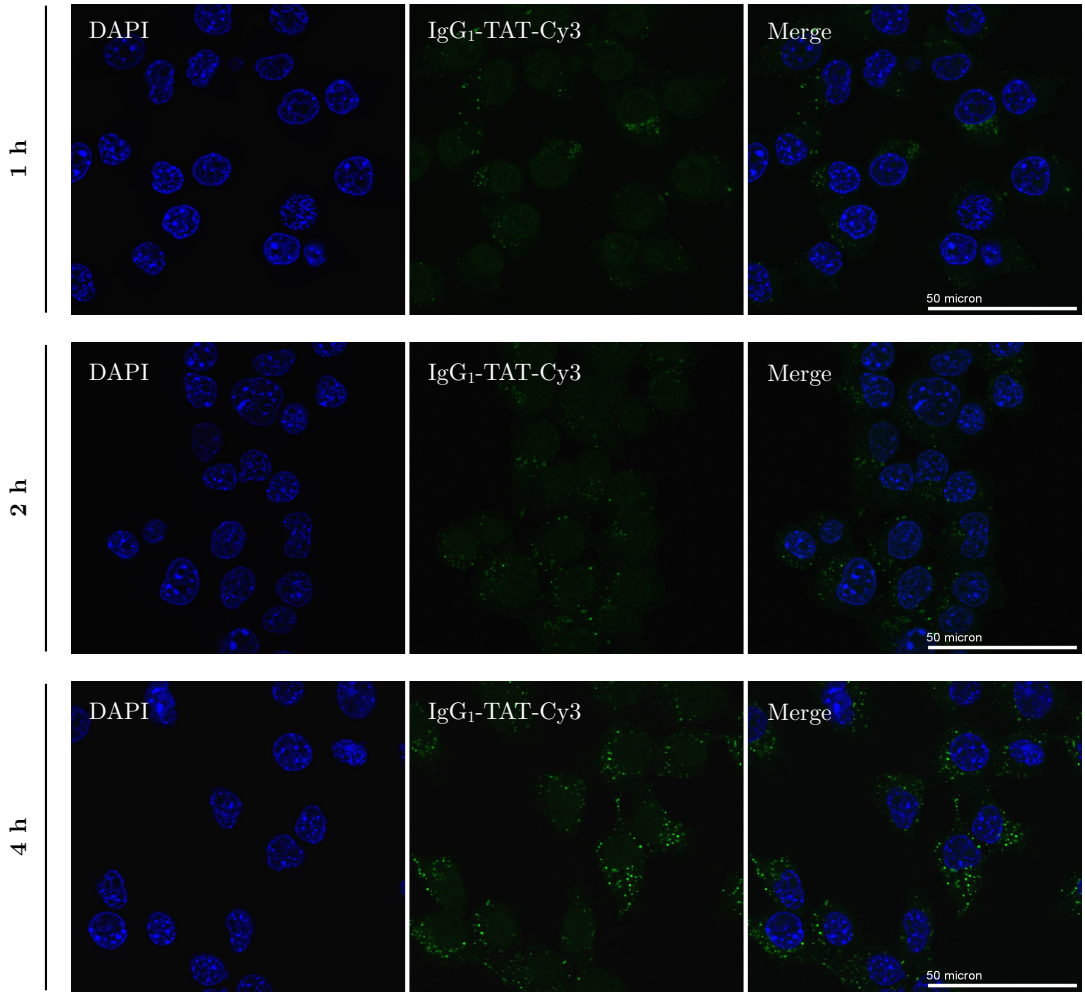

Figure 4.9: Cellular localisation of IgG_1-TAT-Cy3 over time in P2FIR cells. Fluorescence microscopy images of IgG_1-TAT-Cy3 conjugate (green) internalisation in P2FIR cells after 1 h, 2 h, and 4 h incubation. Cells were then washed and fixed. Nuclei were visualised using DAPI (blue). Scale bars are 50 µm.

Following the evaluation of the time of entry of the IgG_1-TAT-Cy3 into the cell and nucleus, both B8484 and P2FIR cells were incubated with anti-p53 (1C12)-TAT-Cy3 conjugate for 2 h and the internalisation efficiency of the conjugates was compared to that of the antibody alone (without TAT) conjugated to the Cy3 dye (anti-p53 (1C12)-Cy3).

As shown in Figure 4.10, B8484 cells demonstrated an intracellular punctate Cy3 cytoplasmic staining with a low amount of vesicular fluorescence, and showed a high degree of internalisation of the anti-p53 (1C12)-TAT-Cy3 conjugate (Figure 4.10a, top); while the anti-p53 (1C12)-Cy3 was distributed almost exclusively in vesicles mainly presenting perinuclear staining (Figure 4.10a, bottom). In contrast, P2FIR cells showed a low and uniquely vesicular staining for both the anti-p53 (1C12)-TAT-Cy3 (Figure 4.10b, top) and anti-p53 (1C12)-Cy3 (Figure 4.10b, bottom) conjugates similar to that observed in the IgG_1-TAT-Cy3 (Figure 4.9).

4.3.2 Immunoreactivity of TAT-conjugated antibody

Since the conjugation of antibody to the TAT peptide may alter its targeting properties, the immunoreactivity of anti-p53 (1C12)-TAT was investigated by western blot analysis. B8484 and P2FIR whole cell protein extracts were loaded onto a 4-12% Bis-Tris protein gels and membranes were then blotted with anti-p53 (1C12) and anti-p53 (1C12)-TAT. As shown in Figure 4.11a, the anti-p53 (1C12)-TAT antibody presented similar immunoreactivity to p53 protein in lysates from both B8484 and P2FIR cells (Figure 4.11a, left) when compared to the unmodified antibody (Figure 4.11a, right), evident by the similar band density. The observations were further validated by the

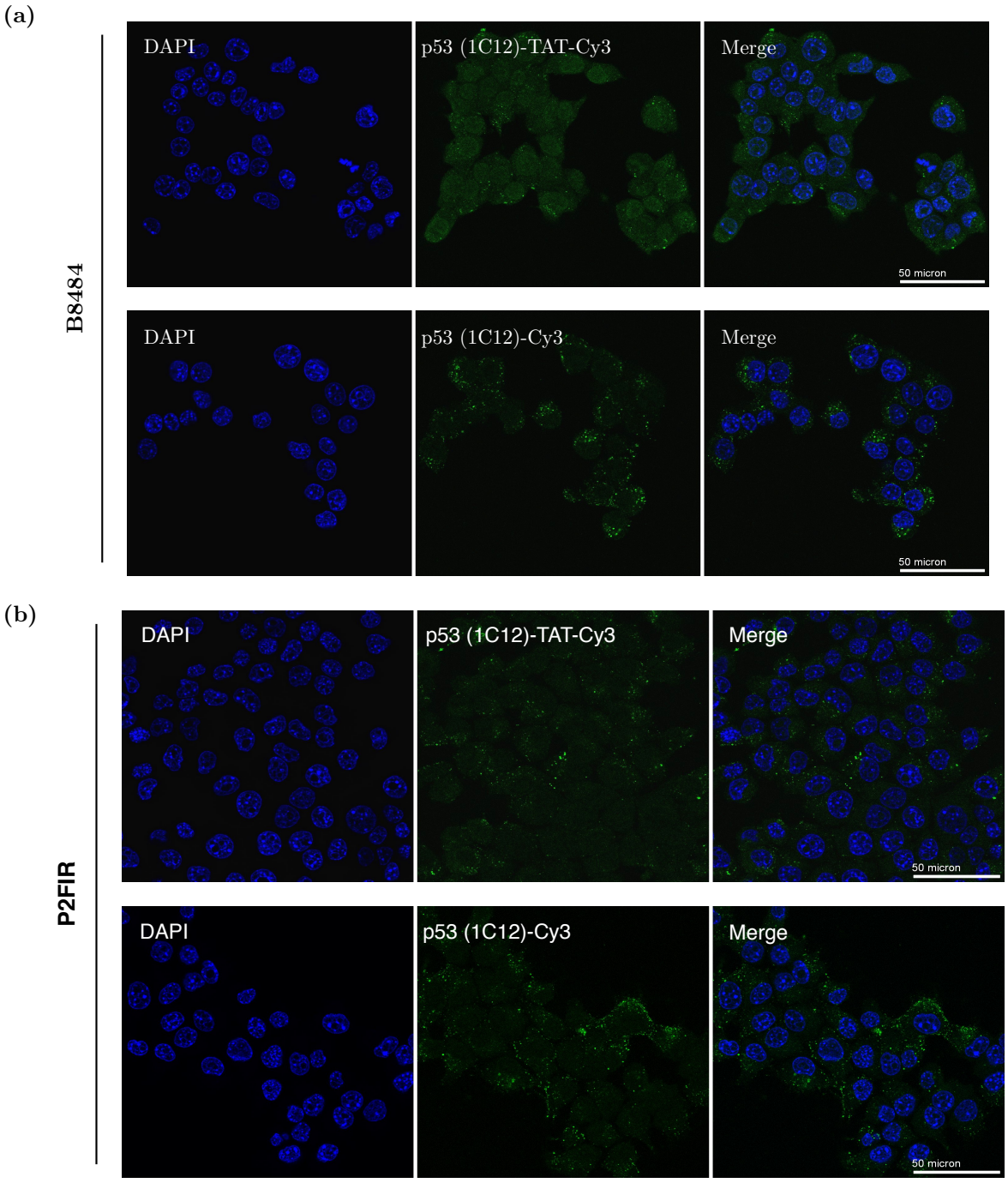

Figure 4.10: Cellular localisation of anti-p53 (1C12)-TAT-Cy3 and anti-p53 (1C12)-Cy3 (green) in B8484 (a) and P2FIR (b) cells. Cells were incubated with the respective conjugates for 2 h, washed and fixed. Nuclei were visualised using DAPI (blue). Scale bars are 50 μm.

analysis of the band density of each blot using Image studio ™ Lite (LI-COR), which showed no significant difference in the protein fold change, representing the ratio of

p53 to β-Actin, (Student's t-test, p = 0.8097) when probed with either the anti-p53 (1C12)-TAT or anti-p53 (1C12) (Figure 4.11b).

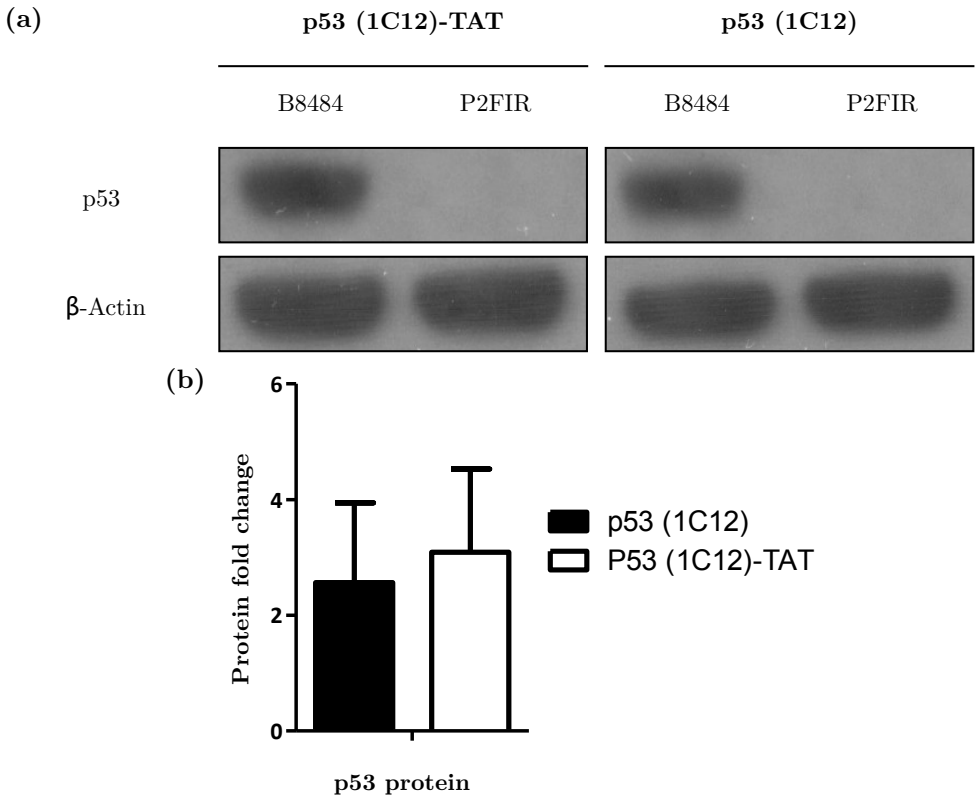

Figure 4.11: Immunoreactivity of anti-p53 (1C12)-TAT by western blot analysis. (a) Whole cell protein extracts were prepared form B8484 and P2FIR cells and probed with anti-p53 (1C12)-TAT or anti-p53 (1C12) antibodies. β-Actin was blotted as the loading control. (b) Graph of the quantification of the p53 protein amount from the western blots probed with each of the antibodies (error bars represent mean ± SEM, n = 3 independent biological experiments).

4.3.3 Binding affinity of BnDTPA-p53 (1C12)-TAT

Following the conjugation of the chelator to the anti-p53 (1C12)-TAT, the binding affinity of BnDTPA-p53 (1C12)-TAT to the p53 target antigen was tested in B8484 cells and was compared to that of the unmodified antibody (determined in Section 3.3.3). The affinity of BnDTPA-p53 (1C12)-TAT was determined using a

non-linear regression model, giving a K_D = 13 ± 5.8 nM, comparable to that of the unmodified anti-p53 (1C12) (K_D = 9 ± 2.2 nM, see Section 3.3.3). A representative graph is shown in Figure 4.12, combining the saturation binding curves of both unconjugated anti-p53 (1C12) and the conjugated BnDTPA-p53 (1C12)-TAT, demonstrating the close to identical characteristics between the two samples.

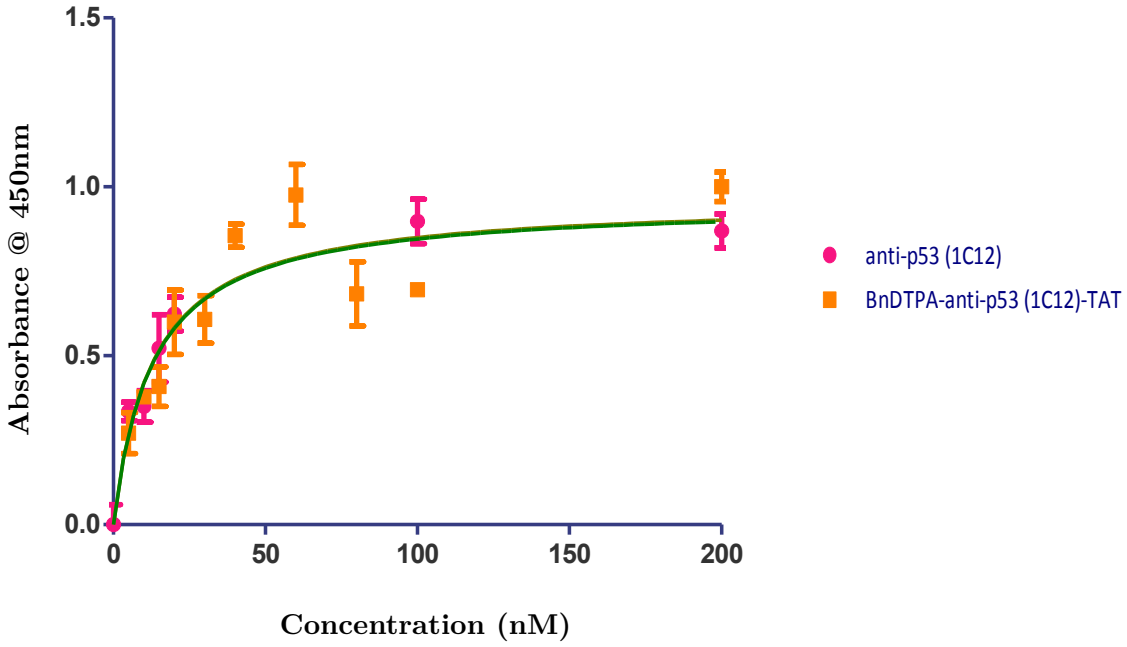

Figure 4.12: Determination of the BnDTPA-p53 (1C12)-TAT binding affinity. Saturation binding curves representing the binding of the unconjugated anti-p53 (1C12) and the conjugated BnDTPA-anti-p53 (1C12)-TAT antibody to the p53 antigen in fixed and permeabilised cells (n = 3 biological replicates).

The equilibrium dissociation constants were then compared using the sum-of-squares F-test, showing no significant difference ($p > 0.05$) between the two K_D values obtained.

4.3.3.1 Radiochemical purity of ^{111}In-labelled antibodies

Radiolabelling was conducted as described in Section 4.2.5.2, and radiolabelling efficiency was routinely above 80% with the results presented in Figure 4.13.

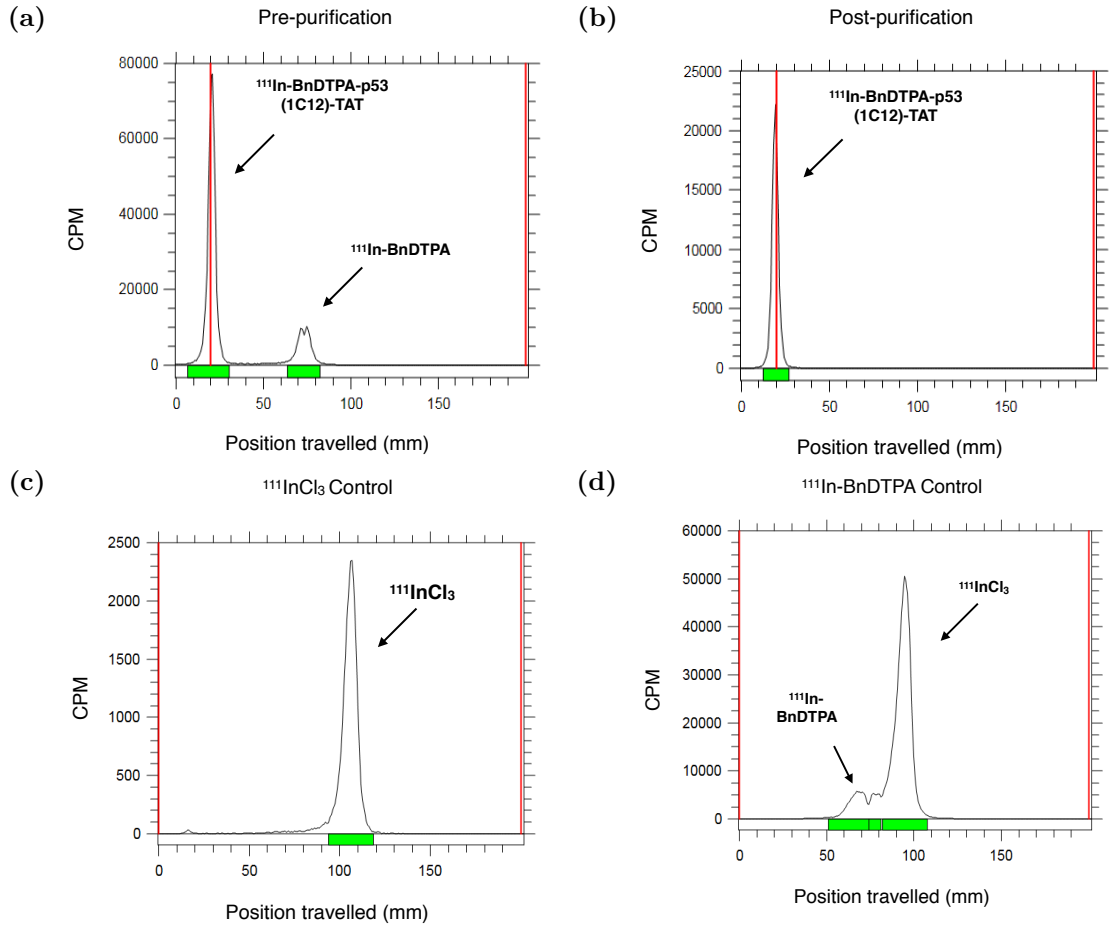

Figure 4.13: iTLC chromatograms of ^{111}In-BnDTPA-p53 (1C12)-TAT. Radiochemical purity of ^{111}In-BnDTPA-p53 (1C12)-TAT were determined before (a) and after (b) purification determined as 81% and 100%, respectively. Chromatogram of $^{111}InCl_3$ (c) and ^{111}In-BnDTPA (d) were also performed in 50 mM EDTA buffer (pH 7) as a mobile phase.

As shown in Figure 4.13, the initial reaction of the BnDTPA-p53 (1C12)-TAT with $^{111}InCl_3$ (Figure 4.13a) showed two species: the intact ^{111}In-BnDTPA-p53 (1C12)-TAT that remained at the origin ($\approx$ 81%), and a small portion of unbound ^{111}In-BnDTPA (< 20%) that migrated with the solvent front (Figure 4.13a). $^{111}InCl_3$ as

well as ^{111}In-BnDTPA were run in parallel as controls (Figure 4.13c and Figure 4.13d, respectively) to ensure that the peak observed earlier corresponded to ^{111}In-BnDTPA as $^{111}InCl_3$ moves further with the front. Purification using a G50 size-exclusion column chromatography resulted in a radiochemical purity of 100% for the ^{111}In-BnDTPA-p53 (1C12)-TAT radioconjugate (Figure 4.13b), ensuring the lack of any free ^{111}In-BnDTPA present in the eluted sample.

Isotopic dilution experiments of the conjugate, using methods described in Section 4.2.5.4, revealed that the number of accessible chelators per antibody was between 1.2–2 chelating groups.

4.3.3.2 *In vitro* stability of ^{111}In-labelled antibodies

Radiolabelled compounds may not only be subjected to degradation or modification by various enzymes in plasma (Chung et al., 2015) but also transchelation processes that may occur, thus affecting the stability of such conjugates. Therefore, to establish the integrity and stability of the antibody after conjugation and radiolabelling, ^{111}In-BnDTPA-p53 (1C12)-TAT conjugates were incubated in mouse serum at 37 °C, as well as in PBS buffer, which mimicked the *in vivo* and storage conditions, respectively. At 24 h, 48 h, and 72 h, samples in mouse serum were analysed in triplicate on 4-12% Bis-Tris gels using non-reducing conditions and an autoradiograph (Figure 4.14a, right) was produced to determine the degree of labelling, while for the samples incubated in PBS (Figure 4.14b), iTLCs were performed at all times, as described in Section 4.2.5.5.

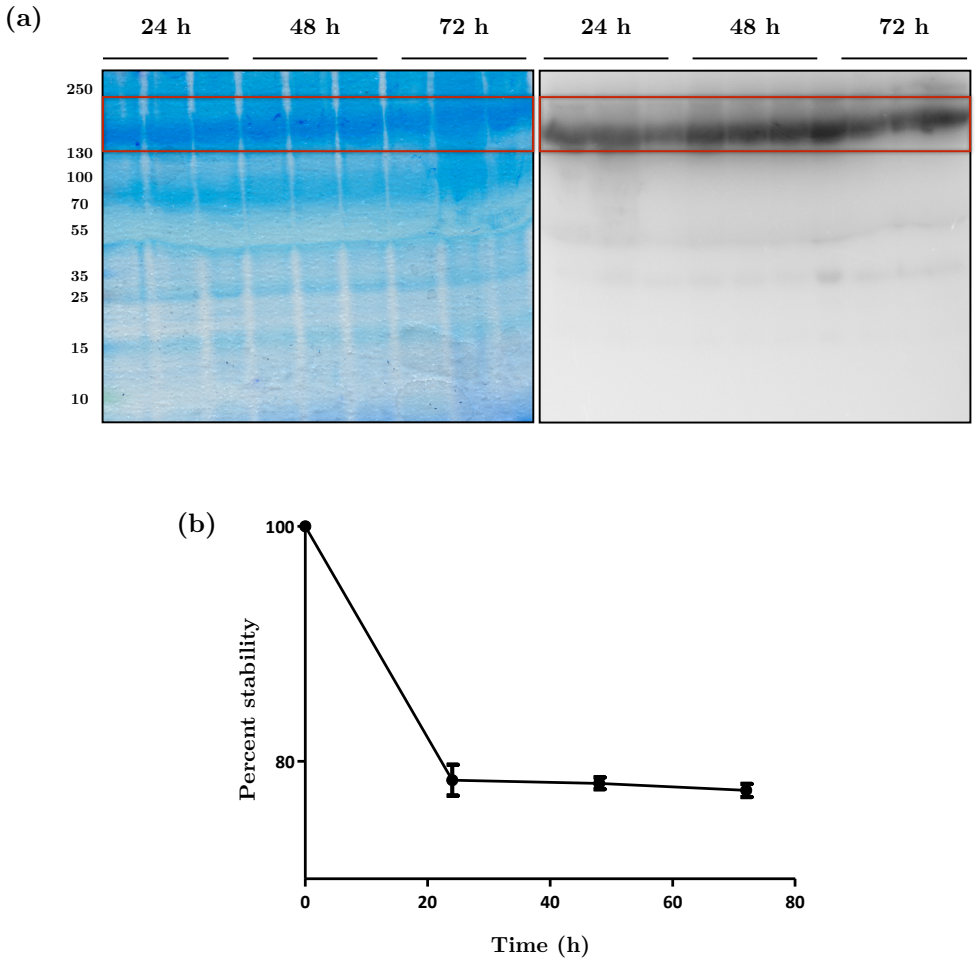

Figure 4.14: Stability of ^{111}In-BnDTPA-p53 (1C12)-TAT. ^{111}In-BnDTPA-p53 (1C12)-TAT was incubated in mouse serum (a) and in PBS (b) for 24 h, 48 h, and 72 h. Samples in serum were run on SDS-PAGE (left) in triplicate for each condition and autoradiogram (right) was performed on the same gel after coomassie staining while samples in PBS were run on iTLC and percent stability was determined (Error bars represent mean ± SEM).

As shown in Figure 4.14a, no marked degradation of the antibody was observed throughout the incubation period with negligible radioactivity in bands around 25–50 kDa at all time points, suggesting a good stability of the radioconjugate in plasma. In PBS, the radioconjugate was shown to be stable with minimal reduction of protein-bound radioactivity, showing radiochemical purity of around 80% up to 72 h incubation (Figure 4.14b).

4.3.3.3 Retention of ^{111}In-labelled antibodies

To determine the percentage of ^{111}In-labelled antibodies retained in the cells, B8484 and P2FIR cells were incubated with ^{111}In-BnDTPA-p53 (1C12)-TAT at 37 °C for 2 h. After incubation, cell medium was replaced with fresh medium and the amount of radioactivity was assessed for up to 72 h (detailed in Section 4.2.5.6), with ^{111}In-BnDTPA-IgG$_1$-TAT as the non-specific control.

Figure 4.15a illustrates the cellular radioactivity retention of the two radioconjugates over time in B8484 cells, expressed as the percentage left in the cell from the total amount internalised. Both ^{111}In-BnDTPA-p53 (1C12)-TAT and ^{111}In-BnDTPA-IgG$_1$-TAT compounds displayed a gradual decrease in the radioactivity retained with noticeable differences between the two. In particular, there was a significant difference in the amount of ^{111}In-BnDTPA-p53 (1C12)-TAT retained in the B8484 cells at time points over 1 h of externalisation over the ^{111}In-BnDTPA-IgG$_1$-TAT non-specific control, stabilising at 72 h (p values of 0.6941, 0.0005, 0.0349, 0.0017, 0.0012, 0.2862 from 1-72 h, respectively. Student's t-test).

In contrast, the retention of ^{111}In-BnDTPA-p53 (1C12)-TAT in P2FIR cells only showed significant differences to the levels of ^{111}In-BnDTPA-IgG$_1$-TAT at time points 2 h and 48 h (p values of 0.0270 and 0.0034, respectively. Student's t-test), which reached background levels at 72 h (Figure 4.15b). Therefore, after 2 h of internalisation, followed by a 72 h externalisation process, only 3% and 2% of the ^{111}In-BnDTPA-p53 (1C12)-TAT radioconjugates were retained in B8484 and P2FIR, respectively.

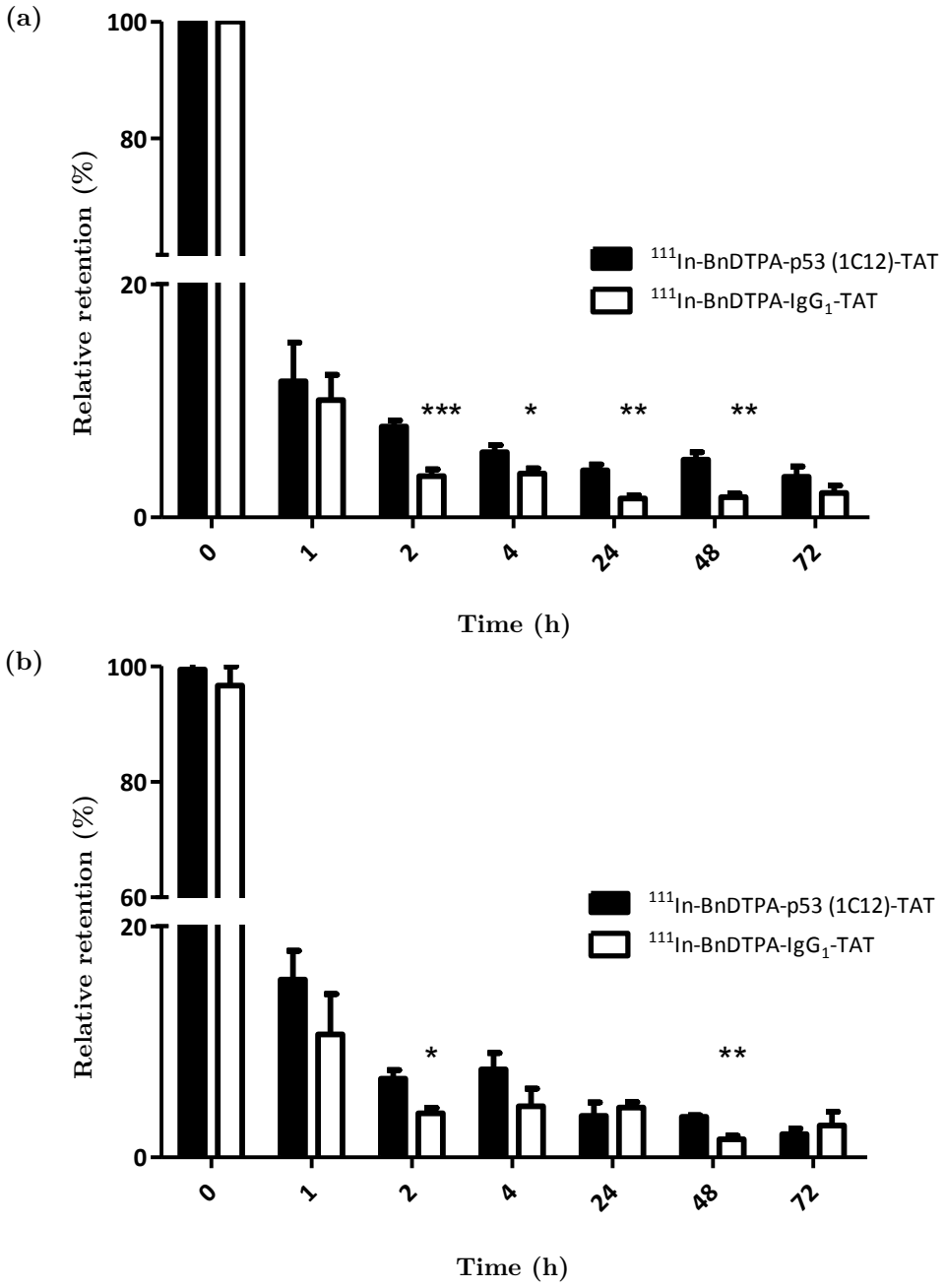

Figure 4.15: Cellular retention of ^{111}In-BnDTPA-p53 (1C12)-TAT and ^{111}In-BnDTPA-IgG$_1$-TAT in B8484 (a) and P2FIR (b) cells. Cells were incubated with the radioconjugates for 2 h and the remaining cell-associated radioactivity was measured at various time points. p values were obtained by Student's t-test at each time point and marked above the bars ($*$ $p \leq 0.05$; $**$ $p \leq 0.01$; $***$ $p \leq 0.001$) . Error bars represent mean ± SEM (n = 6 independent biological experiments).

4.3.3.4 Effect of BnDTPA-p53 (1C12)-TAT on cell viability

To evaluate the influence of the retained BnDTPA-p53 (1C12)-TAT on cell survival, the resazurin cell viability assay was performed as described in Section 4.2.6 in both B8484 and P2FIR cells. The effect of the radioisotope on cell survival has been previously described with ^{111}In-BnDTPA-γH2AX-TAT, both *in vitro* and *in vivo*, and was shown not to cause a significant decrease in cell survival when compared to untreated controls (Cornelissen et al., 2012), and was therefore not determined.

Cells were exposed to the conjugate for 2 h at 37 °C. After incubation, cells were washed with PBS and fresh medium was added, followed by further incubation for up to 24 h and 48 h. Resazurin dye was then added and fluorescence was recorded after 2 h further incubation. As observed in Figure 4.16, upon addition of the conjugate, B8484 (Figure 4.16a) and P2FIR (Figure 4.16b) cells showed a similar reduction rate of resazurin throughout the 48 h period when compared to their respective untreated controls, presenting no statistically significant difference at any time points ($p < 0.05$, Student's t-test).

As a positive control, both cell lines were also treated with staurosporine (20 μM), known to induce apoptosis, as a validation of assay reliability. This treatment with staurosporine showed a marked inhibition of proliferation in both cell lines with flat growth curves, indicating growth arrest of the cells when compared to antibody-treated and untreated samples.

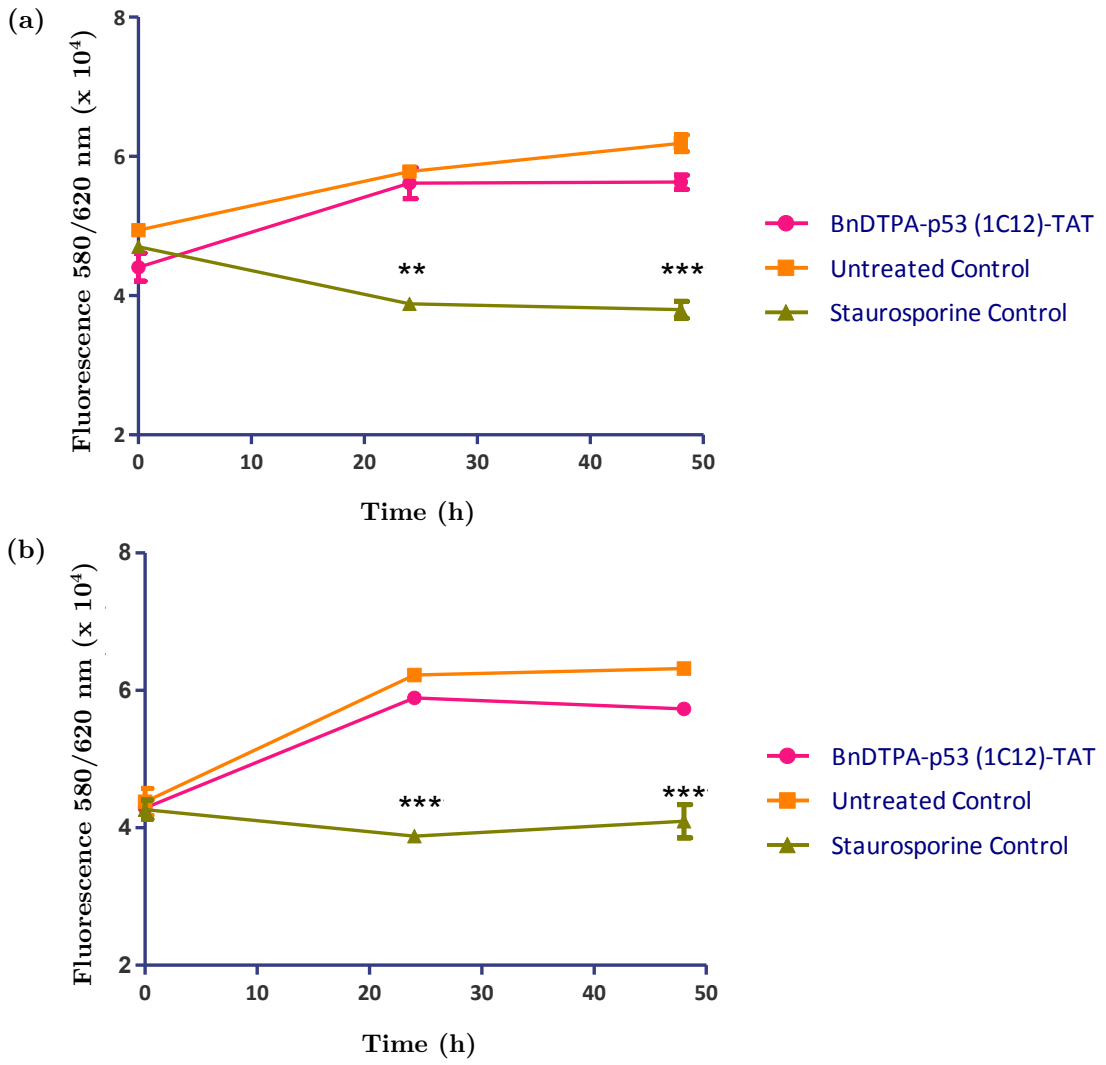

Figure 4.16: Resazurin cell viability assay upon treatment with BnDTPA-p53 (1C12)-TAT. B8484 (a) and P2FIR (b) cells were incubated with the antibody conjugate for 2 h and resazurin reduction was measured at 0 h, 24 h, and 48 h. Untreated controls and staurosporine (20 µM) positive controls were included for both cell lines. Error bars represent mean ± SEM (** $p \leq 0.01$; *** $p \leq 0.001$, n = 3 independent biological experiments).

4.4 Discussion

This chapter focused on the *in vitro* characterisation of the conjugated anti-p53 (1C12) monoclonal antibody. In particular, the antibody was conjugated to the TAT peptide, which facilitated the delivery into the cell, and thus reaching the intracellular

target. This was followed by conjugation to *p*-SCN-Bn-DTPA chelator subsequently labelled with ^{111}In. Validation *in vitro* was performed after each conjugation step in B8484 and P2FIR cell lines.

4.4.1 Conjugation of cell penetrating peptide facilitates intracellular delivery

The TAT protein of HIV-1 has been described as a cell penetrating peptide, which facilitates intracellular and intranuclear delivery of biomolecules (Frankel and Pabo, 1988; Heitz et al., 2009). In Section 4.3.1 it was demonstrated that in fixed cells, the TAT peptide conjugated to anti-p53 (1C12), was able to promote the delivery of the antibody into the cell. In particular, the anti-p53 (1C12)-TAT was efficiently labelled with Cy3 dye (Figure 4.7) to visualise its intracellular distribution. The conjugate was shown to localise in the cytoplasm and nucleus of B8484 cells (Figure 4.10a), achieving the maximum internalisation after 2 h incubation in a similar manner to IgG_1-TAT-Cy3 (Figure 4.8). In contrast, anti-p53 (1C12)-Cy3 was largely trapped in vesicles (Figure 4.10a), which is typical for molecules of such size, as they enter the cells by active uptake and remain in the endosomes where they will potentially undergo degradation by lysosomes (Marschall et al., 2011). This intracellular translocation of the TAT-conjugated antibodies was similar to that previously demonstrated by Niesner *et al.* where they showed that only a TAT-conjugated antibody fragment, specific for a marker of angiogenesis, was taken up by HEK 293 cells when compared to unmodified antibodies (Niesner et al., 2002).

The fluorescence distribution of anti-p53 (1C12)-TAT-Cy3 in P2FIR cells was only

observed in the vesicles, showing no cytoplasmic staining, similar to the anti-p53 (1C12)-Cy3 (Figure 4.10b) and the non-specific control IgG_1-TAT-Cy3 (Figure 4.9). These observations could be due to the variable internalisation pattern of TAT in different cell types (Suzuki et al., 2002) as well as to the specificity of the conjugated antibody for the p53 target since cytoplasmic or nuclear localisation was only present in B8484 cells, harbouring mutant p53. The internalisation mechanisms of TAT peptide are not fully understood to date. Multiple pathways have been suggested and several studies support the presence of more than one uptake route which can be cell type dependent (Thorén et al., 2003), possibly explaining the difference observed in staining pattern between the B8484 and P2FIR cells. In addition, it has been suggested that the TAT peptide carrying a cargo that binds to a specific target may enter the cells through a different internalisation route than that of a non-binding version, as may be in the case of B8484 due to the presence of mutant p53 (Richard et al., 2005; Joliot and Prochiantz, 2004).

The chemistry applied to facilitate TAT conjugation utilised primary amine groups present in the antibody, including its active site, hence leading to a random distribution of TAT peptides across antibody domains. Therefore, this may result in alterations to the binding capacity of the antibody to its target antigen or even complete inactivation (Acchione et al., 2012). Nonetheless, in Section 4.3.2, it was shown by western blot analysis that the immunoreactivity of anti-p53 (1C12) was not affected after TAT conjugation (Figure 4.11a) as suggested by the identical band density observed in the two blots probed with the anti-p53 (1C12)-TAT and the unmodified anti-p53 (1C12). Quantification of p53 to β-Actin ratios showed no significant dif-

ference between the two antibodies (Figure 4.11b), thus demonstrating the preserved functionality of the anti-p53 (1C12)-TAT active site. These data are consistent with previous findings reported by Hu et al. (Hu et al., 2007) where, using different antibodies against $p21^{WAF\text{-}1/Cip\text{-}1}$, the authors showed that the conjugation of the TAT peptide did not have a significant effect on the immunoreactivity of antibody towards its target.

4.4.2 Evaluation of radiolabelling with ^{111}In

Following TAT conjugation, the antibody was conjugated to *p*-SCN-Bn-DTPA, chosen for the presence of a stable thiourea linkage between the chelator and the antibody (Cooper et al., 2012), and *in vitro* evaluation was performed. The binding affinity was assessed once more, to confirm that the chelator did not interfere with the binding domain, by ELISA, and the K_D value was directly compared to that obtained for the unconjugated antibody (Figure 4.12). The binding of the BnDTPA-p53 (1C12)-TAT antibody was found to be comparable to that of unconjugated anti-p53 (1C12), with K_D values of 13 ± 5.8 nM and 9 ± 2.2 nM, respectively, suggesting that the conjugation process does not affect the antigen binding site, especially with the number of accessible chelators per antibody being estimated between 1.2 and 2. Similar results were obtained by Torres *et al.*, in a study in which the authors tested the binding affinity of anti-claudin 4 antibody after *p*-SCN-Bn-DTPA conjugation by flow cytometry reporting no difference between the conjugated and unconjugated antibodies (Torres et al., 2017). These results, in addition to the unaffected immunoreactivity of anti-p53 (1C12)-TAT shown by western blot (Section 4.3.2), suggested that the BnDTPA-p53

(1C12)-TAT maintained its target binding capacity despite the conjugation to the TAT peptide and *p*-SCN-Bn-DTPA chelator.

The BnDTPA-p53 (1C12)-TAT antibody was then labelled with ^{111}In to enable visualisation of the probe *in vivo* by SPECT imaging. ^{111}In was chosen as the radioisotope for labelling for its two key attributes: i. its physical half-life of $t_{1/2} = 67.32$ h, making it suitable for studies duration (Abdel-Nabi and Doerr, 1993); and ii., its lower energy gamma and the lack of beta emission, making it a better choice for localisation imaging studies (Esteban et al., 1987). Radiolabelling yields, assessed by iTLC at all times (Section 4.3.3.1), showed good labelling efficiency of > 80% (Figure 4.13a) with the unbound ^{111}In-BnDTPA species completely removed after G50 size-exclusion chromatography (Figure 4.13b) giving a radiochemical purity of greater than 95%. This was reproducible amongst several experiments, suggesting the robustness of the labelling method.

The stability of ^{111}In-BnDTPA-p53 (1C12)-TAT was then tested at 37°C in mouse serum and PBS for up to 72 h, to determine the integrity of the radioconjugate following the labelling process as transchelation of the radioisotope from the chelator to intracellular proteins may occur (Reilly et al., 1992). ^{111}In-BnDTPA-p53 (1C12)-TAT was equally stable in mouse serum (Figure 4.14a) and PBS (Figure 4.14b) at all time points as determined by SDS-PAGE and iTLC, respectively, with minimal sites of transchelation and radiolabelling yields of 80%. Good stability of ^{111}In-BnDTPA-labelled antibodies was also observed previously by Dijkers *et al.*, who reported even smaller loss of protein-bound radioactivity (approximately 0.5%/day) for ^{111}In-trastuzumab, a monoclonal antibody against human epidermal growth factor receptor

2 (HER2/neu) (Dijkers et al., 2009), the use of which was also demonstrated in the clinic (Perik et al., 2006).

After evaluating cellular internalisation and localisation in fixed cells (Section 4.3.1), retention of the ^{111}In-BnDTPA-p53 (1C12)-TAT radioconjugate was determined, as the amount of compound retained in the targeted cells may affect their applicability *in vivo*. This was performed in B8484 and P2FIR cells and was compared to the non-specific control ^{111}In-BnDTPA-IgG$_1$-TAT for up to 72 h post-incubation. The percentage of retained ^{111}In-BnDTPA-p53 (1C12)-TAT in B8484 cells was significantly higher than that of ^{111}In-BnDTPA-IgG$_1$-TAT throughout the majority of the time course (Figure 4.15a). Slight differences between the two radioconjugates were also observed in P2FIR cells at 2 h and 48 h (Figure 4.15b). However, the externalisation process was rapid in both cell lines, with a small amount of ^{111}In-BnDTPA-p53 (1C12)-TAT retained in the cells by 72 h (3 and 2%, respectively). The fast externalisation of the radioconjugates from the cells may be due to the acidic environment of several subcellular compartments, such as the endosomes, leading to the entrapment and rapid degradation of the molecule, resulting in relatively small portion of the targeting cargo to reach the site of interest, implying the limitations of using TAT as a delivery agent (Richard et al., 2005). However, no efflux studies on compartmentalised fractions of the cell were performed to estimate the exact mechanism of the TAT internalisation.

Finally, the impact of the retained ^{111}In-BnDTPA-p53 (1C12)-TAT on cell survival was investigated over a 48 h time period to estimate the potential cytotoxicity of the conjugate and whether it could be used solely as an imaging agent. As shown in

Figure 4.16, addition of the radioconjugate did not cause any growth rate inhibition in both B8484 and P2FIR cell lines (Figure 4.16a, Figure 4.16b, respectively) when compared to the untreated controls. This data was in accordance with previous studies reporting no change in cell survival and tumour growth upon administration of similar compounds (Cornelissen et al., 2014; Knight et al., 2015). In particular, Cornelissen *et al.* (Cornelissen et al., 2014) showed that repeated administration of ^{111}In-BnDTPA-γH2AX-TAT had no effect on tumour-free survival of BALB-*neu*T mice. Therefore, it can be hypothesised that such radioconjugates could be used as imaging agents without causing adverse effects to the host.

4.5 Conclusions

In summary, this chapter demonstrated the potential feasibility but also challenges of applying ^{111}In-BnDTPA-p53 (1C12)-TAT in *in vivo* studies. *In vitro* internalisation assays with fluorophore-labelled TAT-antibody conjugates showed the ability of the CPP to direct its cargo into the cell when compared to no-TAT fluorophore-labelled molecules. The distribution of this peptide, showed differences between B8484 and P2FIR cells, with the former presenting a cytoplasmic and nuclear pattern, likely attributable to the presence of accumulated mutant p53, while exclusive vesicular localisation was observed in the latter, lacking p53. The immunoreactivity of anti-p53 (1C12)-TAT was not affected in either cell line, and even upon the conjugation to *p*-SCN-Bn-DTPA, the binding affinity was comparable to the unmodified antibody. Upon labelling with ^{111}In, the radiochemical purity of ^{111}In-BnDTPA-p53 (1C12)-

TAT was determined as > 95% after purification, indicating the reproducibility of the labelling procedure, and was stable for 72 h in mouse serum with transchelation observed and < 20% degradation in PBS. Unfortunately, the retention of ^{111}In-BnDTPA-p53 (1C12)-TAT in B8484 cells was as low as 3% and, although statistically significant, was not hugely different than the similarly labelled IgG_1 non-specific control, thus challenging the suitability of the conjugate *in vivo*.

These variabilities in internalisation and uptake of the same peptide in different cell lines have been previously observed by other groups. In their review paper, Joliot and Prochiantz (Joliot and Prochiantz, 2004) described the variable components affecting localisation of various cell penetrating peptides, including TAT. Amongst these components, the authors suggested the binding affinity of the cargo to its target. In a different study, Jiao *et al.* (Jiao et al., 2009) compared the binding of cell penetrating peptides in positive and negative cells (CHO) for cell membrane heparan sulfate proteoglycans, which act as receptors for extracellular TAT uptake, and demonstrated internalisation of peptides to a different extent in the two cell lines.

Taken together, the present study may suggest that the good affinity of BnDTPA-p53 (1C12)-TAT observed (Figure 4.12) in B8484 cells may contribute to the intracellular distribution of ^{111}In-BnDTPA-p53 (1C12)-TAT in these cells. In the absence of the p53 target (in P2FIR cells) TAT may follow a different route of internalisation being first trapped in endosomes but was unable to bind to the cytoplasm upon release. No information was provided for B8484 and P2FIR cell lines regarding the presence of heparan sulfate receptors, and further research needs to be performed to understand whether this membrane component might be responsible for the uptake pattern

observed in P2FIR cells.

Chapter 5

In vivo imaging of p53

5.1 Introduction

The purpose of this chapter was to evaluate the imaging capability of ^{111}In-BnDTPA-p53 (1C12)-TAT radioconjugate *in vivo*, in two main animal models: subcutaneous allografts of the KPC-derived cell lines (B8484, P2FIR), and the genetically engineered KPC mouse model of PDAC, by SPECT imaging.

The incidence rate of PDAC is constantly growing with a median survival rate of 3–5 months (Hariharan et al., 2008). A study by Keane *et al.*, showed that the frequency of disease increased by 3% between 2000–2010 in the UK and is expected to increase even more by 2020 (Keane et al., 2014). Unfortunately, effective ways to provide early detection do not exist until today, and most of the patients have a fully developed PDAC at the time of clinical presentation. Surgical resection of the head of the pancreas is the only curative option but is only applicable to the early stages, when the disease is mainly asymptomatic (Becker et al., 2014). Despite the eligibility of some patients, their prognosis after surgery remains poor with local recurrence appearing at approximately 40% and metastases observed in 50% of the cases (Bittoni et al., 2014). Chemotherapy continues to be the standard treatment option for locally advanced or metastatic disease with minimal improvement in survival rates and patients developing acquired resistance over the treatment course (Long et al., 2011b).

Few biomarkers have been identified to either predict therapy response or monitor tumour progression and recurrence (Cid-Arregui and Juarez, 2015). One such example is the well-characterised serum carbohydrate antigen 19-9 (CA19-9), the only diagnostic and prognostic biomarker routinely used in the clinic to date. Elevated

levels of the antigen however, have been observed in patients with benign lesions and inflammatory diseases, which frequently leads to false positive results (Kannagi, 2007).

Ultrasound, CT, MRI, and endoscopy imaging methods are currently used as the main sources for diagnosis of pancreatic tumours, providing anatomical, and physiological information about the tissue of interest. These modalities however, are not able to characterise molecular features of the tissue of interest in the micromolar or even nanomolar scale. Molecular imaging approaches, using radiolabelled probes, enable the sensitive, non-invasive, and real-time detection of molecular pathways involved in carcinogenesis (England et al., 2015). Several targets have been investigated so far for imaging pancreatic cancer by PET or SPECT, including the endothelial growth factor receptor 2 (VEGFR2) (Korpanty et al., 2007), plectin-1 (Konkalmatt et al., 2013) or claudin-4 (Foss et al., 2007; Torres et al., 2017).

Mutations of *TP53* are found in 50-75% cases of human PDAC, often adapting a gain-of-function (GOF) behaviour with dominant negative characteristics and a potential role in the pathogenesis of the disease, first depicted by the presence of p53-immunoreactive cells in the intraductal component of pancreatic cancer (Scarpa et al., 1993). Because *TP53* is mutated rather than deleted, the mutant p53 provides an advantage for tumour cell growth, as was depicted by mice, carrying mutant p53 allele, that presented more aggressive and metastatic tumours when compared to those originating from their p53 null counterparts (Morton et al., 2010).

Considering the significance of *TP53* in cancer, imaging of p53 mutations may provide valuable information for detection and diagnosis of the disease and has been

an attractive concept throughout the years. Doubrovin *et al.*, initially attempted to image p53 using a reporter gene-based assay in tumours with potential application in drug assessment and novel therapeutic approaches (Doubrovin et al., 2001). The authors used PET imaging ([^{124}I]FIAU) in two xenograft tumour models from p53 wild-type and p53 deleted cell lines transduced with a retrovirus carrying the reporter system. Upon DNA damage they managed to image *in vivo* the upregulation of p53 transcriptional activity and correlate it with other p53-related targets, suggesting the feasibility of imaging endogenous gene expression. This gene reporter system, however, does not provide a direct imaging of the protein itself.

Direct antibody imaging of important biological targets, including p53, may be a beneficial approach for identifying patients at the earlier stages of the tumour progression or those more likely to respond to certain therapy regimes, improving the current survival rate. The many advantages of antibodies over previous targeting methods, including the inherent specificity towards the target of interest, the ability to attach any type of imaging probe (e.g. radioisotope, nanoparticles, fluorophores etc.) without affecting the binding affinity, the low toxicity, and known biodistribution, make these biomolecules an attractive tool for cancer imaging (Warram et al., 2014).

In vitro validation of newly developed radiolabelled conjugates can provide basic information but it does not answer questions regarding behaviour in a dynamic environment (O'farrell et al., 2013). High resolution imaging systems have encouraged the use of animal models in cancer research with the primary goal to mimic the human condition as close as possible. The athymic nude mouse has greatly contributed

to pre-clinical studies as the absence of functional T-cells can prevent rejection of allografts or xenografts (De Jong et al., 2014). These mouse models are based on the subcutaneous injection of tumour cell lines into the flank of the mouse, providing several advantages such as ease of implementation and tumour growth monitoring, large availability of hosts, and reproducibility of tumour histology (De Jong and Maina, 2010). Although low cost, these mouse models develop tumours of limited complexity and cellular diversity (Gopinathan et al., 2015). Recent advances in genetics have allowed the development of genetically manipulated mice that mimic the pathophysiology and molecular features of human diseases in a similar manner (Frese and Tuveson, 2007). One such model is the KPC mouse, first described by Hingorani et al. (Hingorani et al., 2005). It was generated by the complementary expression of $Kras^{G12D}$ and $Trp53^{R172H}$, both controlled by a pancreas-specific cre-recombinase (*pdx1-cre*). While born with a normal pancreas, this mouse model presents the complete spectra of PanINs precursor lesions to the fully developed PDAC, similar to the human pathology and therefore constitute the most widely used genetically engineered mouse in pre-clinical research of pancreatic cancer (Westphalen and Olive, 2012).

5.2 Materials and methods

5.2.1 Animal models

Two different mouse models of PDAC were used throughout the study; on one hand, B8484 and P2FIR murine allografts and on the other hand KPC mice bearing *LSL-*

Kras$^{G12D/+}$, *LSL-Trp53*$^{R172H/+}$ mutations, governed by *Pdx-1-Cre*. All animal experiments were performed in accordance with the UK Animal Act (Scientific Procedures) 1986 and approved by the local ethics committee. All animals were housed under a 12 h light/dark cycle with food and water supplied *ad libitum*, except when imaging with ^{18}F-FDG. Animals were checked daily for health and behavioural changes throughout the experiments.

5.2.1.1 Cell preparation for inoculations

Culture media was aspirated, cells were washed with sterile PBS and trypsinised as described in Section 2.1.1. Trypsin was neutralised by addition of DMEM media supplemented with FBS. The desired cell number was determined with an automated cell counter (Section 2.1.1). Cells were centrifuged (100 × g, 5 min), using a Heraeus^{TM} Megafuge^{TM} 40 centrifuge (Thermo Fisher Scientific), media was removed and the resulting pellet was re-suspended in PBS at the appropriate concentration (1 × 10^6 cells per mouse).

5.2.1.2 KPC tumour allograft models

Athymic nude mice (20–25 g) (Charles River, UK) were anaesthetised using 2-3% (v/v) isoflurane in oxygen. Previously prepared cell suspensions (Section 5.2.1.1) were agitated and 100 µL (1 x 10^6 cells) of B8484 or P2FIR cells were inoculated subcutaneously (*s.c.*), using a 21 G needle, into the right lower flank of the mouse. To prevent hypothermia, animals were placed on a heated pad during inoculations. The animal was then observed for 10–15 min to ensure full recovery from anaesthesia.

Tumour measurements were collected, using a manual caliper every three days, along the longest two dimensions of the tumour *(x/y)* (Ayers et al., 2010). The width of the tumour was defined to be the same as the shortest dimension (characterised as y). Tumour volumes were then calculated according to the equation described below:

$$\text{Tumour Volume } (\text{mm}^3) = \frac{xy^2}{2}$$

Animals were used for imaging and biodistribution studies when the subcutaneous tumours reached a volume of at least 125 mm^3.

5.2.2 The KPC genetically engineered mouse model

The KPC mouse model, developed by the Tuveson group (Hingorani et al., 2005), consists of animals carrying a conditional mutation in *Kras* and *Trp53* genes which were interbred with *Pdx-1-Cre* transgenic animals, where expression of both *Kras* and *Trp53* is directed by a stop element (Lox-STOP-Lox). Hence, KPC: *LSL-*$Kras^{G12D/+}$;*LSL-*$Trp53^{R172H/+}$; *Pdx-1-Cre* (Section 2.1).

Mice were bred at the central biomedical services building (BSB) at the University of Oxford, genotyped by real-time PCR (Transnetyx, USA) to confirm mutational status, and kept under the same housing conditions as described earlier (Section 5.2.1). Mice were used within the first 150–250 days, as the median survival is approximately 5 months for this model.

5.2.2.1 KPC mice screening

The identification of spontaneous pancreatic tumours developed in the KPC mouse model was achieved by regular screening with a combined T1- and T2-weighted contrast enhanced MRI using a 7T MRI scanner (VNMRS, Varian Inc., USA) equipped with a 32 mm ID quadrature birdcage coil (Rapid Biomedical GmbH, Germany), as described in Torres et al. (2017). Images were acquired using a respiratory gated 3D balanced steady-state free precession (bSSFP) sequence with time interval (TR) 3.268 ms, echo time (TE) 1.134 ms, field of view (FOV) 64 × 32 × 32 mm^3, matrix 256 × 128 × 128 and a 15° degree flip with a 16 μs hard pulse. To assist tumour identification, a respiratory gated 2D spin echo pulse sequence, CPMG sequence using SPLICER with TR 4.38 s, 8 echoes with first TE and echo spacing 6.856 ms, FOV 64×32 mm^2, 72 contiguous 0.33 mm thick slices, was also used. If animals were found positive for the presence of pancreatic tumours, they would undergo SPECT/PET/CT imaging the following week, as described in Section 5.2.4.

5.2.3 SPECT imaging–NanoSPECT/CT$^{\mathbf{PLUS}}$

Following *i.v.* injection in the tail vein of ^{111}In-BnDTPA-p53 (1C12)-TAT or ^{111}In-BnDTPA-IgG_1-TAT (5 MBq (5 μg)), SPECT imaging was performed (24, 48, and 72 h post injection), unless otherwise stated, using a 4-head NanoSPECT/CT γ-camera (Bioscan, USA) with an incorporated cone beam CT imaging system and a custom-built animal bed. Animals were anaesthetised using 4% isoflurane gas (0.5 L/min in oxygen) and placed on the bed in a prone position. Anaesthesia was

maintained at 2% isoflurane and body temperature was kept at 37 °C throughout the imaging session. Image acquisition was performed approximately over 1 h in 24 projections, approximately 100,000 counts per projection, using four multi-pinhole aperture plates each with 9 pinholes of 1.5 mm. Whole-body CT acquisition was performed before each SPECT acquisition, at standard frame resolution, tube voltage of 45 kV, 177 μA, 500 ms of exposure time, for anatomical reference. Reconstruction of both CT and SPECT images was performed in a 256 × 256 matrix using the HiSPECT algorithm in the InVivoScope software (Version 1.42, Bioscan). No corrections for scatter or attenuation were included.

5.2.3.1 *Ex vivo* biodistribution studies

After the last imaging session (at 72 h post-injection), animals were sacrificed by cervical dislocation and blood and tissues of interest were removed. Each tissue was transferred into a pre-weighed counting tube (Greiner Bio-One), weighed and radioactivity was measured using a 2489 WIZARD^2 automatic γ-counter (PerkinElmer). Tissue counts and injected dose for each mouse were decay-corrected to the activity present at time of injection, by measuring the counts in the syringe before and after every injection. Counts per minute were converted to radioactivity units (MBq) using a calibration curve generated from known standards. Radioactivity in tissues was then expressed as percentage of the injected dose per gram of tissue (%ID/g).

5.2.3.2 Image analysis

Reconstructed CT and SPECT data sets were quantified for tumour uptake using the Inveon research workplace software package version 2.2 (Siemens, Germany). To measure ^{111}In uptake, a fixed-volume region of interest (ROI) of 9 mm^3 was drawn around the hottest area within the subcutaneous tumour. The percentage of the injected dose per mL of tissue (%ID/mL) was calculated by dividing the sum of activity within the tumour ROI, expressed as MBq/mL, by the total injected activity, decay-corrected to the activity present at the time of imaging, and normalised to the ROI volume under the assumption that density of tumours was 1 g/mL. To determine tumour-to-blood ratio, heart ROI also drawn around the hottest area, was used to estimate blood concentration.

5.2.4 PET/SPECT imaging–VECTor^{4}CT

Animals were injected with ^{111}In-labelled antibodies as mentioned previously (Section 5.2.3). In the case of the KPC mouse model, animals were fasted for approximately 6 h prior to scanning and injected (*i.v.*) with 5 MBq of ^{18}F-FDG. Image acquisition was performed using the VECTor^{4}CT (MILabs, The Netherlands), enabling simultaneous acquisition of images from radioisotopes emitting at different energy windows. The scanner provides submillimetre-resolution SPECT imaging (down to 0.25 mm) and also contains an integrated CT. A whole-body scan was performed using list-mode acquisition, for 30 min using an ultra-high resolution rat/mouse 1.8 mm collimator (HE-UHR-RM) in six time frames (30 s per bed position, 10 positions) fol-

lowed by a cone-beam CT scan (55 kV, 0.19 mA) for anatomical reference. PET and SPECT images were reconstructed using the U-SPECT-Rec3.22 software, applying a pixel-based algorithm with voxel size 0.8 mm, 32 subsets, 10 iterations for ^{111}In (two energy windows of 161.1-196.9 keV and 227.7-278.3 keV) and 15 iterations for ^{18}F (energy window of 477.9-584.1 keV).

5.2.4.1 Image analysis

Reconstructed images (Section 5.2.4) were transferred to Pmod version 3.7 (Pmod Technologies, Switzerland) for further processing. A standard 3D Gaussian filter was applied (1.0 mm full width at half maximum [FWHM]). Using the fusion tool, SPECT images were registered to corresponding CT images and ROIs were defined manually using a fixed-volume sphere around the most intense voxel (radius of 1.5 mm) for quantification of activity in specific organs. Mean activity concentration (MBq/mL) and standard deviation were measured within each ROI. As before (Section 5.2.3.2), activity within each ROI was expressed as %ID/mL by dividing the sum of activity within the ROI expressed as MBq/mL by the total injected activity and normalised to the ROI volume under the assumption that density of tumours was 1 g/mL. For tumour-to-blood ratio, an ROI drawn around the heart was used to estimate blood concentration.

5.2.5 Staining of tissue sections

Subcutaneous tumours and pancreases were snap-frozen on liquid nitrogen or dry-ice, and stored at −80 °C overnight. Frozen tissues (8 μm thick) were cut using

a OTF5000 cryostat microtome (Bright Instruments Ltd, UK), mounted on slides (25 × 75 × 1.0 mm, Thermo Fisher Scientific) and stored at −80 °C. Upon retrieval, slides were air-dried at room temperature for 10 min and immediately processed for applications described below.

5.2.5.1 Autoradiography and histology

For autoradiography, slides were exposed to a Super Resolution Phosphor screen (12.5 × 25.2 cm, Type SR, PerkinElmer) in autoradiography cassettes (Fisher Biotech, USA) for 48 h at 4 °C. The phosphor screen was then developed with the Cyclone Plus Storage Phosphor system (PerkinElmer).

After autoradiography, tissue sections were stained for hematoxylin and eosin (H&E) to characterise tissue morphology, staining for the nuclei and cytoplasm respectively. Briefly, tissue sections were first washed under running water for 5 min and subsequently stained with filtered Mayer's hematoxylin (Sigma-Aldrich) for 2 min. Slides were rinsed in deionised H_{20} (dH_2O) for 20 min prior to staining with 1% eosin (v/v) for 10 s. Finally, sections were dehydrated in increasing concentrations of ethanol (70%, 95%, and 100% (v/v) in dH_2O; Fisher Scientific) and cleared in xylene (Fisher Scientific). Slides were mounted using DPX (distyrene, plasticiser, and xylene) mounting medium (Fisher Scientific) and scanned at 20 × magnification with the ScanScope CS system (Aperio, USA). H&E staining micrographs were co-registered with autoradiography images using MATLAB-based software developed in-house (MathWorks, UK) with manually chosen landmarks.

5.2.5.2 Immunofluorescence staining of frozen mouse sections

Tissue sections were fixed with 4% PFA for 10 min at 4 °C, followed by washing with PBST (0.05% Tween-20) for 5 min at room temperature. To break protein cross-links, slides were boiled twice for 5 min in 1 × sodium citrate buffer pH 6 (10 × stock : 10 mM sodium citrate, 0.05% Tween-20), and allowed to cool for 20 min. Thereafter, and to minimise non-specific staining caused by endogenous avidin and biotin, sections were incubated with a streptavidin/biotin blocking kit (Vector Laboratories) for 15 min with each reagent, according to manufacturers guidelines. After washing slides twice with PBST for 5 min, samples were blocked with a TNB buffer (Tris-NaCl blocking buffer; 0.1 M Tris-HCl pH 7.5, 0.15 NaCl, 0.5% (w/v) blocking reagent; PerkinElmer, USA) for 45 min at room temperature. Primary antibodies, diluted in TNB buffer, were then added and incubated overnight at 4 °C. To avoid cross-reactivity with the already injected mouse monoclonal antibody radioconjugate and endogenous immunoglobulins, a rabbit polyclonal primary antibody specific for total p53 was used (p53 (CM5), 1 : 2,000, Leica Biosystems). On the next day, slides were washed with PBST and immediately probed with biotynilated secondary antibodies (1 : 200 dilution in TNB buffer) for 30 min at room temperature followed by incubation with a streptavidin conjugated to Cy3 fluorophore (1 : 200 in TNB, Thermo Fisher Scientific) for 30 min at room temperature. Finally, slides were counterstained with DAPI (1 : 1,000 in TNB) to visualise nuclei and mounted using cover-slips and Vectashield mounting medium for fluorescence (Vector Laboratories).

5.2.5.3 Lysis of tissue for western blot analysis

Biopsies of approximately 100 mg of tissue were lysed in 8 M urea buffer (Sigma-Aldrich), supplemented with protease inhibitors, and homogenised with a LabGEN 7 homogeniser (Cole-Parmer, UK). Tissue samples were then placed onto a rotator for 1 h at 4 °C prior to centrifugation at 49,304 × g (4 °C, 35 min). The supernatant was collected and stored at −80 °C until loading on the gel (Section 2.4).

5.2.6 Statistical analysis

All data are reported as mean ± standard error of mean (SEM). Statistical analysis were performed using GraphPad Prism 5 (GraphPad Software,USA). Two-way ANOVA test with Bonferroni multiple comparison correction post-test was used to calculate significance of differences between groups. A Student's t-test (2-tailed, unpaired) was used to compare individual datasets. A paired t-test was used for repeated measures of the same group.

5.3 Results

5.3.1 *In vivo* evaluation in the KPC-allograft mouse model

First, KPC allograft-bearing mouse models were used to evaluate the capacity of ^{111}In-BnDTPA-p53 (1C12)-TAT to target p53 *in vivo*. Athymic nude mice were subcutaneously inoculated, as described in Section 5.2.1.2, with B8484 (*LSL-Kras*$^{G12D/+}$, *LSL-Trp53*$^{R172H/+}$, *Pdx-1-Cre*) and P2FIR (*LSL-Kras*$^{G12D/+}$, *LSL-Trp53*^{flox}, *Pdx-1-Cre*) cells.

5.3.1.1 Growth rate of the subcutaneous KPC-tumours

Following subcutaneous inoculations, longitudinal measurements of tumour volume were performed over a period of approximately 14 days to assess the tumour growth rate of the two cell lines. All animals developed palpable tumours at the site of injection after approximately one week and measurements were obtained, as described in Section 5.2.1.2. As shown in Figure 5.1, the tumour growth rate follows the same trend for both B8484 and P2FIR cell lines, making them ideal for concurrent imaging studies. No signs of distress or weight loss were observed during that period.

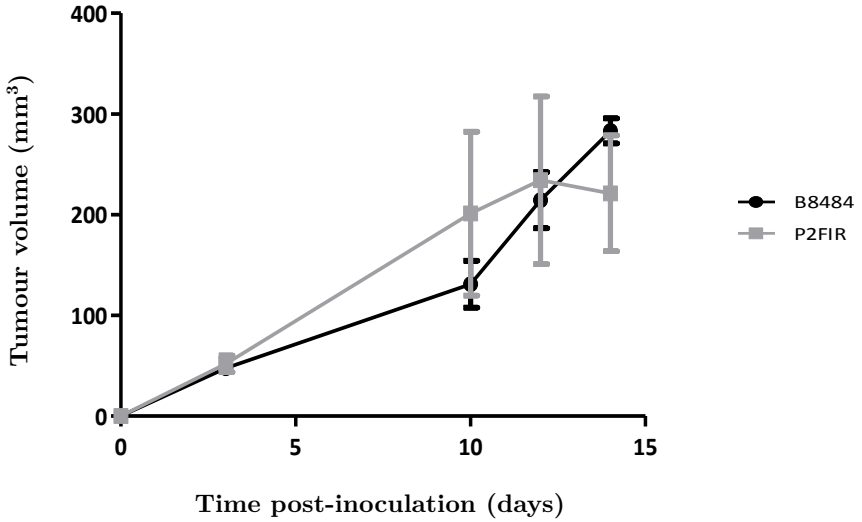

Figure 5.1: Tumour growth curves of the B8484 and P2FIR allograft-bearing mice. Athymic nude mice were subcutaneously inoculated with the B8484 and P2FIR cell lines and tumour volume (mm^3) measurements were acquired throughout a 14 day period. Tumour volumes are represented as the mean ± SEM (n = 5 animals per group).

5.3.1.2 *Ex vivo* biodistribution analysis

B8484 and P2FIR allograft-bearing mice were imaged using a NanoSPECT/CT gamma-camera 24, 48, and 72 h after administration of 5 MBq (1 MBq/μg) ^{111}In-BnDTPA-

p53 (1C12)-TAT. ^{111}In-BnDTPA-IgG$_1$-TAT was used as a non-specific control. *Ex vivo* biodistribution analysis together with SPECT ROI analysis are presented in Figure 5.2. *Ex vivo* biodistribution analysis in B8484 allograft-bearing mice, performed 72 h post-injection of the radiolabelled antibodies, is shown in Figure 5.2a. A high concentration of radioactivity was observed for both radioconjugates in blood (15 ± 1.6 *vs.* 14.5 ± 0.7% ID/g, respectively, $p > 0.05$), kidneys (4.3 ± 0.4 *vs.* 5.9 ± 0.7%ID/g, respectively, $p > 0.05$), spleen (4.4 ± 0.5 *vs.* 4.7 ± 1%ID/g, respectively, $p > 0.05$), lungs (5 ± 0.8 *vs.* 4.9 ± 0.4%ID/g, respectively, $p > 0.05$), and liver (4.2 ± 0.6 *vs.* 4.7 ± 0.3%ID/g, respectively, $p > 0.05$). No significant accumulation in other organs was noted other than the increased skin uptake (in B8484) (3.8 ± 8 *vs.* 4.3 ± 3%ID/g, respectively, $p > 0.05$), which could be a result of cross-contamination between tissues, as suggested by the large standard error. Tumour uptake of the ^{111}In-BnDTPA-p53 (1C12)-TAT (7 ± 2.5%ID/g) showed a slight increase over its non-specific control, ^{111}In-BnDTPA-IgG$_1$-TAT (4.8 ± 1.4%ID/g) which however, demonstrated no statistical significance. Quantification of the SPECT data from the B8484 allograft mice, revealed a tumour uptake of 9.5 ± 4%ID/mL for the anti-p53 (1C12) radioconjugate compared to 4.3 ± 1.4%ID/mL observed in IgG$_1$ non-specific control (Figure 5.2c). However, the difference observed was again not statistically significant ($p = 0.1072$, Student's t-test, 2-tailed).

A similar biodistribution pattern was observed in the p53 null P2FIR allograft-bearing mice (Figure 5.2b) with blood (12 ± 1.9 *vs.* 15.8%ID/g, respectively), kidneys (4.6 ± 0.9 *vs.* 6.4%ID/g, respectively), spleen (5.6 ± 0.6 *vs.* 4.7%ID/g, respectively), and liver (5.5 ± 1 *vs.* 6.3%ID/g, respectively) being the tissues with the highest

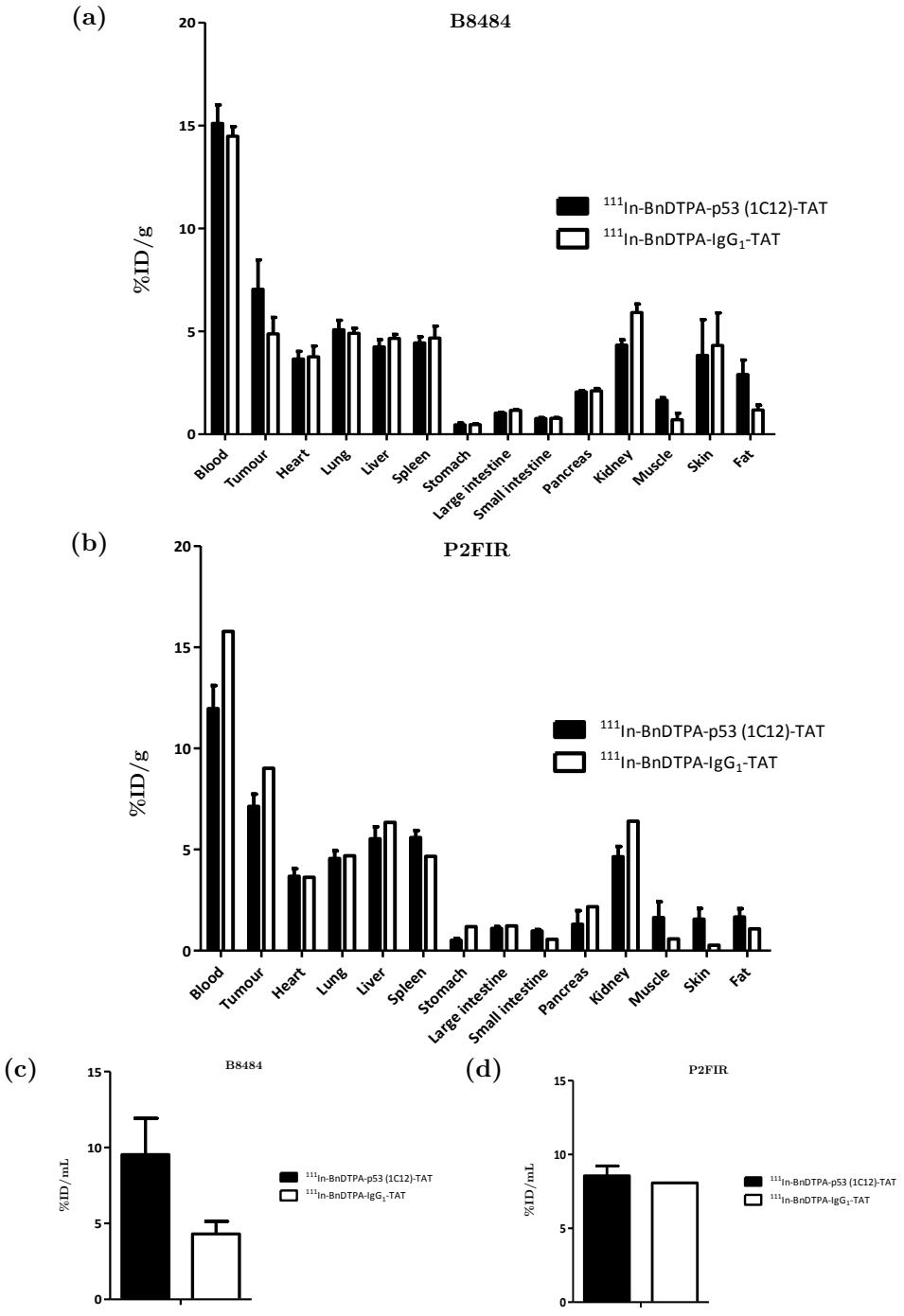

Figure 5.2: *Ex vivo* biodistribution and ROI analysis of ^{111}In-BnDTPA-p53 (1C12)-TAT. Analysis was performed 72 h post-injection of ^{111}In-BnDTPA-p53 (1C12)-TAT and the isotype control ^{111}In-BnDTPA-IgG$_1$-TAT in B8484 (a) and P2FIR (b) allograft-bearing mice. Blood and major tissues are shown (n = 3 mice/group, n = 1 in P2FIR ^{111}In-BnDTPA-IgG$_1$-TAT group). Data are expressed as %ID/g and error bars represent mean ± SEM. Quantification of tumour areas by image analysis was also performed at 72 h post-injection in B8484 (c) and P2FIR (d). Student's t-test was used (unpaired, 2-tailed), showing no statistical significance between groups ($p > 0.05$).

uptake of radioactivity. Surprisingly, tumour uptake of ^{111}In-BnDTPA-p53 (1C12)-TAT was comparable to that observed in B8484 allograft mice (7.1 ± 1.0%ID/g). A comparison between ^{111}In-BnDTPA-p53 (1C12)-TAT and ^{111}In-BnDTPA-IgG$_1$-TAT in P2FIR allograft mice was not possible as there was only one animal in the control group, due to failed *i.v.* injections. It can be observed however, that tumour uptake of ^{111}In-BnDTPA-IgG$_1$-TAT in that one case was approximately 9%ID/g, suggesting high tumour penetration of the non-specific control antibody. Higher concentration of the control antibody was also observed in the blood (15.7%ID/g). Tumour uptake by ROI analysis displayed similar uptake values, as observed in the biodistribution data, for both ^{111}In-BnDTPA-p53 (1C12)-TAT and ^{111}In-BnDTPA-IgG$_1$-TAT (8.6 ± 1.5 *vs.* 8%ID/mL, respectively, Figure 5.2d).

5.3.1.3 SPECT imaging

Whole-body SPECT images were acquired at 24 h, 48 h, and 72 h and were used to evaluate *in vivo* biodistribution of radioconjugates. The tumour-to-blood (T/B) uptake ratios were determined and are shown in Figure 5.3.

As shown in Figure 5.3a, in B8484 allograft-bearing mice accumulation of ^{111}In-BnDTPA-p53 (1C12)-TAT in the tumour continued for up to 72 h and T/B value increased over time from 0.57 ± 0.1 (24 h) to 1.11 ± 0.6 (72 h post-injection), providing the best contrast at 72 h. The ratios observed for the non-specific control ^{111}In-BnDTPA-IgG$_1$-TAT were constant throughout (0.46 ± 0.03 at 24 h and 0.50 ± 0.2 at 72 h). Similarly, the T/B ratio for the ^{111}In-BnDTPA-p53 (1C12)-TAT in P2FIR allograft-bearing mice (Figure 5.3b) was comparable to that observed in B8484

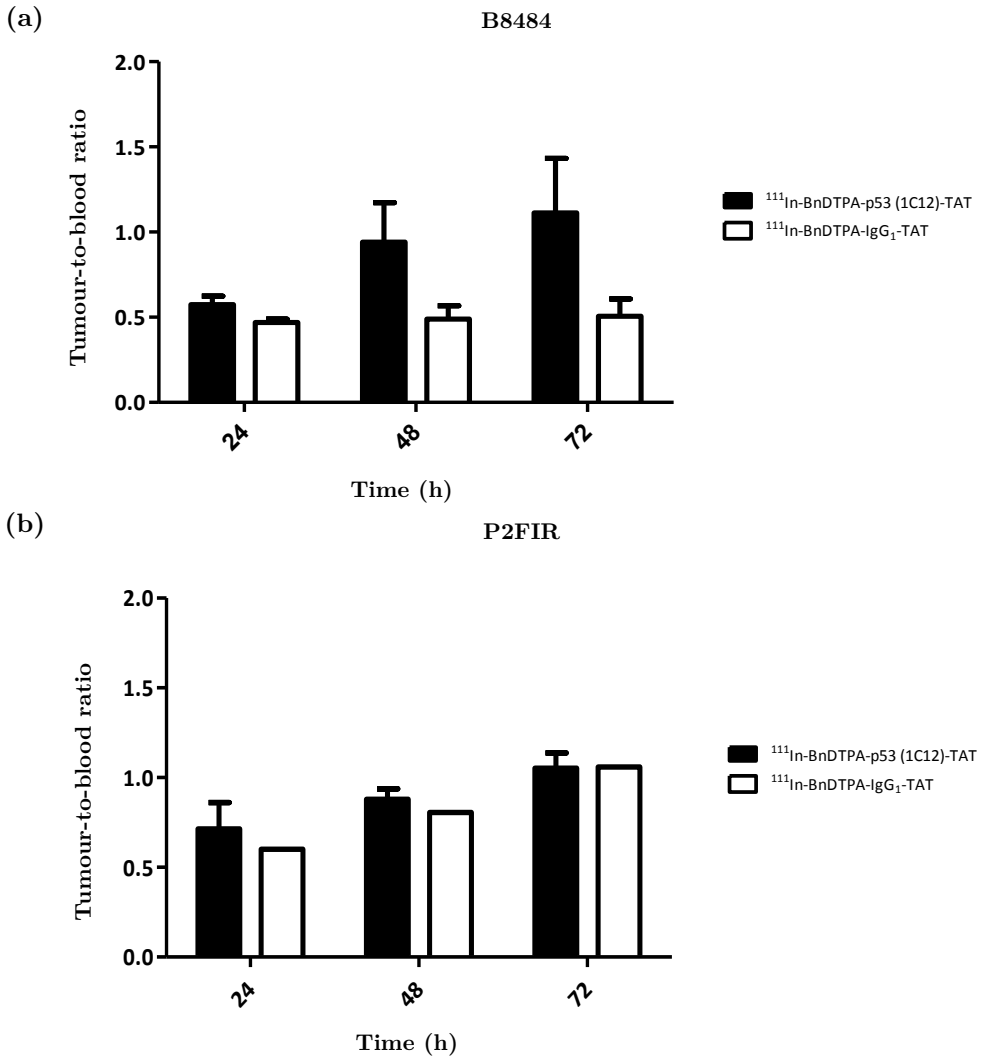

Figure 5.3: ROI analysis of selected tissues of SPECT images. Tumour-to-blood (T/B) uptake ratios for the ^{111}In-BnDTPA-p53 (1C12)-TAT and ^{111}In-BnDTPA-IgG$_1$-TAT in B8484 (a) and P2FIR (b) allograft-bearing mice were calculated at 24 h, 48 h, and 72 h post-injection of radioconjugates. Data represents mean ± SEM (n = 3 animals/group). No statistical significance was observed between individual groups ($p > 0.05$, Student's t-test, 2-tailed, paired).

mice and increased from 0.70 ± 0.1 (24 h) to 1.05 ± 0.2 (72 h). There was an increase in the T/B ratio value for the ^{111}In-BnDTPA-IgG$_1$-TAT radioconjugate from 0.60 (24 h) to 1.06 (72 h), but more mice are needed to determine if this is a significant trend. Representative SPECT maximum intensity projection (MIPs) images of mice injected with ^{111}In-BnDTPA-p53 (1C12)-TAT or ^{111}In-BnDTPA-IgG$_1$-TAT over time

are shown in Figure 5.4 and Figure 5.5, depicting the distribution and blood clearance of the radioconjugates throughout the whole body in B8484 and P2FIR allograft-bearing mice, respectively. Blood, heart, liver, and tumour were noted as the main organs of uptake after administration of ^{111}In-BnDTPA-p53 (1C12)-TAT in B8484 allograft-bearing mice (Figure 5.4), confirming the biodistribution pattern from *ex vivo* tissue counting (Figure 5.2a) and consistent with the pharmacokinetics and catabolic pathways observed for radiolabelled antibodies.

In animals injected with ^{111}In-BnDTPA-IgG$_1$-TAT little radioactivity was detected in the tumours, and uptake in the blood and liver was as high as for the anti-p53 (1C12) radioconjugate. Similar tissue distribution was found in P2FIR p53-null allograft-bearing mice, where high accumulation of both radioconjugates was observed in the tumour (Figure 5.5), consistent with the biodistribution data (Figure 5.2b).

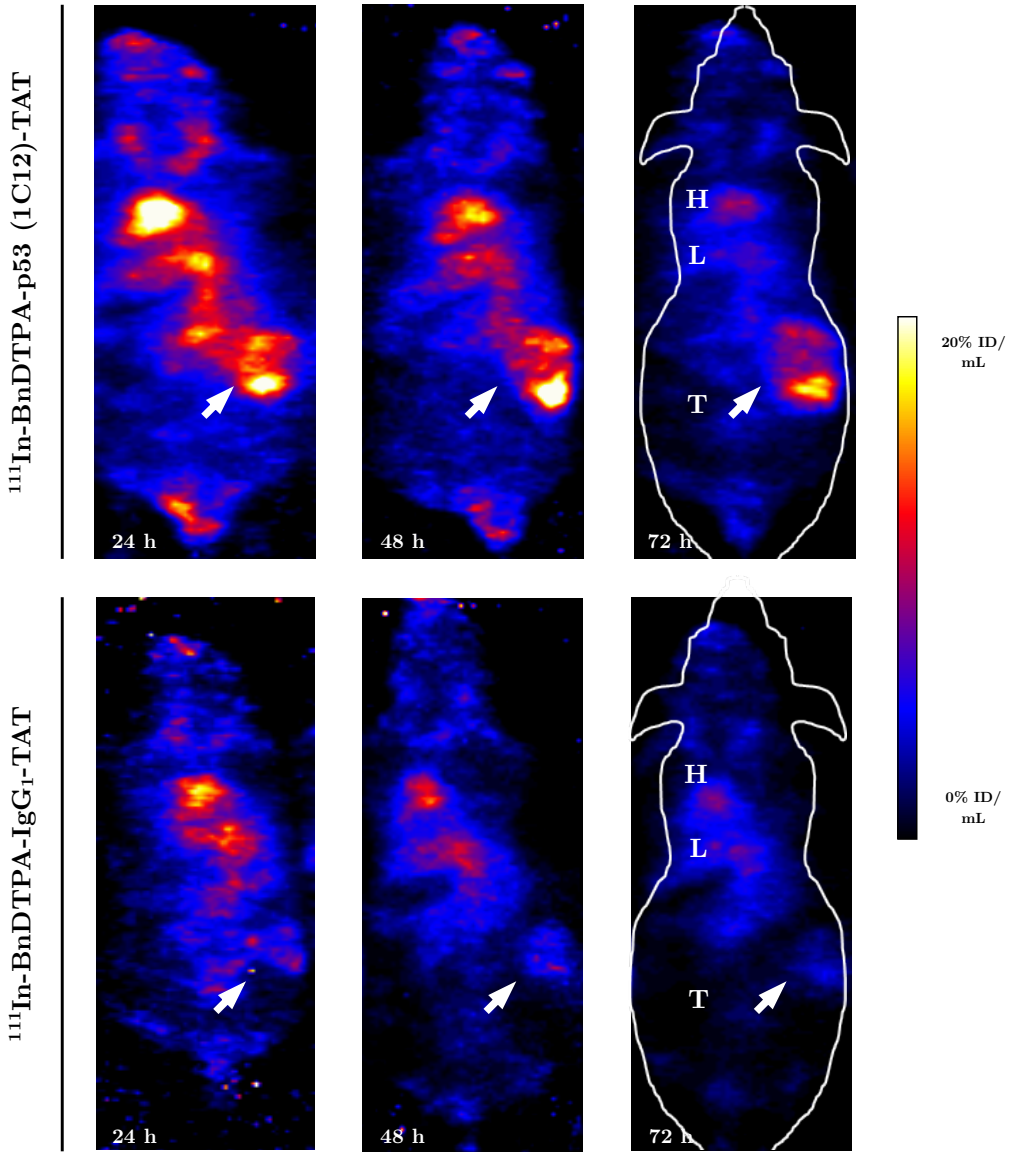

Figure 5.4: Whole-body SPECT MIPs showing biodistribution of ^{111}In-BnDTPA-p53 (1C12)-TAT in B8484 allograft-bearing mice. Representative images of the same mouse taken at 24 h, 48 h, and 72 h post-injection. ^{111}In-BnDTPA-IgG$_1$-TAT was used as a non-specific control. Arrows point to B8484 allograft tumours (T). Heart (H) and liver (L) are also included as organs of high uptake.

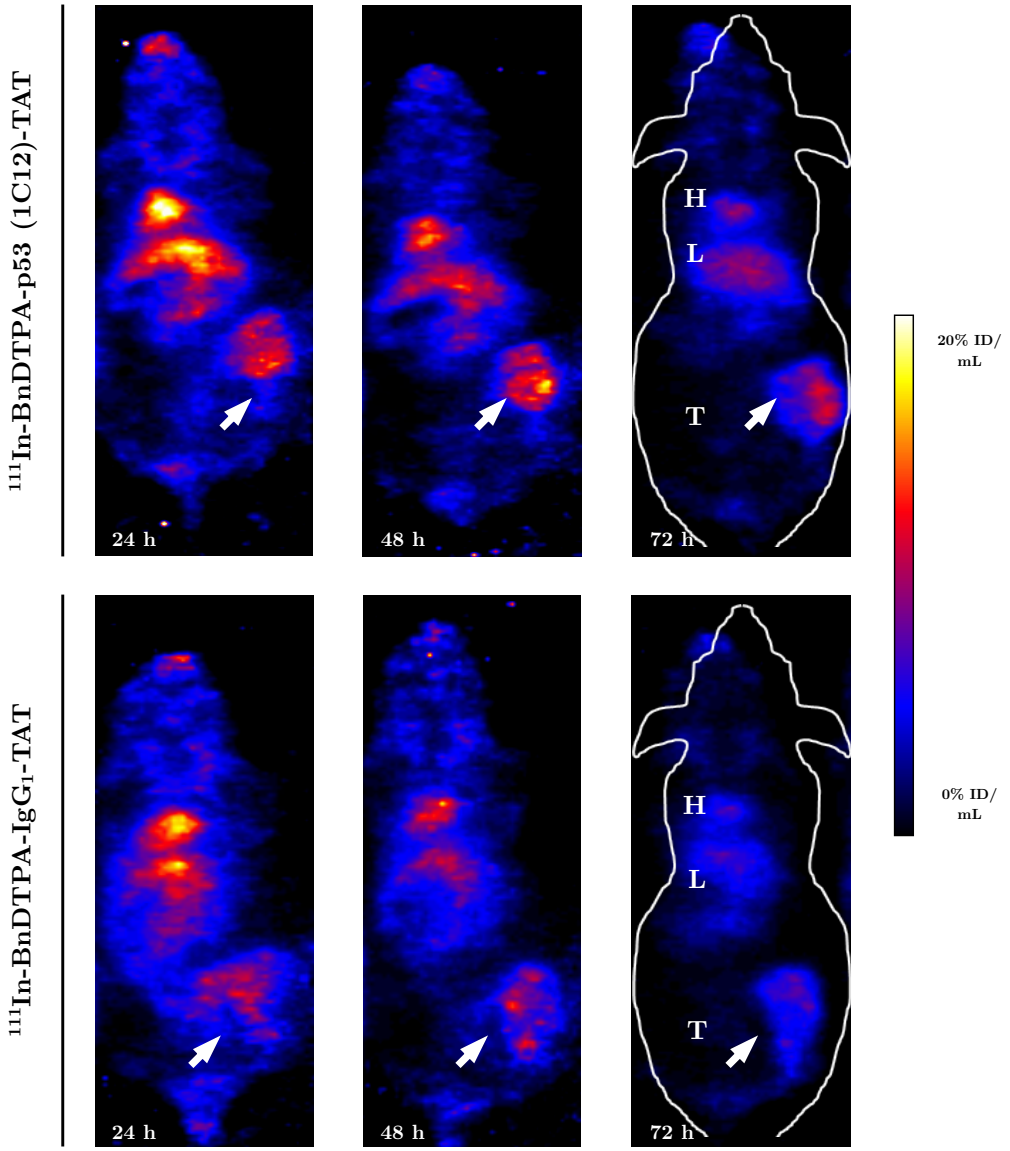

Figure 5.5: Whole-body SPECT MIPs showing biodistribution of ^{111}In-BnDTPA-p53 (1C12)-TAT in P2FIR allograft-bearing mice at 24 h, 48 h, and 72 h post-injection of the radioconjugate. ^{111}In-BnDTPA-IgG$_1$-TAT was used as a non-specific control. Arrows point to P2FIR allograft tumours (T). Heart (H) and liver (L) are also included as organs of high uptake.

5.3.2 *In vivo* optimisation

As a result of the small sample size in the previously mentioned study (n = 1, for the ^{111}In-BnDTPA-IgG$_1$-TAT group in P2FIR allograft-bearing mice) as well as the variability in tissue uptake across samples, an additional imaging session was performed. Radioconjugates not attached to the TAT peptide were also included as controls of TAT internalisation function (^{111}In-BnDTPA-p53 (1C12) and ^{111}In-BnDTPA-IgG$_1$). Due to challenges during the radiolabelling process, a lower specific activity was used (0.5 MBq/μg) and athymic nude mice (n = 3 animals/group) were injected with a total activity of 5 MBq (10 μg of antibody). Animals were scanned at 72 h post-injection due to higher T/B ratio value obtained at this time-point (Figure 5.3), using the VECTor^{4}CT scanner, as described in Section 5.2.4.

Ex vivo biodistribution of all four radioconjugates (^{111}In-BnDTPA-p53 (1C12)-TAT, ^{111}In-BnDTPA-IgG$_1$-TAT, ^{111}In-BnDTPA-p53 (1C12), ^{111}In-BnDTPA-IgG$_1$) at 72 h post-injection was similar in B8484 and P2FIR allograft-bearing mice and is shown in Figure 5.6a and Figure 5.6b, respectively. Accumulation of radioactivity in normal tissues followed a pattern that was observed in the previous study (Figure 5.2) but with higher uptake values probably due to increased antibody dose (10 μg). After *i.v.* injection of radioconjugates, high level of radioactivity was observed in blood, kidneys, spleen, lungs, and liver in all groups. Tumour accumulation of ^{111}In-BnDTPA-p53 (1C12)-TAT in B8484 allograft-bearing mice (Figure 5.6a) (13.4 ± 0.7%ID/g) was comparable to that of all the controls included (13.5 ± 1.7%ID/g for ^{111}In-BnDTPA-IgG$_1$-TAT, 14.04 ± 0.7%ID/g for ^{111}In-BnDTPA-p53 (1C12), and 13.6 ± 4.3%ID/g

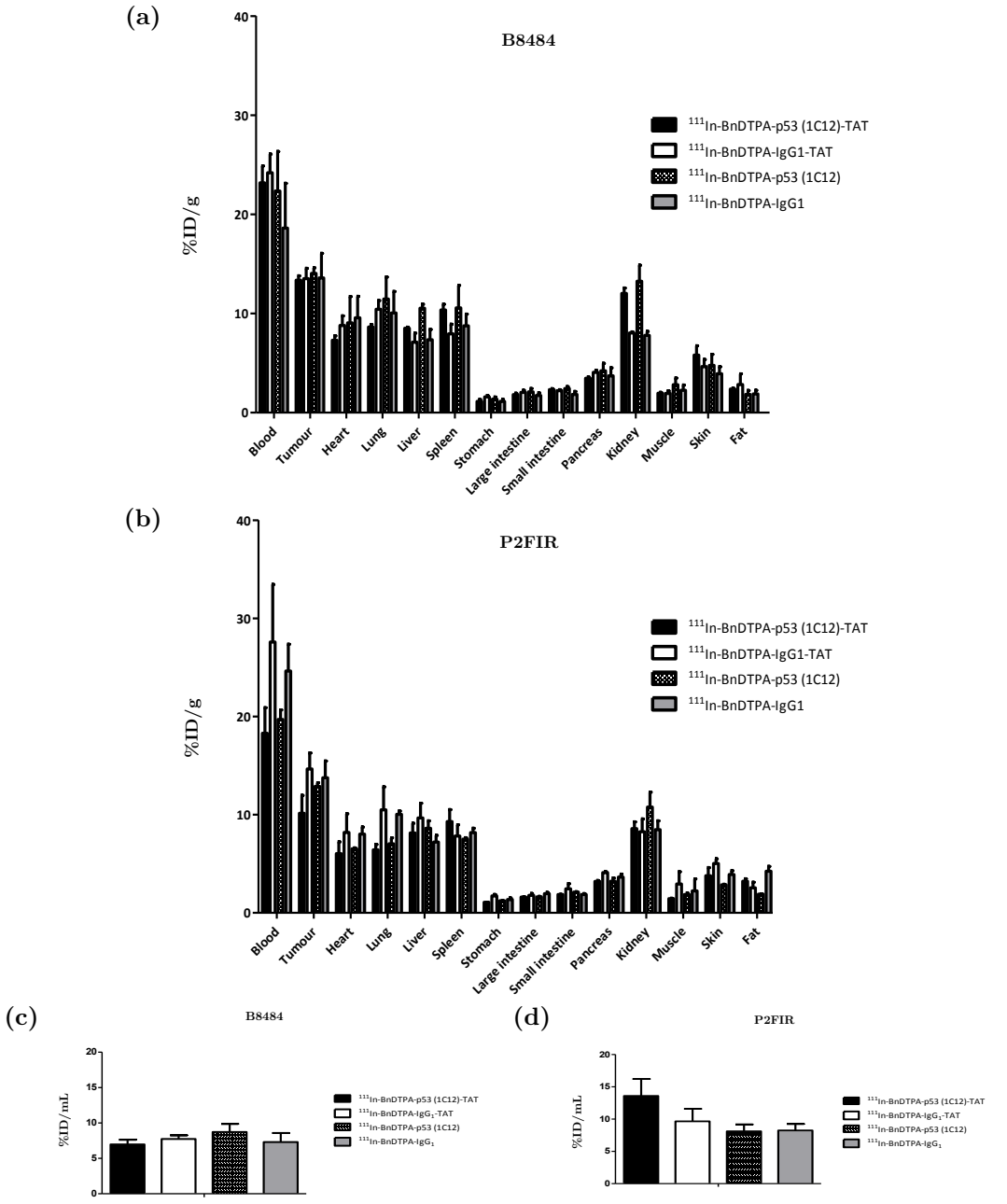

Figure 5.6: Repetition of ^{111}In-BnDTPA-p53 (1C12)-TAT *ex vivo* biodistribution including ^{111}In-BnDTPA-p53 (1C12) and ^{111}In-BnDTPA-IgG$_1$ controls in B8484 (a) and P2FIR (b) allograft-bearing mice at 72 h post-injection. Data are expressed as %ID/g and error bars represent mean ± SEM (n = 3 mice/group). ROI analysis on B8484 (c) and P2FIR (d) tumours is also included and presented as %ID/mL. Two-way analysis of variance (ANOVA) was used for multiple comparisons with a Bonferroni post-test, showing no statistical significance between groups ($p > 0.05$).

for ^{111}In-BnDTPA-IgG$_1$). In P2FIR allograft-bearing mice, tumour uptake was also similar between the four radioconjugates (10.2 ± 2.6%ID/g for ^{111}In-BnDTPA-p53 (1C12)-TAT, 14.7 ± 0.8%ID/g for ^{111}In-BnDTPA-IgG$_1$-TAT, 12.9 ± 0.5%ID/g for ^{111}In-BnDTPA-p53 (1C12), and 13.8 ± 3.0%ID/g for ^{111}In-BnDTPA-IgG$_1$, $p > 0.05$). No statistical significance was observed when comparing the tumour uptake of the three control radioconjugates to that of ^{111}In-BnDTPA-p53 (1C12)-TAT ($p > 0.05$, two-way ANOVA) in both B8484 and P2FIR allograft-bearing mice. ROI quantification of tumour uptake of all radioconjugates for both B8484 (Figure 5.6c) and P2FIR (Figure 5.6d) allograft tumours demonstrated lower values than those obtained from the *ex vivo* biodistribution data (Figure 5.6a and Figure 5.6b, respectively), with similar pattern observed, but no statistical significance. In particular, in B8484 allograft tumours (Figure 5.6c), uptake values were found to be as similar as 7 ± 1.2%ID/mL for ^{111}In-BnDTPA-p53 (1C12)-TAT, 7.7 ± 0.9%ID/mL for ^{111}In-BnDTPA-IgG$_1$-TAT, 8.7 ± 2%ID/mL for ^{111}In-BnDTPA-p53 (1C12), and 7.3 ± 2.2%ID/mL for ^{111}In-BnDTPA-IgG$_1$ ($p > 0.05$, two-way ANOVA). Higher tumour %ID/mL values were obtained in the P2FIR group for ^{111}In-BnDTPA-p53 (1C12)-TAT with high interindividual variability, as determined by the standard error, (13.6 ± 3.7%ID/mL) when compare to those corresponding to the control groups (^{111}In-BnDTPA-IgG$_1$-TAT: 9.6 ± 3.4%ID/mL; ^{111}In-BnDTPA-p53 (1C12): 8 ± 1.5%ID/mL; ^{111}In-BnDTPA-IgG$_1$: 8.2 ± 1.7%ID/mL) ($p > 0.05$).

In line with the *ex vivo* biodistribution data, visible tumour uptake of the ^{111}In-BnDTPA-p53 (1C12)-TAT but also all control radioconjugates was demonstrated by SPECT/CT imaging at 72 h post-injection (Figure 5.7). All image processing was

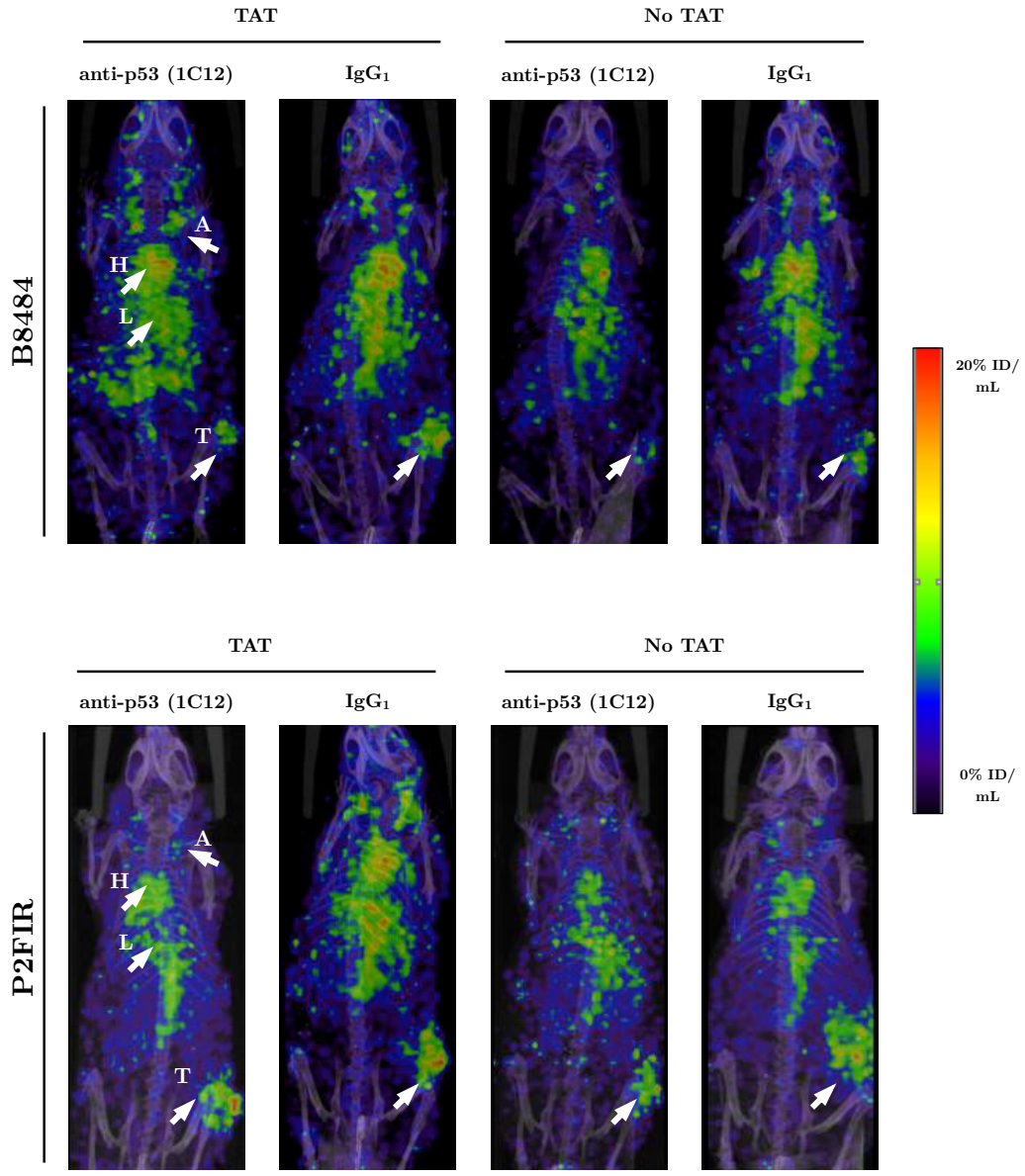

Figure 5.7: Representative MIP SPECT images of B8484 and P2FIR allograft-bearing mice 72 h post-injection with ^{111}In-labelled conjugates: ^{111}In-BnDTPA-p53 (1C12)-TAT and ^{111}In-BnDTPA-IgG$_1$-TAT, ^{111}In-BnDTPA-p53 (1C12), ^{111}In-BnDTPA-IgG$_1$ controls. Arrows point to tissues showing marked uptake of the radioconjugates including heart (H), liver(L), carotid artery (A), and tumour (T).

performed in Pmod image analysis software, as described in Section 5.2.4.1. T/B ratios of ^{111}In-BnDTPA-p53 (1C12)-TAT radioconjugate in both B8484 and P2FIR allograft tumours at 72 h post-injection (0.9 ± 0.2 and 1.4 ± 0.7, respectively) were also obtained and are shown in Figure 5.8, presenting values marginally higher than the ratios found previously (Figure 5.3) but no different to the controls ($p > 0.05$, ^{111}In-BnDTPA-IgG$_1$-TAT: 0.87 ± 0.03 and 1.4 ± 0.20, respectively; ^{111}In-BnDTPA-p53 (1C12): 0.9 ± 0.30 and 1.3 ± 0.06, respectively; ^{111}In-BnDTPA-IgG$_1$: 0.83 ± 0.07 and 1.06 ± 0.30, respectively).

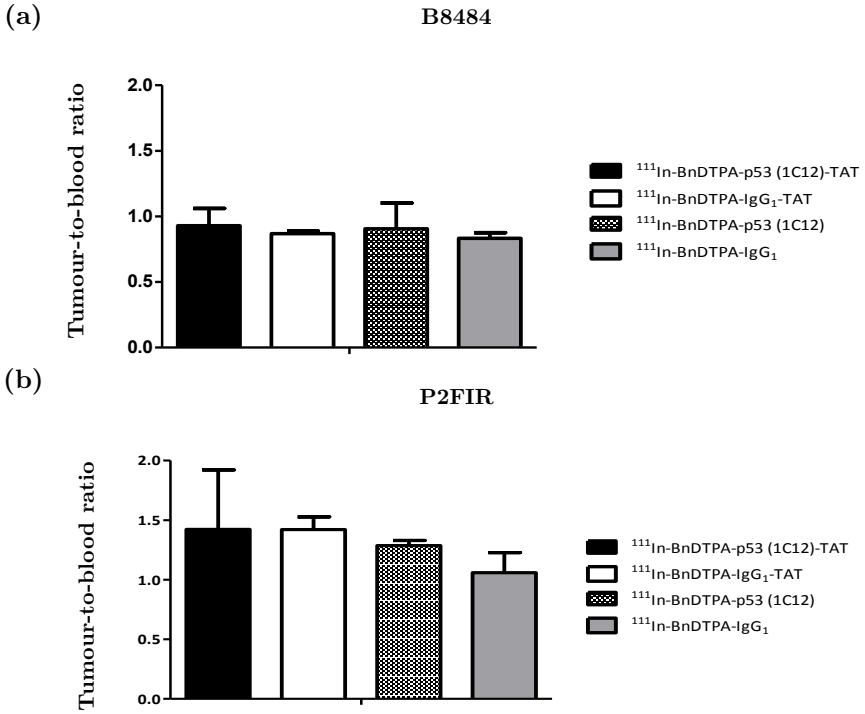

Figure 5.8: Tumour-to-blood (T/B) uptake ratios 72 h after administration of ^{111}In-labelled conjugates in B8484 (a) and P2FIR (b) allograft-bearing mice. Data represents mean ± SEM (n = 3 animals/group). No statistical significance was observed between groups ($p > 0.05$, two-way ANOVA with Bonferroni post-test).

In addition, the trend observed earlier in the B8484 allografts-bearing mice for the T/B ratio of ^{111}In-BnDTPA-p53 (1C12)-TAT (Figure 5.3a) was not as pronounced

in the present study when compared to the non-specific control (7 ± 2.5 *vs.* 4.8 ± 1.4, respectively) (Figure 5.8a). In the P2FIR allograft tumours, however, the same pattern in T/B ratio of the previous study was observed (Figure 5.3b) with no difference between ^{111}In-BnDTPA-p53 (1C12)-TAT and ^{111}In-BnDTPA-IgG$_1$-TAT but slightly increased values than those of the two non-TAT conjugated controls (Figure 5.8b).

5.3.2.1 p53 expression in B8484 and P2FIR allograft tissue

To better determine whether the p53 expression profile of the KPC-derived cells lines remained unaffected following subcutaneous inoculations *in vivo*, a western blot analysis was performed on lysates derived from the tumours (Section 5.2.5.3 and Section 2.4). To avoid cross-reactivity a rabbit polyclonal primary antibody specific for total p53 was used (p53 (CM5)). p53 expression levels were shown to be similar between tissue (Figure 5.9) and cell (Figure 3.1) extracts.

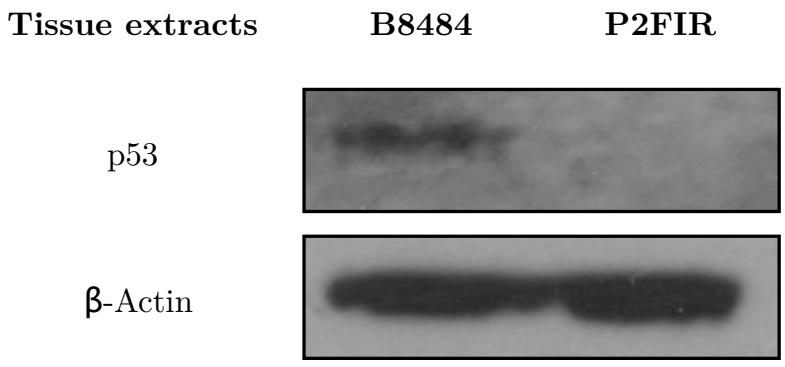

Figure 5.9: Western blot analysis of tissue extracts from B8484 and P2FIR allograft tumours. Total protein (20 μg) was loaded on SDS-PAGE, followed by immunoblotting with rabbit polyclonal anti-p53 (CM5) antibody to avoid cross-reactivity. *β*-Actin was used as a loading control.

As expected, presence of p53 protein was observed only in the extracts from B8484 allograft tumours and no expression was detected in the P2FIR tumours.

Immunohistochemistry on tumour tissues was also performed to further validate the p53 expression of the subcutaneous tumours (Figure 5.10). Tumour tissue sections were prepared, as described in Section 5.2.5, and stained using the same primary antibody used for western blot (anti-p53 (CM5)). Representative confocal images of p53 staining of frozen B8484 and P2FIR allograft tumour sections are shown in Figure 5.10a and Figure 5.10b, respectively.

As evident from Figure 5.10a, strong p53 staining was mainly seen in the nucleus of the B8484 tumour allografts, even though not homogeneously distributed across the selected region, agreeing with the localisation pattern observed *in vitro* in the B8484 cell line (Figure 3.5a). While there was no signal observed in the P2FIR tumour allografts by western blot, p53 staining was detected by immunohistochemistry around nucleus (extracellular localisation) (Figure 5.10b). When compared to the B8484 allograft tumours, there was a relatively lower overall p53 signal in the selected region of the P2FIR allograft tumours and a very different distribution pattern than that observed for mutant p53. Controls omitting the primary antibody were included to assess the level of background. As observed in both B8484 and P2FIR allograft tumour sections, there was a negligible autofluorescence detected (Figure 5.10a and Figure 5.10b lower panels, respectively).

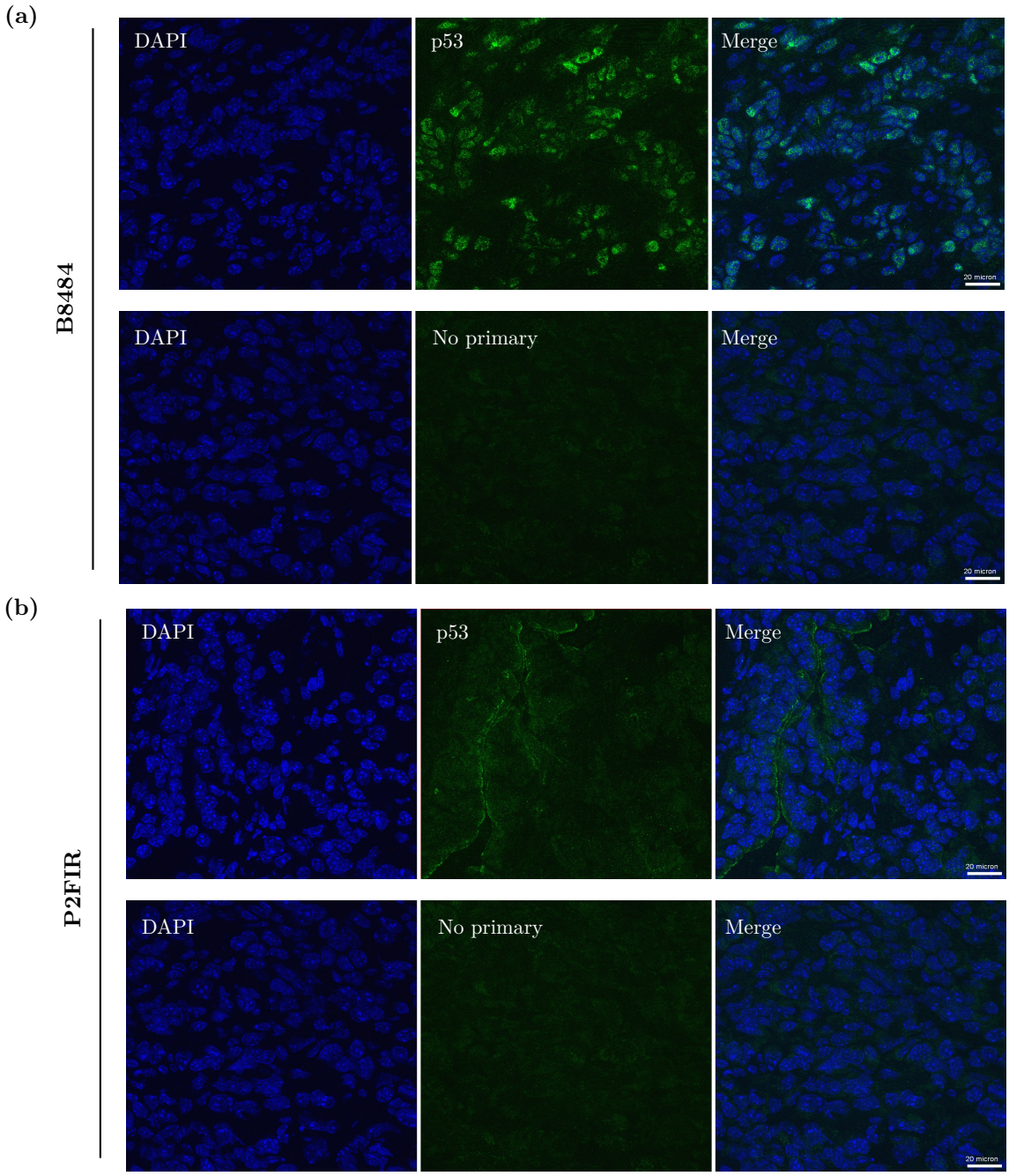

Figure 5.10: Immunohistochemical analysis of p53 expression levels in allograft tumours. Frozen B8484 (a) and P2FIR (b) allograft tumour sections were stained with the anti-p53 (CM5) rabbit polyclonal antibody (green) following antigen retrieval. Nuclei were visualised using DAPI (blue). Scale bar is 20 μm for all images.

5.3.2.2 Tissue distribution of ^{111}In-activity in B8484 and P2FIR allograft tumours

The distribution of ^{111}In-BnDTPA-p53 (1C12)-TAT in B8484 and P2FIR allograft tumours was tested by *ex vivo* autoradiography and compared to that of the non-specific control, ^{111}In-BnDTPA-IgG$_1$-TAT. After SPECT image acquisition, tumour tissue was excised, sectioned and prepared for autoradiography as well as H&E staining, as described in Section 5.2.5.1. Representative digital autoradiographs were obtained by exposing tissue sections to a phosphor screen and histology staining was used to assess the general morphology of the same sections. Shown in Figure 5.11a and Figure 5.12a are representative tumour sections of each study group, revealing the distribution patterns of radioactivity at 72 h post-injection of ^{111}In-BnDTPA-p53 (1C12)-TAT.

The radioconjugate primarily accumulated in the outer rim of the tumour in both B8484 and P2FIR allografts. Interestingly, while in B8484 allograft tumours radioactivity distribution coincided with areas of enlarged nuclei and signs of vascularisation (Figure 5.11a), in P2FIR allograft tumours tracer accumulation seemed to co-localise with connective tissue, as evidenced by histology (Figure 5.12a).

Weak accumulation of ^{111}In-BnDTPA-IgG$_1$-TAT was observed (Figure 5.11b) in the surrounding areas of B8484 allograft tumour sections. Similar distribution of radioactivity as ^{111}In-BnDTPA-p53 (1C12)-TAT was detected for ^{111}In-BnDTPA-IgG$_1$-TAT in P2FIR allograft tumours, mainly accumulating in areas of connective tissue (Figure 5.12b).

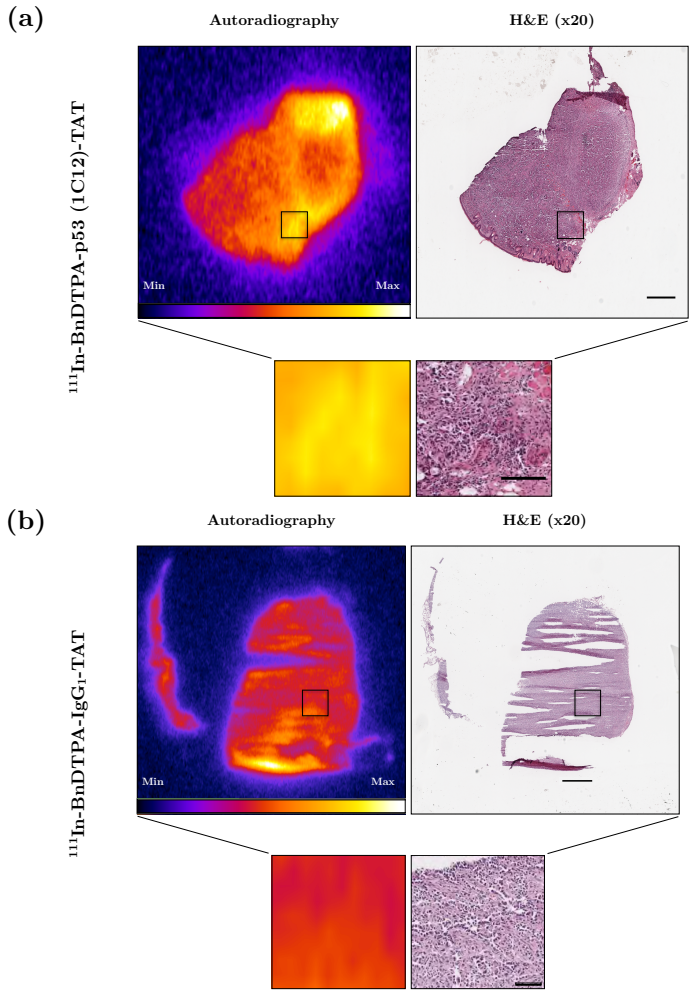

Figure 5.11: Representative *ex vivo* autoradiography and H&E images of ^{111}In-BnDTPA-p53 (1C12)-TAT (a) and ^{111}In-BnDTPA-IgG$_1$-TAT (b) distribution in B8484 allograft-bearing tumours. Scale bars of the full histology and cropped images are 500 µm and 200 µm, respectively.

The ^{111}In-BnDTPA-p53 (1C12)-TAT radioconjugate was also assessed in the KPC genetically engineered mouse model for the first time, which presents an accurate correlation to human PDAC as development of clinical features is similar to those observed in patients (cachexia, bowel obstruction, ascites) as well as the histopathological appearance (tumour microenvironment, metastatic potential) (Lee et al., 2016). Unfortunately, no uptake was observed in the tumour (see Appendix A.4 for experimental data collected).

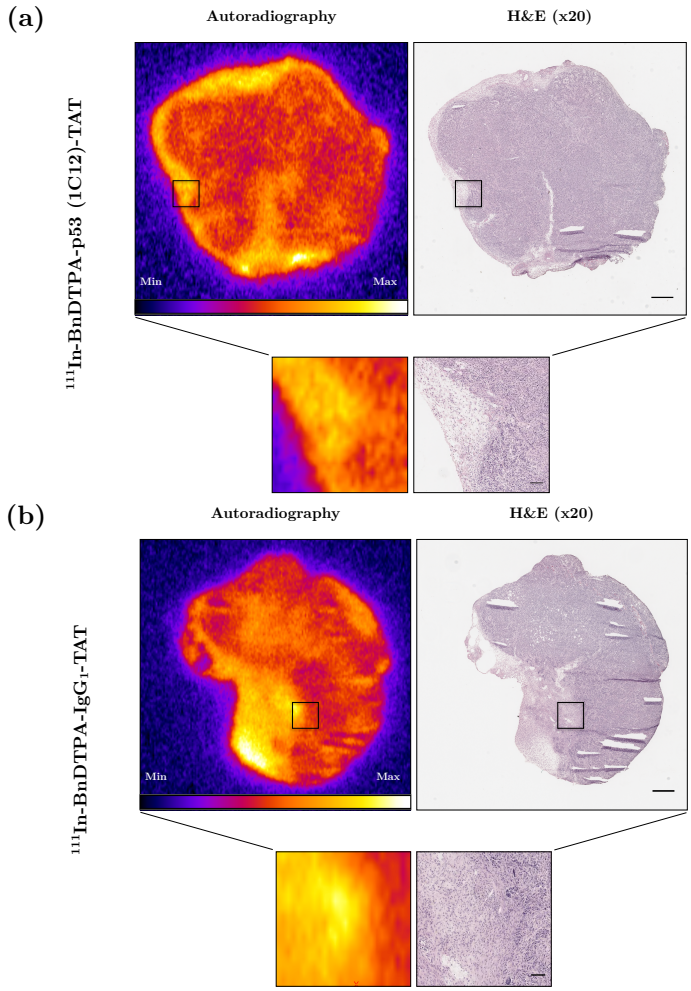

Figure 5.12: Representative *ex vivo* autoradiography and H&E images of ^{111}In-BnDTPA-p53 (1C12)-TAT (a) and ^{111}In-BnDTPA-IgG$_1$-TAT (b) distribution in P2FIR allograft-bearing tumours. Scale bars of the full histology and cropped images are 500 µm and 200 µm, respectively.

5.4 Discussion

Although considerable research has been directed towards the development of diagnostic markers for PDAC, there are still limitations regarding their clinical applicability with CA19-9 the only FDA approved marker for clinical use (Le et al., 2016). The advent of molecular imaging and its combination with monoclonal antibodies presents an attractive method of diagnostic tumour characterisation. Hence, in this study the

^{111}In-labelled anti-p53 (1C12) monoclonal antibody, conferring internalisation and binding specificity to p53 *in vitro*, was evaluated *in vivo* in two mouse models of PDAC: subcutaneous allografts of KPC-derived cell lines and genetically engineered KPC mice.

5.4.1 Imaging p53 in KPC-derived cell line allografts

Athymic nude mice offer several advantages over KPC genetically engineered mice including ease of validation in a short time period, accurate monitoring of tumour growth, and cost (Vandamme, 2014). The KPC-derived cell lines B8484 and P2FIR were evaluated for their ability to form subcutaneous tumours *in vivo* and showed no difference in growth rate, allowing imaging and validation of the radioconjugate in animals of the same age.

Biodistribution of ^{111}In-labelled full length monoclonal antibodies has been well documented *in vivo* since the late 80s (Fawwaz et al., 1985; Hassan et al., 1999; McLarty et al., 2009; Tolmachev et al., 2014; Yip et al., 2014), presenting strong retention in healthy tissues and relatively slow circulation, which affects the contrast of the imaging method at early time points after injection. Therefore, the *in vivo* distribution of ^{111}In-BnDTPA-p53 (1C12)-TAT in this particular model was evaluated and compared to that of a non-specific control (^{111}In-BnDTPA-IgG$_1$-TAT) at 72 h post-injection. In agreement with the studies mentioned above, strong accumulation of the radioconjugates was observed in blood, kidneys, and liver by SPECT imaging and *ex vivo* biodistribution analysis in both B8484 and P2FIR allograft-bearing mice (Figure 5.2), suggesting in particular the slow blood clearance of the radioconjugates.

Even though ROI image and *ex vivo* counting analysis revealed slightly higher retention of ^{111}In-BnDTPA-p53 (1C12)-TAT in B8484 allograft tumours when compared to non-specific control, ^{111}In-BnDTPA-IgG$_1$-TAT (Figure 5.3a), the %ID/g difference between the groups was not statistically significant, suggesting the non-specificity of the ^{111}In-labelled anti-p53 (1C12) antibody *in vivo* (Figure 5.2a and Figure 5.3a).
In the P2FIR allograft tumours, uptake values of ^{111}In-BnDTPA-p53 (1C12)-TAT, determined by *ex vivo* biodistribution and image analysis, were identical to those of ^{111}In-BnDTPA-IgG$_1$-TAT at all times (Figure 5.2b and Figure 5.3b) while showing very similar %ID/g to the uptake values observed in B8484 allograft tumours at 72 h. It should be noted that tail vein injections of the control radioconjugate were not successful for every animal and therefore there was only one mouse for that particular group, making any comparisons inconclusive considering the intratumoral variability that may appear between animals. The similarity observed between the value of uptake of ^{111}In-BnDTPA-p53 (1C12)-TAT in P2FIR allograft tumours, bearing negative p53 status, and the uptake of the ^{111}In-BnDTPA-IgG$_1$-TAT control, may be suggestive of non-specific tumour uptake due to the enhanced permeability and retention (EPR) effect, a phenomenon attributed to abnormal tumour vasculature that causes leakage of long circulating molecules into tumour tissue and retention due to limited lymphatic drainage (Kobayashi et al., 2014). Since the EPR effect largely depends on the physical characteristics (size, charge, polarity) of the injected molecules and not on their binding properties, it was hard to discriminate between the specific binding and non-specific uptake of these antibodies (Ogawa et al., 2009; Heneweer et al., 2011).

To verify the biodistribution trend of ^{111}In-BnDTPA-p53 (1C12)-TAT observed in this study, an additional imaging session was performed including two no-TAT controls (^{111}In-BnDTPA-p53 (1C12), ^{111}In-BnDTPA-IgG$_1$). *Ex vivo* biodistribution and ROI-based image analysis did not reveal any difference between ^{111}In-BnDTPA-p53 (1C12)-TAT and the control radioconjugates (^{111}In-BnDTPA-IgG$_1$-TAT, ^{111}In-BnDTPA-p53 (1C12), ^{111}In-BnDTPA-IgG$_1$) in B8484 and P2FIR allograft tumours (Figure 5.6), suggesting again the non-specificity of the p53 conjugate and poor tumour penetration. Slightly more increased tumour uptake of radioconjugates was observed, probably attributed to the availability of a higher dose in the bloodstream (Misri et al., 2011). Tumour-to-blood ratios (Figure 5.8) were comparable to the initial values obtained (Figure 5.3). Comparison of %ID/g values from biodistribution and ROI analysis revealed an underestimation of tumour uptake, as determined by ROI, for all the radioconjugates. This may be due to quantitative biases associated with the partial volume effects (PVE) caused by the limited spatial resolution of the emission devise (Ritt et al., 2011). In small structures with heterogeneously distributed activity, tumour uptake quantification may lead to underestimation of accumulated activity because of spill out effect into neighbouring voxels. Also, since only a small region of the tumour was used as a representation of tumour uptake, dead-space may have been included in the ROI delineation. Lastly, measurements acquired by γ-counting may have been affected by cross-contamination between tissues, incomplete dissection, and weighing errors leading to discrepancies in the biodistribution results as well.

Western blot analysis on the tumour tissues confirmed the sustained expression of p53

protein only in B8484 allograft tumours while no signal was detected in the P2FIR sections (Figure 5.9). Immunohistochemical analysis however, revealed p53 signal in the P2FIR tumour sample that was not noted by western blot (Figure 5.10b) probably because of differences in detection sensitivity between the two assays but also the fact that one recognises proteins in their native form while in western blot the protein is denatured and some antibodies may not be able to bind. The signal resembled extracellular or even stromal expression of p53 compared to nuclear staining that was observed in the B8484 allograft tumours (Figure 5.10a). It is generally accepted that tumour microenvironment plays an important role in malignancy, consisting of a complex cellular network with stroma as one of the major compartments (Kidd et al., 2012; Chen et al., 2015; Hensel et al., 2017). In their study, Farmaki *et al.* suggested that selective pressure from the tumour microenvironment may lead to the selection of populations from stromal cells carrying altered properties such as genetic instability, self-maintained replication, uncontrolled growth and extended cell survival (Farmaki et al., 2012). Thus, it can be hypothesised that p53 expression of the host may be responsible for the immunohistochemical signal observed in the P2FIR allograft tumour sections.

Autoradiography images (Figure 5.11), overlaid with morphological staining, showed a similar distribution pattern of ^{111}In-BnDTPA-p53 (1C12)-TAT between the two tumour models. Minimal signs of accumulation were observed in areas with enlarged nuclei in B8484 tissue sections (Figure 5.11a) and the outer rim of the tumour was the primary accumulation site in both allograft tumour models with some uptake observed in the connective tissue of the P2FIR allograft tumours (Figure 5.12a). This

uptake in P2FIR tumours can be correlated to the endosomal entrapment observed *in vitro* with the fluorophore-based version of the anti-p53 (1C12)-TAT in P2FIR cells (Chapter 4, Figure 4.10), suggesting a possible entrapment of the radioconjugate in the tissue. A similar uptake pattern was also detected for ^{111}In-BnDTPA-IgG$_1$ (Figure 5.12b) in the B8484 and P2FIR tumours (Figure 5.11b) with accumulation of radioactivity around the tumour and in areas characterised by cutting artefacts. Uptake of control radioconjugates is expected in part due to the presence of the TAT peptide but also their inherent tendency to internalise into the cells, and the grade of this uptake and their excretion from the tumour area, may be dependant on factors such as tumour size and blood flow (Hagan et al., 1986). In addition, it has been previously suggested that the positive charge of the TAT peptide itself may affect tumour permeability leading to poor tumour uptake of such conjugates (Niesner et al., 2002). It is therefore challenging to discriminate between specific and non-specific uptake of ^{111}In-BnDTPA-p53 (1C12)-TAT in this tumour model.

In addition to the allograft tumour model, imaging of p53 mutations in PDAC progression and development was performed in KPC genetically engineered mouse models using the ^{111}In-BnDTPA-p53 (1C12)-TAT. CT is the most common diagnostic method of PDAC lesions to date, although it can provide false positive findings for detection of primary tumours (Delbeke and Pinson, 2004). Even pre-clinically, there are limitations for identification of PDAC in the KPC mouse model as tumour development is relatively slow and occurs with variable latency (Gopinathan et al., 2015).

In this study KPC mice were screened every two weeks using MRI due to its superior soft tissue contrast for tumour growth monitoring. In Appendix A.4, imaging with

^{111}In-BnDTPA-p53 (1C12)-TAT was performed upon a suspected tumour after MRI screening (Figure A.4). This was followed by an ^{18}F-FDG-PET scanning session as an additional tumour confirmation method which offers superior sensitivity in separating benign from tumourigenic lesions, as identification of biochemical changes may occur even before any anatomical or structural differences (Laeseke et al., 2015). *Ex vivo* biodistribution data (Figure A.5) showed low %ID/g values than those observed before in the allograft studies, suggesting the possible effect of immunological profile of the host on tracer biodistribution, as suggested before for ^{111}In-labelled compounds (Vilhelmsson-Timmermand et al., 2015). Together with the SPECT/PET/CT images Figure A.7), both data showed marked uptake in the bladder, heart, facial papillomas, and diffuse spots in the lower abdomen that were hard to discriminate for the presence of a tumour. ^{18}F-FDG-PET images showed uptake in bladder, heart, spinal cord, and brain even though low. No uptake was observed in the area of a suspected tumour, determined by MRI, which could be suggestive of several factors involved during the scanning session. Fueger *et al.*, hypothesised that uptake of ^{18}F-FDG is dependant upon parameters such as the surrounding temperature, diet, and anaesthesia caused by the great variability in imaging protocols utilised for pre-clinical studies (Fueger et al., 2006). They were able to demonstrate that warming and fasting of animals can increase tumour accumulation by more than 3-fold. In the current study, and even though all animals were fasted overnight, fluctuations in body temperature were often unavoidable probably explaining absence of a greater signal at the tumour site. *Ex vivo* pancreas and tumour (dissected from the pancreatic tissue) autoradiography demonstrated minimal accumulation of ^{111}In-BnDTPA-p53 (1C12)-TAT throughout

the whole tissue section (Figure A.8, Figure A.9). Interestingly, examining the pancreatic tissue, uptake was also observed in areas characterised for the presence of PanIN lesions. Whether these regions represent PanIn-3 stage lesions, in which p53 is mutated in most of the cases, has yet to be elucidated, as an additional specialised confirmation needs to be performed. The presence of papillary architecture however, in combination with moderate nuclear atypia, is suggestive of a grade higher than PanIN-1, characterised by a more flat and columnar cell phenotype (Scarlett et al., 2011).

Immunohistochemical analysis of the tissue sections (pancreas and tumour) depicted a more cytosolic staining pattern with no signal in the nucleus (Figure A.10), posing more questions towards the suitability of this model for imaging p53 mutations.

5.5 Conclusions

Imaging of p53 mutations in cancer has proven challenging, with some studies attempting to image interaction of p53 with other targets (i.e., Mdm2) (Goh et al., 2014) rather than direct endogenous protein levels. In the present study, the non-invasive *in vivo* imaging p53 mutations was attempted using radiolabelled monoclonal antibodies. There are however, certain limitations involved in this approach. The Combination of both *in vivo* studies in subcutaneous allografts of KPC-derived cell lines showed very little uptake of the ^{111}In-BnDTPA-p53 (1C12)-TAT radioconjugate in the B8484 allograft-bearing mice, characterised by the presence of p53 mutations and the specificity of this uptake was hard to discriminate due to concomitant accumu-

lation not only of the ^{111}In-BnDTPA-IgG$_1$-TAT non-specific control radioconjugates but also accumulation of both in the P2FIR allograft-bearing tumours (p53 null). Despite the increasing trend observed, the distribution of ^{111}In-BnDTPA-p53 (1C12)-TAT in a p53 mutant background, is suggestive of a inefficient or non-specific uptake. In addition, this chapter provides the first attempt of imaging p53 in the KPC genetically engineered mouse model, showing also no accumulation of ^{111}In-BnDTPA-p53 (1C12)-TAT, as depicted by *ex vivo* biodistribution analysis. These results support further challenges towardsa the use of ^{111}In-BnDTPA-p53 (1C12)-TAT as an imaging tool for pancreatic cancer.

Chapter 6

In vivo imaging of extracellular targets

6.1 Introduction

The aim of this chapter was to evaluate the biodistribution and tumour uptake of a novel antibody, T1-116C, which acts as a T-cell receptor mimic and recognises a wild-type p53-derived peptide presented by human leukocyte antigen haplotype HLA-A2 on the cell surface. The T1-116C antibody was developed by the Banham group at Oxford university, who reported its ability to recognise the p53-derived peptide *in vitro* in 15 cancer cell lines positive for both p53 and HLA-A2 (Li et al., 2017). As part of the study, here, the targeting of the p53-derived peptide by the T1-116C antibody was evaluated in vivo using T1-116C binding MDA-MB-231 and T1-116C non-binding MDA-MB-468 breast cancer xenograft-bearing mouse models.

Most proteins are found within the cell, regulating cell growth, proliferation, apoptosis and many are often mutated in a cancer cell, where traditional monoclonal antibody therapies cannot reach (Chang et al., 2016). Intracellular proteins are constantly being degraded by the proteasome machinery. Briefly, the polypeptide cofactor ubiquitin is conjugated to the ϵ amino moiety of lysines. The protein is then digested by the 26S proteasome into oligopeptides that are of the correct size for presentation and if not are extended on their N-terminus. Various aminopeptidases in the cytosol or endoplasmic reticulum (ER) cut these extended peptides into the right size and the peptides are transported via a transporter associated with antigen presentation (TAP) to the ER and loaded to the major histocompatibility complex (MHC) class-I molecules, referred to as human leukocyte antigen (HLA) class-I in humans (Goldberg et al., 2002; Neefjes et al., 2011). The MHC class-I molecules bind to the peptides

produced, transferring them to the cell surface for display to the immune system (Rock et al., 2004). The presentation of these peptides on the cell surface allows the recognition of intracellular antigens by the immune system and more specifically, by the $CD8^+$ T cells where the T cell receptors (TCRs) specifically bind to the MHC class-I presented peptides, enabling T cell targeted killing of cells expressing foreign or altered self antigens (Kloetzel, 2004).

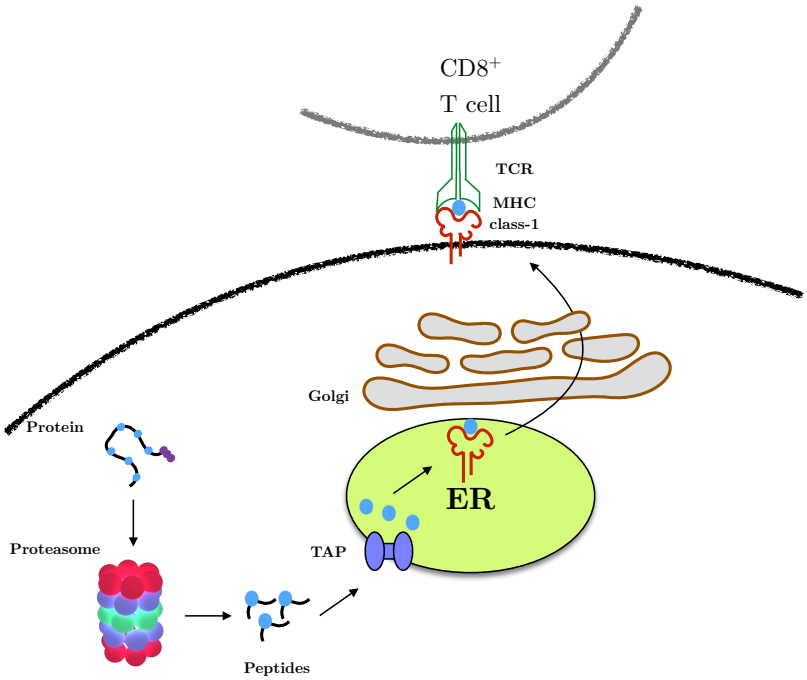

Figure 6.1: Schematic representation depicting the antigens presented by the MHC class-I molecules. Proteins are degraded into small peptides by the proteasome and subsequently transported via the TAP transporter to the ER. MHC class-I molecules, waiting in the ER, bind to the peptides and transport them to the plasma membrane. The presented peptide can then be recognised by immune system. ER: endoplasmic reticulum, TCR: T cell receptors.

The specificity of TCRs in differentiating the peptides presented by MHC class-I, has opened new possibilities to validate disease-specific targets (Weidanz et al., 2011). The advance of new technologies has allowed the generation of antibodies carrying TCR-like characteristics (TCRm) that specifically recognise tumour antigen derived

peptide/MHC complexes on the cell surface, providing the selectivity of T cell-like recognition (Dao et al., 2013). Even though challenging, several antibodies have been generated by phage display or hybridoma fusion technology, using the MHC tetramers as immunogenes. One potential hurdle in the use of such antibodies is the limited density of the epitope on the cell surface which is dependant on a number of factors such as protein expression levels, protein half-life, HLA levels and presentation (Dubrovsky et al., 2016). Therefore, the ideal targets for TCRm antibodies are those found in abundance on the cell surface, most likely the result of overexpressed proteins with short half-lives that are constantly being degraded into peptides with strong affinity for patient's HLA (Bassani-Sternberg et al., 2015). Such TCRm targets, following the above criteria, can be classified into three categories. These are: 1. antigens presented by the tumour itself (e.g. peptides produced from mutated proteins) (Worley et al., 2001), 2. oncofetal proteins (e.g. CEA) (Tsang et al., 1995), 3. tumour microenvironment cells (e.g. tumour associated macrophages) (Noy and Pollard, 2014). Targeting commonly mutated proteins is of utmost interest as it may open a new window for current cancer therapy approaches. Besides therapy, these targeting moieties could be in principle also used as tumour-imaging agents for diagnostic purposes.

There are a number of advantages of TCRm antibodies over their TCR counterparts. In comparison to TCR, TCRm antibodies show higher binding affinity towards the target, comprising them useful for targeting low abundance epitopes on the MHC-I molecules. In addition, TCRm presents a variety of orientations in regards to their binding to the peptide/MHC-I complex, which may allow binding to the areas of MHC that are inaccessible to TCR and T cell-based therapies. Even though production

of antibodies is easily performed and on a large scale, one of the disadvantages of TCRm is that they are restricted to a specific HLA haplotype. This issue can be circumvented by developing TCRm against a few commonest HLA haplotypes in humans and the combination of these TCRm will cover the majority of the whole human population. The HLA-A2 (found in approximately 50% of Caucasians) and HLA-A24 (common in Asian populations) haplotypes are the most favoured for such applications (Dubrovsky et al., 2016).

Considering the prevalence of p53 mutations in human cancer, it is one of the most extensively studied tumour-associated antigens. Some studies have reported the presence of high copy numbers of wild-type p53 peptide/MHC-I complex in tumour cells in comparison to low expression in normal cells (Vierboom et al., 2000). Various immunotherapy strategies can be employed to target MHC class-I presented peptides, such as those derived from p53, including TCRm antibodies. Due to commonly appearing missense mutations of p53 that lead to accumulation or overexpression of the protein in the cytosol, the protein is more readily available for antigenic processing of both the mutant and wild-type peptides (DeLeo, 2006).

Li *et al.* (Li et al., 2017), developed a TCRm antibody (T1-116C) against the HLA-A2 presented $p53_{65-73}$ epitope (RMPEAAPPV) and characterised its binding specificity in a variety of cancers but also therapeutic potential by initiating immune effector functions to kill tumour cells *in vitro*. The antibody was shown to inhibit tumour growth of breast cancer xenografts that express the $p53_{65-73}$ peptide *in vivo* and thus representing a promising agent for future cancer therapy.

Although cell penetrating peptides (CPPs) have the ability to translocate various

cargoes into the cell and into the nucleus, there are still a lot of challenges, as have been addressed in the previous chapters, regarding cell specificity, internalisation mechanism and endosomal escape. Those challenges are reflected by the development of imaging and therapeutic markers for mainly extracellular targets, some of which have been approved by FDA for clinical use (Hong and Zeng, 2014). Therefore, this study aims to evaluate an alternative imaging agent targeting extracellular p53 peptides, providing a means of comparison to the detection efficiency of intracellular endogenous p53.

6.2 Materials and methods

6.2.1 Cell lines

Human breast cancer cell lines, MDA-MB-231 and MDA-MB-468, were purchased from ATCC and cultured in Dulbecco's modified Eagle's medium (DMEM) (Sigma Aldrich, UK), supplemented with 10% (v/v) of foetal bovine serum (FBS) (Gibco, USA), 100 units/mL penicillin, 100 μg/mL streptomycin and 2 mM L-glutamine (Sigma Aldrich). Cells were maintained in a humidified chamber at 37°C and 5% CO_2, and handled in a class II microbial safety hood.

6.2.2 Animal models

Female BALB/c *nu/nu* mice (20-25 g) (Charles River, UK), were inoculated subcutaneously (*s.c.*), using a 21 G needle, in the right lower flank with MDA-MB-231 or MDA-MB-468 breast cancer cell lines, prepared as described in Section 5.2.1.1

(1 x 10^6 cells in 100 µL cell suspension). During inoculation all animals were anaesthetised using 2-3% (v/v) isoflurane in oxygen and kept on a heating bed to prevent hypothermia. Animals were observed for 10-15 min to ensure full recovery from anaesthesia. Tumour volume measurements were collected every 3 days, as described in Section 5.2.1.2.

6.2.3 Antibody conjugation and radiolabelling

The T1-116C mouse monoclonal antibody ($mIgG_2a$) (Li et al., 2017) or a non-specific isotype-matched control (IgG2a) (500 µg each, 1 mg/mL stock) were reacted with a 20-molar excess of *S*-2-(4-isothiocyanatobenzyl)-diethylenetriamine pentaacetic acid (*p*-SCN-Bn-DTPA), as described in Section 4.2.5.1. DTPA-conjugated antibodies were then labelled with ^{111}In, as described in Section 4.2.5.2. ^{111}In-BnDTPA-T1-116C or ^{111}In-BnDTPA-IgG2a (5 MBq (5 µg)) were administered intravenously in to the tail vein, when subcutaneous tumours had reached a volume of at least 125 mm^3.

6.2.4 SPECT imaging

SPECT imaging was performed at 24 h, 48 h, and 72 h post injection, using a 4-head NanoSPECT/CT γ-camera (Bioscan, USA) with an incorporated cone beam CT imaging system, as described in Section 5.2.3. Tumour uptake was quantified at each time point based on the reconstructed SPECT images, using the Inveon research workplace software package version 2.2 (Siemens, Germany), as described in Section 5.2.3.2. At 72 h, after the last scanning session, animals were sacrificed by cervical dislocation and *ex vivo* biodistribution analysis was performed, as described

in Section 5.2.3.1. Radioactivity in tumour and other selected tissues was expressed as percentage of the injected dose per gram tissue (%ID/g).

6.2.5 Statistical analysis

All data are reported as mean ± standard error of mean (SEM). Statistical analysis was performed using GraphPad Prism 5 (GraphPad Software,USA). Two-way analysis of variance ANOVA test with Bonferroni multiple comparison correction post-test was used for comparison of more than two groups mean.

6.3 Results

6.3.1 Biodistribution of ^{111}In-BnDTPA-T1-116C

Ex vivo biodistribution studies were performed in MDA-MB-468 and MDA-MB-231 breast cancer xenograft-bearing mouse models at 72 h post-injection of radiolabelled T1-116C antibody and the non-specific control and are summarised in Figure 6.2. Tumour models were selected according to their ability to bind T1-116C and hence, acting as positive (MDA-MB-231) and negative (MDA-MB-468) controls.

After injection of ^{111}In-BnDTPA-T1-116C, high levels of radioactivity, were observed in blood with 21.1 ± 2.5%ID/g and 14.4 ± 7.0%ID/g for MDA-MB-468 and MDA-MB-231, respectively. Uptake of the non-specific control, ^{111}In-BnDTPA-IgG2a, was also high in the blood for both xenograft models (16.4 ± 8.7%ID/g in MDA-MB-468 and 10.2 ± 6.7%ID/g in MDA-MB-231 xenografts). Relatively high uptake of ^{111}In-BnDTPA-T1-116C and ^{111}In-BnDTPA-IgG2a was observed in the heart (8.2 ± 2.7

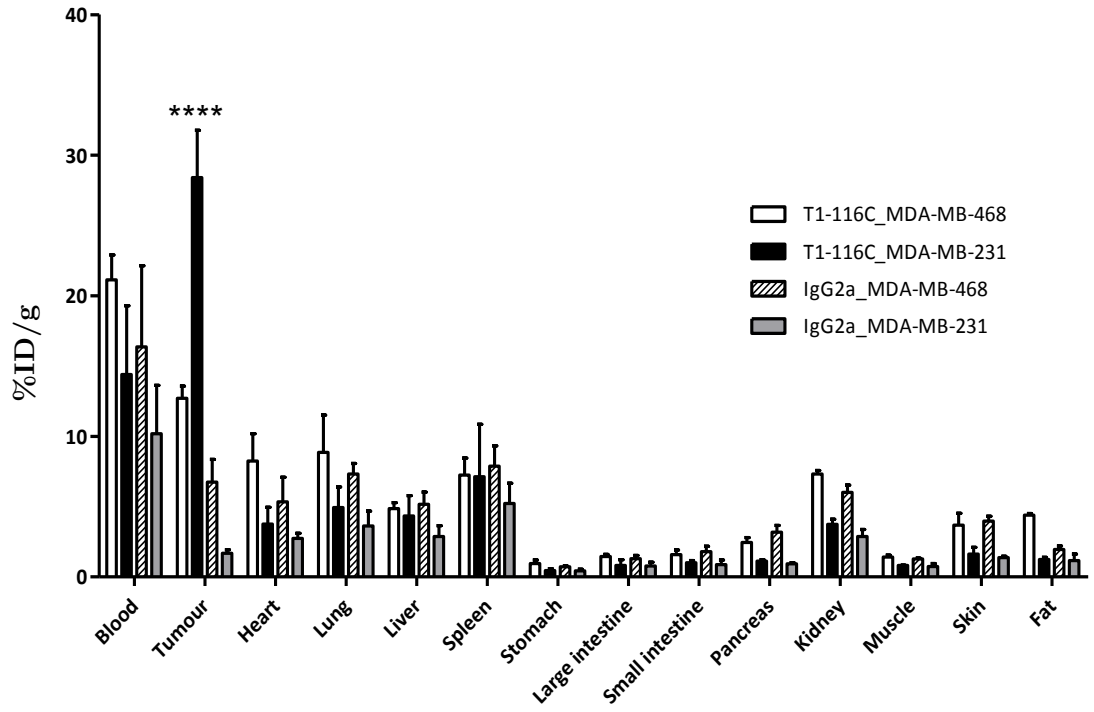

Figure 6.2: Biodistribution of ^{111}In-BnDTPA-T1-116C (n = 2) and ^{111}In-BnDTPA-IgG2a (n = 3) in MDA-MB-468 and MDA-MB-231 breast cancer xenograft-bearing mouse models at 72 h post-injection. Data is presented as %ID/g and error bars represent mean ± SEM. Two-way analysis of variance (ANOVA) was used for multiple comparisons (**** $p < 0.0001$).

and 5.3 ± 3.9%ID/g, respectively), lungs (8.9 ± 3.7 and 7.3 ± 1.7%ID/g, respectively), and spleen (7.2 ± 1.7 and 7.9 ± 3.4%ID/g, respectively) of MDA-MB-468 mice. The same tissues did not present a significant accumulation of radioactivity in the MDA-MB-231 mice, apart from the spleen (^{111}In-BnDTPA-T1-116C: 7.1 ± 5.3%ID/g, ^{111}In-BnDTPA-IgG2a: 5.2 ± 2.5%ID/g). Significantly increased tumour uptake of ^{111}In-BnDTPA-T1-116C, and as high as 28.4 ± 4.7%ID/g, was seen in the MDA-MB-231 mice and was greater than the uptake of ^{111}In-BnDTPA-IgG2a non-specific control (1.7 ± 0.5%ID/g) in the same mouse model ($p < 0.0001$), suggesting great specificity of the T1-116C antibody towards the target of interest. Tumour accumulation in the MDA-MB-468 mice reached 12.7 ± 1.2%ID/g for ^{111}In-BnDTPA-T1-116C and

6.7 ± 2.8%ID/g for the non-specific control and was lower than uptake values in the MDA-MB-231 mice.

6.3.2 SPECT imaging

In vivo SPECT maximum intensity projection images (MIPs) were acquired at 24 h, 48 h, and 72 h after administration of 5 MBq (5 μg) of ^{111}In-BnDTPA-labelled T1-116C and IgG2a. Figure 6.3 and Figure 6.4 show the distribution over time of the labelled antibodies in MDA-MB-468 and MDA-MB-231 xenograft-bearing mice, respectively. Considerably higher tumour accumulation of radioactivity was observed in MDA-MB-231 mice (Figure 6.4) injected with ^{111}In-BnDTPA-T1-116C, especially when compared to its corresponding non-specific control with near non-detectable uptake, but also to MDA-MB-468 xenograft animals (Figure 6.3). These results were in agreement with the biodistribution data (Figure 6.2).

High uptake amongst healthy tissues was observed in the heart, liver, and carotid arteries during the first 24 h in MDA-MB-468 and MDA-MB-231 xenograft-bearing mice, suggesting a similar blood clearance profile for both. The background uptake signal decreased over time, leading to better tumour contrast at 72 h. Region of interest (ROI) analysis showed a significantly higher accumulation of ^{111}In-BnDTPA-T1-116C in MDA-MB-231 mice at all time points, but peaked at 48 h and 72 h (22.7 ± 5.8 and 22.4 ± 1.7%ID/mL, respectively), while it only reached 9.3 ± 0.5%ID/mL in the MDA-MB-468 group ($p < 0.001$) (Figure 6.5a).

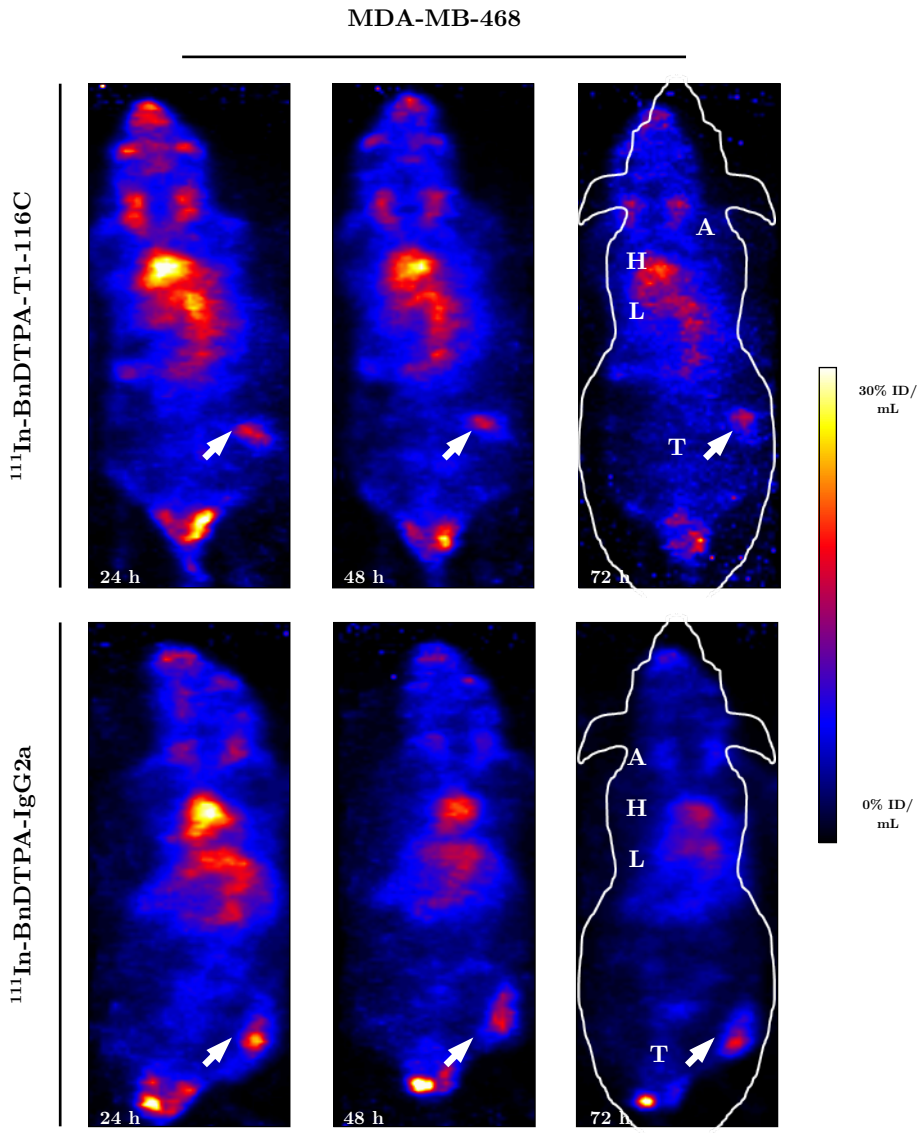

Figure 6.3: Representative SPECT maximum intensity projections of ^{111}In-BnDTPA-T1-116C and ^{111}In-BnDTPA-IgG2a in MDA-MB-468 xenograft-bearing mice. Images of the same mouse were taken at 24 h, 48 h, and 72 h post-injection. ^{111}In-BnDTPA-IgG2a was used as control for evaluation of non-specific binding. Arrows point to MDA-MB-468 xenograft tumours (T). Heart (H), liver (L), and carotid arteries (A) are also included as organs of high uptake.

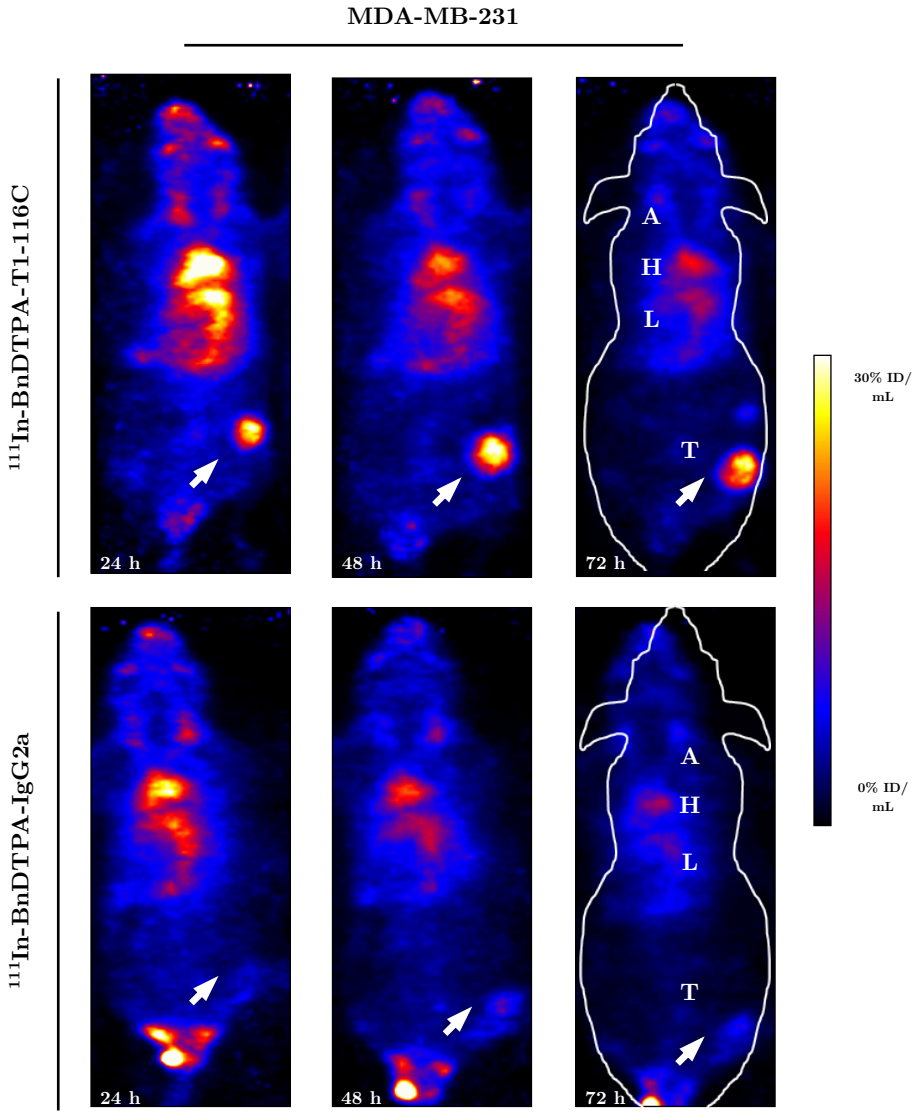

Figure 6.4: Representative SPECT maximum intensity projections of ^{111}In-BnDTPA-T1-116C in MDA-MB-231 xenograft-bearing mice at 24 h, 48 h, and 72 h post-injection. ^{111}In-BnDTPA-IgG2a was used as control for evaluation of non-specific binding. Arrows point to MDA-MB-468 xenograft tumours (T). Heart (H), liver (L), and carotid arteries (A) are also included as organs of high uptake.

Tumour-to-blood (T/B) ratios (heart was used for estimation of blood concentration) also confirmed the gradual increase of ^{111}In-BnDTPA-T1-116C in MDA-MB-231 tumours over time, with a value of 1.9 ± 0.3 at 72 h. In comparison, uptake ratio of ^{111}In-BnDTPA-IgG2a in the same model was as low as 0.5 ± 0.3 at 72 h. T/B ratio values in the MDA-MB-468 mice were also lower and similar between the ^{111}In-BnDTPA-T1-116C and ^{111}In-BnDTPA-IgG2a (1 ± 0.4 *vs.* 0.9 ± 0.1, respectively) (Figure 6.5b).

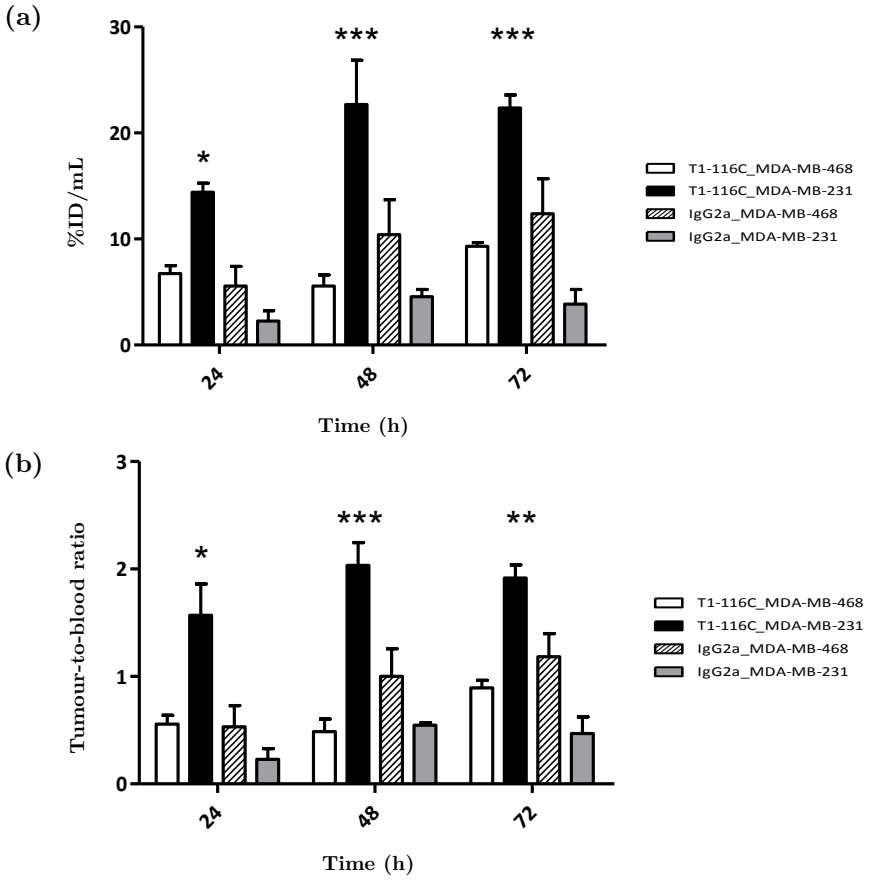

Figure 6.5: Tumour uptake (a) and tumour-to-blood ratios (b) for ^{111}In-BnDTPA-T1-116C as determined by ROI analysis. ROIs were estimated for both ^{111}In-BnDTPA-T1-116C and the non-specific control ^{111}In-BnDTPA-IgG2a at 24 h, 48 h, and 72 h post-injection. (^{111}In-BnDTPA-T1-116C: n = 2 animals/group, ^{111}In-BnDTPA-IgG2a: n = 3 animals/group). $*$ $p < 0.05$; $**$ $p < 0.01$; $***$ $p < 0.001$.

Taken together, these data confirm the specificity of the T1-116C antibody for tar-

geting the $p53_{65-73}$ epitope at the tumour site *in vivo*, in agreement with the *in vitro* validation performed by the other authors of the same study. More specifically, it was proved that binding of T1-116C antibody is not only dependant on the p53 expression but is also restricted to HLA-A2, and since MDA-MB-468 are HLA-A2-negative, they did not observe any binding of T1-116C *in vitro* (Li et al., 2017).

6.4 Discussion

The majority of cellular proteins involved in tumourigenic processes, take place within the cell and are, therefore, hard to reach by conventional molecular imaging methodologies, such as monoclonal antibodies. Previous sections of this thesis discussed a proof-of-principle for targeting intracellular endogenous p53 protein using CPPs. Despite their great potential as delivering agents, CPPs still lack tumour specificity and have good but limited cell penetrating ability, which remains a major challenge for molecular imaging. Here, instead of directly visualising intracellular endogenous p53 protein, a T1-116C antibody, raised against the HLA-A2 presented $p53_{65-73}$ epitope on the cell surface, was evaluated *in vivo*. Two breast cancer tumour models were used with presence (MDA-MB-231 xenograft-bearing mice) or absence (MDA-MB-468 xenograft-bearing mice) of the antibody epitope, as was determined by *in vitro* studies reported by Li *et al.* (Li et al., 2017).

Similar to common monoclonal antibodies, TCRm antibodies, such as T1-116C, have the ability to target disease-related peptide/MHC-I complexes, binding both the peptide and the MHC class-I molecule in a specific manner and therefore, expanding

targetable antigens into intracellular proteins without compromising cell membrane. In the present study, the T1-116C antibody was shown to bind p53 peptide/MHC-I expressing tumour tissue *in vivo*. *Ex vivo* biodistribution studies revealed that uptake of ^{111}In-BnDTPA-T1-116C in the MDA-MB-231 xenograft tumours exceeded that in all other tissues and was significantly higher than the uptake in the control groups. In addition, ^{111}In-BnDTPA-T1-116C resulted in high tumour-to-blood contrast (approximately 2) in MDA-MB-231 xenograft tumours, at 72 h after administration. Tumour accumulation of ^{111}In-BnDTPA-T1-116C in the MDA-MB-231 xenograft animals was high at all times and peaked at 48 h and 72 h post-injection, suggesting specific targeting *in vivo*.

To our knowledge, this is the first study using a TCRm antibody for imaging of antigen presentation *in vivo*. Even though use of TCRm antibodies is limited due to low epitope densities, the T1-116C antibody presents a superior tumour uptake when comparing to the traditional approaches against cellular proteins. However, the T1-116C recognises only a very specific region of the p53 protein. Mutations of p53 can occur within different regions of the protein with the majority appearing in the core DNA-binding domain (DBD) (Olivier et al., 2010). The particular epitope ($p53_{65-73}$) recognised by the T1-116C antibody is outside this highly mutated region and has very few mutations reported. Therefore, when a cell presents with a p53 mutation, there is a high possibility that the target peptide recognised by the T1-116C antibody will contain the specific wild-type sequence. The mechanisms of epitope presentation however, on the cell surface are poorly understood and are not entirely predictable. Even though several reports have suggested the presence of high copy numbers of

wild-type p53 peptide/MHC-I complexes in tumour cells (Theobald et al., 1998), p53 mutations are not always associated with enhanced processing of the wild-type p53 sequence, and may be a product of other genetic events or even viral integration (DeLeo and Whiteside, 2008). Other challenges include cross-reactivity, as most TCRm antibodies bind only a short linear sequence of their target peptide and thus may recognise off-target epitopes that share the same sequences. Finally, the HLA restriction makes these antibodies applicable for only a subset of patients with certain HLA types (Chang et al., 2016).

6.5 Conclusions

The work presented in this chapter reported the successful targeting of an extracellular p53-derived epitope. Cell surface targets have been mainly explored for the development of diagnostic imaging agents due to lack of plasma membrane barrier and ease of detection. On the other hand, intracellular targets play a much more important role in cellular biology and development of tumours and therefore, have been the major focus for tumour diagnostics and therapy. Selecting the best target may prove challenging and requires further research to better understand the biology underlying these targets and their potential for clinical use.

Chapter 7

Summary and future work

7.1 Summary

The work presented in the current thesis describes a novel method for the detection of p53 in PDAC using a monoclonal antibody (mAb) approach, facilitated by the conjugation to TAT, a cell penetrating peptide (CPP), and a metal ion chelator for radiolabelling with ^{111}In for SPECT imaging. To our knowledge, this is the first "proof-of-concept" study on a non-invasive mean of imaging of p53, which could have important diagnostic implications for various types of cancer.

The advance of hybridoma technologies and the resulting tumour-associated mAbs, have significantly helped to exploit biomarkers that discriminate tumour cells from normal cells. The discovery of antibodies, described as "magic bullets" by Paul Ehrlich (Ehrlich, 1878), has led to mass production of thousands of different types of these biomolecules by biotechnology companies. However, the information supplied from commercial data sheets and academic publications is not always sufficient to enable their use in diagnostic applications and therefore requires further validation of the antibody's performance.

The first aim of this study was to evaluate a commercially available antibody, anti-p53 (1C12), against total p53, as discussed in Chapter 3. The anti-p53 (1C12) mouse mAb showed good specificity for the target in cell lines derived from a PDAC mouse model (KPC) with varying p53 status, B8484 and P2FIR (p53 mutant and p53 null, respectively), by a number of assays. The mAb achieved good experimental reproducibility between different antibody batches, and demonstrated high affinity (K_d = 9 ± 2.2 nM) towards the antigen of interest. These validations supported the selection

of this particular antibody for subsequent studies. However, the sub-cellular localisation of p53 in the model system of interest was confirmed in the nucleus, suggesting the necessity for cell membrane penetration and nuclear translocation.

7.1.1 Unravelling TAT

The intracellular distribution of p53 required the use of CPPs in the design of the p53-targeting imaging agent. In Chapter 4, the anti-p53 (1C12) antibody was conjugated to the TAT CPP to facilitate entry into the cell and into the nucleus.

It was shown that the anti-p53 (1C12)-TAT-Cy3 was localised in the cytoplasmic and nuclear compartment of fixed B8484 KPC-derived cells, carrying mutant p53. Conversely, anti-p53 (1C12)-Cy3 alone was trapped in sub-cellular vesicles, most likely endosomes, as cellular uptake of such molecules has been reported to occur through endocytosis, leading to their encapsulation within the endosome and subsequent degradation (Erazo-Oliveras et al., 2012). A similar endosomal trapping profile was observed in P2FIR cells (p53 null) for both anti-p53 (1C12)-TAT-Cy3 and anti-p53 (1C12)-Cy3, demonstrating the specificity and internalisation capacity of the TAT-conjugated anti-p53 (1C12) antibody in p53-positive cell line. Fixed cells, however, may not represent the true internalisation pattern of the TAT peptide, and may be the cause of redistribution artefacts, as previously pointed out in the literature (Lundberg and Johansson, 2002; Richard et al., 2003).

Prior to radiolabelling with ^{111}In, the anti-p53 (1C12)-TAT conjugate was reacted with the *p*-SCN-Bn-DTPA metal ion chelator, yielding approximately 1.2–2 accessible ligands grafted per antibody. Interestingly, the number of conjugation found in the

present study differs from previous studies. In particular, Cooper *et al.*, suggested the presence of 3.6 ± 1 DTPA chelators per antibody (rituximab) (Cooper et al., 2012) while Ackova *et al.* reported 8.8 groups for the same antibody (Ackova et al., 2016) after addition of 40- or 20-molar excess, respectively. From this difference, it can be hypothesised that the addition of the TAT peptide may affect the conformation of the antibody itself, reducing the number of accessible conjugation sites. This may be similar to the study reported by Tong *et al.*, which showed reduced conjugation efficiency upon initial conjugation of a peptide to a human IgG_1 antibody (Tong et al., 2013).

Despite the relatively low, but sufficient number of chelators per anti-p53 (1C12)-TAT molecule, high radiochemical purities (> 80% prior to purification), were achieved following reaction with ^{111}In radioisotope. Since all of these chemical modifications could potentially affect the properties of monoclonal antibodies, binding affinity and stability were also tested and proven unaffected after the addition of TAT, DTPA, and ^{111}In.

In the present study, targeted tumour cells, B8484 and P2FIR, were analysed for retention of radioconjugates *in vitro* and presented similar uptake and excretion pattern despite their difference in p53 status. The remaining cell-associated ^{111}In activity, retained in both cell lines did not exceed 3% at 72 h post-incubation, suggesting rapid degradation of the radiolabelled antibodies by intracellular compartments and possible excretion.

7.1.2 Imaging p53 as a diagnostic tool

The concept of diagnostic imaging using antibodies that are directed against tumour-associated antigens was introduced in the 80s, and since then has been of the highest interest for clinical translation (Carrasquillo et al., 1984). Mutations of the *TP53* gene occur in almost every type of cancer (38–50% of cases) and are often associated with an aggressive phenotype (Olivier et al., 2010). This realisation led to hopes that p53 may entail a major diagnostic significance and become an important target for the much anticipated "magic bullet" concept. This however, due to complicated underlying biology of p53, has not been fully achieved (Boyd and Vlatkovic, 2008).

In Chapter 5, initial SPECT imaging suggested potential p53 detection via increased accumulation of ^{111}In-BnDTPA-p53 (1C12)-TAT in B8484 allograft tumours, carrying p53 mutations, when compared to the non-specific IgG_1 controls. Equally evident however, was the uptake of ^{111}In-labelled anti-p53 (1C12) and IgG_1 antibodies observed in the P2FIR allograft tumours (p53 null) as well. Although there was no statistical significance between the ^{111}In-labelled anti-p53 (1C12) and its controls (TAT and no-TAT) in the B8484 allograft tumours, overlayed autoradiography and H&E images have shed some light on the distribution of these radioconjugates within the tumour. The accumulation of radiolabelled antibodies was shown to be heterogeneous between all groups and interestingly, uptake in the inner areas of B8484 tumour tissue was observed while mainly connective tissue was highlighted in the P2FIR and control IgG_1 groups. This phenotype, combined with the extracellular presence of p53 in the P2FIR tumour tissue by immunohistochemistry, poses the question of whether

accumulation in the P2FIR group occurs due to stromal expression of p53 or whether it is a non-specific uptake caused by vesicular entrapment of the molecule.

The inconclusive uptake pattern of ^{111}In-BnDTPA-p53 (1C12)-TAT as well as the limited clinical relevance of allograft models, led to subsequent studies on KPC genetically engineered mice. SPECT images did not reveal any evident accumulation of the tracer in the pancreas, with only a diffuse uptake pattern observed in the lower abdomen and was hard to define anatomically. Nevertheless, promising results were obtained using autoradiography and H&E, where the *ex vivo* characterisation revealed accumulation of the ^{111}In-labelled anti-p53 (1C12)-TAT antibody in precursor PanIn lesions as well as fully developed PDAC tumours in the pancreas.

7.1.3 Extracellular versus intracellular targets

Most FDA approved radiolabelled imaging agents are directed against extracellular receptors since access to intracellular markers is limited by membrane penetration (Van Dongen et al., 2007). Following the attempt of imaging intracellular p53, a SPECT imaging tracer detecting cell surface presented p53 peptide/MHC-I complex was also tested, detailed in Chapter 6. ^{111}In-labelled T1-116C antibody showed prominent tumour uptake in T1-116C binding MDA-MB-231 xenograft-bearing mice when compared to controls. A major factor that needs to be considered, however, is the availability of expressed antigens recognised by this particular antibody which may only benefit a small number of patients. Therefore, understanding of molecular biology behind the disease of interest is essential for the successful development of imaging probes and careful consideration is needed when choosing extracellular or

intracellular targets that will provide relevant diagnostic significance.

7.2 Future work

While this thesis demonstrated a "proof-of-concept" for non-invasive imaging of intracellular p53 *in vivo*, several points remain to be addressed that could extend the scope of this project.

An ideal imaging agent should exhibit appropriate absorption and clearance rates to produce high target-to-background ratio *in vivo*. When targeting tumour cell markers in the body, the signal generated by contrast probes should be higher than the background produced by non-specific uptake, and even when the imaging modality is of great sensitivity and resolution towards the target of interest, it would still be masked by high background levels. Hence, the development of a successful imaging probe needs to overcome the challenges of slow blood clearance, non-specific uptake (e.g. liver, spleen, bone marrow), and low levels of target expression (Frangioni, 2008). In the present study, the basal abundance of p53 protein in the tumour model used remains to be elucidated, and even though *in vitro* immunofluorescence studies were performed in the KPC-derived cell lines, no quantification of the copy numbers was conducted at that time. Lakatos *et al.*, characterised the basal p53 protein expression with single cell resolution in human breast and colorectal cancer cell lines, showing that the absolute p53 abundance may vary between 10^4–10^6 p53 proteins per cell, with the highest number present upon mutation (Lakatos et al., 2017). The question now remains whether these antigen expression levels are too low to discriminate p53-

mediated tracer uptake from antibody accumulation due to enhanced permeability and retention (EPR) effects in the tumour site.

Looking carefully at the two studies performed on the KPC-bearing mouse allografts, it can be noticed that different concentrations of radioconjugate (5 μg *vs.* 10 μg) were used. It can be hypothesised that if the endogenous p53 copy numbers were low, and in conjugation with the high concentration of the radioconjugate, the epitope sites may be saturated resulting in a greater degree of non-specific binding. Therefore, a titration study of antibody concentrations may help discriminate the specific uptake of the anti-p53 (1C12) conjugate from the non-specific IgG_1 binding.

Although the internalisation properties of TAT-conjugated antibodies were demonstrated, quantitative analysis of the number of peptides per antibody was hard to achieve. Evaluation of the conjugation efficiency combined with live-cell validation of TAT internalisation, to exclude any fixation artefacts, could provide further insights into the delivery properties and retention of the TAT-antibody conjugate into the tumour site.

The tumour uptake observed in the P2FIR-p53 null group by SPECT, together with the presence of extracellular p53 staining in the tumour tissue shown by immunohistochemistry, may imply the activation of p53 in the tumour microenvironment (TME) of the host. Additional experiments that could evaluate the expression status of p53 protein throughout the different cell types (e.g. cancer associated fibroblasts, macrophages, immune cells) in the TME of P2FIR allograft tumours, could explain the unexpected uptake of ^{111}In-BnDTPA-p53 (1C12)-TAT in the p53-null tumour tissue and whether it is indeed a result of p53 activation of the host, as implicated

previously in cancer initiation (Wang et al., 2017). Therefore, a better understanding on the ability of p53 radioconjugate to detect the very early changes in tumourigenesis would likely aid cancer screening and diagnosis.

The possible endosomal entrapment of the TAT-conjugated antibodies and the inability to exit these vesicles, may require a CPP with improved excretion mechanism allowing its cargo to properly interact with the target molecule (El-Sayed et al., 2009). Akishiba *et al.*, suggested the use of cationic amphiphilic peptides carrying a strong membrane-lytic activity, facilitating cytosolic release (Akishiba et al., 2017). Therefore, and even though in early stages of evaluation, the use of such peptide in our current model system may increase the accessibility of the anti-p53 (1C12) conjugate, improving tumour uptake.

The high cost of the bulk monoclonal antibody used followed by the large amounts required for *in vivo* studies, led to a collaboration with the Banham group at the University of Oxford, to create a mouse monoclonal anti-p53 antibody against total p53 and recognising a similar epitope as the commercially available one. The antibody is being currently validated in-house using the same model system as it was described in this thesis. The immunogenicity of murine mAbs to humans however, largely limits their clinical application. Therefore, the in-house anti-p53 antibody should be humanised to enable its use in PDAC patients.

Finally, targeting tumour cells remains difficult for most imaging agents due to the limiting properties of solid tumours (e.g. irregular, vascularisation, high interstitial pressure, and lack of functional lymphatics), and the size of mAbs severely affects tissue penetration resulting in increased antibody plasma levels that may warrant

FDA placing a clinical hold for their use (Wu, 2014). Current technological advances have enable the generation of recombinant antibody fragments that show as high specificity and affinity but have much shorter biodistribution kinetics (Aldeghaither et al., 2015). These short antibody structures may be able to penetrate deeper the largely heterogeneous PDAC tumours and could increase the potential of diagnostic imaging.

Collectively, these additional experiments could address several aspects discussed throughout this thesis and will likely provide insight into the dynamics of ^{111}In-BnDTPA-p53 (1C12)-TAT behaviour in the tumour models used.

Bibliography

Tarek Abbas and Anindya Dutta. p21 in cancer: intricate networks and multiple activities. *Nature reviews. Cancer*, 9(6):400, 2009.

Hani Abdel-Nabi and Ralph J Doerr. Clinical applications of indium-111-labeled monoclonal antibody imaging in colorectal cancer patients. *Seminars in nuclear medicine*, 23(2):99–113, 1993.

Mauro Acchione, Hyewon Kwon, Claudia M Jochheim, and William M Atkins. Impact of linker and conjugation chemistry on antigen binding, fc receptor binding and thermal stability of model antibody-drug conjugates. *MAbs*, 4(3):362–372, 2012.

Darinka G Ackova, Katarina Smilkov, and Emilija Janevik-Ivanovska. Physicochemical evaluation of lyophilized formulation of p-scn-bn-dota-and p-scn-bn-dtpa-rituximab for nhl radio immunotherapy. *Iranian journal of pharmaceutical research: IJPR*, 15(3):295, 2016.

Sunjida Ahmed, Azore-Dee Bradshaw, Shweta Gera, Zahidunnabi M Dewan, and Ruliang Xu. The tgf-β/smad4 signaling pathway in pancreatic carcinogenesis and its clinical significance. *Journal of clinical medicine*, 6(1):5, 2017.

Michaela Aichler, Christopher Seiler, Monica Tost, Jens Siveke, Pawel K Mazur, Da Silva-Buttkus, Detlef K Bartsch, Peter Langer, Sara Chiblak, Anna Dürr, et al. Origin of pancreatic ductal adenocarcinoma from atypical flat lesions: a comparative study in transgenic mice and human tissues. *The Journal of pathology*, 226(5): 723–734, 2012.

Misao Akishiba, Toshihide Takeuchi, Yoshimasa Kawaguchi, Kentarou Sakamoto, Hao-Hsin Yu, Ikuhiko Nakase, Tomoka Takatani-Nakase, Fatemeh Madani, Astrid Gräslund, and Shiroh Futaki. Cytosolic antibody delivery by lipid-sensitive endosomolytic peptide. *Nature chemistry*, 9(8):751, 2017.

Dalal Aldeghaither, Brandon G Smaglo, and Louis M Weiner. Beyond peptides and mabs—current status and future perspectives for biotherapeutics with novel constructs. *The Journal of Clinical Pharmacology*, 55(S3), 2015.

Margaret Ashcroft and Karen H Vousden. Regulation of p53 stability. *Oncogene*, 18 (53), 1999.

The Human Protein Atlas. Expression of tp53 in pancreatic cancer, 2017. URL `https://www.proteinatlas.org/ENSG00000141510-TP53/pathology/tissue/pancreatic+cancer`.

Gregory D Ayers, Eliot T McKinley, Ping Zhao, Jordan M Fritz, Rebecca E Metry, Brenton C Deal, Katrina M Adlerz, Robert J Coffey, and H Charles Manning. Volume of preclinical xenograft tumors is more accurately assessed by ultrasound

imaging than manual caliper measurements. *Journal of Ultrasound in Medicine*, 29(6):891–901, 2010.

Peter Bailey, David K Chang, Katia Nones, Amber L Johns, Ann-Marie Patch, Marie-Claude Gingras, David K Miller, Angelika N Christ, Tim JC Bruxner, Michael C Quinn, et al. Genomic analyses identify molecular subtypes of pancreatic cancer. *Nature*, 2016.

Michael L Baker, Scott E Seeley, Reetesh Pai, Arief A Suriawinata, Mari Mino-Kenudson, Giuseppe Zamboni, Günter Klöppel, and Daniel S Longnecker. Invasive mucinous cystic neoplasms of the pancreas. *Experimental and molecular pathology*, 93(3):345–349, 2012.

Suzanne J Baker, Eric R Fearon, Janice M Nigro, Stanley R Hamilton, Ann C Preisinger, Milburn J Jessup, Peter VanTuinen, David H Ledbetter, David F Barker, Yusuke Nakamura, et al. Chromosome 17 deletions and p53 gene mutations in colorectal carcinomas. *Science*, 244(4901):217–221, 1989.

Judit P Banáth and Peggy L Olive. Expression of phosphorylated histone h2ax as a surrogate of cell killing by drugs that create dna double-strand breaks. *Cancer Research*, 63(15):4347–4350, 2003.

Yaacov Barak, Tamar Juven, Rebecca Haffner, and Moshe Oren. mdm2 expression is induced by wild type p53 activity. *The EMBO journal*, 12(2):461, 1993.

Kevin J Barnum and Matthew J O'Connell. Cell cycle regulation by checkpoints. *Cell Cycle Control: Mechanisms and Protocols*, pages 29–40, 2014.

Michal Bassani-Sternberg, Sune Pletscher-Frankild, Lars Juhl Jensen, and Matthias Mann. Mass spectrometry of human leukocyte antigen class i peptidomes reveals strong effects of protein abundance and turnover on antigen presentation. *Molecular & Cellular Proteomics*, 14(3):658–673, 2015.

Chérine Bechara and Sandrine Sagan. Cell-penetrating peptides: 20 years later, where do we stand? *FEBS letters*, 587(12):1693–1702, 2013.

Andrew E Becker, Yasmin G Hernandez, Harold Frucht, and Aimee L Lucas. Pancreatic ductal adenocarcinoma: risk factors, screening, and early detection. *World J Gastroenterol*, 20(32):11182–11198, 2014.

Rachel Beckerman and Carol Prives. Transcriptional regulation by p53. *Cold Spring Harbor perspectives in biology*, 2(8):a000935, 2010.

Qiwen Ben, Maojin Xu, Xiaoyan Ning, Jun Liu, Shangyou Hong, Wen Huang, Huagao Zhang, and Zhaoshen Li. Diabetes mellitus and risk of pancreatic cancer: a meta-analysis of cohort studies. *European journal of cancer*, 47(13):1928–1937, 2011.

Carol Bernstein, Anil R Prasad, Valentine Nfonsam, and Harris Bernstein. Dna damage, dna repair and cancer. In *New Research Directions in DNA Repair*. InTech, 2013.

Sibaprasad Bhattacharyya and Manish Dixit. Metallic radionuclides in the development of diagnostic and therapeutic radiopharmaceuticals. *Dalton Transactions*, 40 (23):6112–6128, 2011.

Alessandro Bittoni, Matteo Santoni, Andrea Lanese, Chiara Pellei, Kalliopi Andrikou, and Cascinu Stefano. Neoadjuvant therapy in pancreatic cancer: an emerging strategy. *Gastroenterology research and practice*, 2014, 2014.

Mikhail V Blagosklonny. Loss of function and p53 protein stabilization. *Oncogene*, 15(16), 1997.

Paul J Bohdiewicz. Indium-111 satumomab pendetide: the first fda-approved monoclonal antibody for tumor imaging. *Journal of nuclear medicine technology*, 26(3): 155–163, 1998.

Cristina Bosetti, Valentina Rosato, Donghui Li, Debra Silverman, Gloria M Petersen, Paige M Bracci, Rachel E Neale, Joshua Muscat, Kristin Anderson, Steven Gallinger, et al. Diabetes, antidiabetic medications, and pancreatic cancer risk: an analysis from the international pancreatic cancer case-control consortium. *Annals of oncology*, 25(10):2065–2072, 2014.

Fred T Bosman, Fatima Carneiro, Ralph H Hruban, Neil D Theise, et al. *WHO classification of tumours of the digestive system.* Number 4. World Health Organization, 2010.

Kirsten Bouchelouche, Peter L Choyke, and Jacek Capala. Prostate specific membrane antigen—a target for imaging and therapy with radionuclides. *Discovery medicine*, 9(44):55, 2010.

Mark T Boyd and Nikolina Vlatkovic. p53: a molecular marker for the detection of cancer. *Expert opinion on medical diagnostics*, 2(9):1013–1024, 2008.

Lodewijk AA Brosens and Johan G Offerhaus. Molecular pathology of pancreatic cancer precursor lesions. In *Molecular Genetics of Pancreatic Cancer*, pages 27–47. Springer, 2013.

Lodewijk AA Brosens, Wenzel M Hackeng, Johan G Offerhaus, Ralph H Hruban, and Laura D Wood. Pancreatic adenocarcinoma pathology: changing "landscape". *Journal of gastrointestinal oncology*, 6(4):358, 2015.

Kieran Brune, Tadayoshi Abe, Marcia Canto, Lauren O'Malley, Alison P Klein, Anirban Maitra, Volkan N Adsay, Elliot K Fishman, John L Cameron, Charles J Yeo, et al. Multifocal neoplastic precursor lesions associated with lobular atrophy of the pancreas in patients having a strong family history of pancreatic cancer. *The American journal of surgical pathology*, 30(9):1067, 2006.

Kristin E Bullok, Mary Dyszlewski, Julie L Prior, Christina M Pica, Vijay Sharma, and David Piwnica-Worms. Characterization of novel histidine-tagged tat-peptide complexes dual-labeled with 99mtc-tricarbonyl and fluorescein for scintigraphy and fluorescence microscopy. *Bioconjugate chemistry*, 13(6):1226–1237, 2002.

Jorge A Carrasquillo, Kenneth A Krohn, Paul Beaumier, Robert W McGuffin, Joseph P Brown, Karl E Hellström, Ingegerd Hellström, and Steven M Larson. Diagnosis of and therapy for solid tumors with radiolabeled antibodies and immune fragments. *Cancer treatment reports*, 68(1):317–328, 1984.

Ilaria Casari and Marco Falasca. Diet and pancreatic cancer prevention. *Cancers*, 7 (4):2309–2317, 2015.

Raphael Ceccaldi, Beatrice Rondinelli, and Alan D D'Andrea. Repair pathway choices and consequences at the double-strand break. *Trends in cell biology*, 26(1):52–64, 2016.

Ratna Chakrabarti, Dwane E Wylie, and Sheldon M Schuster. Transfer of monoclonal antibodies into mammalian cells by electroporation. *Journal of Biological Chemistry*, 264(26):15494–15500, 1989.

Aaron Y Chang, Ron S Gejman, Elliott J Brea, Claire Y Oh, Melissa D Mathias, Dmitry Pankov, Emily Casey, Tao Dao, and David A Scheinberg. Opportunities and challenges for tcr mimic antibodies in cancer therapy. *Expert opinion on biological therapy*, 16(8):979–987, 2016.

John C Chang and Madappa Kundranda. Novel diagnostic and predictive biomarkers in pancreatic adenocarcinoma. *International journal of molecular sciences*, 18(3): 667, 2017.

Zhe Chang, Huaiqiang Ju, Jianhua Ling, Zhuonan Zhuang, Zhongkui Li, Huamin Wang, Jason B Fleming, James W Freeman, Dihua Yu, Peng Huang, et al. Cooperativity of oncogenic k-ras and downregulated p16/ink4a in human pancreatic tumorigenesis. *PloS one*, 9(7):e101452, 2014.

Suresh T Chari, Kimberly Kelly, Michael A Hollingsworth, Sarah P Thayer, David A Ahlquist, Dana K Andersen, Surinder K Batra, Teresa A Brentnall, Marcia Canto, Deborah F Cleeter, et al. Early detection of sporadic pancreatic cancer: summative review. *Pancreas*, 44(5):693, 2015.

Fei Chen, Xueqian Zhuang, Liangyu Lin, Pengfei Yu, Ying Wang, Yufang Shi, Guohong Hu, and Yu Sun. New horizons in tumor microenvironment biology: challenges and opportunities. *BMC medicine*, 13(1):45, 2015.

Kai Chen and Xiaoyuan Chen. Design and development of molecular imaging probes. *Current topics in medicinal chemistry*, 10(12):1227–1236, 2010.

Yunje Cho, Svetlana Gorina, Philip D Jeffrey, and Nikola P Pavletich. Crystal structure of a p53 tumor suppressor-dna complex: understanding tumorigenic mutations. *Science*, pages 346–355, 1994.

Angela Chou, Nicola Waddell, Mark J Cowley, Anthony J Gill, David K Chang, Ann-Marie Patch, Katia Nones, Jianmin Wu, Mark Pinese, Amber L Johns, et al. Clinical and molecular characterization of her2 amplified-pancreatic cancer. *Genome medicine*, 5(8):78, 2013.

Thomas DY Chung, David B Terry, and Layton H Smith. In vitro and in vivo assessment of adme and pk properties during lead selection and lead optimization–guidelines, benchmarks and rules of thumb. *Assay Guidance Manual*, 2015.

Angel Cid-Arregui and Victoria Juarez. Perspectives in the treatment of pancreatic adenocarcinoma. *World Journal of Gastroenterology: WJG*, 21(31):9297, 2015.

Eric A Collisson, Christy L Trejo, Jillian M Silva, Shenda Gu, James E Korkola, Laura M Heiser, Roch-Philippe Charles, Brian A Rabinovich, Byron Hann, David Dankort, et al. A central role for raf→ mek→ erk signaling in the genesis of pancreatic ductal adenocarcinoma. *Cancer discovery*, 2(8):685–693, 2012.

Anna Comel, Giovanni Sorrentino, Valeria Capaci, and Giannino Del Sal. The cytoplasmic side of p53's oncosuppressive activities. *FEBS letters*, 588(16):2600–2609, 2014.

Thierry Conroy, Françoise Desseigne, Marc Ychou, Olivier Bouché, Rosine Guimbaud, Yves Bécouarn, Antoine Adenis, Jean-Luc Raoul, Sophie Gourgou-Bourgade, Christelle de la Fouchardière, et al. Folfirinox versus gemcitabine for metastatic pancreatic cancer. *New England Journal of Medicine*, 364(19):1817–1825, 2011.

Maggie S Cooper, Michelle T Ma, Kavitha Sunassee, Karen P Shaw, Jennifer D Williams, Rowena L Paul, Paul S Donnelly, and Philip J Blower. Comparison of 64cu-complexing bifunctional chelators for radioimmunoconjugation: labeling efficiency, specific activity, and in vitro/in vivo stability. *Bioconjugate chemistry*, 23(5):1029–1039, 2012.

Dana M Copolovici, Kent Langel, Elo Eriste, and Ulo Langel. Cell-penetrating peptides: design, synthesis, and applications. *ACS nano*, 8(3):1972–1994, 2014.

Bart Cornelissen, Meiduo Hu, Kristin McLarty, Dan Costantini, and Raymond M Reilly. Cellular penetration and nuclear importation properties of 111 in-labeled and 123 i-labeled hiv-1 tat peptide immunoconjugates in bt-474 human breast cancer cells. *Nuclear medicine and biology*, 34(1):37–46, 2007.

Bart Cornelissen, Veerle Kersemans, Kristin McLarty, Lara Tran, and Raymond M Reilly. 111in-labeled immunoconjugates (ics) bispecific for the epidermal growth

factor receptor (egfr) and cyclin-dependent kinase inhibitor, p27kip1. *Cancer Biotherapy and Radiopharmaceuticals*, 24(2):163–173, 2009.

Bart Cornelissen, Veerle Kersemans, Sonali Darbar, James Thompson, Ketan Shah, Kate Sleeth, Mark A Hill, and Katherine A Vallis. Imaging dna damage in vivo using γh2ax-targeted immunoconjugates. *Cancer research*, 71(13):4539–4549, 2011.

Bart Cornelissen, Sonali Darbar, Veerle Kersemans, Danny Allen, Nadia Falzone, Jody Barbeau, Sean Smart, and Katherine A Vallis. Amplification of dna damage by a γh2ax-targeted radiopharmaceutical. *Nuclear medicine and biology*, 39(8): 1142–1151, 2012.

Bart Cornelissen, Sarah Able, Christiana Kartsonaki, Veerle Kersemans, Danny Allen, Federica Cavallo, Jean-Baptiste Cazier, Manuela Iezzi, James Knight, Ruth Muschel, et al. Imaging dna damage allows detection of preneoplasia in the balb-neut model of breast cancer. *Journal of Nuclear Medicine*, 55(12):2026–2031, 2014.

Danny L Costantini, Conrad Chan, Zhongli Cai, Katherine A Vallis, and Raymond M Reilly. 111in-labeled trastuzumab (herceptin) modified with nuclear localization sequences (nls): an auger electron-emitting radiotherapeutic agent for her2/neu-amplified breast cancer. *Journal of Nuclear Medicine*, 48(8):1357–1368, 2007.

Botond Cseh, Eszter Doma, and Manuela Baccarini. "raf" neighborhood: Protein–protein interaction in the raf/mek/erk pathway. *FEBS letters*, 588(15):2398–2406, 2014.

Chao Dai and Wei Gu. p53 post-translational modification: deregulated in tumorigenesis. *Trends in molecular medicine*, 16(11):528–536, 2010.

Tao Dao, Su Yan, Nicholas Veomett, Dmitry Pankov, Liang Zhou, Tatyana Korontsvit, Andrew Scott, Joseph Whitten, Peter Maslak, Emily Casey, et al. Targeting the intracellular wt1 oncogene product with a therapeutic human antibody. *Science translational medicine*, 5(176):176ra33–176ra33, 2013.

Marion De Jong and Theodosia Maina. Of mice and humans: are they the same? implications in cancer translational research. *Journal of Nuclear Medicine*, 51(4): 501–504, 2010.

Marion De Jong, Jeroen Essers, and Wytske M Van Weerden. Imaging preclinical tumour models: improving translational power. *Nature Reviews Cancer*, 14(7): 481–493, 2014.

Roeland F De Wilde, Ralph H Hruban, Anirban Maitra, and Johan GA Offerhaus. Reporting precursors to invasive pancreatic cancer: pancreatic intraepithelial neoplasia, intraductal neoplasms and mucinous cystic neoplasm. *Diagnostic Histopathology*, 18(1):17–30, 2012.

Dominique Delbeke and Wright C Pinson. Pancreatic tumors: role of imaging in the diagnosis, staging, and treatment. *Journal of Hepato-Biliary-Pancreatic Sciences*, 11(1):4–10, 2004.

Albert B DeLeo. p53-based immunotherapy of cancer. *Cancer Drug Resistance*, pages 491–505, 2006.

Albert B DeLeo and Theresa L Whiteside. Development of multi-epitope vaccines targeting wild-typesequence p53 peptides. *Expert review of vaccines*, 7(7):1031–1040, 2008.

Daniele Derossi, Alain H Joliot, Gerard Chassaing, and Alain Prochiantz. The third helix of the antennapedia homeodomain translocates through biological membranes. *Journal of Biological Chemistry*, 269(14):10444–10450, 1994.

Daniele Derossi, Sophie Calvet, Alain Trembleau, Alié Brunissen, Gérard Chassaing, and Alain Prochiantz. Cell internalization of the third helix of the antennapedia homeodomain is receptor-independent. *Journal of Biological Chemistry*, 271(30): 18188–18193, 1996.

Puneet Dhar, Shrivardhan Kalghatgi, and Vivek Saraf. Pancreatic cancer in chronic pancreatitis. *Indian journal of surgical oncology*, 6(1):57–62, 2015.

Sameer A Dhayat, Philip Mirgorod, Christina Lenschow, Norbert Senninger, Christoph Anthoni, and Thorsten Vowinkel. Challenges in pancreatic adenocarcinoma surgery-national survey and current practice guidelines. *PloS one*, 12(3): e0173374, 2017.

Amardeep S Dhillon, Suzanne Hagan, Oliver Rath, and Walter Kolch. Map kinase signalling pathways in cancer. *Oncogene*, 26(22):3279, 2007.

Eli CF Dijkers, Jos GW Kosterink, Anna P Rademaker, Lars R Perk, Guus AMS van Dongen, Joost Bart, Johan R de Jong, Elisabeth GE de Vries, and Marjolijn N Lub-

de Hooge. Development and characterization of clinical-grade 89zr-trastuzumab for her2/neu immunopet imaging. *Journal of Nuclear Medicine*, 50(6):974–981, 2009.

Wolfgang G Dippold, Gilbert Jay, Albert B DeLeo, George Khoury, and Lloyd J Old. p53 transformation-related protein: detection by monoclonal antibody in mouse and human cells. *Proceedings of the National Academy of Sciences*, 78(3): 1695–1699, 1981.

Marius Distler, Daniela Aust, Jürgen Weitz, Christian Pilarsky, and Robert Grützmann. Precursor lesions for sporadic pancreatic cancer: Panin, ipmn, and mcn. *BioMed research international*, 2014, 2014.

Dirk Dittmer, Sibani Pati, Gerard Zambetti, Shelley Chu, Angelika K Teresky, Mary Moore, Cathy Finlay, and Arnold J Levine. Gain of function mutations in p53. *Nature genetics*, 4(1):42–46, 1993.

Michael Doubrovin, Vladimir Ponomarev, Tatiana Beresten, Julius Balatoni, William Bornmann, Ronald Finn, John Humm, Steven Larson, Michel Sadelain, Ronald Blasberg, et al. Imaging transcriptional regulation of p53-dependent genes with positron emission tomography in vivo. *Proceedings of the National Academy of Sciences*, 98(16):9300–9305, 2001.

Leonid Dubrovsky, Tao Dao, Ron S Gejman, Elliott J Brea, Aaron Y Chang, Claire Y Oh, Emily Casey, Dmitry Pankov, and David A Scheinberg. T cell receptor mimic antibodies for cancer therapy. *Oncoimmunology*, 5(1):e1049803, 2016.

Vjekoslav Dulić, Georges-Edouard Beney, Guillaume Frebourg, Linda F Drullinger,

and Gretchen H Stein. Uncoupling between phenotypic senescence and cell cycle arrest in aging p21-deficient fibroblasts. *Molecular and cellular biology*, 20(18): 6741–6754, 2000.

Vyacheslav I Egorov, Roman V Petrov, Elena N Solodinina, Gregory G Karmazanovsky, Natalia S Starostina, and Natalia A Kuruschkina. Computed tomography-based diagnostics might be insufficient in the determination of pancreatic cancer unresectability. *World journal of gastrointestinal surgery*, 5(4):83, 2013.

Paul Ehrlich. *Beiträge für Theorie und Praxis der histologischen Färbung*. Leipzig., 1878.

Ayman El-Sayed, Shiroh Futaki, and Hideyoshi Harashima. Delivery of macromolecules using arginine-rich cell-penetrating peptides: ways to overcome endosomal entrapment. *The AAPS journal*, 11(1):13–22, 2009.

Harold Ellis. Anatomy of the pancreas and the spleen. *Surgery (Oxford)*, 31(6): 263–266, 2013.

Anna Elmquist, Maria Lindgren, Tamas Bartfai, and Ülo Langel. Ve-cadherin-derived cell-penetrating peptide, pvec, with carrier functions. *Experimental cell research*, 269(2):237–244, 2001.

Christopher G England, Reinier Hernandez, Savo Bou Zein Eddine, and Weibo Cai. Molecular imaging of pancreatic cancer with antibodies. *Molecular pharmaceutics*, 13(1):8–24, 2015.

Alfredo Erazo-Oliveras, Nandhini Muthukrishnan, Ryan Baker, Ting-Yi Wang, and Jean-Philippe Pellois. Improving the endosomal escape of cell-penetrating peptides and their cargos: strategies and challenges. *Pharmaceuticals*, 5(11):1177–1209, 2012.

Joaquin M Espinosa and Beverly M Emerson. Transcriptional regulation by p53 through intrinsic dna/chromatin binding and site-directed cofactor recruitment. *Molecular cell*, 8(1):57–69, 2001.

Jose M Esteban, Jeffrey Schlom, Otto A Gansow, Robert W Atcher, Martin W Brechbiel, Diane E Simpson, and David Colcher. New method for the chelation of indium-111 to monoclonal antibodies: biodistribution and imaging of athymic mice bearing human colon carcinoma xenografts. *J Nucl Med*, 28(5):861–70, 1987.

Elena Farmaki, Ioulia Chatzistamou, Panagiotis Bourlis, Eleni Santoukou, George Trimis, Athanasios G Papavassiliou, and Hippokratis Kiaris. Selection of p53-deficient stromal cells in the tumor microenvironment. *Genes & cancer*, 3(9-10): 592–598, 2012.

Rashid A Fawwaz, Theodore ST Wang, Alyson Estabrook, Joel M Rosen, Mark A Hardy, Philip O Alderson, Suresh C Srivastava, Powell Richards, and Soldano Ferrone. Immunoreactivity and biodistribution of indium-111-labeled monoclonal antibody to a human high molecular weight-melanoma associated antigen. *Journal of nuclear medicine*, 26(5):488–492, 1985.

Antonio Fittipaldi and Mauro Giacca. Transcellular protein transduction using the tat protein of hiv-1. *Advanced drug delivery reviews*, 57(4):597–608, 2005.

Antonio Fittipaldi, Aldo Ferrari, Monica Zoppé, Caterina Arcangeli, Vittorio Pellegrini, Fabio Beltram, and Mauro Giacca. Cell membrane lipid rafts mediate caveolar endocytosis of hiv-1 tat fusion proteins. *Journal of Biological Chemistry*, 278(36):34141–34149, 2003.

Emmy DG Fleuren, Yvonne MH Versleijen-Jonkers, Sandra Heskamp, Carla ML van Herpen, Wim JG Oyen, Winette TA van der Graaf, and Otto C Boerman. Theranostic applications of antibodies in oncology. *Molecular oncology*, 8(4):799–812, 2014.

Josep V Forment and Stephen P Jackson. A flow-cytometry-based method to simplify the analysis and quantification of protein association to chromatin in mammalian cells. *Nature protocols*, 10(9):1297, 2015.

Catherine A Foss, James J Fox, Georg Feldmann, Anirban Maitra, Christine Iacobuzio-Donohue, Scott E Kern, Ralph Hruban, and Martin G Pomper. Radiolabeled anti-claudin 4 and anti-prostate stem cell antigen: initial imaging in experimental models of pancreatic cancer. *Molecular imaging*, 6(2):7290–2007, 2007.

John V Frangioni. New technologies for human cancer imaging. *Journal of clinical oncology*, 26(24):4012–4021, 2008.

Alan D Frankel and Carl O Pabo. Cellular uptake of the tat protein from human immunodeficiency virus. *Cell*, 55(6):1189–1193, 1988.

Amanda C Freise and Anna M Wu. In vivo imaging with antibodies and engineered fragments. *Molecular immunology*, 67(2):142–152, 2015.

Kristopher K Frese and David A Tuveson. Maximizing mouse cancer models. *Nature Reviews Cancer*, 7(9):654–658, 2007.

Barbara J Fueger, Johannes Czernin, Isabel Hildebrandt, Chris Tran, Benjamin S Halpern, David Stout, Michael E Phelps, and Wolfgang A Weber. Impact of animal handling on the results of 18f-fdg pet studies in mice. *Journal of Nuclear Medicine*, 47(6):999–1006, 2006.

Sara Gandini, Edoardo Botteri, Simona Iodice, Mathieu Boniol, Albert B Lowenfels, Patrick Maisonneuve, and Peter Boyle. Tobacco smoking and cancer: A meta-analysis. *International journal of cancer*, 122(1):155–164, 2008.

Michael P Gillmeister, Michael J Betenbaugh, and Paul S Fishman. Cellular trafficking and photochemical internalization of cell penetrating peptide linked cargo proteins: a dual fluorescent labeling study. *Bioconjugate chemistry*, 22(4):556–566, 2011.

Luciana E Giono and James J Manfredi. The p53 tumor suppressor participates in multiple cell cycle checkpoints. *Journal of cellular physiology*, 209(1):13–20, 2006.

Mark D Girgis, Vania Kenanova, Tove Olafsen, Katelyn E McCabe, Anna M Wu, and James S Tomlinson. Anti-ca19-9 diabody as a pet imaging probe for pancreas cancer. *Journal of Surgical Research*, 170(2):169–178, 2011.

Walter L Goh, Min Yen Lee, Thomas L Joseph, Soo Tng Quah, Christopher J Brown, Chandra Verma, Sydney Brenner, Farid J Ghadessy, and Yin Nah Teo. Molecular rotors as conditionally fluorescent labels for rapid detection of biomolecular interactions. *Journal of the American Chemical Society*, 136(17):6159–6162, 2014.

Alfred L Goldberg, Paolo Cascio, Tomo Saric, and Kenneth L Rock. The importance of the proteasome and subsequent proteolytic steps in the generation of antigenic peptides. *Molecular immunology*, 39(3):147–164, 2002.

Marlies C Goorden, Frans van der Have, Rob Kreuger, Ruud M Ramakers, Brendan Vastenhouw, Peter JH Burbach, Jan Booij, Carla FM Molthoff, and Freek J Beekman. Vector: a preclinical imaging system for simultaneous submillimeter spect and pet. *Journal of Nuclear Medicine*, 54(2):306–312, 2013.

Aarthi Gopinathan, Jennifer P Morton, Duncan I Jodrell, and Owen J Sansom. Gemms as preclinical models for testing pancreatic cancer therapies. *Disease models & mechanisms*, 8(10):1185–1200, 2015.

Julia B Greer and David C Whitcomb. Inflammation and pancreatic cancer: an evidence-based review. *Current opinion in pharmacology*, 9(4):411–418, 2009.

Lukasz Filip Grochola, Helge Taubert, Thomas Greither, Umesh Bhanot, Andrej Udelnow, and Peter Würl. Elevated transcript levels from the mdm2 p1 promoter and low p53 transcript levels are associated with poor prognosis in human pancreatic ductal adenocarcinoma. *Pancreas*, 40(2):265–270, 2011.

Carmen Guerra and Mariano Barbacid. Genetically engineered mouse models of pancreatic adenocarcinoma. *Molecular oncology*, 7(2):232–247, 2013.

Zhengrong Guo, Huanyan Peng, Jiwen Kang, and Dianxing Sun. Cell-penetrating peptides: Possible transduction mechanisms and therapeutic applications. *Biomedical reports*, 4(5):528–534, 2016.

Phillip L Hagan, Samuel E Halpern, Robert O Dillman, Daniel L Shawler, Duane E Johnson, Agnes Chen, Lakshmy Krishnan, James Frincke, Richard M Bartholomew, Gary S David, et al. Tumor size: effect on monoclonal antibody uptake in tumor models. *Journal of nuclear medicine*, 27(3):422–427, 1986.

Stephan Hailfinger, Maike Jaworski, Philip Marx-Stoelting, Ines Wanke, and Michael Schwarz. Regulation of p53 stability in p53 mutated human and mouse hepatoma cells. *International journal of cancer*, 120(7):1459–1464, 2007.

Cornelia Halin and Dario Neri. Antibody-based targeting of angiogenesis. *Critical Reviews™ in Therapeutic Drug Carrier Systems*, 18(3), 2001.

Susan R Hall, Linda E Campbell, and David W Meek. Phosphorylation of p53 at the casein kinase ii site selectively regulates p53-dependent transcriptional repression but not transactivation. *Nucleic acids research*, 24(6):1119–1126, 1996.

Garth Hamilton, Aswin G Abraham, Jennifer Morton, Oliver Sampson, Dafni E Pefani, Svetlana Khoronenkova, Anna Grawenda, Angelos Papaspyropoulos, Nigel Jamieson, Colin McKay, et al. Akt regulates npm dependent arf localization and p53mut stability in tumors. *Oncotarget*, 5(15):6142, 2014.

Douglas Hanahan and Robert A Weinberg. The hallmarks of cancer. *cell*, 100(1): 57–70, 2000.

Douglas Hanahan and Robert A Weinberg. Hallmarks of cancer: the next generation. *cell*, 144(5):646–674, 2011.

Deepak Hariharan, Abdul Saied, and Hemant M Kocher. Analysis of mortality rates for pancreatic cancer across the world. *Hpb*, 10(1):58–62, 2008.

Raffit Hassan, Chuanchu Wu, Martin W Brechbiel, Inger Margulies, Robert J Kreitman, and Ira Pastan. 111indium-labeled monoclonal antibody k1: Biodistribution study in nude mice bearing a human carcinoma xenograft expressing mesothelin. *International journal of cancer*, 80(4):559–563, 1999.

Beate Haugk. Pancreatic intraepithelial neoplasia–can we detect early pancreatic cancer? *Histopathology*, 57(4):503–514, 2010.

Ygal Haupt, Ruth Maya, Anat Kazaz, and Moshe Oren. Mdm2 promotes the rapid degradation of p53. *nature*, 387(6630):296, 1997.

Jay P Heiken. Carcinoma of the pancreas: detection and staging using ct and mri. *Cancer Imaging*, 2(1):19, 2015.

Frederic Heitz, May C Morris, and Gilles Divita. Twenty years of cell-penetrating peptides: from molecular mechanisms to therapeutics. *British journal of pharmacology*, 157(2):195–206, 2009.

Thomas Helleday, Saeed Eshtad, and Serena Nik-Zainal. Mechanisms underlying mutational signatures in human cancers. *Nature reviews. Genetics*, 15(9):585, 2014.

Carola Heneweer, Jason P Holland, Vadim Divilov, Sean Carlin, and Jason S Lewis. Magnitude of enhanced permeability and retention effect in tumors with different phenotypes: 89zr-albumin as a model system. *Journal of Nuclear Medicine*, 52(4): 625–633, 2011.

Jonathan A Hensel, Vinayak Khattar, Carnellia Lee, Gene P Siegal, and Selvarangan Ponnazhagan. Location of tumor affects local and distant immune cell type and number. *Immunity, inflammation and disease*, 5(1):85–94, 2017.

Heiko Hermeking, Christoph Lengauer, Kornelia Polyak, Tong-Chuan He, Lin Zhang, Sam Thiagalingam, Kenneth W Kinzler, and Bert Vogelstein. 14-3-3$\sigma$is a p53-regulated inhibitor of g2/m progression. *Molecular cell*, 1(1):3–11, 1997.

Inmaculada Hernńdez-Muñoz, Anouchka Skoudy, Francisco X Real, and Pilar Navarro. Pancreatic ductal adenocarcinoma: cellular origin, signaling pathways and stroma contribution. *Pancreatology*, 8(4-5):462–469, 2008.

Aram F Hezel, Alec C Kimmelman, Ben Z Stanger, Nabeel Bardeesy, and Ronald A DePinho. Genetics and biology of pancreatic ductal adenocarcinoma. *Genes & development*, 20(10):1218–1249, 2006.

Rodney J Hicks and Michael S Hofman. Is there still a role for spect–ct in oncology in the pet–ct era? *Nature reviews Clinical oncology*, 9(12):712–720, 2012.

Manuel Hidalgo, Stefano Cascinu, Jörg Kleeff, Roberto Labianca, J-Matthias Löhr, John Neoptolemos, Francisco X Real, Jean-Luc Van Laethem, and Volker Heinemann. Addressing the challenges of pancreatic cancer: future directions for improving outcomes. *Pancreatology*, 15(1):8–18, 2015.

Sunil R Hingorani, Lifu Wang, Asha S Multani, Chelsea Combs, Therese B Deramaudt, Ralph H Hruban, Anil K Rustgi, Sandy Chang, and David A Tuveson. Trp53r172h and krasg12d cooperate to promote chromosomal instability and widely metastatic pancreatic ductal adenocarcinoma in mice. *Cancer cell*, 7(5):469–483, 2005.

Khoo K Hoe, Chandra S Verma, and David P Lane. Drugging the p53 pathway: understanding the route to clinical efficacy. *Nature reviews. Drug discovery*, 13(3): 217, 2014.

Jason P Holland, Vadim Divilov, Neil H Bander, Peter M Smith-Jones, Steven M Larson, and Jason S Lewis. 89zr-dfo-j591 for immunopet of prostate-specific membrane antigen expression in vivo. *Journal of Nuclear Medicine*, 51(8):1293–1300, 2010.

Cheng W Hong and Qi Zeng. Tapping the treasure of intracellular oncotargets with immunotherapy. *FEBS letters*, 588(2):350–355, 2014.

Hao Hong, Jiangtao Sun, and Weibo Cai. Radionuclide-based cancer imaging targeting the carcinoembryonic antigen. *Biomarker insights*, 3:435, 2008.

Ralph H Hruban, Michael Goggins, Jennifer Parsons, and Scott E Kern. Progression model for pancreatic cancer. *Clinical cancer research*, 6(8):2969–2972, 2000.

Meiduo Hu, Paul Chen, Judy Wang, Conrad Chan, Deborah A Scollard, and Raymond M Reilly. Site-specific conjugation of hiv-1 tat peptides to igg: a potential route to construct radioimmunoconjugates for targeting intracellular and nuclear epitopes in cancer. *European journal of nuclear medicine and molecular imaging*, 33(3):301–310, 2006.

Meiduo Hu, Paul Chen, Judy Wang, Deborah A Scollard, Katherine A Vallis, and Raymond M Reilly. 123i-labeled hiv-1 tat peptide radioimmunoconjugates are imported into the nucleus of human breast cancer cells and functionally interact in vitro and in vivo with the cyclin-dependent kinase inhibitor, p21waf-1/cip-1. *European journal of nuclear medicine and molecular imaging*, 34(3):368–377, 2007.

Wenwei Hu, Zhaohui Feng, and Arnold J Levine. The regulation of multiple p53 stress responses is mediated through mdm2. *Genes & cancer*, 3(3-4):199–208, 2012.

Rachel Huxley, Alireza Ansary-Moghaddam, Amy Berrington De González, Federica Barzi, and Mark Woodward. Type-ii diabetes and pancreatic cancer: a meta-analysis of 36 studies. *British journal of cancer*, 92(11):2076, 2005.

Toshinori Ide, Yoshiaki Tsuji, Sadahiko Ishibashi, and Youji Mitsui. Reinitiation of host dna synthesis in senescent human diploid cells by infection with simian virus 40. *Experimental cell research*, 143(2):343–349, 1983.

Milena Ilic and Irena Ilic. Epidemiology of pancreatic cancer. *World journal of gastroenterology*, 22(44):9694, 2016.

John R Jeffers, Evan Parganas, Youngsoo Lee, Chunying Yang, JinLing Wang, Jennifer Brennan, Kirsteen H MacLean, Jiawen Han, Thomas Chittenden, James N Ihle, et al. Puma is an essential mediator of p53-dependent and-independent apoptotic pathways. *Cancer cell*, 4(4):321–328, 2003.

Claire Jenkinson, Julie Earl, Paula Ghaneh, Christopher Halloran, Alfredo Carrato, William Greenhalf, John Neoptolemos, and Eithne Costello. Biomarkers for early diagnosis of pancreatic cancer. *Expert review of gastroenterology & hepatology*, 9 (3):305–315, 2015.

Joon Jeong, Young N Park, Joon S Park, Dong-Sup Yoon, Hoon S Chi, and Byong R Kim. Clinical significance of p16 protein expression loss and aberrant p53 protein expression in pancreatic cancer. *Yonsei medical journal*, 46(4):519–525, 2005.

Priyanka Jha and Bijan Bijan. Pet/ct for pancreatic malignancy: potential and pitfalls. *Journal of nuclear medicine technology*, 43(2):92–97, 2015.

Chen-Yu Jiao, Diane Delaroche, Fabienne Burlina, Isabel D Alves, Gérard Chassaing, and Sandrine Sagan. Translocation and endocytosis for cell-penetrating peptide internalization. *Journal of Biological Chemistry*, 284(49):33957–33965, 2009.

Andreas C Joerger and Alan R Fersht. The tumor suppressor p53: from structures to drug discovery. *Cold Spring Harbor perspectives in biology*, 2(6):a000919, 2010.

Alain Joliot and Alain Prochiantz. Transduction peptides: from technology to physiology. *Nature cell biology*, 6(3):189–196, 2004.

Alain Joliot, Christine Pernelle, Hermine Deagostini-Bazin, and Alain Prochiantz. Antennapedia homeobox peptide regulates neural morphogenesis. *Proceedings of the National Academy of Sciences*, 88(5):1864–1868, 1991.

Siân Jones, Xiaosong Zhang, Donald W Parsons, Jimmy C Lin, Rebecca J Leary, Philipp Angenendt, Parminder Mankoo, Hannah Carter, Hirohiko Kamiyama, Antonio Jimeno, et al. Core signaling pathways in human pancreatic cancers revealed by global genomic analyses. *science*, 321(5897):1801–1806, 2008.

Stephen N Jones, Amy E Roe, Lawrence A Donehower, and Allan Bradley. Rescue of embryonic lethality in mdm2-deficient mice by absence of p53. *nature*, 378(6553): 206–208, 1995.

Reiji Kannagi. Carbohydrate antigen sialyl lewis a – its pathophysiological significance and induction mechanism in cancer progression. *Chang Gung medical journal*, 30(3):189, 2007.

Sukhwinder Kaur, Ganesh Venktaraman, Maneesh Jain, Shantibhusan Senapati, Pradeep K Garg, and Surinder K Batra. Recent trends in antibody-based oncologic imaging. *Cancer letters*, 315(2):97–111, 2012.

Margaret G Keane, Laura J Horsfall, Greta Rait, and Stephen P Pereira. Sociodemographic trends in the incidence of pancreatic and biliary tract cancer in uk primary care. *PloS one*, 9(9):e108498, 2014.

David J Kerr, Daniel G Haller, Cornelis JH van de Velde, and Michael Baumann. *Oxford textbook of oncology*. Oxford University Press, 2016.

Veerle Kersemans and Bart Cornelissen. Targeting the tumour: Cell penetrating peptides for molecular imaging and radiotherapy. *Pharmaceuticals*, 3(3):600–620, 2010.

Magdy M Khalil, Jordi L Tremoleda, Tamer B Bayomy, and Willy Gsell. Molecular spect imaging: an overview. *International journal of molecular imaging*, 2011, 2011.

Shannon Kidd, Erika Spaeth, Keri Watson, Jared Burks, Hongbo Lu, Ann Klopp, Michael Andreeff, and Frank C Marini. Origins of the tumor microenvironment: quantitative assessment of adipose-derived and bone marrow–derived stroma. *PloS one*, 7(2):e30563, 2012.

Tae K Kim and James H Eberwine. Mammalian cell transfection: the present and the future. *Analytical and bioanalytical chemistry*, 397(8):3173–3178, 2010.

Moritz F Kircher, Hedvig Hricak, and Steven M Larson. Molecular imaging for personalized cancer care. *Molecular oncology*, 6(2):182–195, 2012.

Malka Kitayner, Haim Rozenberg, Naama Kessler, Dov Rabinovich, Lihi Shaulov, Tali E Haran, and Zippora Shakked. Structural basis of dna recognition by p53 tetramers. *Molecular cell*, 22(6):741–753, 2006.

Jorg Kleeff, Murray Korc, Minoti Apte, Carlo La Vecchia, Colin D Johnson, Andrew V Biankin, Rachel E Neale, Margaret Tempero, David A Tuveson10, Ralph H Hruban11, et al. Pancreatic cancer. 2016.

Peter M Kloetzel. The proteasome and mhc class i antigen processing. *Biochimica et Biophysica Acta (BBA)-Molecular Cell Research*, 1695(1):225–233, 2004.

James C Knight, Caitríona Topping, Michael Mosley, Veerle Kersemans, Nadia Falzone, José M Fernández-Varea, and Bart Cornelissen. Pet imaging of dna damage using 89zr-labelled anti-γh2ax-tat immunoconjugates. *European journal of nuclear medicine and molecular imaging*, 42(11):1707–1717, 2015.

Scott M Knowles and Anna M Wu. Advances in immuno–positron emission tomography: antibodies for molecular imaging in oncology. *Journal of Clinical Oncology*, 30(31):3884–3892, 2012.

Hisataka Kobayashi, Rira Watanabe, and Peter L Choyke. Improving conventional enhanced permeability and retention (epr) effects; what is the appropriate target? *Theranostics*, 4(1):81, 2014.

Prasad R Konkalmatt, Defeng Deng, Stephanie Thomas, Michael T Wu, Craig D Logsdon, Brent A French, and Kimberly A Kelly. Plectin-1 targeted aav vector for the molecular imaging of pancreatic cancer. *Frontiers in oncology*, 3:84, 2013.

Grzegorz Korpanty, Juliet G Carbon, Paul A Grayburn, Jason B Fleming, and Rolf A Brekken. Monitoring response to anticancer therapy by targeting microbubbles to tumor vasculature. *Clinical Cancer Research*, 13(1):323–330, 2007.

Guenter J Krejs. Pancreatic cancer: epidemiology and risk factors. *Digestive diseases*, 28(2):355–358, 2010.

Gabby SF Krens, Herman P Spaink, and Ewa B Snaar-Jagalska. Functions of the mapk family in vertebrate-development. *FEBS letters*, 580(21):4984–4990, 2006.

Mie Kristensen, Henrik Franzyk, Mia Thorne Klausen, Anne Iversen, Jesper Søborg Bahnsen, Rikke Bjerring Skyggebjerg, Vito Foderà, and Hanne Mørck Nielsen. Penetratin-mediated transepithelial insulin permeation: Importance of cationic residues and ph for complexation and permeation. *The AAPS journal*, 17(5):1200–1209, 2015.

Kurt A Krummel, Crystal J Lee, Franck Toledo, and Geoffrey M Wahl. The c-terminal lysines fine-tune p53 stress responses in a mouse model but are not required for stability control or transactivation. *Proceedings of the National Academy of Sciences of the United States of America*, 102(29):10188–10193, 2005.

Paul F Laeseke, Ru Chen, Brooke R Jeffrey, Teresa A Brentnall, and Jürgen K Willmann. Combining in vitro diagnostics with in vivo imaging for earlier detection of pancreatic ductal adenocarcinoma: Challenges and solutions. *Radiology*, 277(3): 644–661, 2015.

Eszter Lakatos, Ali Salehi-Reyhani, Michael Barclay, Michael PH Stumpf, and David R Klug. Protein degradation rate is the dominant mechanism accounting for the differences in protein abundance of basal p53 in a human breast and colorectal cancer cell line. *PloS one*, 12(5):e0177336, 2017.

Nicholas D Lakin and Stephen P Jackson. Regulation of p53 in response to dna damage. *Oncogene*, 18(53), 1999.

David P Lane. p53, guardian of the genome. *Nature*, 358:15–16, 1992.

David P Lane and Lionel V Crawford. T antigen is bound to a host protein in sy40-transformed cells. *Nature*, 278(5701):261–263, 1979.

Gene A Lang, Tomoo Iwakuma, Young-Ah Suh, Geng Liu, Ashutosh V Rao, John M Parant, Yasmine A Valentin-Vega, Tamara Terzian, Lisa C Caldwell, Louise C Strong, et al. Gain of function of a p53 hot spot mutation in a mouse model of li-fraumeni syndrome. *Cell*, 119(6):861–872, 2004.

Nha Le, Malin Sund, Alessio Vinci, et al. Prognostic and predictive markers in pancreatic adenocarcinoma. *Digestive and Liver Disease*, 48(3):223–230, 2016.

Eun S Lee and Jeong M Lee. Imaging diagnosis of pancreatic cancer: a state-of-the-art review. *World journal of gastroenterology: WJG*, 20(24):7864, 2014.

Jae W Lee, Chad A Komar, Fee Bengsch, Kathleen Graham, and Gregory L Beatty. Genetically engineered mouse models of pancreatic cancer: The kpc model (lsl-krasg12d/+; lsl-trp53r172h/+; pdx-1-cre), its variants, and their application in immuno-oncology drug discovery. *Current protocols in pharmacology*, pages 14–39, 2016.

Ming T Lee, Wei C Hung, Fang Y Chen, and Huey W Huang. Many-body effect of antimicrobial peptides: on the correlation between lipid's spontaneous curvature and pore formation. *Biophysical journal*, 89(6):4006–4016, 2005.

Arnold J Levine and Moshe Oren. The first 30 years of p53: growing ever more complex. *Nature reviews. Cancer*, 9(10):749, 2009.

Demin Li, Carol Bentley, Amanda Anderson, Sarah Wiblin, Kirstie LS Cleary, Sofia Koustoulidou, Tasneem Hassanali, Jenna Yates, Jenny Greig, Marloes Olde Nordkamp, et al. Development of a t cell receptor mimic antibody against wild-type p53 for cancer immunotherapy. *Cancer research*, pages canres–3247, 2017.

Junan Li, Ming J Poi, and Ming-Daw Tsai. Regulatory mechanisms of tumor suppressor p16ink4a and their relevance to cancer. *Biochemistry*, 50(25):5566–5582, 2011.

Gao Ling, Åsa Persson, Berit Berne, Mathias Uhlén, Joakim Lundeberg, and Fredrik Ponten. Persistent p53 mutations in single cells from normal human skin. *The American journal of pathology*, 159(4):1247–1253, 2001.

Daniel IH Linzer, Warren Maltzman, and Arnold J Levine. The sv40 a gene product is required for the production of a 54,000 mw cellular tumor antigen. *Virology*, 98 (2):308–318, 1979.

Dong-ping Liu, Hoseok Song, and Yang Xu. A common gain of function of p53 cancer mutants in inducing genetic instability. *Oncogene*, 29(7):949, 2010.

Lefteris Livieratos. Basic principles of spect and pet imaging. In *Radionuclide and Hybrid Bone Imaging*, pages 345–359. Springer, 2012.

Craig D Logsdon and Weiqin Lu. The significance of ras activity in pancreatic cancer initiation. *International journal of biological sciences*, 12(3):338, 2016.

Jiang Long, Yuqing Zhang, Xianjun Yu, Jingxuan Yang, Drake G LeBrun, Changyi

Chen, Qizhi Yao, and Min Li. Overcoming drug resistance in pancreatic cancer. *Expert opinion on therapeutic targets*, 15(7):817–828, 2011a.

Jiang Long, Yuqing Zhang, Xianjun Yu, Jingxuan Yang, Drake G LeBrun, Changyi Chen, Qizhi Yao, and Min Li. Overcoming drug resistance in pancreatic cancer. *Expert opinion on therapeutic targets*, 15(7):817–828, 2011b.

Mathias Lundberg and Magnus Johansson. Positively charged dna-binding proteins cause apparent cell membrane translocation. *Biochemical and biophysical research communications*, 291(2):367–371, 2002.

Fatemeh Madani, Staffan Lindberg, Ülo Langel, Shiroh Futaki, and Astrid Gräslund. Mechanisms of cellular uptake of cell-penetrating peptides. *Journal of Biophysics*, 2011, 2011.

Harald J Maier, Thomas Wirth, and Hartmut Beug. Epithelial-mesenchymal transition in pancreatic carcinoma. *Cancers*, 2(4):2058–2083, 2010.

David A Mann and Alan D Frankel. Endocytosis and targeting of exogenous hiv-1 tat protein. *The EMBO journal*, 10(7):1733, 1991.

Natasha D Marchenko, Sonja Wolff, Susan Erster, Kerstin Becker, and Ute M Moll. Monoubiquitylation promotes mitochondrial p53 translocation. *The EMBO journal*, 26(4):923–934, 2007.

Edyta Marcon, Harshika Jain, Anandi Bhattacharya, Hongbo Guo, Sadhna Phanse, Shuye Pu, Gregory Byram, Ben C Collins, Evan Dowdell, Maria Fenner, et al.

Assessment of a method to characterize antibody selectivity and specificity for use in immunoprecipitation. *Nature methods*, 12(8):725–731, 2015.

Andrea LJ Marschall, André Frenzel, Thomas Schirrmann, Manuela Schüngel, and Stefan Dubel. Targeting antibodies to the cytoplasm. *MAbs*, 3(1):3–16, 2011.

Katsumi Matsuzaki, Shuji Yoneyama, Osamu Murase, and Koichiro Miyajima. Transbilayer transport of ions and lipids coupled with mastoparan x translocation. *Biochemistry*, 35(25):8450–8456, 1996.

Susan T Mayne, Mary C Playdon, and Cheryl L Rock. Diet, nutrition, and cancer: past, present and future. *Nature Reviews Clinical Oncology*, 13(8):504–515, 2016.

Satyajit Mayor and Richard E Pagano. Pathways of clathrin-independent endocytosis. *Nature reviews Molecular cell biology*, 8(8):603–612, 2007.

Kristin McLarty, Bart Cornelissen, Deborah A Scollard, Susan J Done, Kathy Chun, and Raymond M Reilly. Associations between the uptake of 111in-dtpa-trastuzumab, her2 density and response to trastuzumab (herceptin) in athymic mice bearing subcutaneous human tumour xenografts. *European journal of nuclear medicine and molecular imaging*, 36(1):81–93, 2009.

David W Meek. Tumour suppression by p53: a role for the dna damage response? *Nature reviews. Cancer*, 9(10):714, 2009.

Daniel Menendez, Alberto Inga, and Michael A Resnick. The expanding universe of p53 targets. *Nature reviews. Cancer*, 9(10):724, 2009.

Guido Middeler, Katharina Zerf, Siegfried Jenovai, Anja Thuelig, Mathias Tschoedrich-Rotter, Ulrich Kubitscheck, and Reiner Peters. The tumor suppressor p53 is subject to both nuclear import and export, and both are fast, energy-dependent and lectin-inhibited. *Oncogene*, 14(12):1407–1417, 1997.

Carol A Midgley and David P Lane. p53 protein stability in tumour cells is not determined by mutation but is dependent on mdm2 binding. *Oncogene*, 15(10), 1997.

Shallu Midha, Saurabh Chawla, and Pramod K Garg. Modifiable and non-modifiable risk factors for pancreatic cancer: A review. *Cancer letters*, 381(1):269–277, 2016.

Francesca Milletti. Cell-penetrating peptides: classes, origin, and current landscape. *Drug discovery today*, 17(15):850–860, 2012.

Diane M Milne, David G Campbell, Barry F Caudwell, and David W Meek. Phosphorylation of the tumor suppressor protein p53 by mitogen-activated protein kinases. *Journal of Biological Chemistry*, 269(12):9253–9260, 1994.

Abhijit Mishra, Ghee H Lai, Nathan W Schmidt, Victor Z Sun, April R Rodriguez, Rong Tong, Li Tang, Jianjun Cheng, Timothy J Deming, Daniel T Kamei, et al. Translocation of hiv tat peptide and analogues induced by multiplexed membrane and cytoskeletal interactions. *Proceedings of the National Academy of Sciences*, 108 (41):16883–16888, 2011.

Ripen Misri, Katayoun Saatchi, Sylvia SW Ng, Ujendra Kumar, and Urs O Häfeli.

Evaluation of (111)in labeled antibodies for spect imaging of mesothelin expressing tumors. *Nuclear medicine and biology*, 38(6):885–896, 2011.

Dennis J Mitchell, Lawrence Steinman, Dewey T Kim, Garrison C Fathman, and Jonathan B Rothbard. Polyarginine enters cells more efficiently than other polycationic homopolymers. *Chemical Biology & Drug Design*, 56(5):318–325, 2000.

Fumihiko Miura, Tadahiro Takada, Hodaka Amano, Masahiro Yoshida, Shigeru Furui, and Koji Takeshita. Diagnosis of pancreatic cancer. *HPB*, 8(5):337–342, 2006.

Roberto Montes de Oca Luna, Daniel S Wagner, and Guillermina Lozano. Rescue of early embryonic lethality in mdm2-deficient mice by deletion of p53. *Nature*, 378 (6553):203, 1995.

Patrick S Moore, Stefania Beghelli, Giuseppe Zamboni, and Aldo Scarpa. Genetic abnormalities in pancreatic cancer. *Molecular cancer*, 2(1):7, 2003.

Eugenia Morselli, Ezgi Tasdemir, Maria C Maiuri, Lorenzo Galluzzi, Oliver Kepp, Alfredo Criollo, José M Vicencio, Thierry Soussi, and Guido Kroemer. Mutant p53 protein localized in the cytoplasm inhibits autophagy. *Cell cycle*, 7(19):3056–3061, 2008.

Jennifer P Morton, Paul Timpson, Saadia A Karim, Rachel A Ridgway, Dimitris Athineos, Brendan Doyle, Nigel B Jamieson, Karin A Oien, Andrew M Lowy, Valerie G Brunton, et al. Mutant p53 drives metastasis and overcomes growth arrest/senescence in pancreatic cancer. *Proceedings of the National Academy of Sciences*, 107(1):246–251, 2010.

De-Qing Mu, Guo-Feng Wang, and Shu-You Peng. p53 protein expression and ca19. 9 values in differential cytological diagnosis of pancreatic cancer complicated with chronic pancreatitis and chronic pancreatitis. *World Journal of Gastroenterology: WJG*, 9(8):1815, 2003.

Cristina Müller and Roger Schibli. Single photon emission computed tomography tracer. In *Molecular Imaging in Oncology*, pages 65–105. Springer, 2013.

Patricia AJ Muller and Karen H Vousden. p53 mutations in cancer. *Nature cell biology*, 15(1):2–8, 2013.

Patricia AJ Muller and Karen H Vousden. Mutant p53 in cancer: new functions and therapeutic opportunities. *Cancer cell*, 25(3):304–317, 2014.

Patricia AJ Muller, Karen H Vousden, and Jim C Norman. p53 and its mutants in tumor cell migration and invasion. *The Journal of cell biology*, 192(2):209–218, 2011.

Were LL Munyendo, Huixia Lv, Habiba Benza-Ingoula, Lilechi D Baraza, and Jianping Zhou. Cell penetrating peptides in the delivery of biopharmaceuticals. *Biomolecules*, 2(2):187–202, 2012.

Shoji Nakamori, Kazuo Yashima, Yoshinori Murakami, Osamu Ishikawa, Hiroaki Ohigashi, Shingi Imaoka, Sadanori Yaegashi, Yoichi Konishi, and Takao Sekiya. Association of p53 gene mutations with short survival in pancreatic adenocarcinoma. *Cancer Science*, 86(2):174–181, 1995.

Jacques Neefjes, Marlieke LM Jongsma, Petra Paul, and Oddmund Bakke. Towards a systems understanding of mhc class i and mhc class ii antigen presentation. *Nature reviews. Immunology*, 11(12):823, 2011.

Uwe Niesner, Cornelia Halin, Luisa Lozzi, Maja Günthert, Paolo Neri, Heidi Wunderli-Allenspach, Luciano Zardi, and Dario Neri. Quantitation of the tumor-targeting properties of antibody fragments conjugated to cell-permeating hiv-1 tat peptides. *Bioconjugate chemistry*, 13(4):729–736, 2002.

Roy Noy and Jeffrey W Pollard. Tumor-associated macrophages: from mechanisms to therapy. *Immunity*, 41(1):49–61, 2014.

Johannes Oehlke, Anne Scheller, Burkhard Wiesner, Eberhard Krause, Michael Beyermann, Erhard Klauschenz, Mathias Melzig, and Michael Bienert. Cellular uptake of an α-helical amphipathic model peptide with the potential to deliver polar compounds into the cell interior non-endocytically. *Biochimica et Biophysica Acta (BBA)-Biomembranes*, 1414(1-2):127–139, 1998.

Alice C O'farrell, Steven D Shnyder, Gemma Marston, Louise P Coletta, and Jason H Gill. Non-invasive molecular imaging for preclinical cancer therapeutic development. *British journal of pharmacology*, 169(4):719–735, 2013.

Mikako Ogawa, Celeste AS Regino, Peter L Choyke, and Hisataka Kobayashi. In vivo target-specific activatable near-infrared optical labeling of humanized monoclonal antibodies. *Molecular cancer therapeutics*, 8(1):232–239, 2009.

Jonathan D Oliner, Jennifer A Pietenpol, Sam Thiagalingam, Jeno Gyuris, Ken-

neth W Kinzler, and Bert Vogelstein. Oncoprotein mdm2 conceals the activation domain of tumour suppressor p53. *Nature*, 362(6423):857, 1993.

Kenneth P Olive and David A Tuveson. The use of targeted mouse models for preclinical testing of novel cancer therapeutics. *Clinical Cancer Research*, 12(18): 5277–5287, 2006.

Kenneth P Olive, David A Tuveson, Zachary C Ruhe, Bob Yin, Nicholas A Willis, Roderick T Bronson, Denise Crowley, and Tyler Jacks. Mutant p53 gain of function in two mouse models of li-fraumeni syndrome. *Cell*, 119(6):847–860, 2004.

Magali Olivier, Monica Hollstein, and Pierre Hainaut. Tp53 mutations in human cancers: origins, consequences, and clinical use. *Cold Spring Harbor perspectives in biology*, 2(1):a001008, 2010.

Steffen Ormanns, Jens T Siveke, Volker Heinemann, Michael Haas, Bence Sipos, Anna M Schlitter, Irene Esposito, Andreas Jung, Rüdiger P Laubender, Stephan Kruger, et al. perk, pakt and p53 as tissue biomarkers in erlotinib-treated patients with advanced pancreatic cancer: a translational subgroup analysis from aio-pk0104. *BMC cancer*, 14(1):624, 2014.

Niki A Ottenhof, Roeland F de Wilde, Anirban Maitra, Ralph H Hruban, and G Johan A Offerhaus. Molecular characteristics of pancreatic ductal adenocarcinoma. *Pathology research international*, 2011, 2011.

Dhavan A Parikh, Blythe Durbin-Johnson, and Shiro Urayama. Utility of serum ca19-9 levels in the diagnosis of pancreatic ductal adenocarcinoma in an endoscopic

ultrasound referral population. *Journal of gastrointestinal cancer*, 45(1):74–79, 2014.

Jinseu Park, Jiyoon Ryu, Kyeong-Ae Kim, Hak J Lee, Jae H Bahn, Kyuhyung Han, Eui Y Choi, Kil S Lee, Hyeok Y Kwon, and Soo Y Choi. Mutational analysis of a human immunodeficiency virus type 1 tat protein transduction domain which is required for delivery of an exogenous protein into mammalian cells. *Journal of general virology*, 83(5):1173–1181, 2002a.

John W Park, Keelung Hong, Dmitri B Kirpotin, Gail Colbern, Refaat Shalaby, Jose Baselga, Yvonne Shao, Ulrik B Nielsen, James D Marks, Dan Moore, et al. Anti-her2 immunoliposomes. *Clinical Cancer Research*, 8(4):1172–1181, 2002b.

Leena N Patel, Jennica L Zaro, and Wei-Chiang Shen. Cell penetrating peptides: intracellular pathways and pharmaceutical perspectives. *Pharmaceutical research*, 24(11):1977–1992, 2007.

Kathelijne Peremans, Bart Cornelissen, Bieke Van Den Bossche, Kurt Audenaert, and Christophe Van de Wiele. A review of small animal imaging planar and pinhole spect γ camera imaging. *Veterinary Radiology & Ultrasound*, 46(2):162–170, 2005.

Patrick J Perik, Marjolijn N Lub-De Hooge, Jourik A Gietema, Winette TA van der Graaf, Alexander M de Korte, Sharon Jonkman, Jos GW Kosterink, Dirk J van Veldhuisen, Dirk T Sleijfer, Pieter L Jager, et al. Indium-111–labeled trastuzumab scintigraphy in patients with human epidermal growth factor receptor 2–positive metastatic breast cancer. *Journal of Clinical Oncology*, 24(15):2276–2282, 2006.

Audrey Petitjean, Ewy Mathe, Shunsuke Kato, Chikashi Ishioka, Sean V Tavtigian, Pierre Hainaut, and Magali Olivier. Impact of mutant p53 functional properties on tp53 mutation patterns and tumor phenotype: lessons from recent developments in the iarc tp53 database. *Human mutation*, 28(6):622–629, 2007.

Christine E Pietsch, Stephen M Sykes, Steven B McMahon, and Maureen E Murphy. The p53 family and programmed cell death. *Oncogene*, 27(50):6507, 2008.

Valery Polyakov, Vijay Sharma, Julie L Dahlheimer, Christina M Pica, Gary D Luker, and David Piwnica-Worms. Novel tat-peptide chelates for direct transduction of technetium-99m and rhenium into human cells for imaging and radiotherapy. *Bioconjugate chemistry*, 11(6):762–771, 2000.

Margus Pooga, Mattias Hällbrink, Matjal Zorko, et al. Cell penetration by transportan. *The FASEB Journal*, 12(1):67–77, 1998.

Viktoriia Postupalenko, Annie-Paule Sibler, Dominique Desplancq, Yves Nominé, Danièle Spehner, Patrick Schultz, Etienne Weiss, and Guy Zuber. Intracellular delivery of functionally active proteins using self-assembling pyridylthiourea-polyethylenimine. *Journal of Controlled Release*, 178:86–94, 2014.

Yehonathan Pouny, Doron Rapaport, Amram Mor, Pierre Nicolas, and Yechiel Shai. Interaction of antimicrobial dermaseptin and its fluorescently labeled analogs with phospholipid membranes. *Biochemistry*, 31(49):12416–12423, 1992.

Parviz M Pour, Krishan K Pandey, and Surinder K Batra. What is the origin of pancreatic adenocarcinoma? *Molecular cancer*, 2(1):13, 2003.

Eric W Price, Brian M Zeglis, Jason S Lewis, Michael J Adam, and Chris Orvig. H 6 phospa-trastuzumab: bifunctional methylenephosphonate-based chelator with 89 zr, 111 in and 177 lu. *Dalton Transactions*, 43(1):119–131, 2014.

Marybeth A Pysz, Sanjiv S Gambhir, and Jürgen K Willmann. Molecular imaging: current status and emerging strategies. *Clinical radiology*, 65(7):500–516, 2010.

Arman Rahmim and Habib Zaidi. Pet versus spect: strengths, limitations and challenges. *Nuclear medicine communications*, 29(3):193–207, 2008.

Chary Rangacharyulu and Christine K Roh. Isotopes for combined pet/spect imaging. *Journal of Radioanalytical and Nuclear Chemistry*, 305(1):87–92, 2015.

Janice M Reichert. Antibodies to watch in 2017. In *MAbs*, volume 9, pages 167–181. Taylor & Francis, 2017.

Raymoind Reilly, Nicole Lee, Sylvain Houle, John Law, and Alexander Marks. In vitro stability of edta and dtpa immunoconjugates of monoclonal antibody 2g3 labeled with indium-111. *International journal of radiation applications and instrumentation. Part A. Applied radiation and isotopes*, 43(8):961–967, 1992.

Raul C Ribeiro, Fabiano Sandrini, Bonald Figueiredo, Gerard P Zambetti, Edson Michalkiewicz, Antony R Lafferty, Luiz DeLacerda, Mark Rabin, Craig Cadwell, Gilberto Sampaio, et al. An inherited p53 mutation that contributes in a tissue-specific manner to pediatric adrenal cortical carcinoma. *Proceedings of the National Academy of Sciences*, 98(16):9330–9335, 2001.

Jean P Richard, Kamran Melikov, Eric Vives, Corinne Ramos, Birgit Verbeure, Mike J Gait, Leonid V Chernomordik, and Bernard Lebleu. Cell-penetrating peptides a reevaluation of the mechanism of cellular uptake. *Journal of Biological Chemistry*, 278(1):585–590, 2003.

Jean P Richard, Kamran Melikov, Hilary Brooks, Paul Prevot, Bernard Lebleu, and Leonid V Chernomordik. Cellular uptake of unconjugated tat peptide involves clathrin-dependent endocytosis and heparan sulfate receptors. *Journal of Biological Chemistry*, 280(15):15300–15306, 2005.

Terry L Riss, Richard A Moravec, Andrew L Niles, Sarah Duellman, Hélène A Benink, Tracy J Worzella, and Lisa Minor. Cell viability assays. 2016.

Philipp Ritt, Hans Vija, Joachim Hornegger, and Torsten Kuwert. Absolute quantification in spect. *European journal of nuclear medicine and molecular imaging*, 38 (1):69–77, 2011.

Caio M Rocha Lima, Mark R Green, Robert Rotche, Wilson H Miller Jr, Mark G Jeffrey, Laura A Cisar, Adele Morganti, Nicoletta Orlando, Gabriela Gruia, and Langdon L Miller. Irinotecan plus gemcitabine results in no survival advantage compared with gemcitabine monotherapy in patients with locally advanced or metastatic pancreatic cancer despite increased tumor response rate. *Journal of Clinical Oncology*, 22(18):3776–3783, 2004.

Kenneth L Rock, Ian A York, and Alfred L Goldberg. Post-proteasomal antigen

processing for major histocompatibility complex class i presentation. *Nature immunology*, 5(7):670, 2004.

Alessandro Rufini, Paola Tucci, Ivana Celardo, and Gerry Melino. Senescence and aging: the critical roles of p53. *Oncogene*, 32(43):5129, 2013.

Christopher J Scarlett, Elizabeth L Salisbury, Andrew V Biankin, and James Kench. Precursor lesions in pancreatic cancer: morphological and molecular pathology. *Pathology*, 43(3):183–200, 2011.

Aldo Scarpa, Paola Capelli, Kiyoshi Mukai, Giuseppe Zamboni, Tatsuya Oda, Calogero Iacono, and Setsuo Hirohashi. Pancreatic adenocarcinomas frequently show p53 gene mutations. *The American journal of pathology*, 142(5):1534, 1993.

Nathan Schmidt, Abhijit Mishra, Ghee H Lai, and Gerard CL Wong. Arginine-rich cell-penetrating peptides. *FEBS letters*, 584(9):1806–1813, 2010.

Steven R Schwarze, Alan Ho, Adamina Vocero-Akbani, and Steven F Dowdy. In vivo protein transduction: delivery of a biologically active protein into the mouse. *Science*, 285(5433):1569–1572, 1999.

Armon Sharei, Janet Zoldan, Andrea Adamo, Woo Y Sim, Nahyun Cho, Emily Jackson, Shirley Mao, Sabine Schneider, Min-Joon Han, Abigail Lytton-Jean, et al. A vector-free microfluidic platform for intracellular delivery. *Proceedings of the National Academy of Sciences*, 110(6):2082–2087, 2013.

Jerry W Shay, Olivia M Pereira-Smith, and Woodring E Wright. A role for both rb

and p53 in the regulation of human cellular senescence. *Experimental cell research*, 196(1):33–39, 1991.

Chanjuan Shi, Ralph H Hruban, and Alison P Klein. Familial pancreatic cancer. *Archives of pathology & laboratory medicine*, 133(3):365–374, 2009.

Sheau-Yann Shieh, Masako Ikeda, Yoichi Taya, and Carol Prives. Dna damage-induced phosphorylation of p53 alleviates inhibition by mdm2. *Cell*, 91(3):325–334, 1997.

Hung P Shih, Allen Wang, and Maike Sander. Pancreas organogenesis: from lineage determination to morphogenesis. *Annual review of cell and developmental biology*, 29:81–105, 2013.

Ronit V Sionov, Igal L Hayon, and Ygal Haupt. The regulation of p53 growth suppression. In *Madame Curie Bioscience Database*. Landes Bioscience, 2013.

Hayla K Sluss, Heather Armata, Judy Gallant, and Stephen N Jones. Phosphorylation of serine 18 regulates distinct p53 functions in mice. *Molecular and cellular biology*, 24(3):976–984, 2004.

Hoseok Song, Monica Hollstein, and Yang Xu. p53 gain-of-function cancer mutants induce genetic instability by inactivating atm. *Nature cell biology*, 9(5):573, 2007.

Oliver Strobel and Markus W Büchler. Pancreatic cancer: Fdg-pet is not useful in early pancreatic cancer diagnosis. *Nature Reviews Gastroenterology and Hepatology*, 10(4):nrgastro–2013, 2013.

Tomoki Suzuki, Shiroh Futaki, Miki Niwa, Seigo Tanaka, Kunihiro Ueda, and Yukio Sugiura. Possible existence of common internalization mechanisms among arginine-rich peptides. *Journal of Biological Chemistry*, 277(4):2437–2443, 2002.

Koichi Tanaka, Koei Okazaki, Noriko Okazaki, Takafumi Ueda, Akio Sugiyama, Hiroshi Nojima, and Hiroto Okayama. A new cdc gene required for s phase entry of schizosaccharomyces pombe encodes a protein similar to the cdc 10+ and swi4 gene products. *The EMBO journal*, 11(13):4923, 1992.

William R Taylor and George R Stark. Regulation of the g2/m transition by p53. *Oncogene*, 20(15):1803, 2001.

Matthias Theobald, Thomas Ruppert, Ulrike Kuckelkorn, Javier Hernandez, Annett Häussler, Edite Antunes Ferreira, Ulrike Liewer, Judith Biggs, Arnold J Levine, Christoph Huber, et al. The sequence alteration associated with a mutational hotspot in p53 protects cells from lysis by cytotoxic t lymphocytes specific for a flanking peptide epitope. *Journal of Experimental Medicine*, 188(6):1017–1028, 1998.

Per EG Thorén, Daniel Persson, Petter Isakson, Mattias Goksör, Agneta Önfelt, and Bengt Nordén. Uptake of analogs of penetratin, tat (48–60) and oligoarginine in live cells. *Biochemical and biophysical research communications*, 307(1):100–107, 2003.

Vladimir Tolmachev, Jennie Malmberg, Sergio Estrada, Olof Eriksson, and Anna Orlova. Development of a 124i-labeled version of the anti-psma monoclonal an-

tibody capromab for immunopet staging of prostate cancer: Aspects of labeling chemistry and biodistribution. *International journal of oncology*, 44(6):1998–2008, 2014.

Huimin Tong, Lei Zhang, Allan Kaspar, Matthew J Rames, Liqing Huang, Gary Woodnutt, and Gang Ren. Peptide-conjugation induced conformational changes in human igg1 observed by optimized negative-staining and individual-particle electron tomography. *Scientific reports*, 3:1089, 2013.

Vladimir P Torchilin, Ram Rammohan, Volkmar Weissig, and Tatyana S Levchenko. Tat peptide on the surface of liposomes affords their efficient intracellular delivery even at low temperature and in the presence of metabolic inhibitors. *Proceedings of the National Academy of Sciences*, 98(15):8786–8791, 2001.

Julia Baguña Torres, James C Knight, Michael J Mosley, Veerle Kersemans, Sofia Koustoulidou, Danny Allen, Paul Kinchesh, Sean Smart, and Bart Cornelissen. Imaging of claudin-4 in pancreatic ductal adenocarcinoma using a radiolabelled anti-claudin-4 monoclonal antibody. *Molecular Imaging and Biology*, pages 1–8, 2017.

Sara Trabulo, Ana-Luísa Cardoso, Miguel Mano, and Maria C Pedroso De Lima. Cell-penetrating peptides—mechanisms of cellular uptake and generation of delivery systems. *Pharmaceuticals*, 3(4):961–993, 2010.

Kwong Y Tsang, Sam Zaremba, Carol A Nieroda, Ming Z Zhu, Michael J Hamilton, and Jeffrey Schlom. Generation of human cytotoxic t cells specific for human carci-

noembryonic antigen epitopes from patients immunized with recombinant vaccinia-cea vaccine. *JNCI: Journal of the National Cancer Institute*, 87(13):982–990, 1995.

Federica Turati, Valeria Edefonti, Cristina Bosetti, Monica Ferraroni, Matteo Malvezzi, Silvia Franceschi, Renato Talamini, Maurizio Montella, Fabio Levi, Luigino Dal Maso, et al. Family history of cancer and the risk of cancer: a network of case–control studies. *Annals of oncology*, 24(10):2651–2656, 2013.

Mathias Uhlen, Anita Bandrowski, Steven Carr, Aled Edwards, Jan Ellenberg, Emma Lundberg, David L Rimm, Henry Rodriguez, Tara Hiltke, Michael Snyder, et al. A proposal for validation of antibodies. *Nature methods*, 2016.

Asad Umar, Barbara K Dunn, and Peter Greenwald. Future directions in cancer prevention. *Nature reviews. Cancer*, 12(12):835, 2012.

Felix Unverdorben, Fabian Richter, Meike Hutt, Oliver Seifert, Pauline Malinge, Nicolas Fischer, and Roland E Kontermann. Pharmacokinetic properties of igg and various fc fusion proteins in mice. In *MAbs*, volume 8, pages 120–128. Taylor & Francis, 2016.

Karen Van Audenhaege, Roel Van Holen, Stefaan Vandenberghe, Christian Vanhove, Scott D Metzler, and Stephen C Moore. Review of spect collimator selection, optimization, and fabrication for clinical and preclinical imaging. *Medical physics*, 42(8):4796–4813, 2015.

Guus AMS Van Dongen, Gerard WM Visser, Marjolijn N Lub-de Hooge, Elisabeth G

De Vries, and Lars R Perk. Immuno-pet: a navigator in monoclonal antibody development and applications. *The oncologist*, 12(12):1379–1389, 2007.

Thierry F Vandamme. Use of rodents as models of human diseases. *Journal of pharmacy & bioallied sciences*, 6(1):2, 2014.

Homayoun Vaziri, Michael D West, Richard C Allsopp, Timothy S Davison, Yu-Sung Wu, Cheryl H Arrowsmith, Guy G Poirier, and Samuel Benchimol. Atm-dependent telomere loss in aging human diploid fibroblasts and dna damage lead to the post-translational activation of p53 protein involving poly (adp-ribose) polymerase. *The EMBO journal*, 16(19):6018–6033, 1997.

Michel PM Vierboom, Sander Zwaveling, Gerard MJ Bos, Marlies Ooms, Menno G Krietemeijer, Cornelis JM Melief, and Rienk Offringa. High steady-state levels of p53 are not a prerequisite for tumor eradication by wild-type p53-specific cytotoxic t lymphocytes. *Cancer research*, 60(19):5508–5513, 2000.

Oskar Vilhelmsson-Timmermand, Elmer Santos, Daniel LJ Thorek, Susan Evans-Axelsson, Anders Bjartell, Hans Lilja, Steven M Larson, Sven-Erik Strand, Thuy A Tran, and David Ulmert. Radiolabeled antibodies in prostate cancer: A case study showing the effect of host immunity on antibody bio-distribution. *Nuclear medicine and biology*, 42(4):375–380, 2015.

Audrey Vincent, Joseph Herman, Rich Schulick, Ralph H Hruban, and Michael Goggins. Pancreatic cancer. *The Lancet*, 378(9791):607–620, 2011.

Paolo Vineis and Christopher P Wild. Global cancer patterns: causes and prevention. *The Lancet*, 383(9916):549–557, 2014.

Eric Vives, Priscille Brodin, and Bernard Lebleu. A truncated hiv-1 tat protein basic domain rapidly translocates through the plasma membrane and accumulates in the cell nucleus. *Journal of Biological Chemistry*, 272(25):16010–16017, 1997.

Nicola Waddell, Marina Pajic, Ann-Marie Patch, David K Chang, Karin S Kassahn, Peter Bailey, Amber L Johns, David Miller, Katia Nones, Kelly Quek, et al. Whole genomes redefine the mutational landscape of pancreatic cancer. *Nature*, 518(7540): 495–501, 2015.

Susan S Wallace. Base excision repair: a critical player in many games. *DNA repair*, 19:14–26, 2014.

Maonan Wang, Jingzhou Zhao, Lishen Zhang, Fang Wei, Yu Lian, Yingfeng Wu, Zhaojian Gong, Shanshan Zhang, Jianda Zhou, Ke Cao, et al. Role of tumor microenvironment in tumorigenesis. *Journal of Cancer*, 8(5):761, 2017.

Xinjiang Wang, Jan Taplick, Naama Geva, and Moshe Oren. Inhibition of p53 degradation by mdm2 acetylation. *FEBS letters*, 561(1-3):195–201, 2004.

Yan Wang and Carol Prives. Increased and altered dna binding of human p53 by s and g2/m but not g1 cyclin-dependent kinases. *Nature*, 376(6535):88, 1995.

Jason M Warram, Esther de Boer, Anna G Sorace, Thomas K Chung, Hyunki Kim, Rick G Pleijhuis, Gooitzen M van Dam, and Eben L Rosenthal. Antibody-based

imaging strategies for cancer. *Cancer and Metastasis Reviews*, 33(2-3):809–822, 2014.

Jon A Weidanz, Oriana Hawkins, Bhavna Verma, and William H Hildebrand. Tcr-like biomolecules target peptide/mhc class i complexes on the surface of infected and cancerous cells. *International reviews of immunology*, 30(5-6):328–340, 2011.

Lilach Weisz, Amir Zalcenstein, Perry Stambolsky, Yehudit Cohen, Naomi Goldfinger, Moshe Oren, and Varda Rotter. Transactivation of the egr1 gene contributes to mutant p53 gain of function. *Cancer research*, 64(22):8318–8327, 2004.

James M Wells and Douglas A Melton. Vertebrate endoderm development. *Annual review of cell and developmental biology*, 15(1):393–410, 1999.

Benedikt C Westphalen and Kenneth P Olive. Genetically engineered mouse models of pancreatic cancer. *Cancer journal (Sudbury, Mass.)*, 18(6):502, 2012.

Scott B Worley, Leon T van den Broeke, Theresa J Goletz, C David Pendleton, Emily M Daschbach, Elaine K Thomas, Francesco M Marincola, Lee J Helman, and Jay A Berzofsky. Antigenicity of fusion proteins from sarcoma-associated chromosomal translocations. *Cancer research*, 61(18):6868–6875, 2001.

Anna M Wu. Engineered antibodies for molecular imaging of cancer. *Methods*, 65(1): 139–147, 2014.

Shu-Yuan Xiao. Intraductal papillary mucinous neoplasm of the pancreas: an update. *Scientifica*, 2012, 2012.

Lu Xin. p53: A target and a biomarker of cancer therapy? In *Recent Advances in Cancer Research and Therapy*, pages 197–213. Elsevier, 2012.

Nicole J Yang and Marlon J Hinner. Getting across the cell membrane: an overview for small molecules, peptides, and proteins. *Site-Specific Protein Labeling: Methods and Protocols*, pages 29–53, 2015.

Sung-Tae Yang, Elena Zaitseva, Leonid V Chernomordik, and Kamran Melikov. Cell-penetrating peptide induces leaky fusion of liposomes containing late endosome-specific anionic lipid. *Biophysical journal*, 99(8):2525–2533, 2010.

Chai-Hong Yeong, Mu-hua Cheng, and Kwan-Hoong Ng. Therapeutic radionuclides in nuclear medicine: current and future prospects. *Journal of Zhejiang University Science B*, 15(10):845–863, 2014.

Victor Yip, Enzo Palma, Devin B Tesar, Eduardo E Mundo, Daniela Bumbaca, Elizabeth K Torres, Noe A Reyes, Ben Q Shen, Paul J Fielder, Saileta Prabhu, et al. Quantitative cumulative biodistribution of antibodies in mice: Effect of modulating binding affinity to the neonatal fc receptor. In *MAbs*, volume 6, pages 689–696. Taylor & Francis, 2014.

Zhong Kang Yu, Rory K Geyer, and Carl G Maki. Mdm2-dependent ubiquitination of nuclear and cytoplasmic p53. *Oncogene*, 19(51):5892, 2000.

Qimin Zhan, Michael J Antinore, Xin W Wang, France Carrier, Martin L Smith, Curtis C Harris, and Albert J Fornace Jr. Association with cdc2 and inhibition of

cdc2/cyclin b1 kinase activity by the p53-regulated protein gadd45. *Oncogene*, 18 (18), 1999.

QiuBo Zhang, ShaoJie Chen, LinJuan Zeng, YinTing Chen, GuoDa Lian, ChenChen Qian, JiaJia Li, RuiJie Xie, and Kai-Hong Huang. New developments in the early diagnosis of pancreatic cancer. *Expert review of gastroenterology & hepatology*, 11 (2):149–156, 2017.

Yan Zhang and Long-Chuan Yu. Microinjection as a tool of mechanical delivery. *Current opinion in biotechnology*, 19(5):506–510, 2008.

Appendix A

Appendix

A.1 Full developed gel

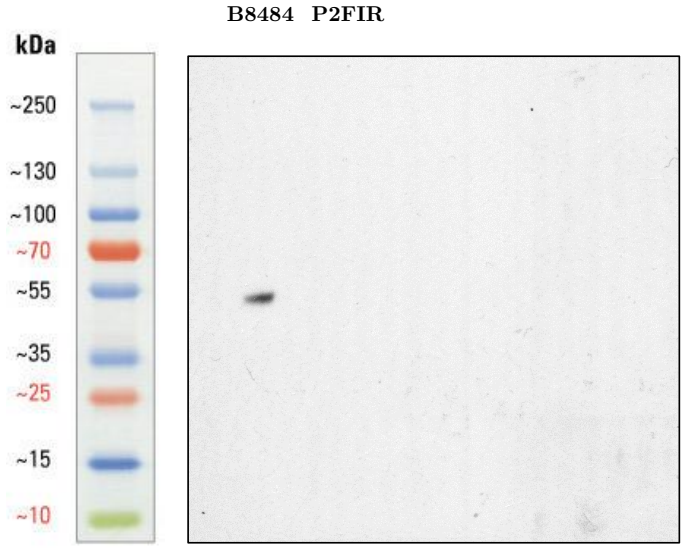

Figure A.1: Full developed film of p53 protein expression levels. The developed film indicated a single band at approximately 53 KDa for p53 protein expression in B8484 and no band in P2FIR KPC-derived cells. Film was developed by ECL detection and no other bands were observed.

A.2 *In vitro* reproducibility

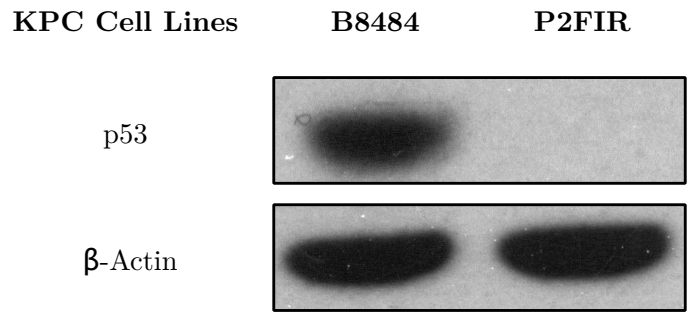

Figure A.2: p53 protein expression levels in B8484 and P2FIR KPC-derived cells. Immunoblotting with mouse monoclonal 1C12 antibody, Lot No 10. β-Actin was blotted as loading control.

A.3 Sub-cellular fractionation

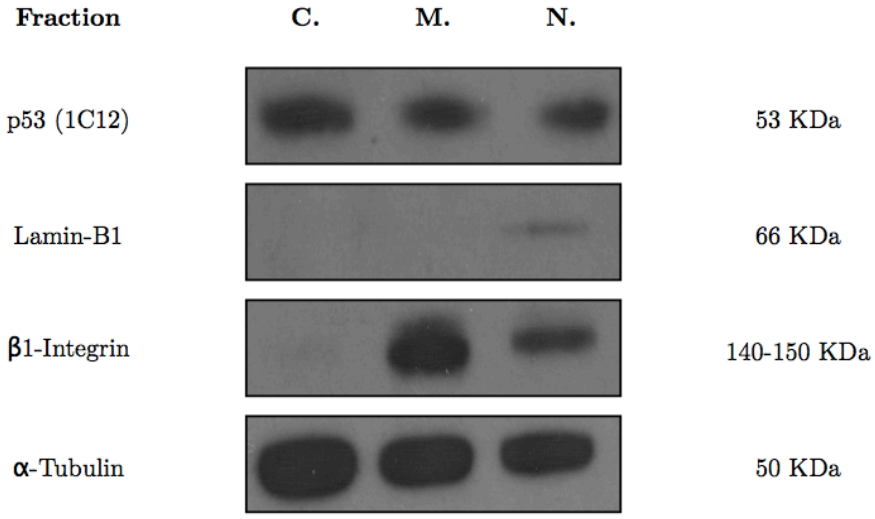

Figure A.3: Sub-cellular fractionation in B8484 KPC-derived cell line. Immunoblotitng with mouse monoclonal anti-p53 (1C12) antibody was performed after fractionation of B8484 whole cell lysate into cytoplasmic (C.), membrane (M.) and nuclear (N.) fractions. Lamin-B1 was used as nuclear fraction control, β1-Integrin as a membrane fraction control and α-Tubulin as a cytoplasmic fraction control.

A.4 Imaging of KPC genetically engineered mouse models

The ^{111}In-BnDTPA-p53 (1C12)-TAT radioconjugate was also assessed in the KPC genetically engineered mouse model, which presents an accurate histopathological correlation to human PDAC. All animals were evaluated by MRI for spontaneous PDAC development following initiation of the pre-invasive lesions.

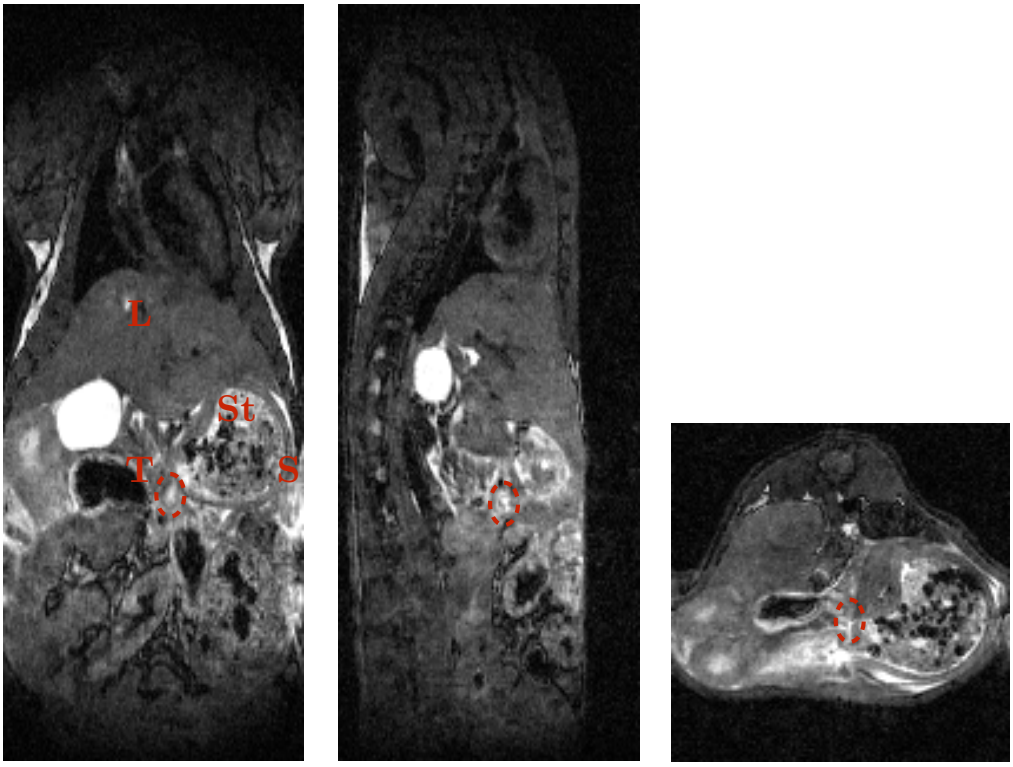

Figure A.4: Identification of pancreatic tumours by MRI. Representative combined T1- and T2-weighted 3D gradient-echo sequence coronal (left), sagittal (centre), and axial (right) images of a KPC mouse model. Stomach (St), liver (L), and spleen (S) are indicated to determine the position of pancreas. Suspected tumour (T) is highlighted by dashed circle.

When a tumour was detected by MRI (Figure A.4), animals (≈ 20 week old) were injected with ^{111}In-BnDTPA-p53 (1C12)-TAT and 72 h later injected again with ^{18}F-

FDG (5 MBq), which was used to delineate tumour tissue. Dual tracer imaging sessions were carried out using the VECTor^{4}CT following 1 h uptake after ^{18}F-FDG injection, as described in Section 5.2.4.

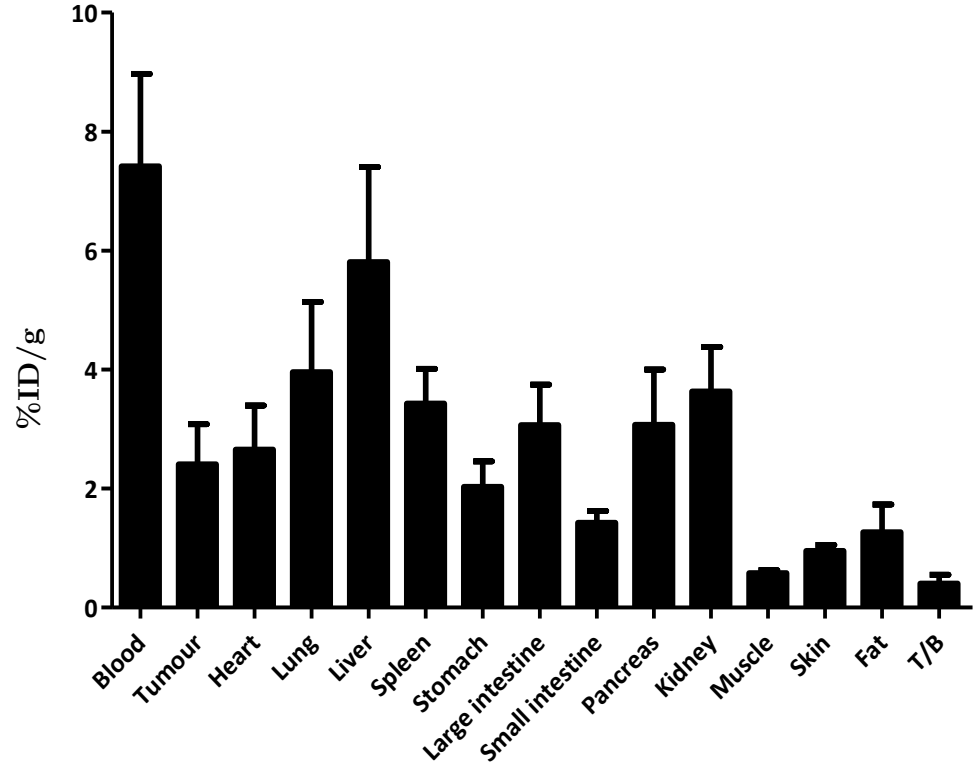

Figure A.5: *Ex vivo* biodistribution analysis showing uptake of ^{111}In-BnDTPA-p53 (1C12)-TAT in KPC mice 72 h post-injection. Data are expressed as %ID/g and error bars represent mean ± SEM (n = 4 mice/group).

Figure A.5 shows the *ex vivo* biodistribution of ^{111}In-BnDTPA-p53 (1C12)-TAT at 72 h post-injection. Accumulation of ^{111}In-BnDTPA-p53 (1C12)-TAT was similar across different organs, with blood, liver, and lungs (7.4 ± 3.0, 5.8 ± 3.2, and 4.0 ± 2.4%ID/g, respectively) showing the highest uptake of radioactivity but markedly lower %ID/g values than those observed in an allograft mouse models (Figure 5.2 and Figure 5.6). Uptake of radioactivity in the tumour, dissected from the pancreatic tissue, was as low as 2.4 ± 1.4%ID/g with the T/B ratio reaching only 0.4 ± 0.3 (as determined

by *ex vivo* biodistribution). Accumulation of ^{111}In-BnDTPA-p53 (1C12)-TAT in the pancreas was no different to that of the tumour (3.1 ± 1.9%ID/g, p = 0.5846, Student's t-test).

Surprisingly, uptake of ^{18}F-FDG within the tumour and pancreas was low (1.5 ± 1.2 and 1.7 ± 1.3%ID/g, respectively) and similar to the homogeneous distribution in normal tissues (excluding heart, Figure A.6).

These low uptake values of ^{18}F-FDG may have occurred due to environmental factors during the scanning period (heating, anaesthesia and fasting) and therefore, could have affected the uptake of the tracer, as described in (Fueger et al., 2006), and therefore direct comparisons cannot be made.

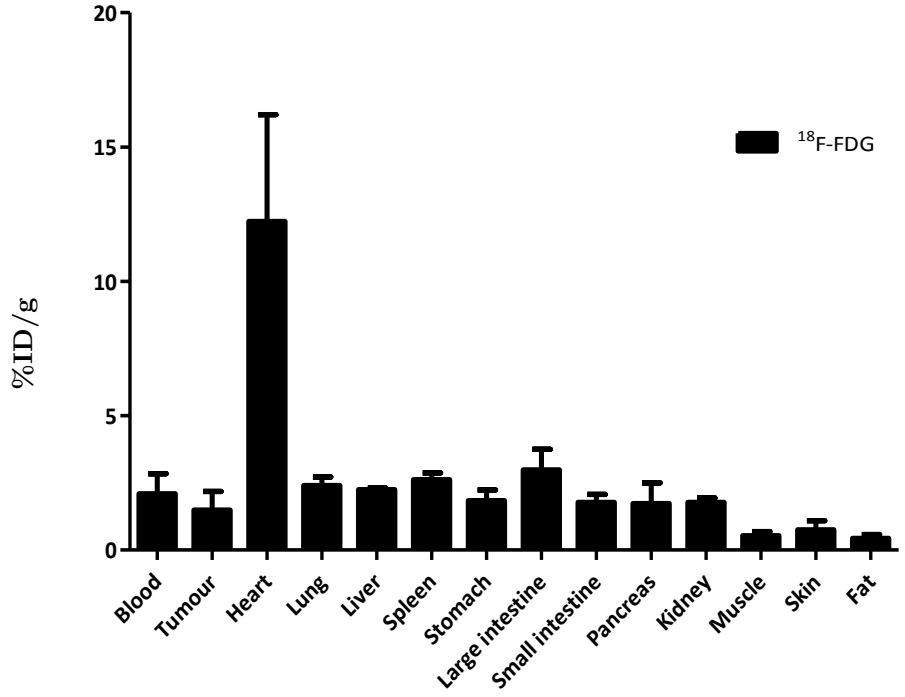

Figure A.6: *Ex vivo* Biodistribution of ^{18}F-FDG in the KPC mouse model following 1 h uptake.Data are expressed as %ID/g and error bars represent mean ± SEM (n = 4 mice/group).

Representative SPECT and PET MIP images demonstrate the uptake pattern of

^{111}In-BnDTPA-p53 (1C12)-TAT (Figure A.7, left panel) and ^{18}F-FDG (Figure A.7, right panel). Diffuse spots of ^{111}In-BnDTPA-p53 (1C12)-TAT accumulation were present across the body, most evidently in the bladder, heart, and facial papillomas. Some uptake was also observed in the upper surface of the abdomen. ^{18}F-FDG uptake could be mostly noted in the bladder, heart, and brain. Minimum uptake was also spotted below heart and on the spinal cord. No evident tumour uptake was identified, making the correlation of ^{18}F-FDG signal to the one from SPECT images, difficult.

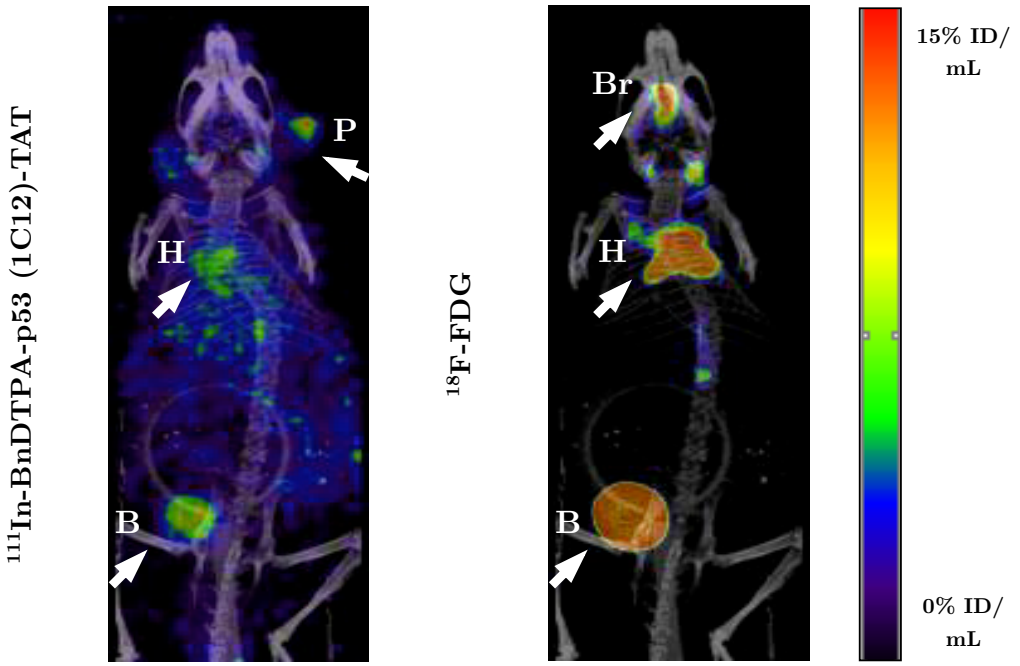

Figure A.7: *In vivo* imaging of the KPC mice by SPECT/PET/CT. Representative maximum intensity projection images of a KPC mouse injected with ^{111}In-BnDTPA-p53 (1C12)-TAT (left) and 72 h later with ^{18}F-FDG (right). Arrows point to tissues showing marked uptake of ^{111}In-BnDTPA-p53 (1C12)-TAT and ^{18}F-FDG including heart (H), bladder (B), facial papillomas (P) from SPECT/CT image, brain (Br) from ^{18}F-FDG PET/CT image.

A.4.1 Tissue distribution of ^{111}In-BnDTPA-p53 (1C12)-TAT in the KPC model

Co-localisation of ^{111}In-BnDTPA-p53 (1C12)-TAT in the pancreatic tumour and the remaining pancreatic tissue was tested by *ex vivo* autoradiography and H&E staining (Section 5.2.5.1). Figure A.8 shows co-registered images of a representative KPC-derived pancreas where distribution of the radioconjugate is observed throughout the whole tissue surface and within the inner area of the pancreas. A closer look on the histology images (Figure A.8, lower panel) revealed the presence of PanIN-like lesions, corresponding to areas of ^{111}In-BnDTPA-p53 (1C12)-TAT accumulation.

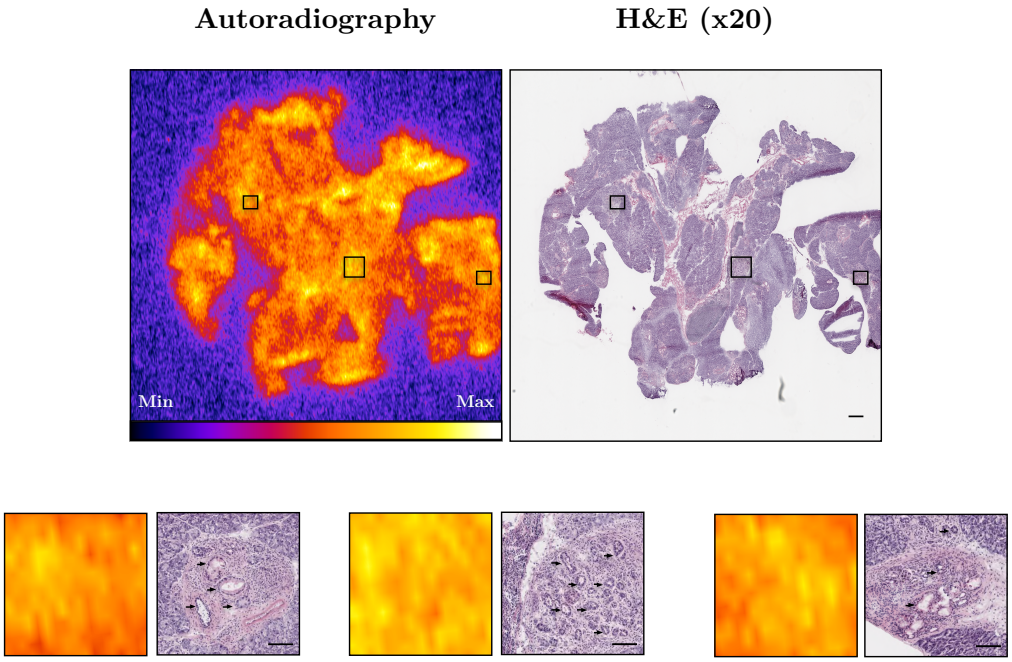

Figure A.8: Distribution of ^{111}In-BnDTPA-p53 (1C12)-TAT in the pancreas of a KPC mouse model. Cropped autoradiography and histology images follow the assigned area from left to right on the whole tissue image. Arrows point to PanIN-like lesions showing co-localisation to the accumulated ^{111}In-BnDTPA-p53 (1C12)-TAT radioconjugate. Scale bar on the full histology images is 500 µm and for the cropped image is 200 µm.

These particular lesions present evident cytological and architectural atypia, noted by nuclear clustering and papillary architecture, suggesting prob ably a higher grade than PanIN-1 stage, even though accurate histopathological examination is necessary. The dissected pancreatic tumour also showed high levels of ^{111}In-BnDTPA-p53 (1C12)-TAT accumulation through the majority of the section (Figure A.9), which was characterised by complete architectural disorganisation and enlarged nuclei.

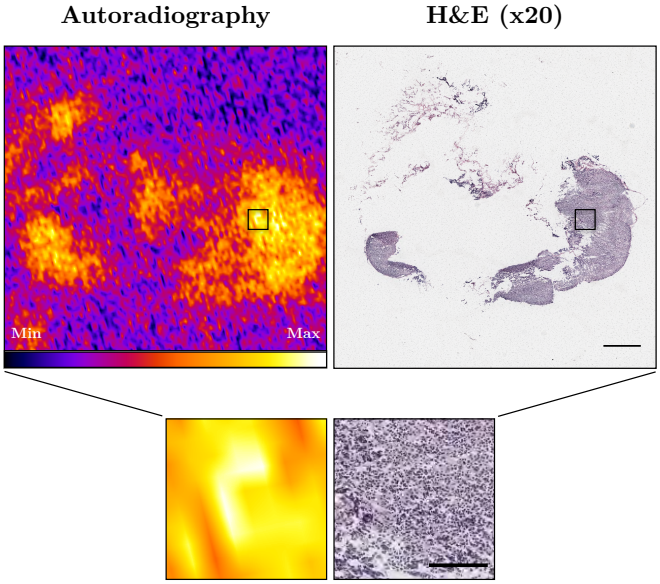

Figure A.9: Representative image of ^{111}In-BnDTPA-p53 (1C12)-TAT distribution in the dissected pancreatic tumour of a KPC mouse model as defined by *ex vivo* autoradiography referenced to a hematoxylin and eosin staining. Scale bar on the full histology images is 500 µm and for the cropped image is 200 µm.

To further validate whether the accumulation of radioactivity corresponds to a true p53 signal, immunohistochemistry was performed on frozen sections, as described before (Section 5.2.5.2) using the anti-p53 (CM5) primary antibody. Both tissue sections, pancreas and tumour, showed a more cytosolic signal (Figure A.10), that did not correspond to the nuclear localisation pattern observed above, suggesting the unsuitability of this model for imaging p53 (Figure 5.10).

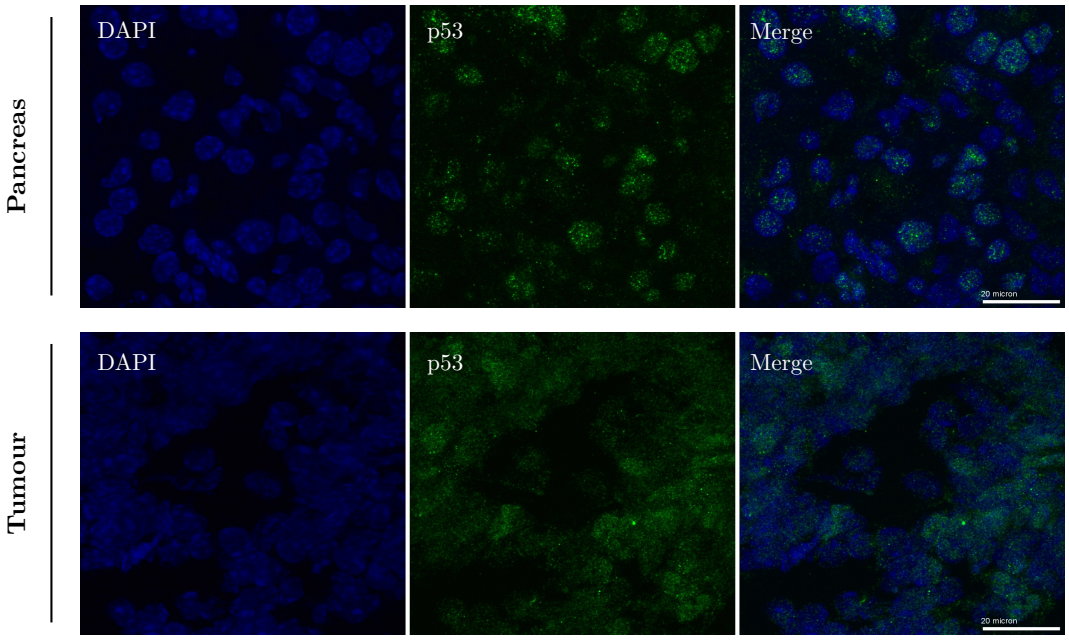

Figure A.10: Endogenous p53 expression levels in KPC-derived tissues. KPC-derived pancreas and tumour were were stained with the anti-p53 (CM5) antibody (green), nuclei were counterstained using DAPI (blue) and tissues were examined by fluorescence microscopy. Scale bar is 20 µm for all images.